Statistical Mechanics of the Square Lattice Planar Rotator Model and Metamagnetism in Bilayer Strontium Ruthenate $Sr_3Ru_2O_7$

by

Matthew Robson

A thesis submitted to
The University of Birmingham
for the degree of
DOCTOR OF PHILOSOPHY

School of Physics and Astronomy
College of Engineering and Physical Sciences
The University of Birmingham
September 2017

UNIVERSITY OF
BIRMINGHAM

University of Birmingham Research Archive

e-theses repository

This unpublished thesis/dissertation is copyright of the author and/or third parties. The intellectual property rights of the author or third parties in respect of this work are as defined by The Copyright Designs and Patents Act 1988 or as modified by any successor legislation.

Any use made of information contained in this thesis/dissertation must be in accordance with that legislation and must be properly acknowledged. Further distribution or reproduction in any format is prohibited without the permission of the copyright holder.

Acknowledgements

First and foremost I would like to thank my supervisor, Martin Long, who is the real originator of all of the work reported in this thesis. I am grateful to have been allowed to participate in the research, and to be exposed to lots of interesting physics. Great thanks also go to Amy Briffa, Richard Mason and Andy Cave, all of whom taught, mentored and encouraged me in the early days. Thank you to Jordan Moodie and Manjinder Kainth, who thanks to me have spent a huge chunk of the first year of their PhD's proof-reading this thesis.

Thanks to some PhD pals: Matt (for teaching me to play Bridge!), Jack, Greg, Austin, John, Ehren, Filippo, Raul, Max and Hannah.

Lastly, thanks, Mum and Dad, for everything.

Abstract

We have investigated the thermodynamics of the square lattice planar rotator model. By calculating a variety of thermodynamic quantities for the planar rotator model on a sequence of one-dimensional geometries using transfer functions, we find evidence that the square lattice model exhibits an ordinary thermodynamic phase transition, with power-law singularities in the thermodynamics described by the usual set of critical exponents. This is in contrast to the widely-held view that the phase transition in the model should be of the Kosterlitz-Thouless type.

We have contructed a Hubbard-type model of bilayer strontium ruthenate $Sr_3Ru_2O_7$. We find that the Hartree-Fock mean field solution of our model can be made to exhibit a metamagnetic jump that matches that seen in $Sr_3Ru_2O_7$, and this is clearly associated with a certain quasi one-dimensional feature in the electronic structure. We therefore suggest that this is the origin of the metamagnetism in $Sr_3Ru_2O_7$. The metamagnetism in our modelling is associated with a phase-separated mixture of low- and high-magnetisation solutions, which we suggest corresponds to the nematic phase in $Sr_3Ru_2O_7$.

Contents

List of Figures

Part I

Statistical Mechanics of the Square Lattice Planar Rotator Model

We have investigated the phase transition in the square lattice planar rotator model using transfer operators. We consider the model on a one-dimensional geometry which will become the infinite square lattice in the limit that a certain parameter tends to infinity; we calculate the thermodynamics for a series of systems and perform a polynomial extrapolation to this limit. This technique is essentially an application of exact diagonalisation. The same method has already been applied to a variety of classical spin models, and these investigations are reported in the PhD theses of R. Mason and A. M. Cave. The work in the present thesis is connected to A. M. Cave's thesis, which studied the square lattice clock model: one of the two phase transitions in this model is the same as the phase transition in the planar rotator model, and therefore this thesis and A. M. Cave's are to a great extent alternative approaches to the same problem. We calculate a variety of thermodynamic quantities. Our results are indicative that in the two-dimensional limit the thermodynamics of the planar rotator model will become divergent, and that there is a regular phase transition with ordinary critical exponents. This is contradictory to the strong expectation regarding the phase transition in this model that it should be a Kosterlitz-Thouless transition.

Chapter 1

Overview of Classical Statistical Mechanics and the Planar Rotator Model

This investigation is concerned with the phase transition in the square lattice planar rotator model. To set this work in context, it is necessary first to introduce both classical phase transitions in general, and what is known about the thermodynamics of this particular model. The square lattice planar rotator model is an archetypal example of a system which undergoes a finite temperatue phase transition despite it being forbidden to have long range order. The well-established picture of how such a system can have a phase transition is the Kosterlitz-Thouless transition, which is mediated by vortices, and is characterised by very particular critical behaviour which is very unlike other thermodynamic phase transitions. This chapter is intended to provide an overview of these physical ideas. The techniques of the transfer matrix and one-to-two dimensional crossover and the actual investigation of the planar rotator model is dealt with in the next chapter.

We begin in section 1.1 with a brief overview of classical phase transitions. We establish the standard picture of a regular phase transition and the associated ideas of an order parameter and critical exponents. We also describe the concepts of universality and the renormalisation group. Section 1.2 then narrows the scope to discuss low-dimensional classical spin systems. We define the three paradigms of disorder, long-range order and quasi-long-range order using the spin-spin correlation

function. We then carefully provide the argument due to Landau which prevents long-range order in one-dimensional discrete spin-systems, and the Mermin-Wagner theorem which forbids long-range order in isotropic systems in one and two dimensions. We conclude this section with a proof of the Mermin-Wagner theorem for the planar rotator model. Section 1.3 is devoted entirely to the planar rotator model. In section 1.3.1 we describe the relationship of the planar rotator model to other statistical mechanics models, and in section 1.3.2 we discuss its relationship to bosonic systems. We provide the argument for the existence of a phase transition based on the long-range form of the spin-spin correlation function in the high- and low-temperature limits in sections 1.3.3 and 1.3.4. In section 1.3.5 we describe the helical stiffness, which is a quantity which is somewhat like an order parameter in the absence of long-range order. We conclude by giving a brief exposition of the Kosterlitz-Thouless theory in section 1.3.6.

1.1 Statistical mechanics and phase transitions

Because our investigation of the square lattice planar rotator model is concerned entirely with the phase transition in that model, it is essential to first introduce classical phase transitions. This section is intended as a whistle-stop tour of the key concepts in classical phase transitions, at the level of an introductory undergraduate course. In section 1.1.1 we introduce phase transitions as being associated with singularities in thermodynamic functions, we define the order parameter and the critical exponents, and we introduce the idea of universality. We pose the problem of phase transitions, from a theoretical physics perspective, as explaining universality and calculating the critical exponents for specific systems. In section 1.1.2 we discuss mean field theories of phase transitions. We discuss how mean field theory can provide a phase transition, but that it can only produce a very restricted set of values for the critical exponents, and that its qualitative predictions are completely incorrect for low-dimensional systems. In section 1.1.3 we discuss the renormalisation group, which provides a theoretical framework in which to explain universality and does allow the calculation of non-trivial critical exponents.

1.1.1 Continuous phase transitions: singularities in thermodynamic functions

A phase transition is a change in the character of a system associated with a non-analyticity in the thermodynamic functions of that system. Phase transitions are of course familiar to the layperson in the form of the solid-to-liquid transition of, for example, ice. This is an example of a *first order* phase transition, which is signalled by a discontinuity in the first derivative of the free energy with respect to temperature. In a great many cases, phase transitions take place between phases which are characterised as having distinct symmetries. In an example of the solid-to-liquid transition, one can picture the solid phase as a crystal lattice, with a particular set of translational symmetries which map the lattice points onto one another, while in the liquid phase any translation whatsoever is a symmetry. The transition between these two phases occurs at a very particular temperature, the *critical temperature* T_C, and is undergone with the absorption or the release of a quantity of heat, the *latent heat*, while the system remains at the temperature T_C.

In a first order transition, both the distinct phases correspond to local minima in the free energy of the system; the lower energy of these two minima at any given fixed temperature is the thermodynamically preferred phase, and the transition is the changing of which of the two local minima is the lower, the transition point itself being the point where the two minima have the same free energy. First order phase transitions could be said to be "accidental", in that they are the crossing of well-separated local free energy minima. Furthermore, they do not always occur with a change of symmetry, a counterexample being the transition between the liquid and gaseous states. There also occur more fundamental phase transitions which involve only a single minimum in the free energy. These are second-order or higher order phase transitions, for which discontinuities or singularities occur in the higher derivatives of the free energy. These transitions are also labelled as *continuous* phase transitions, owing to the characteristic that the critical temperature is passed through without the absorption or release of heat(1). These transitions are always associated with changing of symmetry, and the question of how and why a system abruptly and spontaneously undergoes a change in its symmetry has been one of the most studied subjects in theoretical condensed matter physics.

One of the archetypal real-world examples of a continuous phase transition, and the one which drove a great deal of important early theoretical work on the subject(2), is the so-called lambda-transition between the normal and superfluid phases of liquid ^{4}He(2; 3). Some measurements of the specific heat of ^{4}He close to the transition are shown in Figure 1.1; they show a sharp λ-shaped peak at the

transition temperature (this being the origin of the term "lambda transition").

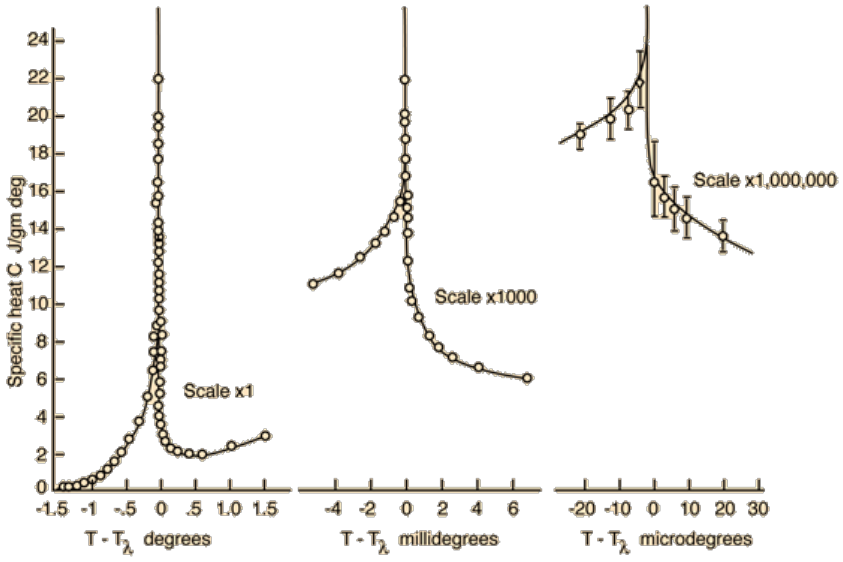

Figure 1.1: Specific heat of ^{4}He showing the Lambda transition.
(Image taken from `http://hyperphysics.phy-astr.gsu.edu/hbase/lhel.html`,
using data from reference (2).)

For most continuous phase transitions, there exists an *order parameter*, which is some thermodynamic quantity which is zero in the high-temperature phase and finite in the low-temperature phase, and which increases continuously from zero as the temperature is reduced from T_C. In a ferromagnetic system, the order parameter is the magnetisation $\vec{M}$, which is the ensemble average of the variable $\vec{S}(\vec{r})$ which describes the spin located at the position $\vec{r}$,

$$\vec{M} = \langle \vec{S}(\vec{r}) \rangle. \tag{1.1}$$

Close to the transition temperature, the asymptotic temperature dependence of the order parameter is typically a power law,

$$M \sim |T - T_C|^{\beta}, \quad T \to T_{C-} \tag{1.2}$$

where the exponent β is called a *critical exponent*. In a second order transition, the specific heat exhibits a divergence, and this divergence is typically a power law,

$$C \sim |T - T_C|^{-\alpha}, \quad T \to T_C, \tag{1.3}$$

and α is a second critical exponent.

There are two important critical exponents in the case that there exists a conjugate variable to the order parameter, that is a "field" $\vec{B}$ which gives rise to a term $-\vec{B}\cdot\vec{M}$ in the free energy of the system. In the example of a ferromagnet, $\vec{B}$ would be an externally applied magnetic field. The corresponding susceptibility, which is defined as

$$\chi = -\left.\frac{\partial M}{\partial B}\right|_{B\to 0},$$

has the critical temperature dependence,

$$\chi \sim |T - T_C|^{-\gamma}, \quad T \to T_{C+}. \tag{1.4}$$

In addition, for finite but extremely small values of B applied precisely at the transition temperature $T = T_C$, the order parameter is typically proportional to a non-integer power of B, with an associated critical exponent δ which is usually defined according to,

$$M \sim B^{1/\delta}, \quad T = T_C, \quad B \to 0. \tag{1.5}$$

The order parameter is closely related to the spatial correlation function, for which we use the symbol $\mathcal{K}(\vec{r})$. In the ferromagnet example, this is defined as

$$\mathcal{K}(\vec{r}) = \langle \vec{S}(\vec{0}) \cdot \vec{S}(\vec{r}) \rangle. \tag{1.6}$$

Typically one expects in the long range limit $|\vec{r}| \to \infty$ the form

$$\mathcal{K}(\vec{r}) \sim M^2 + De^{-|\vec{r}|/\xi}, \tag{1.7}$$

where D is some constant and the important length-scale ξ is termed the *correlation length*. At the transition temperature ξ diverges with an associated critical exponent ν

$$\xi \sim |T - T_C|^{-\nu}, \quad T \to T_C. \tag{1.8}$$

At exactly the transition point, where the correlation length is infinite and the order parameter is zero,

the long range limit of the correlation function has a power law form

$$\mathcal{K}(\vec{r}) \sim \left(\frac{1}{|\vec{r}|}\right)^{d-2+\eta}, \tag{1.9}$$

where d is the spatial dimensionality of the system and η is a further critical exponent. This functional form, the power law, has the property that it is self-similar under changes of scale: if the underlying measure of length is re-scaled by a factor b, then the new correlation function is proportional to the original,

$$\mathcal{K}(b\vec{r}) = b^{-(d-2+\eta)}\mathcal{K}(\vec{r}).$$

This property, that precisely at the transition point the system appears the same under changes of scale, is an extremely important property of phase transitions, and we shall shortly come to discuss it more.

This type of singular behaviour we have outlined, characterised by the critical exponents, is exhibited in a wide variety of different systems which are governed by quite different microscopic physics. Furthermore, such different physical systems are often found to have the same values for the critical exponents. It is found that only two of the critical exponents are independent, the six exponents β, α, γ, δ, ν, and η being related by the four so-called *scaling laws*(4):

$$\alpha = 2 - \nu d \tag{1.10}$$

$$\gamma = \nu d - 2\beta \tag{1.11}$$

$$\beta\delta = \beta + \gamma \tag{1.12}$$

$$\gamma = (2 - \eta)\nu \tag{1.13}$$

These empirical observations, that the same critical behaviour is observed in quite different physical systems and is controlled by only a very restricted number of critical exponents, is conceptually referred to as *universality*, and systems which have the same values for the critical exponents are said to belong to the same *universality class*. The challenge to theoretical condensed matter physics regarding phase transitions is to provide a quantitative description from which the scaling laws can be derived and actual values of the critical exponents calculated for specific systems(5).

The magnitude of this task stems from the immense mathematical difficulty in the direct calculation of thermodynamic quantities and correlation functions for even the simplest model systems which are

capable of exhibiting a phase transition. There are two main reasons for this, the first being that phase transitions arise out of interactions between the miscroscopic degrees of freedom, and the inclusion of interactions renders the calculations for any sizeable system non-trivial. In addition to this, the thermodynamics of any finite interacting system are smooth and infinitely differentiable functions of temperature, and the phase transition, that is the singular behaviour in the thermodynamics, occurs only in the thermodynamic limit that the system-size is made infinitely large. Viewed in these terms, it is not surprising that exact calculations of thermodynamic phase transitions represent such a hopelessly difficult task in the vast majority of cases. There remains only a small number of exact solutions to statistical mechanics models which exhibit phase transitions(6).

1.1.2 Mean field theory of phase transitions

Approximate desriptions of phase transitions may be obtained from mean field theories, in which one replaces the real Hamiltonian with some effective Hamiltonian H^{mf} in which there are no interactions. The interaction energies in the original Hamiltonian are approximated by a mean field which is coupled to all of the miscroscopic variables in the system. In a Heisenberg ferromagnet, one would replace the interaction term $-J\vec{S}_1 \cdot \vec{S}_2$ in the original Hamiltonian by

$$-J\vec{S}_1 \cdot \vec{S}_2 \Rightarrow -J\vec{M} \cdot \vec{S}_1 - J\vec{M} \cdot \vec{S}_2 + JM^2 \tag{1.14}$$

where the mean field $\vec{M}$ is the average of the spin variables, $\vec{M} = \langle \vec{S} \rangle$, which is precisely the magnetisation. The term JM^2 is included to compensate for the fact that in replacing the spin-variables by the mean field one has effectively included the single interaction term twice. The thermodynamics of the mean field Hamiltonian H^{mf} reduce to the partition function for a single particle, or in the ferromagnetic example a single spin, which can be calculated exactly. One can calculate the ensemble average $\langle \vec{S} \rangle$ for this partition function, which is of course the imposed mean field; this provides a so-called *self-consistent equation* for the order parameter,

$$M = m(M), \tag{1.15}$$

where $m(h)$ is an analytic function which describes the average moment induced in a single spin by the application of an appropriately scaled magnetic field h. Typically, as a consequence of the underlying symmetry with respect to the direction of the applied field, the function $m(h)$ will have a Taylor

expansion of the form,

$$m(h) = A(T)h - B(T)h^3 + ..., \tag{1.16}$$

where $A(T)$ and $B(T)$ are positive and analytic functions of the temperature T, and therefore small-M solutions of the self-consistent equation are given approximately by

$$M = A(T)M - B(T)M^3. \tag{1.17}$$

One always obtains the trivial solution $M = 0$ where the system is not magnetised, but in addition one also has the second approximate solution,

$$M = \sqrt{\frac{A(T) - 1}{B(T)}} \tag{1.18}$$

provided that $(A(T) - 1)/B(T) > 0$. As a function of temperature, the non-trivial solution to the self-consistent equation has qualitatively the behaviour we have outlined above for the order parameter: it varies continuously with temperature and goes to zero at a certain temperature T_C^{mf}, corresponding to

$$(A(T_C^{mf}) - 1)/B(T_C^{mf}) = 0,$$

and above this temperature the solution ceases to exist. In addition, it can be shown that as T_C^{mf} is approached from below the form of the solution has the power law behaviour 1.2, and the critical exponent is obtained for a wide variety of cases, referred to as the Ising class of mean field theories, to be $\beta = 1/2$.

The specific heat can be calculated close to the transition within the mean field theory and is found to be always finite, but to exhibit a discontinuous jump at the transition temperature T_C^{mf}. The critical exponent α is therefore predicted to have the value zero. In addition, it is a trivial extension to include a real external field in the mean field theory in order to calculate values of the exponents γ and δ; one finds the values $\gamma = 1$ and $\delta = 3$ for the Ising class of mean field theories.

Landau provided a formulation of mean field theory such that one does not even need to consider the Hamiltonian of the system. Thus it can in principle be used to approximate the thermodynamics of real systems for which the underlying Hamiltonian may not be known. However, of perhaps greater importance, this approach contains the idea that the thermodynamics close to the transition does not depend on the precise microscopic physics but only on quite general properties of the system, such

as the dimensionality of the order parameter(4); as we shall shortly come to discuss, these concepts would later be expanded upon to great effect in Renormalisation Group methods. Landau's theory begins with the assumption that close to some unknown transition temperature the free energy can be written as a power series in the order parameter, which must be a small quantity close to the transition, where the coefficients are functions of temperature which it is assumed can be Taylor expanded about the transition temperature to at least first order in $(T - T_C)$. The self consistent equation 1.15 is obtained by minimising the free energy with respect to the order parameter. The theory is found to predict a phase transition, that is the order parameter is predicted to have a finite value, if there is a temperature for which the leading order coefficient in the expansion of the free energy changes sign. One can obtain the functional form of the order parameter, the specific heat and the susceptibility close to the transition, and the values of the critical exponents β, α, γ and δ; the results are precisely what is obtained applying mean field theory directly to a specific Hamiltonian, although the precise values of thermodynamic properties must be expressed in terms of unknown parameters which are related to the coefficients in the free energy expansion. It should also be noted that there is no way within the theory to obtain any estimate of the transition temperature T_C; this remains the case in Renormalisation Group theories.

An extension to Landau theory, called Ginzburg-Landau theory, includes a spatial-dependence of the order parameter. This theory allows one to calculate correlation functions, from which one can calculate the critical exponent ν, the value $\nu = 1$ being obtained for the Ising class of mean field theories. The form of the correlation function precisely at the transition can be calculated, and is found always, whatever are the symmetries of the free energy and the form of the order parameter, to have the form,

$$\mathcal{K}(\vec{r}) \sim \left(\frac{1}{|\vec{r}|}\right)^{d-2}, \tag{1.19}$$

that is the exponent η is always predicted to have the value zero. This fact stems from the fact that in Ginzburg-Landau theory one only deals with analytic functions which can be written as Taylor series, and therefore the theory can only produce an integer exponent for the power law form of the correlation function(5).

Ginzburg-Landau theory can also be applied to investigate the importance of fluctuations of the order parameter about its predicted mean field value. It is found that there is a value of the spatial dimensionality $d = d_C$, below which the fluctuations are found to diverge at the transition, indicating that mean field theory fails here. d_C is called the *upper critical dimension* and is equal to four for the

Ising class of mean field theories. For $d \geq d_C$, mean field theory correctly describes the character of the phase transition and provides the correct values for the critical exponents. Of course the majority of systems occurring in nature have $d < 4$, and so mean field theory typically does not provide the correct critical behaviour in systems of interest(4).

It is important to note the shortcomings of mean field theory. It is not only in the values of the critical exponents, but in the very existence of a phase transition at all, that mean field theory can fail. As we shall discuss in detail in section 1.2, it is known that phase transitions do not occur at all in $d = 1$, and it is known at the very least that the value of the order parameter is always strictly zero for certain systems in $d = 2$. The planar rotator model is a case of the latter.

1.1.3 The Renormalisation Group

We now come to discuss the Renormalisation Group theories that represent the most advanced theoretical understanding of phase transitions. The term Renormalisation Group describes a set of concepts and calculational techniques that stem from two key features of phase transitions which we have already mentioned: the property that systems at the critical point are self-similar, and the idea of universality.

As we have stated above, self-similarity is the property that at the transition point the system is statistically the same under a change of length scale. If one pictures a system of spins on a lattice with ferromagnetic interactions and focuses on some region of the lattice which is finite but still encompasses a large number of lattice sites, a typical configuration of the system close to the critical point has some pattern of domains in which the spins are locally aligned. Rescaling the system can be pictured as expanding the picture to a larger region of the lattice, or "zooming out"; one finds on doing this some pattern of larger domains. Self-similarity means that, if one considers many "typical" configurations of the system, one cannot on average tell the difference between the original and zoomed out pictures: the domain structures which occur, although they are different for each microstate of the system, are statistically the same in the two pictures. This only strictly occurs at the transition point; close to the transition, the system is approximately self-similar, but *repeated* iterations of the rescaling procedure eventually produces pictures which are not similar to the originals. The critical point is said to be an *unstable fixed point* of the system with respect to rescaling, as if the system is at precisely this point it will remain critical but will otherwise move away from criticality. Through this crude, intuitive picture, we have reached the crucial touchstone that critical points are unstable fixed points of rescaling, or more generally of RG transformations. One has also *stable fixed points*, which correspond to the cases

of either zero or infinite temperature(4).

In our schematic picture, it is intuitive to imagine that, if the length-scale is changed by a large enough factor, or after many rescalings, one has lost track of the individual lattice sites, and in viewing the rescaled system one can only see the average of the direction of the miscroscopic spins in some region. One can describe the rescaled system mathematically by introducing a field $\vec{S}(\vec{r})$, which is well-defined for all values of $\vec{r}$, which represents the average value of the spins in the microscopic region located at $\vec{r}$. This procedure is called *coarse graining*. Alternatively, the average of the original spins can be represented with new lattice variables, which are defined on a new re-scaled lattice. This procedure is called *decimation*, because typically this is done in practice by eliminating some proportion of the original lattice sites such that the remaining sites form the same lattice rescaled, although the fraction of sites eliminated is rarely 1/10!

The point is that the rescaled system can be described in terms of new degrees of freedom, the original microscopic degrees of freedom having been got rid of. What this means in practice is that one goes from the original Hamiltonian to some new Hamiltonian, and in principle this can be made mathematically exact. Because in general the system which is constructed in this transformation is not at the same temperature as the original system, one must work with the reduced Hamiltonian,

$$\mathcal{H}(\{\vec{S}\}) = \beta H(\{\vec{S}\}), \tag{1.20}$$

where $\{\vec{S}\}$ denotes the set of all the spin variables in the system. The rescaling leads to a new set of spin-variables $\{\vec{S}'\}$ and a new reduced Hamiltonian $\mathcal{H}'(\{\vec{S}'\})$.

The simplest scenario is that $\mathcal{H}'$ describes the same model as $\mathcal{H}$, but at a different temperature; one can proceed to find the fixed points of the RG transformation to deduce whether there occurs a phase transition and the associated transition temperature. In principle, one can then linearise the transformation about the non-trivial fixed point in order to deduce the critical exponents.

In practice, for almost all interesting cases, $\mathcal{H}'$ does not describe the same model as $\mathcal{H}$, but instead the Hamiltonian actually becomes increasingly complicated with successive iterations of the transformation. For example, if the original model contains only interactions between nearest neighbours, applying the RG transformation will typically generate longer-range interactions, and repeated iterations will produce still longer-range interactions. One considers a reduced Hamiltonian which is essentially completely general, this being a sum of all possible interaction terms with a set of coefficients, or *couplings*, K_1, K_2,...(5). With the notation that the vector $\underline{K}$ stands for the set of couplings,

from this viewpoint the RG transformation is an operator $\hat{R}$ which acts on this object to produce a new set of couplings,

$$\underline{K}' = \hat{R}\,(\underline{K})\,. \tag{1.21}$$

Let the set of couplings which correspond to a fixed point of the transformation be $\underline{K}^*$, so that,

$$\underline{K}^* = \hat{R}\,(\underline{K}^*)\,. \tag{1.22}$$

If the reduced Hamiltonian is in the near vicinity of the fixed point, we can linearise the RG transformation about this point. We write $\underline{K} = \underline{K}^* + \underline{\delta K}$ where $\underline{\delta K}$ is in some sense small, and under the action of $\hat{R}$,

$$\hat{R}\,(\underline{K}^* + \underline{\delta K}) \approx \hat{R}\,(\underline{K}^*) + \underline{\underline{\tau}}\,\underline{\delta K} = \underline{K}^* + \underline{\underline{\tau}}\,\underline{\delta K}, \tag{1.23}$$

where $\underline{\underline{\tau}}$ is a matrix.

Now, the matrix $\underline{\underline{\tau}}$ has some set of eigenvectors $\underline{\phi}_i$ with corresponding eigenvalues λ_i, and $\underline{\delta K}$ can be expanded in this basis,

$$\underline{\delta K} = \sum_i u_i \underline{\phi}_i. \tag{1.24}$$

Close to the fixed point the reduced Hamiltonian can be described in terms of the components u_i. In the vicinity of the fixed point, the effect of the RG transformation is to multiply each of the components by the corresponding eigenvalue λ_i, and so for several iterations we obtain,

$$\underline{\underline{\tau}}^m\,\underline{\delta K} = \sum_i u_i (\lambda_i)^m \underline{\phi}_i. \tag{1.25}$$

The components which correspond to eigenvalues whose modulus is less than unity are therefore made smaller by each application of the transformation, and therefore move towards the value zero which corresponds to the fixed point. These components are said to be *irrelevant* variables. Conversely, the components corresponding to eigenvalues whose modulus is greater than one move away from the fixed point values with each application of the RG transformation and are said to be *relevant*(7).

Every initial reduced Hamiltonian which has all of the *relevant* variables equal to the critical value zero will flow towards the fixed point under the action of the RG transformation. Now, the non-trivial fixed point corresponds to the phase transition in the original model. Therefore this family of reduced Hamiltonians, which have the relevant variables tuned to zero, are all themselves critical, that is they

are tuned to a phase transition point, and this phase transition, which corresponds to the fixed point in question, is the same in all of these systems. This is precisely the phenomenon of universality, and the universality class is comprised of this family of reduced Hamiltonians in the vicinity of the fixed point which flow towards the fixed point under the action of the RG transformation(5).

We introduced the RG transformation as being associated with a rescaling by a length-scale b. Now, this length-scale is ultimately arbitrary, and we have the constraint that under two successive rescalings, say by factors b_1 and then b_2, we ought to reach the same reduced Hamiltonian as a single rescaling by the factor $b_1 b_2$. This implies that the eigenvalues of the RG transformation for rescaling by b have the form,

$$\lambda_i^{(b)} = (b)^{y_i}\,, \tag{1.26}$$

where the quantities y_i are independent of the rescaling factor b. The exponents y_i are closely associated with the critical exponents which characterise the phase transition. We have indicated that there are frequently only two independent critical exponents; this scenario corresponds to there being only two relevant couplings in the vicinity of the fixed point. These are identified with the reduced temperature $t = T - T_C$, the distance from the phase transition, and an externally applied field h. Close to the transition, the non-analytic part of any thermodynamic quantity can be written in terms of these two variables, and the change in this quantity with rescaling is essentially controlled by $t \to b^{y_t} t$, $h \to b^{y_h} h$. In particular, one has the so-called *scaling hypothesis* for the free energy close to the critical point(4),

$$F(t,h) = b^{-d} F(b^{y_t} t, b^{y_h} h); \tag{1.27}$$

as the name implies, this was originally a conjecture but within the framework of the RG transformation is on quite solid footing. The scaling relations between the critical exponents can all be derived from the expression 1.27(8; 9). Furthermore, these two exponents, and therefore the full set of critical exponents for the associated universality class, can be obtained by finding the eigenvalues of the appropriate RG transformation.

This does not solve the problem of how to characterise phase transitions in general: it is not the case that there is a recipe for how to design the RG transformation and then find its eigenvalues to deduce the critical exponents, and RG schemes have to be carefully worked out on a case by case basis. Much of the time, one requires the scaling parameter b in the RG transformation to be a continuous variable. It is therefore difficult to directly apply RG to models on lattices. Typically one invokes the

fact that close to the transition long range behaviour is dominant to argue that appropriate continuum models can be analysed to find the critical behaviour of the original lattice model.

1.2 Long range order in classical spin systems

The system we are investigating, the square lattice planar rotator model, is an archetypal example of a system which undergoes a thermodynamic phase transition despite long range order being strictly forbidden in this system at finite temperature. It is therefore necessary to discuss long range order, and why it is forbidden in this model.

In this section we introduce the formal definitions of the terms long range order (LRO) and quasi long range order (qLRO) which we will work with throughout this thesis. We then move on to discussing the crucial role which the spatial dimensionality of the system plays regarding the existence of LRO at finite temperatures. We first deal with the absence of LRO at finite temperature in one-dimensional systems. We then discuss the Mermin-Wagner theorem which forbids LRO at finite temperatures for one- and two-dimensional systems which possess a continuous symmetry. The square lattice planar rotator model exhibits the consequences of this: LRO is forbidden in this system, and instead qLRO occurs at low temperature, with a finite-temperature phase transition to a disordered state. We close this section with a proof of the Mermin-Wagner theorem for the planar rotator model.

1.2.1 Definitions of long range order and quasi long range order

Consider first a model of classical spin variables on a lattice. We use the generic notation $\vec{S}_j$ to represent these degrees of freedom, where the subscript j labels the lattice sites. For the present general statements, the spin-variables are to be regarded as unit vectors, but we do not specify their dimensionality. In addition, we consider the possibility that the spins are restricted to a discrete number of states. The Ising model is a case of this, where the spins are restricted to two equivalent directions. Furthermore, at this stage we consider the spins to inhabit any periodic lattice. It is important to stress at this stage that the dimensionality of the spin-variables is entirely independent from the dimensionality of the lattice.

For a finite lattice, with $\mathcal{N}$ lattice sites, there is some specified Hamiltonian which is a function of

the spin-variables, $H(\vec{S}_1, \vec{S}_2, ..., \vec{S}_{\mathcal{N}})$, and one has in principle to evaluate the partition function,

$$\mathcal{Z}_{\mathcal{N}} = \prod_{j=1}^{\mathcal{N}} \int d\Omega_j e^{-\beta H(\vec{S}_1, \vec{S}_2, ..., \vec{S}_{\mathcal{N}})} \tag{1.28}$$

where the symbol $d\Omega_j$ indicates the summation over the spin-variable $\vec{S}_j$.

At present, consider the spin-systems in question to be ferromagnetic, that is the lowest-energy configurations have all of the spin-variables parallel, or at the least have the quantity $\vec{S}_j \cdot \vec{S}_{j'}$ tend towards a constant finite value when the lattice sites j and j' are arbitrarily far apart. This quantity provides the definition of long range order which we will work with throughout this thesis. One considers the question of whether this quantity remains nonzero in the presence of thermal fluctuations. More precisely, one considers the thermal average of this quantity, $\langle \vec{S}_j \cdot \vec{S}_{j'} \rangle$, which is also referred to as the spatial correlation function, in the limit of long range as previously indicated and in the limit that the system size tends to infinity,

$$\lim_{|\vec{r}| \to \infty} \lim_{\mathcal{N} \to \infty} \langle \vec{S}_j \cdot \vec{S}_{j+\vec{r}} \rangle,$$

where the label $j + \vec{r}$ is a rather poor but extremely convenient notation for the lattice site which is displaced from the site j by the spatial vector $\vec{r}$. There are three paradigms: the situation where this quantity has a finite value we refer to, by definition, as *long range order* (LRO),

$$\lim_{|\vec{r}| \to \infty} \lim_{\mathcal{N} \to \infty} \langle \vec{S}_j \cdot \vec{S}_{j+\vec{r}} \rangle \sim M^2; \tag{1.29}$$

the situation where the limit is equal to zero and the decay is exponential in the separation is said to be *disordered*,

$$\lim_{|\vec{r}| \to \infty} \lim_{\mathcal{N} \to \infty} \langle \vec{S}_j \cdot \vec{S}_{j+\vec{r}} \rangle \sim e^{-|\vec{r}|/\xi}, \tag{1.30}$$

where the length-scale ξ which characterises the long range decay is called the correlation length; and lastly the situation where the limit of zero is approached as a power law in the separation is referred to as *quasi long range order* (qLRO),

$$\lim_{|\vec{r}| \to \infty} \lim_{\mathcal{N} \to \infty} \langle \vec{S}_j \cdot \vec{S}_{j+\vec{r}} \rangle \sim |\vec{r}|^{-\eta}. \tag{1.31}$$

The square lattice Ising model exhibits LRO at low temperatures and is disordered at high temper-

ature, and there is a phase transition between these two regimes at a certain finite temperature, the transition temperature T_C. We take this as the basic picture of what might naively be expected for the thermodynamics of classical spin-systems which have an energetic tendency towards ferromagnetism. The quantity M in the expression defining the LRO correlations is the magnetisation of the system, the average component of the spin-variables in the ordering direction, and this acts as the order parameter for the transition: this quantity is zero in the disordered phase, and increases continuously from zero as the temperature is reduced below T_C.

1.2.2 Absence of long range order in one-dimensional systems

We now make two extremely important and well-known remarks concerning the impossibility of long range order at finite temperature in systems on one- and two-dimensional lattices. These remarks divide naturally between the cases for which the spin variables $\vec{S}_j$ are discrete or continuous degrees of freedom respectively. The first of these is that long range order is not permitted at any finite temperature in one dimension for models with discrete degrees of freedom. The justification for this is a rather elementary argument given by Landau(1). Consider an Ising model on a spin chain of $\mathcal{N}$ sites, with open boundary conditions, with nearest neighbour interactions only. The minimum energy configuration of such a system is of course to have all of the spins parallel, while the next lowest-lying configuration has two oppositely oriented domains of parallel spins separated by a single domain wall. The imposition of a domain wall costs the system a finite energy, $+2J$ if J is the Ising interaction energy. However, the domain wall can be placed in any of $(\mathcal{N}-1)$ locations to provide a state with the same energy. The free energy of the one-domain wall state relative to the ferromagnetic state is therefore

$$\Delta F = 2J - T\ln(\mathcal{N}-1),$$

and in the thermodynamic limit $\mathcal{N}\to\infty$ the free energy is therefore always made lower by the creation of a domain wall at any finite temperature. The free energy associated with m domain walls is

$$\Delta F = 2mJ - T\ln\left(\frac{(\mathcal{N}-1)!}{m!(\mathcal{N}-1-m)!}\right).$$

Clearly the free energy is reduced by the creation of a multitude of domain walls. This indicates that we may expect a proliferation of domain walls at any finite temperature, which destroys long range order.

In one-dimensional systems, the energetic cost of a domain wall is finite and does not depend upon the size of the system, but the entropy associated with a domain wall increases logarithmically with the system size. This situation is special to one-dimensional systems. In higher dimensions, domain walls are not confined to a single lattice-bond, but are extended objects with an energetic cost which is proportional to their length. For the occurrence of domains which are large enough to destroy long range order, making the arguments made above leads to a different conclusion: at sufficiently high temperatures the domain wall is entropically desired, but at low temperatures the energetic cost of the domain wall outweighs the entropic benefit(10). Indeed, discrete spin models exhibit long range order in two and higher dimensions at sufficiently low temperatures.

1.2.3 The Mermin-Wagner theorem: absence of long range order in one- and two-dimensional isotropic systems

The second remark is the famous Mermin-Wagner theorem, that long range order is not permitted at any finite temperature in one or two dimensions for systems with continuous spins. This statement applies to all one- and two-dimensional systems which have a continuous symmetry(11). Systems with such a symmetry always have excitations of arbitrarily low energy which are known as Goldstone modes(12). For a continuous spin model, these zero-energy excitations arise from the fact that the spins can be distorted from their ground state configuration infinitesimally. In some sense LRO is prevented in continuous spin systems in one and two dimensions because the excitations which tend to disrupt the ground state configuration are arbitrarily low in energy and therefore will always exist at any finite temperature. Continuous-spin systems are frequently referred to as *spin-isotropic* or, as in this thesis, simply as *isotropic*.

We now provide a proof of the Mermin-Wagner theorem for the planar rotator model. We closely follow the method of proof given by Mermin and Wagner in references (11) and (13). This method makes use of an inequality which follows from considering the ensemble average of the product of two quantities to be a scalar product. In particular, reference (13) gives a proof of the theorem for the planar rotator model. This proof considers the planar rotator model with an applied magnetic field, and shows that the magnetisation $\langle \cos \phi_j \rangle$ vanishes in one and two dimensions in the limit that the magnetic field tends to zero. We follow this proof with the modification that we do not include a magnetic field and we focus on the correlation function $\mathcal{K}(\vec{r}) = \langle \cos(\phi_j - \phi_{j+\vec{r}}) \rangle$ instead of the magnetisation, the theorem being proved by showing that the correlation function must tend to zero

in the long range limit $|\vec{r}| \to \infty$. We present the proof in this way in order to be entirely consistent with the definition of long range order in terms of the correlation function which we have outlined above. Despite this difference, the working of the proof is almost identical to that provided in reference (13).

We consider the planar rotator model

$$H = -J \sum_{\langle jj' \rangle} \cos\left(\phi_j - \phi_{j'}\right)$$

where for the present the label j denotes the sites on a d-dimensional hypercubic lattice (this becomes a linear chain for $d = 1$ and for $d = 2$ becomes the case of our real interest, the square lattice) and the summation runs over all nearest neighbour pairs of lattice sites. We shall work with a finite lattice of $\mathcal{N}$ sites but ultimately we will take the thermodynamic limit that $\mathcal{N} \to \infty$. We apply periodic boundary conditions in all of the principle directions; the crucial point for the working of the proof is that all of the lattice sites are completely equivalent to one another, and have the same number of nearest neighbours, including those at the boundary of the system. The partition function is given by the integration of the function $e^{-\beta H}$ over all of the spin variables

$$\mathcal{Z} = \left(\prod_j \int_{-\pi}^{\pi} \frac{d\phi_j}{2\pi} \right) e^{-\beta H}, \tag{1.32}$$

where $\beta = 1/T$ is the inverse temperature expressed in appropriate units, and the ensemble average of some function of the spin-angles $Q(\{\phi\})$ is given by

$$\langle Q \rangle = \frac{1}{\mathcal{Z}} \left(\prod_j \int_{-\pi}^{\pi} \frac{d\phi_j}{2\pi} \right) Q e^{-\beta H}. \tag{1.33}$$

Now, if Q and K are two functions of the spin-variables, then the ensemble average $\langle Q^* K \rangle$ satisfies the conditions which define a scalar product between Q and K. From these conditions follows the Cauchy-Schwartz inequality,

$$\langle |Q|^2 \rangle \langle |K|^2 \rangle \geq |\langle Q^* K \rangle|^2. \tag{1.34}$$

Let us define the functions,

$$Q = Q_{\vec{k}}(\vec{r}) = \sum_j e^{-i\vec{k}\cdot\vec{R}_j} \sin\left(\phi_j - \phi_{j+\vec{r}}\right) \tag{1.35}$$

$$K = K_{\vec{k}} = \sum_j e^{-i\vec{k}\cdot\vec{R}_j} \frac{\partial H}{\partial \phi_j}. \tag{1.36}$$

where $\vec{k}$ is one of the standard Bloch wavevectors. These functions may be considered as being obtained by applying the standard Bloch transform to the functions $\sin\left(\phi_j - \phi_{j+\vec{r}}\right)$ and $\frac{\partial H}{\partial \phi_j}$ respectively. Written explicitly, the quantity $\langle Q^* K \rangle$ is given by

$$\langle Q_{-\vec{k}}(\vec{r}) K_{\vec{k}} \rangle = \sum_j \sum_{j'} e^{-i\vec{k}\cdot\left(\vec{R}_j - \vec{R}_{j'}\right)} \frac{1}{\mathcal{Z}} \left(\prod_{j''} \int_{-\pi}^{\pi} \frac{d\phi_{j''}}{2\pi} \right) \sin\left(\phi_j - \phi_{j+\vec{r}}\right) \frac{\partial H}{\partial \phi_{j'}} e^{-\beta H}. \tag{1.37}$$

This expression can be greatly simplified by first noting

$$\frac{\partial H}{\partial \phi_{j'}} e^{-\beta H} = -\frac{1}{\beta} \frac{\partial}{\partial \phi_{j'}} e^{-\beta H},$$

from which it follows that we may employ integration by parts to re-write the integral in this expression as the ensemble average of a function which does not involve the Hamiltonian. The surface term which occurs in the by parts integration is equal to zero, as all of the involved quantities are periodic functions of the spin angles. One obtains from performing the integration by parts,

$$\langle Q_{-\vec{k}}(\vec{r}) K_{\vec{k}} \rangle = \sum_j \sum_{j'} e^{-i\vec{k}\cdot\left(\vec{R}_j - \vec{R}_{j'}\right)} \frac{1}{\mathcal{Z}} \left(\prod_{j''} \int_{-\pi}^{\pi} \frac{d\phi_{j''}}{2\pi} \right) \frac{1}{\beta} \left(\frac{\partial}{\partial \phi_{j'}} \sin\left(\phi_j - \phi_{j+\vec{r}}\right) \right) e^{-\beta H}, \tag{1.38}$$

and the integral in this expression can be recognised as an ensemble average. This provides,

$$\langle Q_{-\vec{k}}(\vec{r}) K_{\vec{k}} \rangle = \frac{1}{\beta} \sum_j \sum_{j'} e^{i\vec{k}\cdot\left(\vec{R}_j - \vec{R}_{j'}\right)} \langle \frac{\partial}{\partial \phi_{j'}} \sin\left(\phi_j - \phi_{j+\vec{r}}\right) \rangle \tag{1.39}$$

$$= \frac{1}{\beta} \sum_j \left(1 - e^{-i\vec{k}\cdot\vec{r}}\right) \langle \cos\left(\phi_j - \phi_{j+\vec{r}}\right) \rangle \tag{1.40}$$

$$= \frac{1}{\beta} \mathcal{N} \left(1 - e^{-i\vec{k}\cdot\vec{r}}\right) \mathcal{K}(\vec{r}), \tag{1.41}$$

where we have included the assumption that the correlation function $\mathcal{K}(\vec{r}) = \langle \cos\left(\phi_j - \phi_{j+\vec{r}}\right) \rangle$ does not depend upon the lattice index j. The same procedure can be used to evaluate $\langle K^* K \rangle$ to be equal

to,

$$\langle K_{-\vec{k}} K_{\vec{k}} \rangle = \frac{1}{\beta} \sum_j \sum_{j'} e^{i\vec{k}\cdot(\vec{R}_j - \vec{R}_{j'})} \langle \frac{\partial^2 H}{\partial \phi_j \partial \phi_{j'}} \rangle \tag{1.42}$$

$$= \frac{1}{\beta} \sum_j \sum_{\vec{\tau}} \left(1 - e^{-i\vec{k}\cdot\vec{\tau}}\right) \langle J \cos\left(\phi_j - \phi_{j+\vec{\tau}}\right) \rangle, \tag{1.43}$$

where the vector $\vec{\tau}$ runs over all of the relative displacements of a particular lattice site to its nearest neighbours. We recognise in this expression the correlation function for neighbouring lattice sites; of course it can be assumed that this is the same for neighbouring lattice sites in any direction, so that we may write,

$$\langle K_{-\vec{k}} K_{\vec{k}} \rangle = \frac{1}{\beta} \mathcal{N} J \mathcal{K}(\hat{x}) \sum_{\vec{\tau}} \left(1 - e^{-i\vec{k}\cdot\vec{\tau}}\right), \tag{1.44}$$

where the vector $\hat{x}$ connects a lattice site to a nearest neighbour in one of the principal lattice directions.

Finally, $\langle Q^* Q \rangle$ is given by

$$\langle Q_{-\vec{k}}(\vec{r}) Q_{\vec{k}}(\vec{r}) \rangle = \sum_j \sum_{j'} e^{i\vec{k}\cdot(\vec{R}_j - \vec{R}_{j'})} \langle \sin\left(\phi_j - \phi_{j+\vec{r}}\right) \sin\left(\phi_{j'} - \phi_{j'+\vec{r}}\right) \rangle, \tag{1.45}$$

and we note that,

$$\frac{1}{\mathcal{N}^2} \sum_{\vec{k}} \langle Q_{-\vec{k}}(\vec{r}) Q_{\vec{k}}(\vec{r}) \rangle = \frac{1}{\mathcal{N}} \sum_j \langle \sin^2\left(\phi_j - \phi_{j+\vec{r}}\right) \rangle \tag{1.46}$$

$$= \langle \sin^2\left(\phi_j - \phi_{j+\vec{r}}\right) \rangle. \tag{1.47}$$

Now, this correlation is certainly positive and less than or equal to one, owing to the range of the function $\sin^2 x$. We therefore have the inequality,

$$\frac{1}{\mathcal{N}^2} \sum_{\vec{k}} \langle Q_{-\vec{k}}(\vec{r}) Q_{\vec{k}}(\vec{r}) \rangle \leq 1, \tag{1.48}$$

which combined with the inequality 1.34 implies that,

$$\frac{1}{\mathcal{N}^2} \sum_{\vec{k}} \frac{|\langle Q_{-\vec{k}}(\vec{r}) K_{\vec{k}} \rangle|^2}{\langle K_{-\vec{k}} K_{\vec{k}} \rangle} \leq 1. \tag{1.49}$$

Substituting the expressions we have obtained for $\langle Q^* K \rangle$ and $\langle K^* K \rangle$ into this inequality we obtain,

$$\frac{T}{J} \frac{\mathcal{K}(\vec{r})^2}{\mathcal{K}(\hat{x})} \frac{1}{\mathcal{N}} \sum_{\vec{k}} \frac{|1 - e^{-i\vec{k}\cdot\vec{r}}|^2}{\sum_{\vec{\tau}} \left(1 - e^{-i\vec{k}\cdot\vec{\tau}}\right)} \leq 1. \tag{1.50}$$

In the thermodynamic limit the summation over Bloch wavevectors is represented by an integral,

$$\frac{2T}{J} \frac{\mathcal{K}(\vec{r})^2}{\mathcal{K}(\hat{x})} \int \frac{d^d\vec{k}}{(2\pi)^d} \frac{1 - \cos\left(\vec{k}\cdot\vec{r}\right)}{\sum_{\vec{\tau}} \left(1 - e^{-i\vec{k}\cdot\vec{\tau}}\right)} \leq 1, \tag{1.51}$$

where the integration measure for the d-dimensional hypercubic lattice is

$$\int \frac{d^d\vec{k}}{(2\pi)^d} = \prod_{i=1}^{d} \int_{-\pi}^{\pi} \frac{dk_i}{2\pi}.$$

The inequality 1.51 is the crucial result of this analysis. One finds that, in one and two dimensions, the integral in 1.51 diverges in the long range limit $|\vec{r}| \to \infty$; therefore the only way the equality can be satisfied in this limit for non-zero values of temperature is if the correlation function $\mathcal{K}(\vec{r})$ decays at long range so as to cancel out the divergence in the integral. This completes the proof of the Mermin-Wagner theorem for the planar rotator model, in that it shows that, in the thermodynamic limit, there is no LRO - the correlation function does not approach a constant non-zero value at long range.

The integral in 1.51 is closely associated with the so-called lattice Green's function(14; 15) and occurs frequently in problems on lattices. For completeness, we make some brief remarks about the behaviour of the integral in one and two dimensions. For the linear chain, the integral can be evaluated exactly as,

$$\int_{-\pi}^{\pi} \frac{dk}{2\pi} \left(\frac{1 - \cos kr}{2 - 2\cos k} \right) = \frac{r}{2}, \tag{1.52}$$

and this is clearly divergent in the limit $r \to \infty$. This shows that the correlation function must decay at long range at least as quickly as $r^{-1/2}$. In fact, the correlations decay exponentially with r at long range in one-dimensional systems. This is seen in the following chapter where one-dimensional systems are solved using transfer operators. In two dimensions, the integral takes the form,

$$\int_{-\pi}^{\pi} \frac{dk_x}{2\pi} \int_{-\pi}^{\pi} \frac{dk_y}{2\pi} \left(\frac{1 - \cos\vec{k}\cdot\vec{r}}{4 - 2\cos k_x - 2\cos k_y} \right). \tag{1.53}$$

This integral is logarithmically divergent in the limit $|\vec{r}| \to \infty$, and the precise asymptotic form is (for a derivation see reference (16, pp. 148-151)),

$$\int_{-\pi}^{\pi} \frac{dk_x}{2\pi} \int_{-\pi}^{\pi} \frac{dk_y}{2\pi} \left(\frac{1 - \cos \vec{k} \cdot \vec{r}}{4 - 2\cos k_x - 2\cos k_y} \right) \sim \frac{1}{2\pi} \ln |\vec{r}|. \tag{1.54}$$

Consequently for the square lattice the correlation function must fall off at least as rapidly as $(\ln |\vec{r}|)^{-1/2}$. As we discuss below, the correlations in fact fall off as a power law at low temperatures in the square lattice model. In higher dimensions, the integral is finite, and consequently the inequality 1.51 may be satisfied in the presence of LRO.

1.3 The Planar Rotator model

1.3.1 Introduction

The model which we aim to study in this thesis is the two-dimensional planar rotator model, which is described by the Hamiltonian,

$$H = -J \sum_{\langle jj' \rangle} \cos\left(\phi_j - \phi_{j'}\right) \tag{1.55}$$

where the label j labels the sites on a square lattice and the summation is taken over all nearest neighbour pairs of lattice sites. The degrees of freedom ϕ_j are classical variables lying in the range $0 \leq \phi_j < 2\pi$. This model can be pictured as describing a system of planar spins, each spin being pictured as an arrow which is confined to a plane and its direction being parameterised by the corresponding angle ϕ.

The planar rotator model can be thought of as one of a number of models which we may write as

$$H = -J \sum_{\langle jj' \rangle} \vec{S}_j \cdot \vec{S}_{j'} \tag{1.56}$$

where the degrees of freedom $\vec{S}_j$ are classical spins of some dimensionality, a classical spin being simply a vector of a fixed length which in this work shall always be taken to be unity. This is referred to generically as the O(N) vector model, where N refers to the dimensionality of the spins. The cases $N = 1$, $N = 2$ and $N = 3$ are the Ising model, the planar rotator model and the classical Heisenberg model respectively. Apart from on linear spin-chains which are trivial, the only exact solutions of the O(N) vector model are the Ising model on the square lattice(17), and the $N = \infty$ case, which is

equivalent to the so-called spherical model, on any hypercubic lattice(6). In three and higher spatial dimensions these models all have LRO at sufficiently low temperature, and disorder as the temperature is raised in regular phase transitions. However, with the exception of the Ising model all versions of this model are isotropic, and therefore on the square lattice the Mermin-Wagner theorem forbids LRO. As we shall discuss, the planar rotator model undergoes a phase transition from qLRO to disorder, and this is thought to be a very particular phase transition with unusual critical behaviour, the Kosterlitz-Thouless transition. Conversely the spherical model on the square lattice is rigorously known to have no phase transition(6), and RG calculations indicate this to be true of the classical Heisenberg model also(18).

Close to its phase transition, the square lattice planar rotator model is thought to have the same behaviour as a number of related models, including the model of a two-dimensional Coulomb gas and the Villain model(14; 19). The basis for this is that near the transition the behaviour is governed by long-range fluctuations, for which the same effective description can be employed for all of these models. As we sketch out in section 1.3.6, the theory by Kosterlitz and Thouless considers a continuum model which describes these long-range fluctuations and applies an RG scheme to show the existence of a critical point and deduce its properties(20; 21).

The planar rotator model is also closely associated with the q-state clock model, which results from constraining the continuous planar rotator spin-variables ϕ_j to have a set of evenly spaced directions $\phi_j = 2\pi n_j/q$, $n_j = 0, 1, ..., q$; for $q > 4$ this model undergoes two phase transitions, one of which has the same characteristics as the planar rotator phase transition(14). The relationship between the two models is highly significant, but we postpone a discussion of it until the next chapter, section 2.4.1.

There are a number of techniques that have been used to study the square lattice planar rotator model itself, rather than related continuum models. The most widely used of these is Monte Carlo simulation, which samples the equilibrium canonical distribution of a finite system. These studies are consistent with the Kosterlitz-Thouless theory(22; 23; 24; 25), but some authors have in addition found that results can be made to fit a regular phase transition(26). Another technique that has been applied is the use of high temperature expansions, which is simply to calculate the expansions of thermodynamic quantities in powers of the inverse temperature (see section 1.3.3 which contains a description of such a calculation) and these calculations have shown evidence of a regular phase transition(27). A final technique that has been employed is Fisher zeroes(28), which studies the zeroes of the partition function considered as a function of a complex temperature; the zeroes are calculated

for a series of finite systems and are seen to approach the real axis as the system-size is increased, suggesting a real singularity in the thermodynamic limit associated with a phase transition. The results of this work are also consistent with either the Kosterlitz-Thouless transition or a regular phase transition.

The technique which we have used to study the model, one-to-two dimensional crossover, which we describe in the next chapter, is a method that has until recently not been applied to the problem(29). This method is to calculate the thermodynamics of a series of one-dimensional systems which tend towards the finite square lattice in the limit that a certain finite-size parameter tends to infinity. This is essentially an application of the method of exact diagonalisation in quantum mechanics(44). In applying this method we find consistent evidence of a regular phase transition in the model.

In the remainder of this section we discuss a number of important topics related to the phase transition in the planar rotator model. Because the square lattice planar rotator model was originally studied in order to study the phase transition observed in two-dimensional Helium films, it would be remiss not to give some discussion to the relationship of the planar rotator model to bosonic systems, to which we devote section 1.3.2. Thereafter we focus entirely on the phase transition in the square lattice planar rotator model. Sections 1.3.3 and 1.3.4 are intended to establish that a phase transition must exist in the model by examining the spin-spin correlation function in the high and low temperature limits respectively and finding very different behaviour. We then discuss the helical stiffness in section 1.3.5, which is the quantity which plays the role of an order parameter in this phase transition. We conclude in section 1.3.6 with a sketch of the Kosterlitz-Thouless theory.

1.3.2 Relationship to bosonic systems

The planar rotator model was first considered as a crude model of superfluidity(30; 31). Superfluids can be described in terms of a condensate wavefunction $\chi_0(\vec{r})$ which is a complex valued function. The connection to the planar rotator degrees of freedom is made by identifying the spin angles ϕ_j with the phase of the consensate wavefunction; if the modulus of the wavefunction is constant, or approximately so, so that the phase is the only active degree of freedom, a Hamiltonian of the form 1.55 can be argued for as describing a condensate.

We now briefly sketch out some general features of the theory of bosonic systems, following closely the approach of Leggett(32). Our aim is merely to indicate what the central mathematical objects in the theory are, and to connect these to the analogous objects in the planar rotator model. We first

define LRO and qLRO in bosonic systems in a manner which is analogous to the definitions we gave for classical spin models, and make the connection with the phenomenon of Bose-Einstein condensation (BEC). We then proceed to write down a well-known approximate Hamiltonian for a bosonic system, and note that it can also be obtained as an approximation to the planar rotator Hamiltonian.

For a system of $\mathcal{N}$ particles, one must consider a many-body wavefunction $\Psi(\vec{r}_1, \vec{r}_2, ..., \vec{r}_{\mathcal{N}})$ which is a function of all of their positions $\vec{r}_1, \vec{r}_2, ..., \vec{r}_{\mathcal{N}}$. The completely general formalism for such a system follows from the density matrix, which has the following generic form,

$$\rho(\vec{r}_1, \vec{r}_2, ..., \vec{r}_{\mathcal{N}}; \vec{r}_1{}', \vec{r}_2{}', ..., \vec{r}_{\mathcal{N}}{}') = \sum_\alpha p_\alpha \Psi_\alpha(\vec{r}_1, \vec{r}_2, ..., \vec{r}_{\mathcal{N}}) \Psi^*_\alpha(\vec{r}_1{}', \vec{r}_2{}', ..., \vec{r}_{\mathcal{N}}{}'),$$

where the wavefunctions $\Psi_\alpha(\vec{r}_1, \vec{r}_2, ..., \vec{r}_{\mathcal{N}})$ are some complete orthogonal set of many-body wavefunctions, and the sum of the coefficients p_α is unity. For systems composed exclusively of bosons, the wavefunctions must be symmetric under the exchange of the positions of any two particles. The quantity which is the analogue of the spin-spin correlation $\langle \vec{S}_j \cdot \vec{S}_{j'} \rangle$ is the so-called single-particle density matrix, which is obtained as the partial trace of the density matrix over the positions of $\mathcal{N} - 1$ of the particles,

$$\rho(\vec{r}, \vec{r}') = \left(\prod_{j=2}^{\mathcal{N}} \int d\vec{r}_j \right) \rho(\vec{r}, \vec{r}_2, ..., \vec{r}_{\mathcal{N}}; \vec{r}', \vec{r}_2, ..., \vec{r}_{\mathcal{N}}).$$

We can define LRO, qLRO and disorder in Bose systems according to whether, in the thermodynamic limit that the number of particles is large, the long-range limit of $\rho(\vec{r}, \vec{r}')$ is a constant, a power law decay or an exponential decay respectively.

LRO in bosonic systems is associated with Bose-Einstein condensation, which in the simplest possible terms is the occupation of some single-particle state, or some single-particle-like state, by a macroscopic fraction of bosons in the system. The connection to the definition of LRO in terms of correlations can be seen with the following. The single-particle density matrix has some set of eigenvalues n_γ, which can be interpreted as the occupation numbers of some set of single-particle states. Bose-Einstein consensation corresponds to one of these eigenvalues being macroscopically large, that is of order $\mathcal{N}$, while all the other eigenvalues are $O(1)$. Let $\chi_\gamma(\vec{r})$ be the eigenfunction of the single-particle density matrix belonging to the eigenvalue n_γ; then $\rho(\vec{r}, \vec{r}')$ can be written as

$$\rho(\vec{r}, \vec{r}') = \sum_\gamma n_\gamma \chi_\gamma(\vec{r}) \chi^*_\gamma(\vec{r}'). \tag{1.57}$$

If all of the eigenvalues are $O(1)$, which corresponds to the bosonic system being disordered, or in the normal liquid state, then the differing phases of the terms in the sum in equation 1.57 cancel one another in the long-range limit, and the sum vanishes. If one of the eigenvalues, say that corresponding to $\gamma = 0$, is macroscopic and the rest are $O(1)$, the same argument implies that only the contribution of the $\gamma = 0$ eigenvalue survives in the long-range limit,

$$\rho(\vec{r}, \vec{r}') \sim n_0 \chi_0(\vec{r}) \chi_0^*(\vec{r}'). \tag{1.58}$$

This can be seen by breaking the sum in 1.57 up into the contribution of the $\gamma = 0$ term and the sum of all the $O(1)$ terms, and observing that in the long-range limit the latter must vanish for the same reason that the entire sum vanishes in the disordered case.

The function $\chi_0(\vec{r})$ can be regarded as an analogue of a single-particle wavefunction which describes the condensate. Textbook treatments of Bose-Einstein condensates often begin with the Hartree approximation, which proposes for the full many-body wavefunction the ansatz,

$$\Psi(\vec{r}_1, ..., \vec{r}_{\mathcal{N}}) = \prod_{i=1}^{\mathcal{N}} \chi_0(\vec{r}_i). \tag{1.59}$$

The function $\chi_0(\vec{r})$ is called the condensate wavefunction and in the Hartree approximation completely describes the system. The connection to the planar rotator model is the analogy between the planar spins in that model and the phase of the condensate wave function θ. In the case that the modulus of the condensate wavefunction is constant, which corresponds to the physical density of the system being constant, it can be shown that the energy of the bosonic system can be written as

$$E = \frac{\hbar^2}{2m} |\chi_0|^2 \int d\vec{r} \left(\vec{\nabla} \theta(\vec{r}) \right)^2. \tag{1.60}$$

This expression corresponds precisely to what is obtained if one takes the continuum limit of the planar rotator model Hamiltonian 1.55.

1.3.3 The high temperature limit

In this section we discuss the high temperature limit of the spin-spin correlation function in the planar rotator model. We explain how the asymptotic form of the correlation function is calculated within the framework of a high temperature expansion. The calculation shows that the correlation function

has an exponential decay at high temperature and therefore that the model is disordered in this limit.

The high temperature limit corresponds to the limit where the variable β is small: the high temperature expansion is simply the Taylor expansion of a function of β about the point $\beta = 0$. We first consider the partition function, which of course is the summation over all spin-configurations of $e^{-\beta H}$. The starting point of the high temperature expansion is,

$$e^{-\beta H} = \sum_{n=0}^{\infty} \frac{1}{n!} \left(-\beta H\right)^n . \tag{1.61}$$

The partition function is then obtained as a power series in β by simply integrating this expansion term by term. The difficulty in this calculation is in controlling the large number of terms which arise from raising the Hamiltonian to large integer powers. One can represent this graphically by associating each term in H with an arrow pointing from some site on the lattice to one of its nearest neighbours. To be explicit, we first write the Hamiltonian in the form,

$$-\beta H = \frac{\beta J}{2} \sum_{\langle jj' \rangle} \left(e^{i(\phi_j - \phi_{j'})} + e^{i(\phi_{j'} - \phi_j)} \right). \tag{1.62}$$

Now, the term $e^{i(\phi_j - \phi_{j'})}$ can be represented graphically by an arrow drawn from the site j' to the site j. The Hamiltonian is the sum of all such arrows which can be drawn between nearest neighbour lattice sites, going in both directions. The quantity $(-\beta H)^n$ is then the sum of all possible products of n of these directed bonds. These products are represented by drawing the n arrows together on the lattice. A typical term has the form

$$\prod_l e^{i\nu_l \phi_l}$$

where l runs over some *subset* of the lattice sites, those which sit at either the head or tail of an arrow, and the quantity ν_l gives the total number of arrows pointing towards the corresponding lattice site, arrows pointing away from this site corresponding to a negative value so that ν_l can be a positive or negative integer or may be zero. Integrating this quantity over all of the spin-angles one obtains,

$$\left(\prod_{j=1}^{\mathcal{N}} \int_{-\pi}^{\pi} \frac{d\phi_j}{2\pi} \right) \prod_l e^{i\nu_l \phi_l} = \prod_l \delta_{\nu_l, 0}. \tag{1.63}$$

The meaning of this is that only those terms which have the net number of arrows into every lattice site equal to zero survive the integration. Immediately we may recognise that this can only be accomplished

if the total number of arrows that is drawn is even, so that the high temperature expansion of the partition function contains only even powers of β. If $\mathcal{C}_{2m}$ is the number of possible diagrams composed of $2m$ arrows which satisfy the condition that the net number of arrows into every site is zero, we may write,

$$\mathcal{Z} = \sum_{m=0}^{\infty} \frac{\mathcal{C}_{2m}}{(2m)!} \left(\frac{\beta J}{2}\right)^{2m}. \tag{1.64}$$

The quantity which is of real interest is the correlation function, which is given by

$$\langle e^{i\left(\phi_j - \phi_{j+\vec{r}}\right)} \rangle = \frac{1}{\mathcal{Z}} \left(\prod_{j=1}^{\mathcal{N}} \int_{-\pi}^{\pi} \frac{d\phi_j}{2\pi} \right) e^{i\left(\phi_j - \phi_{j+\vec{r}}\right)} e^{-\beta H}. \tag{1.65}$$

We can expand the factor $e^{-\beta H}$ in the integrand in powers of β; to obtain only the leading order behaviour for the correlation function, it is sufficient to replace the factor $1/\mathcal{Z}$ by the zeroth order term in its series, $1/\mathcal{Z} \approx 1$. We therefore obtain,

$$\langle e^{i\left(\phi_j - \phi_{j+\vec{r}}\right)} \rangle \sim \sum_{n=0}^{\infty} \frac{1}{n!} \left(\prod_{j=1}^{\mathcal{N}} \int_{-\pi}^{\pi} \frac{d\phi_j}{2\pi} \right) e^{i\left(\phi_j - \phi_{j+\vec{r}}\right)} \left(-\beta H\right)^n, \tag{1.66}$$

and the leading order expression for the correlation function is given by the first nonzero term in this series. Now, the term $e^{i\left(\phi_j - \phi_{j+\vec{r}}\right)}$ corresponds in the diagrammatic language to some diagram in which the sites j and $j + \vec{r}$ are connected by arrows, with one net flux into the site j and one net flux out of the site $j + \vec{r}$. The terms in $e^{i\left(\phi_j - \phi_{j+\vec{r}}\right)} \left(-\beta H\right)^n$ which survive the integration require that there is no net flux into or out of any site, and consequently these correspond to terms in $\left(-\beta H\right)^n$ which have a net flux out of site $j + \vec{r}$ and into site j. The lowest order diagram which satisfies this has directed arrows along some minimal path connecting the two sites; if the relative displacement of the two lattice sites is $\vec{r} = n_x \hat{x} + n_y \hat{y}$, then the shortest-length paths connecting them are comprised of $|n_x| + |n_y|$ bonds and the number of such paths is $(|n_x| + |n_y|)!/(|n_x|!|n_y|!)$. The leading order term in the high temperature expansion of the correlation function is therefore,

$$\langle e^{i\left(\phi_j - \phi_{j+\vec{r}}\right)} \rangle \sim \frac{1}{|n_x|!|n_y|!} \left(\frac{\beta J}{2}\right)^{|n_x|+|n_y|}. \tag{1.67}$$

The decay in the correlation function with distance is therefore at least as fast as an exponential decay with the separation; this shows that the square lattice planar rotator model is disordered in the high temperature limit.

1.3.4 The low temperature limit

In this section we discuss the low temperature limit of the square lattice planar rotator model. We obtain an effective model to describe the low temperature physics of the planar rotator model which can be solved exactly; we provide an outline of the mathematics of this solution, quoting the relevant results. This shows that the square lattice planar rotator model exhibits power law correlations at low temperature. We also mention a stronger statement in the form of an exact bound on the correlation function below some temperature due to Frohlich and Spencer. This statement of the low temperature limit, in combination with the high temperature limit, shows that the model does undergo a phase transition.

At low temperature the typical deviation in the directions of neighbouring spins may be expected to be small; the cosine in the planar rotator Hamiltonian may therefore be expanded to the second order in its argument to obtain the approximate form,

$$H \approx -2\mathcal{N}J + \frac{J}{2}\sum_{\langle jj'\rangle}\left(\phi_j - \phi_{j'}\right)^2. \tag{1.68}$$

The first term in this expression is the lowest possible energy of the system, associated with a perfect ferromagnetic configuration, and the second term describes the energy of small deviations from this configuration. If one makes the further approximation that the variables ϕ_j be allowed to take any real value, so that the quantity $\phi_j - \phi_{j'}$ is not strictly contrained to lie in the range 0 to 2π, then the statistical physics of this effective model can be calculated exactly. In particular, the model is found to have qLRO: the correlation function $\langle\cos\left(\phi_j - \phi_{j+\vec{r}}\right)\rangle$ can be calculated and is found to exhibit power law decay at long-range.

One can also take the continuum limit that the lattice variable ϕ_j becomes a field $\phi(\vec{R})$ and consider the model(12, p. 465),

$$\Delta H = \frac{J}{2}\int d^2\vec{R}\left(\vec{\nabla}\phi\right)^2, \tag{1.69}$$

and it is found that solving this model produces the same result for the correlation function. We shall discuss the solution of the lattice model 1.68: this is in large part a matter of taste, but in addition it is found that proceeding in this way produces some of the same mathematics which we have already seen in the proof of the Mermin-Wagner theorem in section 1.2.

We now proceed to briefly sketching how the exact solution of this low temperature effective model

is carried out. Using the symbol ΔH for the second term in equation 1.68, this can be written as,

$$\Delta H = -\frac{J}{2} \sum_{j,j'} \phi_j \Delta_{j,j'} \phi_{j'}, \tag{1.70}$$

where the operator $\Delta_{j,j'}$ is the lattice analogue of the Laplacian operator and is defined as(15),

$$\sum_{j'} \Delta_{j,j'} \phi_{j'} = \sum_{j' \text{ n.n. to } j} (\phi_j - \phi_{j'}). \tag{1.71}$$

The corresponding partition function for this effective model is,

$$\mathcal{Z} = \left(\prod_j \int_{-\infty}^{\infty} d\phi_j \right) e^{\frac{\beta J}{2} \sum_{j,j'} \phi_j \Delta_{j,j'} \phi_{j'}}. \tag{1.72}$$

Because the exponent in this expression is quadratic in the variables ϕ_j, the integrals can be evaluated exactly using the well-known techniques of Gaussian integration(12, p. 465). The partition function can be evaluated explicitly to be written in terms of the determinant of the matrix $\Delta_{j,j'}$. However, one can proceed directly to the calculation of the two-point correlation $\langle \phi_j \phi_{j'} \rangle$, which is equal to the inverse of the matrix which occurs in the exponent(15). This may be written as,

$$\langle \phi_j \phi_{j'} \rangle = \frac{1}{\beta J} G\left(\vec{R}_j - \vec{R}_{j'} \right), \tag{1.73}$$

where $G(\vec{r})$ is the square lattice Green's function. For a very clear and thorough exposition of lattice Green's functions, see reference (33, pp. 136-138). $G(\vec{r})$ is the inverse of the lattice Laplacian $\Delta_{j,j'}$; this is expressed explicitly in the equation,

$$\sum_{j''} \Delta_{jj''} G\left(\vec{R}_{j''} - \vec{R}_{j'} \right) = \delta_{j,j'}, \tag{1.74}$$

which can be regarded as a definition of $G(\vec{r})$. Solving the equation 1.74 leads to the solution(33; 16),

$$G(\vec{r}) = \int_{-\pi}^{\pi} \frac{k_x}{2\pi} \int_{-\pi}^{\pi} \frac{k_y}{2\pi} \left(\frac{e^{i\vec{k}\cdot\vec{r}}}{4 - 2\cos k_x - 2\cos k_y} \right). \tag{1.75}$$

This integral is divergent for all values of the argument $\vec{r}$. However, the quantity $G(\vec{0}) - G(\vec{r})$ is convergent for finite $|\vec{r}|$, and is given by precisely the integral which we obtained in the inequality

1.51. Moreover, it is found that this is the relevant object in the present calculation of the correlation function for the effective low temperature model(14). To proceed in the calculation of the correlation function $\langle \cos(\phi_j - \phi_{j+\vec{r}}) \rangle$, we note that we may equally well consider $\langle e^{i(\phi_j - \phi_{j+\vec{r}})} \rangle$, and make use of a further well-known property of Gaussian integration(12, p. 465),

$$\langle e^{i(\phi_j - \phi_{j+\vec{r}})} \rangle = e^{-\langle (\phi_j - \phi_{j+\vec{r}})^2 \rangle / 2}. \tag{1.76}$$

We can evaluate the correlation $\langle (\phi_j - \phi_{j+\vec{r}})^2 \rangle$ in terms of the lattice Green's function,

$$\langle (\phi_j - \phi_{j+\vec{r}})^2 \rangle = \frac{2}{\beta J} \left(G(\vec{0}) - G(\vec{r}) \right). \tag{1.77}$$

We substitute in the long-range asymptotic form which we have already quoted in section 1.2,

$$G(\vec{0}) - G(\vec{r}) \sim \frac{1}{2\pi} \ln |\vec{r}|. \tag{1.78}$$

This at last provides the spin-spin correlation function as,

$$\langle e^{i(\phi_j - \phi_{j+\vec{r}})} \rangle \sim \left(\frac{1}{|\vec{r}|} \right)^{1/2\pi\beta J}. \tag{1.79}$$

This low temperature effective model exhibits power law correlations at all temperatures, where the exponent in the power law varies smoothly with temperature. Clearly, there is no phase transition in this effective model. In making the approximations to the planar rotator model to obtain 1.72, one has seemingly erased whatever behaviour in the original model is pertinent to the phase transition.

This effective quadratic model provides an approximation to the thermodynamics of the square lattice planar rotator model at low temperature, where we expect that the error associated with this approximation is smaller at lower temperatures. A stronger statement about the low temperature physics of the planar rotator model has been provided by Frohlich and Spencer in the form of an exact lower bound(34): there exists a finite temperature below which,

$$\langle \cos(\phi_j - \phi_{j+\vec{r}}) \rangle \geq A \left(\frac{1}{1 + |\vec{r}|} \right)^{1/2\pi f(\beta J)}, \tag{1.80}$$

where the $f(\beta J)$ is some function which tends to infinity as $\beta J \to \infty$, that is as the temperature approaches zero, and A is some constant. Therefore there is a finite temperature below which the

correlation function does not decay exponentially. However by the arguments of the previous section at sufficiently high temperatures the correlation function decays exponentially; this shows that there is a phase transition in the planar rotator model.

1.3.5 The helical stiffness

We have now established precisely why the square lattice planar rotator model is a particularly interesting model in statistical physics. The Mermin-Wagner theorem forbids the existence of LRO at any finite temperature, and this would seem to rule out the standard picture of a magnetic phase transition exemplified by the square lattice Ising model. However, by tackling the low and high temperature limits it has been shown that the model certainly does undergo a finite-temperature phase transition. In the next section we discuss the Kosterlitz-Thouless transition, which is a mechanism by which a two-dimensional isotropic system can undergo a phase transition. In this section we introduce the helical stiffness, which is the quantity which plays the role of an order parameter for such a system.

We begin by describing what the helical stiffness Y is, its relationship to topological excitations of the planar rotator model and its relationship to boundary conditions. We then consider the helical stiffness of the square lattice planar rotator model in both the low and high temperature limits. The low temperature limit is a finite value, $Y = J$. Conversely, it can be shown that the high temperature expansion of Y is identically equal to zero in the thermodynamic limit; this means that $Y = 0$ in the high temperature phase. These two limits therefore serve to show that Y functions as an order parameter for the phase transition in the planar rotator model.

One modifies the square lattice planar rotator Hamiltonian to be

$$H = -J \sum_{\langle jj' \rangle} \cos\left(\phi_j - \phi_{j'}\right) \to -J \sum_{\langle jj' \rangle} \cos\left(\phi_j - \phi_{j'} - \vec{\chi} \cdot \left(\vec{R}_j - \vec{R}_{j'}\right)\right). \tag{1.81}$$

This has the effect that the lowest energy configuration of the system is not to have all of the spins aligned, but for the spins to spiral in the direction of $\vec{\chi}$:

$$\phi_j = \phi_0 + \vec{\chi} \cdot \vec{R}_j. \tag{1.82}$$

The helical stiffness is defined as the change in the free energy associated with an infinitesimal $\vec{\chi}$. We

write the free energy as a Taylor series:

$$F(\vec{\chi}) = F(\vec{0}) + \frac{1}{2}\begin{pmatrix}\chi_x & \chi_y\end{pmatrix}\begin{pmatrix}Y_{xx} & Y_{xy}\\ Y_{yx} & Y_{yy}\end{pmatrix}\begin{pmatrix}\chi_x\\ \chi_y\end{pmatrix} + ... \tag{1.83}$$

where

$$\underline{\underline{Y}} = \begin{pmatrix}Y_{xx} & Y_{xy}\\ Y_{yx} & Y_{yy}\end{pmatrix} \tag{1.84}$$

is the helical stiffness tensor. The square lattice planar rotator model has the x- and y-directions completely equivalent, so that $Y_{xx} = Y_{yy}$ and $Y_{xy} = Y_{yx}$.

As compared with the ferromagnetic groundstate of the original Hamiltonian, the spiral state is an excitation in which every spin in the system is altered; this aspect of the excitation is described in it being said to be a *topological* excitation. The helical stiffness is a measure of the energetic cost of such excitations. Topological excitations are to be compared with Goldstone modes which are said to be *local* excitations.

The helical stiffness is formally identically equal to zero unless appropriate boundary conditions are applied. The spin-angles ϕ_j are measured with respect to some axis which we have the freedom to choose, and moreover we have the freedom to choose this axis differently on different lattice sites. A change from one set of such axes to another is described by the gauge transformation

$$\phi_j \to \phi_j + \gamma_j. \tag{1.85}$$

The transformed Hamiltonian must describe the same physical system; there are then sets of Hamiltonians which can be transformed into each other by such gauge transformations which describe the same physical system. Therefore, if in equation 1.81 the affect of $\vec{\chi}$ can be transformed away by making a gauge transformation, then the modified Hamiltonian must describe the same physical system as the original and therefore the free energy must be identical. Now, naively one might think that one can make a gauge transformation with

$$\gamma_j = \vec{\chi} \cdot \vec{R}_j \tag{1.86}$$

to transform the modified Hamiltonian 1.81 back to the original for any $\vec{\chi}$, and therefore that the helical stiffness must always vanish. However, whether this is so depends upon the boundary conditions that are imposed.

This issue is clearly explained by considering the planar rotator model on a linear chain. Consider first the case of open boundary conditions, which is a chain of M spins and $M-1$ bonds between neighbouring spins,

$$H = -J \sum_{j=1}^{M-1} \cos(\phi_j - \phi_{j+1}), \tag{1.87}$$

and consider the Hamiltonian with the imposed twist,

$$H(\chi) = -J \sum_{j=1}^{M-1} \cos(\phi_j - \phi_{j+1} - \chi); \tag{1.88}$$

in this case the gauge transformation $\phi_j \to \phi_j - \chi j$ maps $H(\chi)$ onto $H(0)$ and consequently these two Hamiltonians describe the same physical system and have the same free energy. Now consider the case of periodic boundary conditions, which can be pictured as a ring of M spins (see figure 1.2); in effect one has added a bond between ϕ_1 and ϕ_M,

$$H = -J \sum_{j=1}^{M-1} \cos(\phi_j - \phi_{j+1}) - J\cos(\phi_M - \phi_1), \tag{1.89}$$

and including the phase shift χ on every bond produces the new Hamiltonian,

$$H(\chi) = -J \sum_{j=1}^{M-1} \cos(\phi_j - \phi_{j+1} - \chi) - J\cos(\phi_M - \phi_1 - \chi). \tag{1.90}$$

Now the same gauge transformation $\phi_j \to \phi_j - \chi j$ maps this Hamiltonian onto

$$-J \sum_{j=1}^{M-1} \cos(\phi_j - \phi_{j+1}) - J\cos(\phi_M - \phi_1 - M\chi), \tag{1.91}$$

and this is not equivalent to the original Hamiltonian except for a special discrete set of values of χ for which $M\chi$ is equal to an integer multiple of 2π. The effect of the gauge transformation has been to shift each of the χ-phase shifts onto a single bond; in general, gauge transformations can be used to distribute the total phase shift $M\chi$ between the bonds in any whatever, but the total phase shift remains fixed. In this instance then gauge transformations cannot be used to eliminate the phase shift for arbitrary values of χ; consequently the phase shift does produce an energy cost and there is a nonzero helical stiffness.

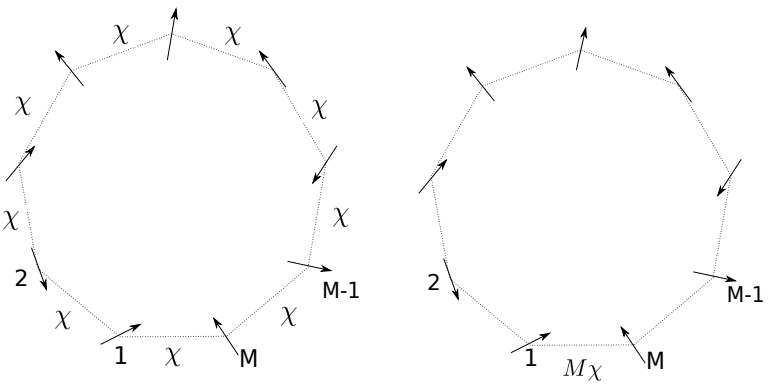

Figure 1.2: Gauge transformation of planar rotator model on a periodic ring subjected to a phase-twist χ.

The dependence on boundary conditions can be given a more physical interpretation. If there exists a configuration of the spins for which the interaction energy of each bond is $-J$, then this is clearly a groundstate, and the groundstate energy is the same as without the phase shift and therefore there is no energy cost. A nonzero helical stiffness relates to the system being "frustrated" by an infinitesimal $\vec{\chi}$, in the sense that it cannot obtain the minimum energy of $-J$ for every bond. This occurs if a "constraint" is placed on the system in the form of a boundary condition, such as the periodicity illustrated in figure 1.2 or a hard wall boundary condition in the form of the spin-angles at sites on the bondary being fixed.

We now come to considering the low and high temperature limits of the helical stiffness for the square lattice planar rotator model. We assume periodic boundary conditions in both of the principal axis directions.

We obtain the low temperature limit by imposing a small phase-twist $\vec{\chi}$ and finding the resulting minimum energy configuration of the system. It is convenient for this particular calculation to adopt the notation $\phi_{m,n}$, where the indices m and n label the co-ordinates of the lattice sites in the x and y directions respectively. The Hamiltonian with the imposed phase-twist is then,

$$H = -J \sum_{m=1}^{M-1} \sum_{n=1}^{N-1} \left[\cos\left(\phi_{m,n} - \phi_{m+1,n} - \chi_x\right) + \cos\left(\phi_{m,n} - \phi_{m,n+1} - \chi_y\right)\right] - J \sum_{n=1}^{N} \cos\left(\phi_{M,n} - \phi_{1,n} - \chi_x\right) - J \sum_{m=1}^{M} \cos\left(\phi_{m,N} - \phi_{m,1} - \chi_y\right) \tag{1.92}$$

where M and N are the system sizes in the x and y directions. We make the assumption that the

minimum energy configuration is for the spins to spiral with a pitch $\vec{q}$:

$$\phi_{m,n} = \theta - mq_x - nq_y. \tag{1.93}$$

Substituting this into the Hamiltonian, the energy of the system is,

$$E = -J\Big\{(M-1)(N-1)\left[\cos(q_x-\chi_x)+\cos(q_y-\chi_y)\right] + N\cos((M-1)q_x+\chi_x) + M\cos((N-1)q_y+\chi_y)\Big\}. \tag{1.94}$$

Minimising this expression with respect to q_x and q_y leads to the equations,

$$(N-1)\sin(q_x-\chi_x) + N\sin((M-1)q_x+\chi_x) = 0, \tag{1.95}$$

$$(M-1)\sin(q_y-\chi_y) + M\sin((N-1)q_y+\chi_y) = 0. \tag{1.96}$$

Now, in the limit that $M \gg 1$ and $N \gg 1$, these equations have the approximate solutions,

$$q_x = \frac{\pi - 2\chi_x}{M}, \tag{1.97}$$

$$q_y = \frac{\pi - 2\chi_y}{N}. \tag{1.98}$$

Substituting these expressions into equation 1.94, one finds the energy per lattice site to be, to leading order,

$$\frac{E}{MN} \sim -J\big[\cos\chi_x + \cos\chi_y\big], \tag{1.99}$$

with $O(1/M, 1/N)$ corrections. Finally expanding this quantity in χ_x and χ_y,

$$\frac{E}{MN} \sim -2J + \frac{J}{2}(\chi_x^2 + \chi_y^2). \tag{1.100}$$

The leading order correction to the groundstate energy per site is therefore $J\chi^2/2$; this implies that the low temperature limit of the helical stiffness is $Y = J$.

To consider the high temperature limit, recall the arguments we presented in section 1.3.3: in the high temperature expansion of the partition function, the $O((\beta J)^{2m})$ term is obtained as the number of possible arrangements of $2m$ arrows between neighbouring sites on the lattice, such that the net number of arrows pointing into or out of every site is zero. In the presence of $\vec{\chi}$, the same diagrams

are included, but the contribution of each diagram is multiplied by the factor

$$e^{i(l_+^x - l_-^x)\chi_x + i(l_+^y - l_-^y)\chi_y}, \tag{1.101}$$

where $l_\pm^x$ and $l_\pm^y$ are that diagram's number of directed arrows in the x- and y-directions respectively. Now, it would appear that in order for the condition that there be no net flux into any lattice site, this phase must perfectly cancel; the exceptions to this are diagrams which span the entire system, so that a lattice site is "connected to itself". Therefore in the high temperature expansion of the partition function, no dependence on $\vec{\chi}$ occurs at orders lower than $O((\beta J)^{L_{x,y}})$ and consequently the helical stiffness is not lower order than $O((\beta J)^{L_{x,y}-1})$; in the thermodynamic limit $L_x \to \infty$, $L_y \to \infty$, therefore, the high temperature expansion of the helical stiffness is identically zero, for all temperatures. This indicates that in the thermodynamic limit $Y = 0$ in the high temperature phase.

1.3.6 The Kosterlitz-Thouless transition

In considering the problem of how a two-dimensional isotropic system could undergo a phase transition, Kosterlitz and Thouless conceived a particular type of transition, the Kosterlitz-Thouless transition, which can occur in such systems. The Kosterlitz-Thouless transition is unique in that it is associated with an *essential* singularity in the thermodynamic functions; it is therefore in effect an *infinite* order phase transition. The critical form of the specific heat and the correlation function are essential singularities rather than power law singularities; this critical behaviour is therefore not characterised by the usual critical exponents α and ν. The strongest signature of the transition is found in the helical stiffness, which is predicted to jump discontinuously from a finite value to zero at the transition temperature.

We here provide an outline of the Kosterlitz-Thouless theory; our approach copies that found in many textbooks on the subject, in particular the treatment in Chaikin and Lubensky(19). We have not attempted to include the full details of the theory however, but more to mention the key physical ideas and equations. The starting point for the theory is to modify the formal continuum limit of the planar rotator model so that it can exhibit vorticity; this is done by the inclusion of a *vortex field* $\psi(\vec{r})$, which is allowed to contain isolated singularities which correspond to individual vortices. In this description the vortices act like point charges of integer charge, and there is an interaction between vortices proportional to the logarithm of their separation. We begin by describing all of this in some

detail. We then provide an outline of the calculation of the helical stiffness in this model, which shows that the presence of vortices at finite temperature acts to reduce the helical stiffness. This provides a basis for a renormalisation group treatment of the model. We provide the renormalisation group differential equations, and then describe the associated critical properties which are deduced from them.

According to standard approaches to phase transitions, it might be assumed that the behaviour of the planar rotator model close to the phase transition must be governed by long-range fluctuations. These long-wavelength fluctuations are described by the low temperature limit (see section 1.3.4), but as we have discussed this effective model does not have a phase transition. Kosterlitz and Thouless noted that this effective description did not have the capacity to describe vorticity. The spin angles ϕ_j in the lattice planar rotator model are periodic variables, in that $\phi_j \to \phi_j + 2\pi$ describes the same configuration of the system. A configuration can exhibit vorticity, in that if one considers the change in the spin-angles around some closed path of the lattice, the result can be non-zero, and can equal 2π times any integer, which is the *winding number* or *vorticity* associated with the closed path.

In a continuum model described by some field $\phi(\vec{r})$, where $\vec{r}$ is the position vector on a two dimensional space, the analogous condition is expressed as

$$\oint_C d\vec{r} \cdot \vec{\nabla}\phi = 2\pi q, \tag{1.102}$$

where

$$\vec{\nabla}\phi = \frac{\partial \phi}{\partial x}\hat{x} + \frac{\partial \phi}{\partial y}\hat{y}, \tag{1.103}$$

and q is the winding number associated with the closed curve C. Now, if $\vec{v}(\vec{r})$ is a vector field on a simply connected domain S enclosed by a curve C, then by Stokes' theorem

$$\oint_C d\vec{r} \cdot \vec{v}(\vec{r}) = \int\int_S \left(\frac{\partial v_y}{\partial x} - \frac{\partial v_x}{\partial y} \right) dxdy. \tag{1.104}$$

Substituting $\vec{v} = \vec{\nabla}\phi$ into this equation shows that the line integral vanishes if it encloses a simply connected domain. Non-zero vorticity requires that the area enclosed by C is not simply connected, that is, that there are singularities in the function $\vec{\nabla}\phi$: these singularities are precisely the individual vortices in the continuum description. Each vortex has an integer vorticity or *charge* q_i, and the

integral is determined by the total charge lying inside C:

$$\oint_C d\vec{r} \cdot \vec{\nabla}\phi = 2\pi \sum_{i \in C} q_i. \tag{1.105}$$

If we introduce a new field $\psi(\vec{r})$ defined by,

$$\vec{\nabla}\phi = \frac{\partial \psi}{\partial y}\hat{x} - \frac{\partial \psi}{\partial x}\hat{y}, \tag{1.106}$$

then the line integral can be expressed as,

$$\oint_C d\vec{r} \cdot \vec{\nabla}\phi = -\int\int_S dxdy \nabla^2 \psi. \tag{1.107}$$

This suggests that $\nabla^2\psi$ is equal to the vorticity locally, which we express in the equation

$$\nabla^2 \psi = -2\pi \sum_i q_i \delta(\vec{r} - \vec{r}_i), \tag{1.108}$$

where $\vec{r}_i$ are the positions of the vortices. This equation determines the field $\psi(\vec{r})$ to be

$$\psi(\vec{r}) = -\sum_i q_i \ln |\vec{r} - \vec{r}_i|. \tag{1.109}$$

This is exactly the same mathematics as the electrostatics of point charges of integer charge in two dimensions, with ψ the analogue of the electric potential.

In order to obtain a continuum description of the planar rotator model with vorticity, we start with the effective Hamiltonian,

$$H_{SW} = \frac{J}{2} \int dxdy \left(\vec{\nabla}\phi\right)^2,$$

which is obtained formally as the continuum limit of the lattice model, which is the same thing as the low temperature limit (see section 1.3.4), and simply add in by hand a vorticity field of the type we have described:

$$\vec{\nabla}\phi \to \vec{\nabla}\phi + \frac{\partial \psi}{\partial y}\hat{x} - \frac{\partial \psi}{\partial x}\hat{y}. \tag{1.110}$$

With this modification it can be shown that the effective Hamiltonian becomes

$$H = +\frac{J}{2}\int dxdy\left[\left(\vec{\nabla}\phi\right)^2 + \left(\vec{\nabla}\psi\right)^2\right] \tag{1.111}$$

$$= -\frac{J}{2}\int dxdy\Big[\phi\nabla^2\phi + \psi\nabla^2\psi\Big], \tag{1.112}$$

where in going from the first to the second line we have performed an integration by parts and assumed that the surface terms are zero. In particular, it can be shown that the surface term associated with the vorticity field diverges logarithmically as,

$$\sim \ln\Omega\left(\sum_i q_i\right)^2, \tag{1.113}$$

where Ω is the system size; for configurations with zero total vorticity this vanishes, while for configurations with finite total vorticity it diverges with the system size and this acts to completely suppress the thermodynamic contributions of such configurations. The resulting Hamiltonian is a sum of H_{SW} which depends on the *spin wave field* ϕ, and a term H_V which depends on the vortex degrees of freedom; because the two degrees of freedom are not coupled, the partition function is factorised according to

$$\mathcal{Z} = \mathcal{Z}_{SW}\mathcal{Z}_V \tag{1.114}$$

where the spin wave partition function can be represented as a functional integral over the field ϕ,

$$\mathcal{Z}_{SW} = \int \mathcal{D}\phi\; e^{-\beta H_{SW}}; \tag{1.115}$$

we discuss the representation of $\mathcal{Z}_V$ presently.

It is tempting to evaluate the vorticity term as

$$\frac{J}{2}\int \psi\nabla^2\psi dxdy = \pi J\sum_i\sum_{i'} q_i q_{i'}\int \ln|\vec{r}-\vec{r}_i|\delta(\vec{r}-\vec{r}_{i'})dxdy \tag{1.116}$$

$$\to \pi J\sum_i\sum_{i'} q_i q_{i'}\ln|\vec{r}_i-\vec{r}_{i'}| \tag{1.117}$$

but the $i = i'$ terms in this expression are divergent. These infinities are related to the fact that we have neglected to include a cutoff imposed by the underlying square lattice. The vortex term employed

by Kosterlitz and Thouless is(20)

$$H_V = -\pi J \sum_{i \neq i'} q_i q_{i'} \ln \left| \frac{\vec{r}_i - \vec{r}_{i'}}{a} \right| - E_C \sum_i q_i^2 \tag{1.118}$$

where a is the cutoff of the theory which for the time being can be regarded as essentially equal to the lattice spacing, and the quantity E_C is the so-called core energy associated with each vortex, which plays the role of a chemical potential for the vortices. To some approximation, only configurations which contain solely vortices of charge $q_i = \pm 1$ are relevant. Moreover, because the total vorticity must vanish, the vortex configurations can be parameterised by the number of dipole pairs of vortices, N, and the positions of the vortices $\vec{r}_i$, $i = 1, ..., 2N$. The partition function for the vortices is then

$$\mathcal{Z}_V = \sum_{N=0}^{\infty} \frac{1}{(N!)^2} y^{2N} \left(\prod_{i=1}^{2N} \int d^2 r_i \right) e^{\pi \beta J \sum_{i \neq j} q_i q_j \ln \left| \frac{\vec{r}_i - \vec{r}_j}{a} \right|}, \tag{1.119}$$

where $y = e^{\beta E_C}$ is called the *fugacity*.

The presence of vortices reduces the helical stiffness. It can be shown that, imposing the uniform twist on the system

$$\vec{\nabla}\phi + \frac{\partial \psi}{\partial y}\hat{x} - \frac{\partial \psi}{\partial x}\hat{y} \rightarrow \vec{\nabla}\phi + \frac{\partial \psi}{\partial y}\hat{x} - \frac{\partial \psi}{\partial x}\hat{y} + \vec{\chi}, \tag{1.120}$$

the Hamiltonian becomes

$$H(\vec{u}) = H(\vec{0}) + \frac{J}{2}\Omega u^2 + J \int d^2 r \; \vec{\chi} \cdot \left(\frac{\partial \psi}{\partial y}\hat{x} - \frac{\partial \psi}{\partial x}\hat{y} \right) \tag{1.121}$$

and therefore the partition function becomes

$$\mathcal{Z}(\vec{u}) = e^{-\frac{\beta J}{2}\Omega u^2} \mathcal{Z}_{SW}(\vec{0}) \int \mathcal{D}\psi \exp \left\{ -\beta H_V(\vec{0}) - \beta J \int d^2 r \; \vec{\chi} \cdot \left(\frac{\partial \psi}{\partial y}\hat{x} - \frac{\partial \psi}{\partial x}\hat{y} \right) \right\}. \tag{1.122}$$

The trace over the vortex degrees of freedom in this expression can be regarded as the average of the function

$$\exp \left\{ -\beta J \int d^2 r \; \vec{\chi} \cdot \left(\frac{\partial \psi}{\partial y}\hat{x} - \frac{\partial \psi}{\partial x}\hat{y} \right) \right\}$$

in the $\vec{\chi} = \vec{0}$ vortex ensemble; because this ensemble is quadratic in ψ, this average can be expressed

in the form,

$$\left\langle \exp\left\{ -\beta J \int d^2r\ \vec{\chi}\cdot\left(\frac{\partial\psi}{\partial y}\hat{x}-\frac{\partial\psi}{\partial x}\hat{y}\right)\right\}\right\rangle = \exp\left\{\frac{1}{2}\beta^2J^2\left\langle\left(\int d^2r\ \vec{\chi}\cdot\left(\frac{\partial\psi}{\partial y}\hat{x}-\frac{\partial\psi}{\partial x}\hat{y}\right)\right)^2\right\rangle\right\}. \tag{1.123}$$

The modified free energy is therefore

$$F(\vec{u}) = F(\vec{0}) + \frac{J}{2}\chi^2 - \frac{1}{2}\beta J^2\left\langle\frac{1}{\Omega}\left(\int d^2r\ \vec{\chi}\cdot\left(\frac{\partial\psi}{\partial y}\hat{x}-\frac{\partial\psi}{\partial x}\hat{y}\right)\right)^2\right\rangle, \tag{1.124}$$

and consequently the modified spin wave stiffness is

$$Y = J\left[1-\beta J\lim_{\chi\to 0}\frac{1}{\chi^2}\left\langle\frac{1}{\Omega}\left(\int d^2r\ \vec{\chi}\cdot\left(\frac{\partial\psi}{\partial y}\hat{x}-\frac{\partial\psi}{\partial x}\hat{y}\right)\right)^2\right\rangle\right]. \tag{1.125}$$

This is the very same quantity that occurs in the exponent in the long-range correlation function (see equation 1.79); in the presence of vortices, one still obtains the power law form of the correlation function, but with the modification that J is replaced by the helical stiffness,

$$\langle\cos\left(\phi_j-\phi_{j+\vec{r}}\right)\rangle \sim \left(\frac{1}{|\vec{r}|}\right)^{1/2\pi\beta Y}. \tag{1.126}$$

The phase transition corresponds to the decay of Y to zero at some finite temperature.

Now, to render the equation 1.125 in a useful form for examining the critical behaviour requires that the integral be represented in terms of the positions of the vortices and the fugacity y; furthermore, y is taken to be a small quantity, which corresponds to the average number of vortices being small, and the integral is expanded to second order in y. Performing this analysis leads to the important equation,

$$\frac{1}{K_R} = \frac{1}{K} + 4\pi^3y^2\int_a^\infty\frac{dr}{a}\left(\frac{r}{a}\right)^{3-2\pi K} \tag{1.127}$$

where $K=\beta J$ and $K_R=\beta Y$.

From this equation one can obtain a pair of renormalisation group (RG) differential equations which can be used to obtain the properties of the critical point. The RG scheme is to rescale the system by a factor $e^{\delta l}$; if the lattice constant is rescaled by $a\to ae^{\delta l}$, an identical equation for K_R can be obtained

in terms of rescaled parameters K' and y':

$$\frac{1}{K_R} = \frac{1}{K'} + 4\pi^3 y'^2 \int_a^\infty \frac{dr}{a} \left(\frac{r}{a}\right)^{3-2\pi K'}, \tag{1.128}$$

where the rescaled parameters are given by

$$\frac{1}{K'} = \frac{1}{K} + 4\pi^3 y^2 \int_a^{ae^{\delta l}} \frac{dr}{a} \left(\frac{r}{a}\right)^{3-2\pi K}, \tag{1.129}$$

$$y' = e^{(2-\pi K)\delta l} y. \tag{1.130}$$

By taking the limit $\delta l \to 0$ the following pair of renormalisation group (RG) differential equations are obtained.

$$\frac{d}{dl} K^{-1} = 4\pi^3 y^2, \tag{1.131}$$

$$\frac{dy}{dl} = (2 - \pi K) y. \tag{1.132}$$

The analysis of these RG equations reveals the existence of a critical point at which K jumps *discontinuously* from the value $2/\pi$ to zero. This is unique behaviour which is not associated with regular phase transitions. Above the transition where Y is zero the correlation function decays exponentially at long range, and the critical form of the correlation length is also highly unique to this particular critical point, and has the form of an essential singularity:

$$\frac{1}{\xi} \sim e^{-a/\sqrt{T - T_{KT}}}, \qquad T \to T_{KT+}, \tag{1.133}$$

where T_{KT} is the transition temperature and a some constant. The critical point is also evident in an essential singularity in the specific heat,

$$C \sim e^{-2a/(T - T_{KT})}, \qquad T \to T_{KT+}. \tag{1.134}$$

That the singular behaviour in the usual thermodynamic quantities is an essential singularity means that the transition can be considered to be an *infinite*-order phase transition. A curious feature of such a transition is that there is no divergence in any temperature derivative of the free energy.

The RG scheme does not provide the transition temperature itself; this has been estimated cal-

culating the helical stiffness for finite systems using Monte Carlo simulation, and applying a scaling analysis that is based on the Kosterlitz-Thouless theory to be $T_{\mathrm{KT}} = 0.89J(23)$. Although the author does not understand this study very well, we regard this value of the transition temperature as a prediction of the Kosterlitz-Thouless theory, and this will be relevant when we come to analyse our own calculations.

The physical picture of the Kosterlitz-Thouless transition is the unbinding of vortex-antivortex pairs; the qLRO corresponds to closely bound dipole pairs of vortices, and they unbind at the transition where there is a proliferation of vorticity. The transition itself occurs without the release of entropy; as the system disorders, there must occur the release of a large amount of entropy and therefore a large peak in the specific heat in the vicinity of the phase transition, but this is nonuniversal and not a part of the Kosterlitz-Thouless theory per se(19). This feature of the Kosterlitz-Thouless picture, that there is a large finite peak in the specific heat that *does not* mark the phase transition itself, is very relevant to the interpretation of our own calculations in the next chapter.

Chapter 2

Transfer Operator Calculations

In this chapter we present investigations of the statistical mechanics of classical spin systems using transfer operators. The primary focus is the planar rotator model on the square lattice, for which the Hamiltonian is,

$$H = -J \sum_{\langle jj' \rangle} \cos\left(\phi_j - \phi_{j'}\right),$$

where the index j labels sites on the square lattice and the summation is over all nearest-neighbour pairs of lattice sites. We shall be particularly concerned with the style of phase transition which occurs in this model. We shall also present some calculations concerning the square lattice Ising model,

$$H = -J \sum_{\langle jj' \rangle} \sigma_j \sigma_{j'},$$

where $\sigma_j \in \{+1, -1\}$ and the label j has the same meaning. It is natural to make use of the Ising model as a point of comparison, as it provides one of the few examples of a classical spin system which exhibits a phase transition for which the thermodynamics are known exactly.

The mathematics which underlies all of our calculations is that of the transfer operator. The partition function of a translationally invariant system can be represented as the repeated application of an operator, the so-called transfer operator. In this chapter, we will apply the transfer operator to periodic systems, and infinite one-dimensional systems. This is the simplest application of transfer operators, and one is likely to have encountered transfer operators being applied in this way to solve the one-dimensional Ising model even at the undergraduate level. The key result is that the partition function is given by the trace of the transfer operator raised to the power of the size of the system, and

therefore that the thermodynamics are provided by finding the eigenvalues of the transfer operator. Furthermore, in the case of the infinite one-dimensional system, the partition function is provided by the largest of the eigenvalues alone.

We have investigated the square lattice models by solving the thermodynamics of *one-dimensional* systems by finding the largest eigenvalue of the appropriate transfer operator, where the one-dimensional system is designed with some scaling parameter N in place such that it becomes the square lattice model in the limit that $N \to \infty$. There is some maximum value of N above which the relevant eigenvector is simply too large to be stored on the computer and the calculation cannot be performed; one simply performs the calculation for all values of N which are available and attempts to extrapolate to the two-dimensional limit. We will refer in general to this method of investigating two-dimensional systems as a limit of some one-dimensional system as *one-to-two dimensional crossover*. This technique is analogous to the technique of exact diagonalisation in quantum mechanics, where one investigates the quantum mechanics of an infinite system by diagonalising a series of finite systems of increasing size. The one-to-two dimensional crossover technique has been previously applied to a variety of classical spin systems, as reported in the theses of R. J. Mason(35), who considered the planar rotator model, the continuous-spin Ising model and the Heisenberg model, and of A. M. Cave(29), who investigated the clock models. The technique has also been applied to "hedgehog models" which result from restricting the classical Heisenberg spin-variables to a discrete number of equivalent directions(36).

The clock models and the planar rotator model are closely related: as we shall discuss in section 2.4.1, one of the two phase transitions in the clock models is the same as the transition in the planar rotator model. The work in this thesis is therefore closely associated with the work of A. M. Cave, and is to a large extent complementary to it. With regard to the phase transition in the square lattice planar rotator model, the two theses offer different but closely related alternative investigations of this transition. Together the two investigations show consistent evidence of a regular phase transition with ordinary critical exponents. These findings are contradictory to the picture that the model should exhibit the Kosterlitz-Thoules transition, on which there is an extremely firm consensus in the literature.

The organisation of the chapter is as follows. In section 2.1 the mathematical formalism of how periodic lattice spin-systems are solved using transfer operators is provided for the two cases of the periodic chain and the toroidal lattice. We show formally that the partition function is given by the trace of the transfer operator raised to the power of the system size. In addition, we obtain generic

forms for the transfer operator which provide the starting point when we come to solving particular models. In section 2.2 we use the transfer operator for the toroidal lattice as a starting point to obtain the exact solution of the Ising model on this lattice, which provides the solution of the infinite square lattice Ising model as a special case. We calculate the specific heat using this solution applied to the finite torus and to the infinite cylinder, the latter being the geometry which results from setting one of the periodicities in the torus equal to infinity, and show how both sets of curves approach the specific heat of the infinite square lattice Ising model as a finite system-size parameter is increased.

Having dealt with these preliminaries, we move on to the primary focus of this chapter, the study of the phase transition in the square lattice planar rotator model using one-to-two dimensional crossover. Section 2.3 introduces the formalism of the one-to-two dimensional crossover technique as it might be applied to a generic system; this essentially applies the transfer operator solution of the periodic chain to the case where the chain becomes infinitely large, but where there is implicitly a scaling parameter N in the model by which the square lattice model corresponds to the limit $N \to \infty$. In order to show how the theory functions in predicting the existence and characteristics of a phase transition, we then apply it to the Ising model. We calculate the specific heat, the correlation length, and the magnetic susceptibility, and show how these calculations can be used to estimate the critical exponents of the transition.

The investigation of the planar rotator model is then presented in section 2.4. We introduce this in section 2.4.1 by discussing the relationship between the planar rotator model and the clock model. We compare calculations for the planar rotator model, and those made for clock models by A. M. Cave previously, to show that both models have identical critical behaviour. This establishes the context of the present investigation as being complementary to the clock model investigations of A. M. Cave: both pieces of work attempt to characterise the planar rotator phase transition by two different methods, and both the methods produce consistent results showing evidence of a regular phase transition. In section 2.4.2 we discuss the representation of the transfer operator for the calculations on the computer; we describe the spin-angles using Fourier series in order to cast the transfer operator as an infinite matrix in Fourier space whose elements are products of Bessel functions, and the properties of these functions allow us to truncate the matrix to be finite while retaining accuracy in the calculation. In section 2.4.3 we formally show how a rotational symmetry in the planar rotator transfer operator can be extracted to reduce the number of degrees of freedom in the problem by one, thereby allowing the calculation to be performed for one larger value of the scaling parameter N. We then present in detail the calculations

of the specific heat, correlation length and magnetic susceptibility in sections 2.4.4, 2.4.5 and 2.4.6 respectively. As we shall show, the correlation length is closely related to the eigenvalue spectrum of the transfer operator, and in section 2.4.5 we shall also present a number of related calculations involving various eigenvalues. The results of these calculations are qualitatively similar to those of the Ising model, consistently showing evidence for a regular phase transition with critical exponents with values close to those for the Ising phase transition. The evidence in the calculations that thermodynamic quantites will become divergent in the two-dimensional limit $N \to \infty$ is in contradiction with the picture that the system should exhibit a Kosterlitz-Thouless transition. We then present calculations of the helical stiffness in section 2.4.7. We find that, as expected, the helical stiffness appears to drop rapidly to zero at a temperature close to the sharp behaviour seen in the specific heat, correlation length and the magnetic susceptibility, but we are not able to establish for certain whether this drop is continuous in the manner of an order parameter in a regular phase transition, or discontinuous as it should be in a Kosterlitz-Thouless transition. We finally offer a discussion of our findings in section 2.4.8.

2.1 Formalism of transfer operators

2.1.1 The transfer operator for a periodic spin-chain

In this section we consider a periodic chain of M spin-variables $\vec{S}_j$, where the index j labels the site in the chain. At this stage, we do not specify the dimensionality of these spin degrees of freedom, or whether they are discrete or continuous. However, it is always to be understood that there is an equivalent degree of freedom, that is an equivalent spin-variable, on each site in the chain, and this will also be the case for all kinds of lattices which we discuss in this chapter. We shall develop the formalism for the following fairly general Hamiltonian of pairwise spin-interactions:

$$H_M = -\sum_{j=1}^{M} \left[\sum_{n=1}^{N} J_n V_n(\vec{S}_j, \vec{S}_{j+n}) \right]. \tag{2.1}$$

The only restrictions which we place on the set of spin-interactions V_n are that they be pairwise and that the interactions only extend up to a range N which is less than the period of the system M. The

most physically common interaction is the scalar product interaction,

$$V_n(\vec{S}_j, \vec{S}_{j+n}) = \vec{S}_j \cdot \vec{S}_{j+n}. \tag{2.2}$$

This will be the only interaction which will be considered after the general formalism of transfer operators is introduced.

The partition function is given by

$$\mathcal{Z}_M = \left(\prod_{j=1}^{M} \int d\Omega_j \right) e^{-\beta H_M}, \tag{2.3}$$

where $\int d\Omega_j$ represents the summation over all possible orientations of the spin $\vec{S}_j$. It is to be understood that this symbol indicates a sum, as opposed to an integral, in the case that the spin degrees of freedom are discrete.

The central result of this section is that there exists an operator $\hat{T}$ such that the partition function can be represented as

$$\mathcal{Z}_M = \mathrm{tr}(\hat{T}^M), \tag{2.4}$$

The calculation of the partition function is thereby reduced to the diagonalisation of the operator $\hat{T}$, which is known as the *transfer function* or *transfer matrix*. Since the trace of any operator is equal to the sum of its eigenvalues, the partition function can be calculated explicitly as

$$\mathcal{Z}_M = \sum_{\alpha} (z_\alpha)^M \tag{2.5}$$

where z_α are the eigenvalues of the transfer operator.

In the remainder of this section, we shall formally prove this result. We begin by essentially guessing a form for the transfer operator. We then formally calculate the left hand side of equation 2.4 and show it to be equal to the partition function. We make use of the Dirac notation for its efficiency and also to highlight how the theory is analogous to quantum mechanics. The only non-trivial part of this theory is that in demanding the transfer operator to be self-adjoint, one is forced to introduce an unconventional analogue of the scalar product.

The transfer operator approach is based in the translational symmetry of the Hamiltonian: each site in the chain is equivalent to any other. Consequently, the quantity $e^{-\beta H_M}$, which depends upon

all the M spins in the chain, can be factorised into the product of M terms which each depend on only a restricted subset of local spins and which have the same functional form:

$$e^{-\beta H_M} = e^{\beta K(\vec{S}_1,\vec{S}_2,...,\vec{S}_{N+1})} e^{\beta K(\vec{S}_2,\vec{S}_3,...,\vec{S}_{N+2})} ... e^{\beta K(\vec{S}_M,\vec{S}_1,...,\vec{S}_N)}, \tag{2.6}$$

where $K(\vec{S}_1, \vec{S}_2, ..., \vec{S}_{N+1})$ is chosen to satisfy the condition,

$$K(\vec{S}_1, \vec{S}_2, ..., \vec{S}_{N+1}) + K(\vec{S}_2, \vec{S}_3, ..., \vec{S}_{N+2}) + ... + K(\vec{S}_M, \vec{S}_1, ..., \vec{S}_N) = -H_M. \tag{2.7}$$

If we associate each of these M factors with one of the summations in equation 2.3, one can guess that the partition function involves the repeated application of an operator $\hat{T}$ defined by

$$\left(\hat{T} f\right)(\vec{S}_2, \vec{S}_3, ..., \vec{S}_{N+1}) = \int d\Omega_1 e^{\beta K(\vec{S}_1,\vec{S}_2,...,\vec{S}_N,\vec{S}_{N+1})} f(\vec{S}_1, \vec{S}_2, ..., \vec{S}_N) \tag{2.8}$$

where f is any function of N spins. The effect of the transfer function is to integrate out one of the spins and "transfer" one site along the chain.

If the function K is chosen to have the symmetry

$$K(\vec{S}_1, \vec{S}_2, ..., \vec{S}_N, \vec{S}_{N+1}) = K(\vec{S}_{N+1}, \vec{S}_N, ..., \vec{S}_2, \vec{S}_1) \tag{2.9}$$

this provides the following natural inner product

$$(f, g) = \left(\prod_{j=1}^{N} \int d\Omega_j\right) f(\vec{S}_N, \vec{S}_{N-1}, ..., \vec{S}_1) g(\vec{S}_1, \vec{S}_2, ..., \vec{S}_N) \tag{2.10}$$

with respect to which the transfer operator is self-adjoint, which precisely means that it satisfies

$$(\hat{T} f, g) = (f, \hat{T} g) \tag{2.11}$$

for any two functions $f(\vec{S}_1, \vec{S}_2, ..., \vec{S}_N)$ and $g(\vec{S}_1, \vec{S}_2, ..., \vec{S}_N)$.

This is the analogue to the scalar product in quantum mechanics. In that theory, the scalar product between two wavefunctions $\Phi(\{x_i\})$ and $\Psi(\{x_i\})$ is

$$(\Phi, \Psi) = \left(\prod_i \int dx_i\right) \Phi^*(\{x_i\}) \Psi(\{x_i\}), \tag{2.12}$$

where $\{x_i\}$ might for example be the co-ordinates of a number of particles.

It is a straightforward matter to represent the theory of the transfer operator in the Dirac notation, where we are guided by the analogue of the inner product 2.10. The function $f(\vec{S}_1, ..., \vec{S}_N)$ describes the components in a particular basis of an underlying vector $|f\rangle$. We express this formally as

$$|f\rangle = \left(\prod_{j=1}^{N} \int d\Omega_j \right) f(\vec{S}_1, \vec{S}_2, ..., \vec{S}_N) |\vec{S}_1, \vec{S}_2, ..., \vec{S}_N\rangle \tag{2.13}$$

where the vectors $|\vec{S}_1, \vec{S}_2, ..., \vec{S}_N\rangle$ are the basis vectors. One has also a dual vector-space, whose members are written as bra vectors, and the vector corresponding to $f(\vec{S}_1, ..., \vec{S}_N)$ in the dual space is $\langle f|$ and is given by,

$$\langle f| = \left(\prod_{j=1}^{N} \int d\Omega_j \right) f(\vec{S}_1, \vec{S}_2, ..., \vec{S}_N) \langle S_1, \vec{S}_2, ..., \vec{S}_N| \tag{2.14}$$

where the vectors $\langle \vec{S}_1, \vec{S}_2, ..., \vec{S}_N|$ are the basis vectors in the dual space. We construct the theory so that the product $\langle f|g\rangle$ provides the scalar product 2.10, in analogy with quantum mechanics. This implies that the products between the basis vectors are given by

$$\langle \vec{S}'_1, ..., \vec{S}'_N | \vec{S}_1, ..., \vec{S}_N \rangle = \prod_{j=1}^{N} \delta_{\vec{S}_j - \vec{S}'_{N+1-j}} \tag{2.15}$$

One can immediately proceed to write down a number of results in exactly the familiar form of quantum mechanics: the completeness condition for the basis states,

$$\left(\prod_{j=1}^{N} \int d\Omega_j \right) |\vec{S}_N, ..., \vec{S}_1\rangle \langle \vec{S}_1, ..., \vec{S}_N| = \hat{I}, \tag{2.16}$$

where $\hat{I}$ is the identity operator; the explicit formula for the function $f(\vec{S}_1, \vec{S}_2, ..., \vec{S}_N)$ in terms of the vectors,

$$f(\vec{S}_1, ..., \vec{S}_N) = \langle \vec{S}_N, ..., \vec{S}_1 | f\rangle = \langle f | \vec{S}_N, ..., \vec{S}_1\rangle; \tag{2.17}$$

and the trace of any operator $\hat{O}$,

$$\mathrm{tr}(\hat{O}) = \left(\prod_{j=1}^{N} \int d\Omega_j \right) \langle \vec{S}_N, ..., \vec{S}_1 | \hat{O} | \vec{S}_1, ..., \vec{S}_N \rangle. \tag{2.18}$$

With this formalism in place, it is a relatively simple matter to calculate the matrix elements of

$\hat{T}$, deduce from these the matrix elements of $\hat{T}^M$, and substitute these into equation 2.18 to calculate the trace.

The application of the transfer operator $\hat{T}$ can be expressed formally in terms of matrix elements as

$$\langle \vec{S}_N, ..., \vec{S}_1 | \hat{T} | f \rangle = \left(\prod_{j=1}^{N} \int d\Omega'_j \right) \langle \vec{S}_N, ..., \vec{S}_1 | \hat{T} | \vec{S}'_1, ..., \vec{S}'_N \rangle \langle \vec{S}'_N, ..., \vec{S}'_1 | f \rangle. \tag{2.19}$$

where $\int d\Omega'_j$ indicates the integration over the corresponding primed spin-variable, $\vec{S}'_j$. One can deduce the matrix elements of $\hat{T}$ by comparing this formal expression with equation 2.8, and the result is found to contain a single $e^{\beta K(...)}$ factor together with $N-1$ delta functions:

$$\langle \vec{S}_N, ..., \vec{S}_1 | \hat{T} | \vec{S}'_1, ..., \vec{S}'_N \rangle = e^{\beta K(\vec{S}'_1, \vec{S}_1, \vec{S}_2, ..., \vec{S}_N)} \times \prod_{j=2}^{N} \delta_{\vec{S}'_j, \vec{S}_{j-1}}. \tag{2.20}$$

It is helpful to relabel the spin-variables to make the expression for the matrix elements more closely resemble equation 2.8:

$$\langle \vec{S}_{N+1}, ..., \vec{S}_2 | \hat{T} | \vec{S}_1, \vec{S}'_2, ..., \vec{S}'_N \rangle = e^{\beta K(\vec{S}_1, \vec{S}_2, ..., \vec{S}_{N+1})} \times \prod_{j=2}^{N} \delta_{\vec{S}'_j, \vec{S}_j}. \tag{2.21}$$

The matrix elements of $\hat{T}^2$, $\hat{T}^3$, ..., can be easily calculated directly; each successive multiplication provides an extra $e^{\beta K(...)}$ factor and results in one fewer delta function, so that for $m < N$ we obtain

$$\langle \vec{S}_{m+N}, ..., \vec{S}_{m+1} | \hat{T}^m | \vec{S}_1, ..., \vec{S}_m, \vec{S}'_{m+1}, ..., \vec{S}'_N \rangle = e^{\beta K(\vec{S}_1, ..., \vec{S}_{N+1})} e^{\beta K(\vec{S}_2, ..., \vec{S}_{N+2})} ... e^{\beta K(\vec{S}_m, ..., \vec{S}_{m+N})} \times \prod_{j=m+1}^{N} \delta_{\vec{S}'_j, \vec{S}_j}. \tag{2.22}$$

Thereafter, raising $\hat{T}$ to higher powers, we obtain,

$$\langle \vec{S}_{2N}, ..., \vec{S}_{N+1} | \hat{T}^N | \vec{S}_1, ..., \vec{S}_N \rangle = e^{\beta K(\vec{S}_1, ..., \vec{S}_{N+1})} e^{\beta K(\vec{S}_2, ..., \vec{S}_{N+2})} ... e^{\beta K(\vec{S}_N, ..., \vec{S}_{2N})}, \tag{2.23}$$

and for $m > N$

$$\langle \vec{S}_{m+N}, ..., \vec{S}_{m+1} | \hat{T}^m | \vec{S}_1, ..., \vec{S}_N \rangle = \left(\prod_{j=N+1}^{m} \int d\Omega_j \right) e^{\beta K(\vec{S}_1, ..., \vec{S}_{N+1})} e^{\beta K(\vec{S}_2, ..., \vec{S}_{N+2})} ... e^{\beta K(\vec{S}_m, ..., \vec{S}_{m+N})}. \tag{2.24}$$

The final expression provides a proof of the identity 2.4; calculating the trace of $\hat{T}^M$ formally by substituting the expression for the matrix elements into equation 2.18, the result is plainly the partition function identically.

2.1.2 The transfer operator of a toroidal spin-system

In this section we shall consider the toroidal lattice illustrated in Figure 2.1. This is equivalent to a finite square lattice with periodic boundary conditions in both of the principal directions. This functions as a precursor to the following section, in which we present the exact solution to the Ising model on this lattice. In the present section, we will derive a result for the partition function of a spin system on the toroidal lattice that is analogous to the result 2.4 which was established for the linear chain.

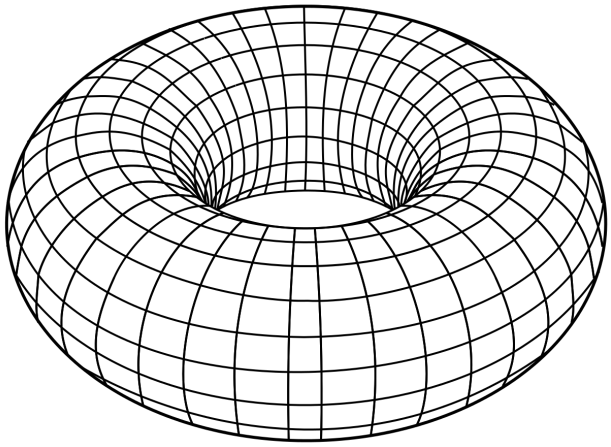

Figure 2.1: Illustration of the torus geometry.
(Taken from `https://commons.wikimedia.org/wiki/File:Simple_Torus.s`).

Consider a toroidal lattice made up of M connected N-fold rings. Let the index i label the position of a lattice site on one of the rings and let the index j label the rings; let $\vec{S}_{i,j}$ be the spin on the ith site on the jth ring. We consider the rather generic spin-Hamiltonian,

$$H_{N,M} = -\sum_{i=1}^{N}\sum_{j=1}^{M}\left[\sum_{r=1}^{R_{\parallel}}\sum_{s=1}^{R_{\perp}} J^{\parallel}_{r,s} V^{\parallel}_{r,s}(\vec{S}_{i,j}, \vec{S}_{i+s,j+r}) + \sum_{s=1}^{R_{\perp}} J^{\perp}_{s} V^{\perp}_{s}(\vec{S}_{i,j}, \vec{S}_{i+s,j})\right]. \tag{2.25}$$

As in section 2.1.1 we make the restriction that the maximum range of the interactions be less than

the size of the system, that is we require that,

$$R_{\|} < M, \qquad R_{\perp} < N. \tag{2.26}$$

We have separated the Hamiltonian into two terms, the first of which contains all the interactions between spins on different rings, and the second of which contains all the interactions between spins on the same ring. This separation will be made use of when we come to discuss the Ising model.

The partition function is

$$\mathcal{Z}_{N,M} = \left(\prod_{i=1}^{N} \prod_{j=1}^{M} \int d\Omega_{i,j} \right) e^{-\beta H_{N,M}}. \tag{2.27}$$

The formalism is simplified if we use the symbol $\vec{\mathcal{S}}_j$ to label the configurations of the set of spins $\{\vec{S}_{1,j}, \vec{S}_{2,j}, ..., \vec{S}_{N,j}\}$ on the jth ring. With this notation, we can factorise $e^{-\beta H_{N,M}}$ in a manner analagous to equation 2.6, and which preserves the separation of the interactions between different rings and the interactions on a single ring:

$$e^{-\beta H_{N,M}} = e^{\beta K_{\perp}(\vec{\mathcal{S}}_1)} e^{\beta K_{\|}(\vec{\mathcal{S}}_1, \vec{\mathcal{S}}_2, ..., \vec{\mathcal{S}}_{R_{\|}+1})} e^{\beta K_{\perp}(\vec{\mathcal{S}}_2)} e^{\beta K_{\|}(\vec{\mathcal{S}}_2, \vec{\mathcal{S}}_3, ..., \vec{\mathcal{S}}_{R_{\|}+2})} ... e^{\beta K_{\perp}(\vec{\mathcal{S}}_M)} e^{\beta K_{\|}(\vec{\mathcal{S}}_M, \vec{\mathcal{S}}_1, ..., \vec{\mathcal{S}}_{R_{\|}})} \tag{2.28}$$

where the function $K_{\|}(\vec{\mathcal{S}}_1, \vec{\mathcal{S}}_2, ..., \vec{\mathcal{S}}_{R_{\|}+1})$ is chosen to satisfy

$$\begin{aligned} K_{\|}(\vec{\mathcal{S}}_1, \vec{\mathcal{S}}_2, ..., \vec{\mathcal{S}}_{R_{\|}+1}) + K_{\|}(\vec{\mathcal{S}}_2, \vec{\mathcal{S}}_3, ..., \vec{\mathcal{S}}_{R_{\|}+2}) + ... + K_{\|}(\vec{\mathcal{S}}_M, \vec{\mathcal{S}}_1, ..., \vec{\mathcal{S}}_{R_{\|}}) \\ = \sum_{i=1}^{N} \sum_{j=1}^{M} \left[\sum_{r=1}^{R_{\|}} \sum_{s=1}^{R_{\perp}} J_{r,s}^{\|} V_{r,s}^{\|}(\vec{S}_{i,j}, \vec{S}_{i+s,j+r}) \right], \end{aligned} \tag{2.29}$$

and $K_{\perp}(\vec{\mathcal{S}}_1)$ is given by

$$K_{\perp}(\vec{\mathcal{S}}_j) = \sum_{i=1}^{N} \left[\sum_{s=1}^{R_{\perp}} J_s^{\perp} V_s^{\perp}(\vec{S}_{i,j}, \vec{S}_{i+s,j}) \right]. \tag{2.30}$$

It is clear that the results of the linear spin chain can be applied to this system, but where one now has the variable $\vec{\mathcal{S}}_j$ as the analogue of a single spin. The partition function is the trace of a transfer function raised to the power M, the number of rings:

$$\mathcal{Z}_{N,M} = \mathrm{tr}(\hat{T}^M). \tag{2.31}$$

The transfer operator can be written so as to preserve the separation of the interactions between different rings and the interactions on a single ring,

$$\hat{T} = \hat{T}_{\parallel}\hat{T}_{\perp}, \tag{2.32}$$

where $\hat{T}_{\parallel}$ functions like the transfer operator of the linear chain and performs the "transfer" from one ring to the next,

$$\left(\hat{T}_{\parallel} f\right)(\vec{\mathcal{S}}_2, \vec{\mathcal{S}}_3, ..., \vec{\mathcal{S}}_{R_{\parallel}+1}) = \left(\prod_{i=1}^{N}\int d\Omega_{i,1}\right) e^{\beta K_{\parallel}(\vec{\mathcal{S}}_1, \vec{\mathcal{S}}_2, ..., \vec{\mathcal{S}}_{R_{\parallel}}, \vec{\mathcal{S}}_{R_{\parallel}+1})} f(\vec{\mathcal{S}}_1, \vec{\mathcal{S}}_2, ..., \vec{\mathcal{S}}_{R_{\parallel}}), \tag{2.33}$$

and $\hat{T}_{\perp}$ is simply defined so as to provide the factors arising from the single-ring interactions,

$$\left(\hat{T}_{\perp} f\right)(\vec{\mathcal{S}}_1, \vec{\mathcal{S}}_2, ..., \vec{\mathcal{S}}_{R_{\parallel}}) = e^{\beta K_{\perp}(\vec{\mathcal{S}}_1)} f(\vec{\mathcal{S}}_1, \vec{\mathcal{S}}_2, ..., \vec{\mathcal{S}}_{R_{\parallel}}). \tag{2.34}$$

2.2 Exact solution of the Ising model on the square lattice

In this section we apply the transfer operator technique to the Ising model on the torus. For this particular model, the trace in equation 2.31 can be calculated analytically. This provides, in the appropriate limit, the well-known exact solution of the Ising model on the infinite square lattice. The reason for reproducing such a well-known exact solution in such detail is that it allows us to illustrate the crossing over of the system from zero- and one-dimension to two dimensions, and the related emerging of a singularity in the thermodynamics, while retaining total mathematical control. This provides a foundation for the subsequent investigations in the planar rotator model which use these ideas in the absence of an exact solution.

The transition temperature of the infinite square lattice model was first provided by Kramers and Wannier using a duality argument(37). The calculation of the free energy was provided by Onsager in a famous paper(17); this calculation was then simplified by Kaufman(38) and together Onsager and Kauffman deduced the functional form of the spontaneous magnetisation close to the phase transition, in work that was never published but which has since been re-evaluated(39). The first published calculation of the free energy was by Yang(40). Since these early works, the solution of the square lattice Ising model has been reproduced by a plethora of different methods; the literature on this subject is vast and the author is much too ignorant of it. We single out the solution by Schultz,

Mattis and Lieb using a fermion representation(41); the solution we present in this section uses the same approach and must be essentially the same as that of Schultz *et al* although we have not closely followed their working. A detailed exposition of a solution along the same lines as Onsager's original solution is given in the book of exact solutions to statistical mechanics models by Baxter(6).

The Ising model considers spins, which we label with the symbol σ, which can be in one of two states, "up" $\sigma = 1$ or "down" $\sigma = -1$, and a scalar product interaction between spins $-J\sigma\sigma'$. With the restriction to nearest-neighbour interactions, the Hamiltonian in equation 2.25 takes the form

$$H_{N,M} = -J_{\parallel} \sum_{j=1}^{M} \sum_{i=1}^{N} \sigma_{i,j}\sigma_{i,j+1} - J_{\perp} \sum_{j=1}^{M} \sum_{i=1}^{N} \sigma_{i,j}\sigma_{i+1,j} \tag{2.35}$$

and the partition function is

$$\mathcal{Z}_{N,M} = \left(\prod_{i=1}^{N} \prod_{j=1}^{M} \sum_{\sigma_{i,j}} \right) e^{-\beta H_{N,M}}. \tag{2.36}$$

The exact solution begins with the results 2.31 and 2.32. We shall first write down the transfer matrix in the most obvious representation. We shall then show how the problem may be represented in terms of quantum spin-physics, and write the transfer operator in terms of Pauli spin operators. Having represented the problem of diagonalising the transfer matrix as a problem in quantum spin-physics, we next map this onto a fermion problem using the Jordan-Wigner transformation. The representation that results from this transformation is equivalent to a non-interacting Fermi problem. One can then extract the translational symmetry of sites around the same ring via a Bloch transformation, which reduces the transfer matrix in size from $2^N \times 2^N$ to 2×2. At this point it is a simple matter to write down the eigenvalues.

The transfer operator in equations 2.31 and 2.32 for the Ising model can be represented as:

$$\langle \{\sigma\} | \hat{T}_{\parallel} | \{\sigma'\} \rangle = \prod_{n=1}^{N} e^{\beta J_{\parallel} \sigma_n \sigma'_n}, \tag{2.37}$$

$$\langle \{\sigma\} | \hat{T}_{\perp} | \{\sigma'\} \rangle = \prod_{n=1}^{N} e^{\beta J_{\perp} \sigma_n \sigma_{n+1}} \delta_{\{\sigma\},\{\sigma'\}}, \tag{2.38}$$

where $\{\sigma\}$ is written in place of the symbol $\vec{\mathcal{S}}$ used above and is the set of Ising spins on a single ring.

The state space of an Ising variable σ is the same as a quantum one half spin, in that there are two possible states. The transfer operator can therefore be represented using the formalism of quantum spin-physics. We map each of the N Ising variables, which label the basis states in equations 2.37 and

2.38, to a quantum one-half spin. The relevant operators in quantum spin-$\frac{1}{2}$ physics are the Pauli spin operators, which give the components of spin in each of the three Cartesian directions:

$$\hat{\sigma}^x = \begin{pmatrix} 0 & 1 \\ 1 & 0 \end{pmatrix}, \quad \hat{\sigma}^y = \begin{pmatrix} 0 & i \\ -i & 0 \end{pmatrix}, \quad \hat{\sigma}^z = \begin{pmatrix} 1 & 0 \\ 0 & -1 \end{pmatrix}. \tag{2.39}$$

There is a set of Pauli operators for each of the N spins, which we indicate by means of the notation $\hat{\sigma}_n^{x,y,z}$.

We must therefore write the operators $\hat{T}_\parallel$ and $\hat{T}_\perp$ in terms of the Pauli matrices. It is straightforward to do this for $\hat{T}_\perp$: it is plain from equation 2.38 that the basis vectors are eigenvectors of $\hat{T}_\perp$, and thus the desired representation is obtained simply by constructing the appropriate function of the $\hat{\sigma}_n^z$ operators. It is clear that

$$\prod_{n=1}^{N} e^{\beta J_\perp \hat{\sigma}_n^z \hat{\sigma}_{n+1}^z} |\sigma_1, \sigma_2, ..., \sigma_N\rangle = \prod_{n=1}^{N} e^{\beta J_\perp \sigma_n \sigma_{n+1}} |\sigma_1, \sigma_2, ..., \sigma_N\rangle \tag{2.40}$$

and so we can identify

$$\hat{T}_\perp = \exp\left(\beta J_\perp \sum_{n=1}^{N} \hat{\sigma}_n^z \hat{\sigma}_{n+1}^z\right). \tag{2.41}$$

The representation for $\hat{T}_\parallel$ is less obvious. Consider the factor $e^{\beta J_\parallel \sigma_n \sigma'_n}$ in equation 2.37: this factor can take one of only two values, according to whether the two Ising variables σ_n and σ'_n are equal or unequal. Thus for every matrix element connecting two states with the same spin on site n, this factor contributes $e^{\beta J_\parallel}$, while for matrix elements connecting states with opposite spins on site n this factor contributes $e^{-\beta J_\parallel}$. The action of $\hat{T}_\parallel$ on the spin σ_n therefore has two contributions, one where the spin is left unchanged and one where the spin is flipped, with factors of $e^{\beta J_\parallel}$ and $e^{-\beta J_\parallel}$ respectively. The action of flipping a spin is represented by $\hat{\sigma}_n^x$, and so we may write

$$e^{\beta J_\parallel \sigma_n \sigma'_n} = \langle\{\sigma\}| \left(e^{\beta J_\parallel} + e^{-\beta J_\parallel} \hat{\sigma}_n^x\right) |\{\sigma'\}\rangle. \tag{2.42}$$

The operator $\hat{T}_\parallel$ is then given by a product of such terms for each of the spins on the ring:

$$\hat{T}_\parallel = \prod_{n=1}^{N} \left(e^{\beta J_\parallel} + e^{-\beta J_\parallel} \hat{\sigma}_n^x\right). \tag{2.43}$$

This operator can be re-written in the form of a single exponential. For a general Pauli operator

$\hat{\Sigma}$ - that is any operator whose square is unity - we have the important identity,

$$e^{A\hat{\Sigma}} = \cosh A + \hat{\Sigma} \sinh A, \tag{2.44}$$

where is A is any real or complex number. This allows us to write

$$e^{\beta J_\parallel} + e^{-\beta J_\parallel} \hat{\sigma}_n^x = e^{X + Y\hat{\sigma}_n^x} \tag{2.45}$$

where the newly-introduced variables X and Y satisfy the equations,

$$\tanh Y = e^{-2\beta J_\parallel}, \tag{2.46}$$

$$e^{2X} = e^{2\beta J_\parallel} - e^{-2\beta J_\parallel}. \tag{2.47}$$

The final representation of the transfer operator in terms of the Pauli matrices is therefore

$$\hat{T} = \exp\left(\sum_{m=1}^{N} (X + Y\hat{\sigma}_m^x)\right) \exp\left(\beta J_\perp \sum_{n=1}^{N} \hat{\sigma}_n^z \hat{\sigma}_{n+1}^z\right). \tag{2.48}$$

Note that, at this stage, the two exponentials must be kept as separate factors, because their arguments do not commute.

We are now in a position to make the second transformation of the transfer operator, the transformation to a representation in terms of fermions, or the so-called Jordan-Wigner transformation(41). Like the transformation from the initial classical Ising variables to the quantum spin-$\frac{1}{2}$ representation, the transformation to the fermion representation is suggested because in a fermion problem there are two natural states: the vacuum state where there is no fermion, $|0\rangle$, and the state where there is a fermion, $f^\dagger|0\rangle$. The essence of the Jordan-Wigner transformation is to associate these two states with the two eigenstates of spin along some axis. We shall use a Jordan-Wigner transformation that maps onto the eigenstates of spin along the x-axis. However, it is notationally convenient to label the Jordan-Wigner spin axis as z. We therefore first relabel the spin directions in 2.48, which is the same as changing the basis in the spin-$\frac{1}{2}$ representation. Under the cyclic relabelling $x \to z$, $y \to x$, $z \to y$ the expression for the transfer matrix in equation 2.48 becomes

$$\hat{T} = \exp\left(\sum_{m=1}^{N} (X + Y\hat{\sigma}_m^z)\right) \exp\left(\beta J_\perp \sum_{n=1}^{N} \hat{\sigma}_n^y \hat{\sigma}_{n+1}^y\right). \tag{2.49}$$

The Jordan-Wigner transformation prescribes

$$|\uparrow\rangle \to |0\rangle, \tag{2.50}$$

$$|\downarrow\rangle \to f^\dagger|0\rangle, \tag{2.51}$$

where $|\uparrow\rangle$ and $|\downarrow\rangle$ are the eigenstates of $\hat{\sigma}^z$. To complete the transformation, one needs to write the original spin operators in terms of the fermion operator $f^\dagger$ and its conjugate f. The z-component of spin can easily be written down as the new representation is an eigenbasis of this operator by construction. One finds for a single spin

$$\hat{\sigma}^z = 1 - 2f^\dagger f, \tag{2.52}$$

where we recognise the number operator $f^\dagger f$ which acts to count the number of fermions. To represent the transfer operator in terms of fermions, we invent fermi creation and annihilation operators for every site, and simply write,

$$\hat{\sigma}^z_n = 1 - 2f^\dagger_n f_n. \tag{2.53}$$

The Fermi operators obey the anticommutation relations,

$$\{f^\dagger_n, f^\dagger_{n'}\} = 0, \qquad \{f_n, f_{n'}\} = 0, \qquad \{f_n, f^\dagger_{n'}\} = \delta_{n,n'}. \tag{2.54}$$

The basis vectors of the fermion representation are states of the form

$$f^\dagger_2 f^\dagger_5 f^\dagger_6 ...|0\rangle,$$

where we take the vacuum to correspond to the state where all the spins are "up", and we operate with the appropriate creation operators to form the state which has the corresponding spins "down". Because the creation operators corresponding to different sites anticommute with each other, the order in which the operators are written to form the basis vectors is important, and to properly define the basis vectors a consistent ordering of the operators must be used. We choose to use the ordering that the operators with a smaller site-index always appear to the left of operators with a larger site-index.

To complete the transformation, we must now write the operator $\hat{\sigma}^y_n \hat{\sigma}^y_{n+1}$ in terms of the fermion operators. The action of $\hat{\sigma}^y$, as can be seen from 2.39, is to flip the spin from up to down with a factor

i, or from down to up with a factor $-i$. Therefore the action of $\hat{\sigma}_n^y \hat{\sigma}_{n+1}^y$ is to flip both of the spins n and $n+1$, with a factor $+1$ or -1. In the fermion representation, the action of the operator on the two relevant spins can be explicitly described as,

$$\begin{aligned}
|\uparrow\uparrow\rangle \to -|\downarrow\downarrow\rangle \qquad & \text{becomes} \qquad |0\rangle \to -f_n^\dagger f_{n+1}^\dagger |0\rangle, \\
|\uparrow\downarrow\rangle \to |\downarrow\uparrow\rangle \qquad & \text{becomes} \qquad f_{n+1}^\dagger |0\rangle \to f_n^\dagger |0\rangle, \\
|\downarrow\uparrow\rangle \to |\uparrow\downarrow\rangle \qquad & \text{becomes} \qquad f_n^\dagger |0\rangle \to f_{n+1}^\dagger |0\rangle, \\
|\downarrow\downarrow\rangle \to -|\uparrow\uparrow\rangle \qquad & \text{becomes} \qquad f_n^\dagger f_{n+1}^\dagger |0\rangle \to -|0\rangle.
\end{aligned}$$

This would seem to imply the representation,

$$\hat{\sigma}_n^y \hat{\sigma}_{n+1}^y = f_n^\dagger f_{n+1} + f_{n+1}^\dagger f_n - f_n^\dagger f_{n+1}^\dagger - f_{n+1} f_n, \tag{2.55}$$

where the first two terms hop particles between neighbouring sites and the last two terms create and annihilate pairs of particles on neighbouring sites. However, the term $\hat{\sigma}_N^y \hat{\sigma}_1^y$ presents additional difficulties. The first and third terms in equation 2.55 give rise to states of the form $f_N^\dagger(...)|0\rangle$ which have the creation operator for the Nth site appearing in the wrong order for how we have defined the basis states. To compare this state with the corresponding basis state, the operator $f_N^\dagger$ must be commuted past the other creation operators present in order to be at the rightmost place, according to our ordering convention. This gives rise to a minus sign if $f_N^\dagger$ must be commuted through an odd number of creation operators; this occurs if the total number of fermions, including that on site N, is even. It follows, therefore, that the state $f_N^\dagger(...)|0\rangle$ is equal to the corresponding basis state if the total number of fermions in the state is odd, and is equal to *minus* the basis state if the number of fermions is even. The action of the second and fourth terms in 2.55 also produce this same minus sign for the case of an even number of particles. We therefore find that we must treat the case of an odd particle number and the case of an even particle number differently, and in the latter case one of the bonds on the ring is special. To be explicit, we find for an odd number of fermions,

$$\sum_{n=1}^{N} \hat{\sigma}_n^y \hat{\sigma}_{n+1}^y = \sum_{n=1}^{N} \left(f_n^\dagger f_{n+1} + f_{n+1}^\dagger f_n - f_n^\dagger f_{n+1}^\dagger - f_{n+1} f_n \right), \tag{2.56}$$

and for an even number of fermions,

$$\sum_{n=1}^{N} \hat{\sigma}_n^y \hat{\sigma}_{n+1}^y = \sum_{n=1}^{N-1} \left(f_n^\dagger f_{n+1} + f_{n+1}^\dagger f_n - f_n^\dagger f_{n+1}^\dagger - f_{n+1} f_n \right) - \left(f_N^\dagger f_1 + f_1^\dagger f_N - f_N^\dagger f_1^\dagger - f_1 f_N \right). \tag{2.57}$$

Now, all of the terms in these operators clearly preserve the evenness or oddness of the number of fermions. This is therefore true of the transfer matrix itself, and the states with even and odd numbers of particles comprise independent subspaces. This means that the necessity of using a different form for the transfer matrix for the even and odd cases is not especially problematic. We adopt the formalism

$$\hat{T} = \hat{T}_+ \hat{P}_+ + \hat{T}_- \hat{P}_-, \tag{2.58}$$

$$\hat{T}^M = \hat{T}_+^M \hat{P}_+ + \hat{T}_-^M \hat{P}_-, \tag{2.59}$$

where $\hat{T}_+$ and $\hat{T}_-$ are the transfer operators for the even and odd subspaces resepectively, and $\hat{P}_+$ and $\hat{P}_-$ are projection operators for those two subspaces. We will come to explicitly writing down these operators presently.

Although the even and odd subspaces are treated separately, in fact one can write $\hat{T}_+$ and $\hat{T}_-$ in essentially the same form. We firstly proceed to make a transformation to the expression 2.57 to make each of the bonds equivalent. This is accomplished by means of the gauge transformation,

$$f_n^\dagger \to e^{i\frac{\pi}{N}n} f_n^\dagger, \tag{2.60}$$

which substituted into equation 2.57 gives the result,

$$\sum_{n=1}^{N} \hat{\sigma}_n^y \hat{\sigma}_{n+1}^y = \sum_{n=1}^{N} \left(e^{-i\frac{\pi}{N}} f_n^\dagger f_{n+1} + e^{i\frac{\pi}{N}} f_{n+1}^\dagger f_n - e^{i(2n+1)\frac{\pi}{N}} f_n^\dagger f_{n+1}^\dagger - e^{-i(2n+1)\frac{\pi}{N}} f_n f_{n+1} \right). \tag{2.61}$$

One can think of the effect of the gauge transformation as sharing the phase π on the N-1 bond - the minus sign in the corresponding term in equation 2.57 - evenly among all the bonds on the ring. This is pictured in Figure 2.2. The effect of a general gauge transformation is to distribute the overall phase π amongst the N bonds in any whatever; this was discussed in section 1.3.5.

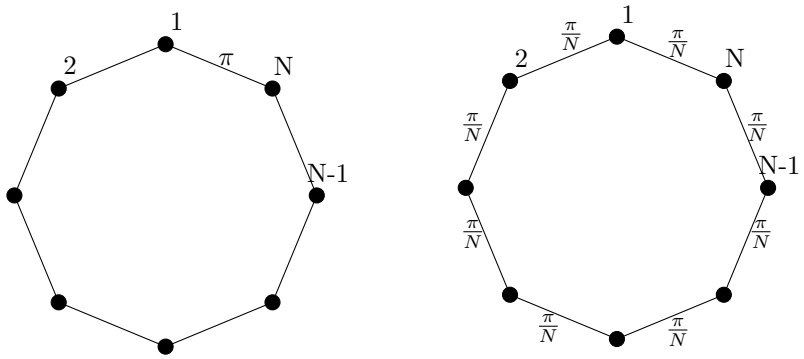

Figure 2.2: Illustration of the gauge transformation 2.60.

Now, in quantum mechanics, it is a well-known technique to extract the translational symmetry in single-particle operators such as 2.56 and 2.61 using the Bloch transformation to new operators $f_k^\dagger$,

$$f_n^\dagger = \frac{1}{\sqrt{N}} \sum_k e^{-ink} f_k^\dagger, \tag{2.62}$$

where the so-called Bloch wavenumbers k are chosen so that the corresponding phase factors are the Nth roots of unity,

$$\left(e^{ik}\right)^N = 1. \tag{2.63}$$

Applying this transformation to equation 2.56 for the odd subspace provides,

$$\sum_{n=1}^{N} \hat{\sigma}_n^y \hat{\sigma}_{n+1}^y = \sum_k \left[2\cos k f_k^\dagger f_k - e^{ik} f_k^\dagger f_{-k}^\dagger - e^{-ik} f_{-k} f_k \right], \tag{2.64}$$

while Bloch transforming the gauge-transformed even subspace, equation 2.61, provides,

$$\sum_{n=1}^{N} \hat{\sigma}_n^y \hat{\sigma}_{n+1}^y = \sum_k \left[2\cos\left(k - \tfrac{\pi}{N}\right) f_k^\dagger f_k - e^{i(k-\frac{\pi}{N})} f_k^\dagger f_{-k+\frac{2\pi}{N}}^\dagger - e^{-i(k-\frac{\pi}{N})} f_{-k+\frac{2\pi}{N}} f_k \right]. \tag{2.65}$$

Now, on close inspection, equation 2.65 has exactly the same form as equation 2.64 with the single alteration that the Bloch wavenumbers are shifted by an amount π/N. We can therefore use the same formula to describe both the even and the odd subspaces, but where for the odd subspace we must use the set of Bloch wavenumbers k_- corresponding to the roots of unity,

$$\left(e^{ik_-}\right)^N = 1, \tag{2.66}$$

and where for the even subspace we must use Bloch wavenumbers shifted by π/N, k_+, which correspond to a set of phase-factors which are the Nth roots of minus one,

$$\left(e^{ik_+}\right)^N = -1. \tag{2.67}$$

The phase-factors for the even and odd subspaces are pictured in Figure 2.3.

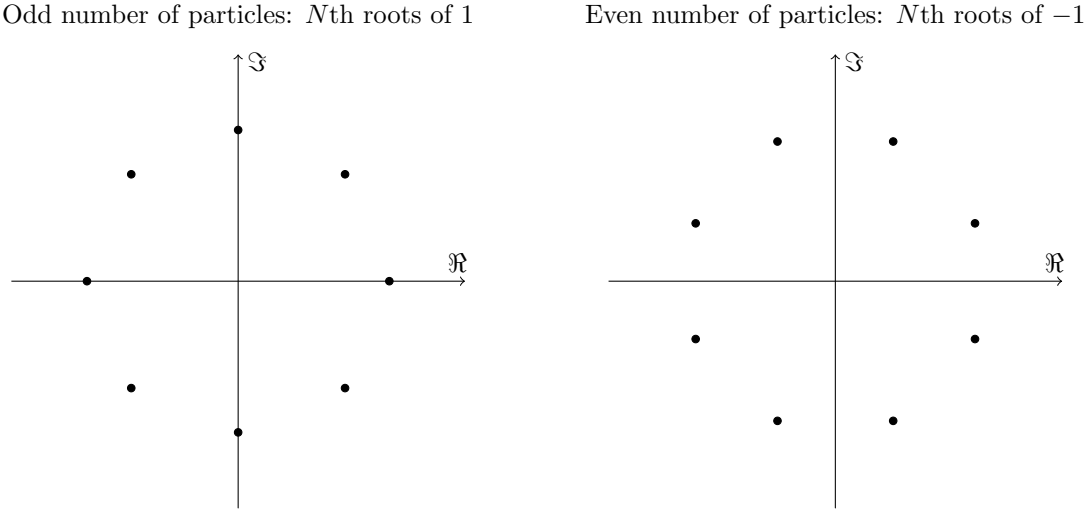

Figure 2.3: Argand diagrams showing the phase-factors for the odd and even subspaces.

With this notation, we can describe the transfer operator for both the even and odd subspaces with a single formula, which we choose to write as,

$$\begin{aligned}\hat{T}_\pm = \exp\left(\sum_{k_\pm}\left[X + Y(1 - f^\dagger_{k_\pm} f_{k_\pm} - f^\dagger_{-k_\pm} f_{-k_\pm})\right]\right) \\ \times \exp\left(\sum_{k_\pm}\left[\beta J_\perp \cos k_\pm (f^\dagger_{k_\pm} f_{k_\pm} + f^\dagger_{-k_\pm} f_{-k_\pm} - 1) + i\beta J_\perp \sin k_\pm (f^\dagger_{k_\pm} f^\dagger_{-k_\pm} - f_{-k_\pm} f_{k_\pm})\right]\right).\end{aligned} \tag{2.68}$$

This expression follows from simply substituting equation 2.64 in for the exponent of $\hat{T}_\perp$ in equation 2.49, with the modification that we have included a new term $-\beta J_\perp \cos k_\pm$ in this exponent; this is permitted because the sum of this quantity over the appropriate set of Bloch wavenumbers vanishes identically,

$$\sum_{k_\pm} \cos k_\pm = 0. \tag{2.69}$$

The other exponent in this expression contains only the number operator and therefore has the same form under any transformation which preserves the number of fermions.

The term $f_k^\dagger f_{-k}^\dagger$ in the exponent of $\hat{T}_\perp$ indicates that the fermionic operator associated with the eigenbasis of this exponent is a linear combination of $f_k^\dagger$ and f_{-k}. This is the Bogoliubov-Valatin transformation(42; 43). It is tempting to proceed to diagonalise the exponent of $\hat{T}_\perp$ using this well-known idea; however, this would not prove useful, as the eigenbasis of the exponent of $\hat{T}_\perp$ is certainly not an eigenbasis of the exponent of $\hat{T}_\parallel$ in general, owing to the fact that the Bogliubov-Valatin transformation does not preserve the number of particles. One must first express the transfer operator 2.68 as a single exponential, and one can then apply the Bogoliubov-Valatin transformation to the fermionic form of the exponent.

Writing the transfer operator as a single exponential appears rather difficult in the fermionic represenation. However, as we shall show presently, the fermionic representation has a simple form in terms of new Pauli operators, and we can exploit the properties of Pauli operators to write the operator as a single exponential. Proceeding in this way, one finds the exponent to be a sum of independent Pauli operators. Since each of these Pauli operators has the eigenvalues $+1$ and -1, one can immediately deduce the eigenvalues of the transfer operator itself. We shall therefore find that there is no need to use the Bogoliubov-Valatin transformation!

With the exception of the possible values $k = 0$ and $k = \pi$, for every value of k which occurs in the sum over the Bloch wavenumbers its negative $-k$ also occurs. The states corresponding to k and $-k$ form a closed subspace. Bringing together the k and $-k$ terms in the sums in equation 2.68 reveals that the relevant part of the transfer matrix for the subspace corresponding to k and $-k$, with the exception of the cases $k = 0$ and $k = \pi$, can be written as,

$$\exp\Big(2X + 2Y(1 - f_k^\dagger f_k - f_{-k}^\dagger f_{-k})\Big) \\ \times \exp\Big(2\beta J_\perp \cos k(f_k^\dagger f_k + f_{-k}^\dagger f_{-k} - 1) + 2i\beta J_\perp \sin k(f_k^\dagger f_{-k}^\dagger - f_{-k} f_k)\Big). \tag{2.70}$$

There are only two operators which occur in this expression, which are

$$1 - f_k^\dagger f_k - f_{-k}^\dagger f_{-k}, \qquad i(f_k^\dagger f_{-k}^\dagger - f_{-k} f_k).$$

Now, in the basis $\{|0\rangle, f_k^\dagger|0\rangle, f_{-k}^\dagger|0\rangle, f_k^\dagger f_{-k}^\dagger|0\rangle\}$ these operators have the representations,

$$(1 - f_k^\dagger f_k - f_{-k}^\dagger f_{-k}) \to \begin{pmatrix} 1 & 0 & 0 & 0 \\ 0 & 0 & 0 & 0 \\ 0 & 0 & 0 & 0 \\ 0 & 0 & 0 & -1 \end{pmatrix}, \tag{2.71}$$

$$i(f_k^\dagger f_{-k}^\dagger - f_{-k} f_k) \to \begin{pmatrix} 0 & 0 & 0 & i \\ 0 & 0 & 0 & 0 \\ 0 & 0 & 0 & 0 \\ -i & 0 & 0 & 0 \end{pmatrix}. \tag{2.72}$$

We see that the states $f_k^\dagger|0\rangle$ and $f_{-k}^\dagger|0\rangle$ constitute a null subspace of these operators, and we recognise the representations in the $\{|0\rangle, f_k^\dagger f_{-k}^\dagger|0\rangle\}$ subspace as the Pauli matrices for the z- and y-components of spin. To make this explicit we introduce the notation,

$$1 - f_k^\dagger f_k - f_{-k}^\dagger f_{-k} = \hat{\Sigma}_k^z, \qquad i(f_k^\dagger f_{-k}^\dagger - f_{-k} f_k) = \hat{\Sigma}_k^y, \tag{2.73}$$

in terms of which the operator 2.70 can be written as,

$$e^{2X + 2Y\hat{\Sigma}_k^z} e^{2\beta J_\perp (\sin k\hat{\Sigma}_k^y - \cos k\hat{\Sigma}_k^z)}. \tag{2.74}$$

We can use the properties of the Pauli operators to write this operator as a single exponential, which achieves the purpose of effectively diagonalising the operator in the $\{|0\rangle, f_k^\dagger f_{-k}^\dagger|0\rangle\}$ subspace, thereby providing the two nontrivial eigenvalues. The Pauli operators have the property that any linear combination of Pauli matrices can be written as some Pauli matrix $\hat{\Sigma}$ multiplied by a coefficient:

$$A\hat{\sigma}^x + B\hat{\sigma}^y + C\hat{\sigma}^z = \sqrt{A^2 + B^2 + C^2}\hat{\Sigma}. \tag{2.75}$$

Substituting the expression $\sin k\hat{\Sigma}_k^y - \cos k\hat{\Sigma}_k^z$ into equation 2.75, one finds the coefficient on the right hand side of the equation to be unity. The operator $\sin k\hat{\Sigma}_k^y - \cos k\hat{\Sigma}_k^z$ is therefore a Pauli matrix. We can therefore use the identity 2.44 to write the operator 2.74 as

$$e^{2X}\left(\cosh 2Y - \sinh 2Y\hat{\Sigma}_k^z\right)\left[\cosh 2\beta J_\perp + \sinh 2\beta J_\perp \left(\sin k\hat{\Sigma}_k^y - \cos k\hat{\Sigma}_k^z\right)\right]. \tag{2.76}$$

Multiplying out this expression, one obtains,

$$e^{2X}\Big\{\cosh 2Y\cosh 2\beta J_\perp - \sinh 2Y\sinh 2\beta J_\perp\cos k + \left[\cosh 2Y\sinh 2\beta J_\perp\cos k - \sinh 2Y\cosh 2\beta J_\perp\right]\hat{\Sigma}_k^z + \cosh 2Y\sinh 2\beta J_\perp\sin k\hat{\Sigma}_k^y - i\sinh 2Y\cosh 2\beta J_\perp\sin k\hat{\Sigma}_k^x\Big\}, \tag{2.77}$$

where we have used a further property of the Pauli matrices,

$$\hat{\sigma}^z\hat{\sigma}^y = -i\hat{\sigma}^x \tag{2.78}$$

and introduced the third Pauli operator $\hat{\Sigma}_k^x$ corresponding to $\hat{\Sigma}_k^z$ and $\hat{\Sigma}_k^y$. The sum of the last three terms in the braces {...} are, by the identity 2.75, proportional to some other Pauli operator, which we denote $\hat{\tilde{\Sigma}}_k$. The quantity in the braces {...} therefore has the same form as the right hand side of equation 2.44, and we may use that equation to write this quantity as a single exponential. We therefore arrive at the expression

$$e^{2X+2\mu_k\hat{\tilde{\Sigma}}_k}, \tag{2.79}$$

where the quantity μ_k satisfies,

$$\cosh 2\mu_k = \cosh 2Y\cosh 2\beta J_\perp - \sinh 2Y\sinh 2\beta J_\perp\cos k. \tag{2.80}$$

Expressing $\cosh 2Y$ and $\sinh 2Y$ as functions of $\beta J_\parallel$ and introducing the parameters,

$$W_\parallel = \frac{\sinh 2\beta J_\parallel}{\cosh 2\beta J_\parallel\cosh 2\beta J_\perp}, \qquad W_\perp = \frac{\sinh 2\beta J_\perp}{\cosh 2\beta J_\parallel\cosh 2\beta J_\perp}, \tag{2.81}$$

equation 2.80 can be rewritten as,

$$\cosh 2\mu_k = \frac{1}{W_\parallel} - \frac{W_\perp}{W_\parallel}\cos k. \tag{2.82}$$

We have arrived at the expression 2.79 as a representation of the operator 2.70 in the $\{|0\rangle, f_k^\dagger f_{-k}^\dagger|0\rangle\}$ subspace, but it is also a representation in the the full four-state space, where the states $f_k^\dagger|0\rangle$ and $f_{-k}^\dagger|0\rangle$ are trivial eigenvectors of the operator $\hat{\tilde{\Sigma}}_k$ with eigenvalue 0. We can therefore deduce the two eigenvalues $e^{2X+2\mu_k}$ and $e^{2X-2\mu_k}$ associated with the $\{|0\rangle, f_k^\dagger f_{-k}^\dagger|0\rangle\}$ subspace and the two trivial

eigenvalues whose value is e^{2X} accociated with the null subspace. The operator $\hat{\tilde{\Sigma}}_k$ describes two fermionic modes, with associated creation operators $\tilde{f}_k^\dagger$ and $\tilde{f}_{-k}^\dagger$, which can in principle be constructed in terms of the original fermion operators by means of the Bogoliubov-Valatin transformation. Each of these fermionic modes can be described with its own spin-operator, and this leads us to write,

$$2\hat{\tilde{\Sigma}}_k = \hat{\tilde{\sigma}}_k + \hat{\tilde{\sigma}}_{-k}. \tag{2.83}$$

We can now decompose the transfer matrix further to obtain the part relevant to a single k-value to be,

$$\hat{T}_k = e^{X+\mu_k\hat{\tilde{\sigma}}_k} = \sqrt{2\cosh 2\beta J_\parallel \cosh 2\beta J_\perp}\sqrt{W_\parallel}e^{\mu_k\hat{\tilde{\sigma}}_k}, \tag{2.84}$$

where we have eliminated the variable X using equation 2.47.

We have described the parts of the transfer operator relevant to all the Bloch wavenumbers, with the exception of the special values $k = 0$ and $k = \pi$. Let k_* be either of these special k-values. The key property that is unique to these k-values is that

$$f_{k_*}^\dagger = f_{-k_*}^\dagger. \tag{2.85}$$

This implies, following from equation 2.68, that the relevant part of the transfer operator for the wavenumber k_* is

$$\hat{T}_{k_*} = \exp\Big(X + Y(1 - 2f_{k_*}^\dagger f_{k_*})\Big)\exp\Big(\beta J_\perp \cos k_*(2f_{k_*}^\dagger f_{k_*} - 1)\Big). \tag{2.86}$$

The only operator which appears in this expression is $1-2f_{k_*}^\dagger f_{k_*}$, which we identify as a Pauli operator in the $\{|0\rangle, f_{k_*}^\dagger|0\rangle\}$ subspace. To be consistent with the formalism for the other k-values, we write

$$\hat{\tilde{\sigma}}_{k_*} = 1 - 2f_{k_*}^\dagger f_{k_*}, \tag{2.87}$$

and we obtain

$$\hat{T}_{k_*} = e^{X+\mu_{k_*}\hat{\tilde{\sigma}}_{k_*}}, \tag{2.88}$$

where

$$\mu_{k_*} = Y - \beta J_\perp \cos k_*. \tag{2.89}$$

The full transfer matrix in either the even or odd subspaces is the product of the operators $\hat{T}_k$ over the appropriate set of Bloch wavenumbers:

$$\hat{T}_{\pm} = \prod_{k_{\pm}} \hat{T}_{k_{\pm}} = \prod_{k_{\pm}} e^{X + \mu_{k_{\pm}} \hat{\tilde{\sigma}}_k}. \tag{2.90}$$

This expression is what we have been working towards throughout this section. This representation of the transfer operator allows us to calculate the partition function according to equation 2.31. It is not necessary to explicitly construct all of the operators $\hat{\tilde{\sigma}}_k$, but rather it is enough that we can identify the operators as Pauli spin operators, and therefore deduce that they each have the two eigenvalues $+1$ and -1. The trace of any operator expressed as a function of the operators $\hat{\tilde{\sigma}}_k$ can therefore be calculated by summing over these eigenvalues. In addition the fact that the equation 2.90 is factorised according to the Bloch wavenumbers means that in performing the trace of $\hat{T}_{\pm}$ - or $\left(\hat{T}_{\pm}\right)^M$ - the sum over each of the spin operators can be performed *independently*. This reduces the trace in equation 2.31 from a hopeless calculation to a trivial one.

In fact, we require one additional result before we can proceed to calculate the partition function, which is the representation of the projection operators $\hat{P}_+$ and $\hat{P}_-$. Now, the evenness or oddness of any given state is reflected in whether the number of the spins which are "down" is even or odd. The crucial point is that this is preserved in the eigenbasis of the new spins $\hat{\tilde{\sigma}}_{k_{\pm}}$. The projection operators can therefore be represented as:

$$\hat{P}_+ = \frac{1}{2}\left(1 + \prod_{k_+} \hat{\tilde{\sigma}}_{k_+}\right), \qquad \hat{P}_- = \frac{1}{2}\left(1 - \prod_{k_-} \hat{\tilde{\sigma}}_{k_-}\right). \tag{2.91}$$

Substituting equations 2.91 and 2.59 into equation 2.31, the explicit formula for the partition function can be written,

$$\mathcal{Z}_{N,M} = \frac{1}{2}\mathrm{tr}\left(\prod_{k_+} \hat{T}_{k_+}^M + \prod_{k_+} \hat{\tilde{\sigma}}_{k_+} \hat{T}_{k_+}^M + \prod_{k_-} \hat{T}_{k_-}^M - \prod_{k_-} \hat{\tilde{\sigma}}_{k_-} \hat{T}_{k_-}^M\right). \tag{2.92}$$

The trace of each of the four terms in this expression can be performed independently, and as we have indicated above, each of these four traces is trivial because the sum over the eigenvalues of each of the

$\hat{\tilde{\sigma}}_{k_\pm}$ spins can be performed independently. The only objects which appear in the calculation are

$$\sum_{\hat{\tilde{\sigma}}_{k_\pm}} e^{M\mu_{k_\pm}\hat{\tilde{\sigma}}_{k_\pm}} = e^{M\mu_{k_\pm}} + e^{-M\mu_{k_\pm}}, \tag{2.93}$$

and

$$\sum_{\hat{\tilde{\sigma}}_{k_\pm}} \hat{\tilde{\sigma}}_{k_\pm} e^{M\mu_{k_\pm}\hat{\tilde{\sigma}}_{k_\pm}} = e^{M\mu_{k_\pm}} - e^{-M\mu_{k_\pm}}. \tag{2.94}$$

We can therefore write the partition function as

$$\mathcal{Z}_{N,M} = \frac{1}{2}\left(\sqrt{2\cosh 2\beta J_\perp \cosh 2\beta J_\parallel}\sqrt{W_\parallel}\right)^{NM}\left\{\prod_{k_+}(e^{M\mu_{k_+}} + e^{-M\mu_{k_+}}) + \prod_{k_+}(e^{M\mu_{k_+}} - e^{-M\mu_{k_+}}) + \prod_{k_-}(e^{M\mu_{k_-}} + e^{-M\mu_{k_-}}) - \prod_{k_-}(e^{M\mu_{k_-}} - e^{-M\mu_{k_-}})\right\} \tag{2.95}$$

We can eliminate the variables $\mu_{k_\pm}$ to obtain a formula in terms of just the parameters $W_\parallel$ and $W_\perp$. The equation 2.80 leaves the sign of the parameters $\mu_{k_\pm}$ undefined. However, if we consider the product of any function of μ_k over either set of wavenumbers, to every factor corresponding to a particular wavenumber k, with the exception of the special cases $k = 0$ and $k = \pi$, there exists also a factor corresponding to its negative $-k$, and both these factors are identical owing to both k and $-k$ corresponding to the same value of μ_k. This means that only the signs of the variables associated with the special wavenumbers, μ_0 and μ_π, are relevant. Substituting in the special wavenumbers into equation 2.89 one obtains,

$$\mu_\pi = Y + \beta J_\perp, \tag{2.96}$$

$$\mu_0 = Y - \beta J_\perp. \tag{2.97}$$

Now Y is a positive, monotonic function of β, which tends to the value zero in the limit that β tends to infinity, and which diverges in the limit that β tends to zero. It follows that μ_π is always positive, but that μ_0 is positive for small values of β, negative for large values of β, and vanishes at a single value of β which depends upon the ratio of the couplings $J_\perp/J_\parallel$. The value $k = 0$ is never to be found in the set k_+ but always occurs in the set k_-. Since the third term in the braces $\{...\}$ in equation 2.95 is a product of even functions of μ_{k_-}, the only term for which the sign of μ_0 is relevant is the fourth

term. We choose to parameterise this sign by introducing the symbol,

$$\Theta \equiv -\mathrm{sgn}(\mu_0). \tag{2.98}$$

With the introduction of this new symbol to take account of the sign of μ_0, we can proceed as if all of the quantities $\mu_{k_\pm}$ were defined to be positive. To this end, we write, using equation 2.89,

$$\sqrt{2W_\parallel}\cosh\mu_k = \sqrt{W_\parallel(\cosh 2\mu_k + 1)} = \sqrt{1 + W_\parallel - W_\perp\cos k}, \tag{2.99}$$

$$\sqrt{2W_\parallel}\sinh\mu_k = \sqrt{W_\parallel(\cosh 2\mu_k - 1)} = \sqrt{1 - W_\parallel - W_\perp\cos k}, \tag{2.100}$$

from which we deduce,

$$\sqrt{2W_\parallel}e^{\mu_k} = \sqrt{1 + W_\parallel - W_\perp\cos k} + \sqrt{1 - W_\parallel - W_\perp\cos k}, \tag{2.101}$$

$$\sqrt{2W_\parallel}e^{-\mu_k} = \sqrt{1 + W_\parallel - W_\perp\cos k} - \sqrt{1 - W_\parallel - W_\perp\cos k}. \tag{2.102}$$

Taking into account the sign of μ_0, this provides the formula,

$$\begin{aligned}
\mathcal{Z}_{N,M} = \frac{1}{2}\left(\sqrt{\cosh 2\beta J_\parallel \cosh 2\beta J_\perp}\right)^{NM} \\
\times \Bigg\{ \prod_{k_+}\Bigg[\left(\sqrt{1 + W_\parallel - W_\perp\cos k_+} + \sqrt{1 - W_\parallel - W_\perp\cos k_+}\right)^M \\
+ \left(\sqrt{1 + W_\parallel - W_\perp\cos k_+} - \sqrt{1 - W_\parallel - W_\perp\cos k_+}\right)^M \Bigg] \\
+ \prod_{k_+}\Bigg[\left(\sqrt{1 + W_\parallel - W_\perp\cos k_+} + \sqrt{1 - W_\parallel - W_\perp\cos k_+}\right)^M \\
- \left(\sqrt{1 + W_\parallel - W_\perp\cos k_+} - \sqrt{1 - W_\parallel - W_\perp\cos k_+}\right)^M \Bigg] \\
+ \prod_{k_-}\Bigg[\left(\sqrt{1 + W_\parallel - W_\perp\cos k_-} + \sqrt{1 - W_\parallel - W_\perp\cos k_-}\right)^M \\
+ \left(\sqrt{1 + W_\parallel - W_\perp\cos k_-} - \sqrt{1 - W_\parallel - W_\perp\cos k_-}\right)^M \Bigg] \\
+ \Theta\prod_{k_-}\Bigg[\left(\sqrt{1 + W_\parallel - W_\perp\cos k_-} + \sqrt{1 - W_\parallel - W_\perp\cos k_-}\right)^M \\
- \left(\sqrt{1 + W_\parallel - W_\perp\cos k_-} - \sqrt{1 - W_\parallel - W_\perp\cos k_-}\right)^M \Bigg] \Bigg\}.
\end{aligned} \tag{2.103}$$

The two different lattice directions appear symmetrically in the Hamiltonian. We might therefore expect to find a formula for the partition function in which the directions appear symmetrically. We can obtain such a formula by making use of a property of the wavenumbers. We have the following two identities,

$$\prod_{k_+} \sqrt{\xi^2 + \eta^2 - 2\xi\eta\cos k_+} = \xi^N + \eta^N, \tag{2.104}$$

$$\prod_{k_-} \sqrt{\xi^2 + \eta^2 - 2\xi\eta\cos k_-} = \left|\xi^N - \eta^N\right|. \tag{2.105}$$

for any two real numbers ξ and η. Each of the four terms in equation 2.103 contains the sum or difference of two quantities raised to the power M. One can use these identities to transform each of these terms into a product of a single square root over the set of Bloch wave numbers corresponding to the Mth roots of either one or minus one. We can therefore simplify 2.103 at the cost of introducing a second product over a second set of Bloch wavenumbers. We denote the second set of wavenumbers q_+ and q_-:

$$\left(e^{iq_+}\right)^M = -1, \qquad \left(e^{iq_-}\right)^M = 1. \tag{2.106}$$

Re-writing each of the four terms in equation 2.103 using this idea, we obtain the comparitively simple formula,

$$\begin{aligned}\mathcal{Z}_{N,M} = \frac{1}{2}&\left(\sqrt{\cosh 2\beta J_\parallel \cosh 2\beta J_\perp}\right)^{NM} \\ &\times \left\{ \prod_{k_+}\prod_{q_+} \sqrt{1 - W_\parallel \cos q_+ - W_\perp \cos k_+} + \prod_{k_+}\prod_{q_-} \sqrt{1 - W_\parallel \cos q_- - W_\perp \cos k_+} \right. \\ &\left. + \prod_{k_-}\prod_{q_+} \sqrt{1 - W_\parallel \cos q_+ - W_\perp \cos k_-} + \Theta \prod_{k_-}\prod_{q_-} \sqrt{1 - W_\parallel \cos q_- - W_\perp \cos k_-} \right\}.\end{aligned} \tag{2.107}$$

The wavenumbers $q_\pm$ are what results from a Bloch transformation in the lateral direction. This formula is, therefore, entirely symmetric in the two axis directions.

The parameterisation in terms of $W_\parallel$ and $W_\perp$ is rather convenient. Both of these parameters are zero in both the low-temperature and high-temperature limits, but are otherwise positive definite and

do not exceed the value unity. Crucially, it can be shown that

$$W_{\parallel} + W_{\perp} \leq 1, \tag{2.108}$$

where the equality occurs for a single value of β, which we label β_c, and furthermore this value satisfies

$$\sinh 2\beta_c J_{\parallel} \sinh 2\beta_c J_{\perp} = 1. \tag{2.109}$$

In addition, with reference to equation 2.97 it can be shown that this value β_c is precisely the point at which the quantity μ_0 is equal to zero, and therefore the point at which there is a change in the sign of the final terms in the expressions for the partition function in equations 2.103 and 2.107.

This special value β_c precisely provides the critical temperature of the phase transition which occurs for the case of the infinite square lattice. Equation 2.109 is a famous equation, which was obtained as a definition of the transition temperature by means of a duality argument by Kramers and Wannier, before the partition function of the model had yet been calculated(37). It is rather pleasant that this value has a great significance for the solution of the finite system also.

We can take limits of our formula of the partition function, which is for a finite and therefore a zero-dimensional system, to obtain the partition function for a one-dimensional system - the geometry of an infinite cylinder - or a two-dimensional system - the infinite square lattice. Mathematically, the two-dimensional limit is that the system-size in both of the principal lattice directions is made to tend to infinity, while the one-dimensional limit is that one of the system-sizes is made to tend to infinity while the other is kept finite. We shall consider the one-dimensional limit first, and then take the appropriate limit of the one-dimensional partition function to obtain the result for the infinite square lattice. In doing this, we shall reproduce the well-known result for the two-dimensional Ising model. That we obtain the correct formula for the two-dimensional case indicates that considering the two-dimensional limit in this way, that is, by letting the system sizes in the two directions diverge "one at a time", is a safe way of obtaining that limit. Although this is not in conflict with one's intuition, it is crucial to the entire study of the planar rotator model which is to follow later in this chapter. In attempting to study the planar rotator model, we shall consider calculations for a one-dimensional system, for which the system size in one direction is infinite, and we shall attempt to study the two-dimensional model by appealing to exactly this limit, that the system size in the other direction also be allowed to tend to infinity.

We can obtain the one-dimensional limit by considering equation 2.103 in the limit that M is allowed to tend to infinity while N is kept fixed. With our convention that all of the variables μ_k be taken to be positive, in the limit that M is very large it is certainly the case that

$$e^{M\mu_k} \gg e^{-M\mu_k}.$$

The corresponding terms can therefore be omitted from equation 2.103 to obtain,

$$\begin{aligned}\mathcal{Z}_{N,M} = &\left(\sqrt{\cosh 2\beta J_{\parallel} \cosh 2\beta J_{\perp}}\right)^{NM} \\ &\times \left\{ \prod_{k_+} \left(\sqrt{1 + W_{\parallel} - W_{\perp}\cos k_+} + \sqrt{1 - W_{\parallel} - W_{\perp}\cos k_+}\right)^{M} \right. \\ &\left. + \frac{1+\Theta}{2} \prod_{k_-} \left(\sqrt{1 + W_{\parallel} - W_{\perp}\cos k_-} + \sqrt{1 - W_{\parallel} - W_{\perp}\cos k_-}\right)^{M} \right\}. \end{aligned} \tag{2.110}$$

Numerically, it appears to be the case that the product over the even wavenumbers k_+ in the expression 2.110 is always larger than the product over the odd wavenumbers k_-,

$$\begin{aligned}&\prod_{k_+} \left(\sqrt{1 + W_{\parallel} - W_{\perp}\cos k_+} + \sqrt{1 - W_{\parallel} - W_{\perp}\cos k_+}\right) \\ &\qquad > \prod_{k_-} \left(\sqrt{1 + W_{\parallel} - W_{\perp}\cos k_-} + \sqrt{1 - W_{\parallel} - W_{\perp}\cos k_-}\right), \end{aligned} \tag{2.111}$$

and therefore that expression 2.110 can be further simplified by neglecting the the product over the odd wavenumbers because we are in the limit $M \to \infty$. This is discussed in the appendix A, wherein we provide numerical calculations of the inequality, and a mathematical proof of the inequality for the case $J_{\parallel} = J_{\perp}$. At present we assume the truth of the inequality and make use of it to obtain the following formula for the free energy per lattice site F,

$$\begin{aligned}-\beta F = \frac{\ln \mathcal{Z}_{N,M}}{NM} = &\frac{1}{N} \sum_{k_+} \ln \left(\sqrt{1 + W_{\parallel} - W_{\perp}\cos k_+} + \sqrt{1 - W_{\parallel} - W_{\perp}\cos k_+}\right) \\ &+ \frac{1}{2} \ln \left(\cosh 2\beta J_{\parallel} \cosh 2\beta J_{\perp}\right). \end{aligned} \tag{2.112}$$

If we now consider this expression in the limit that N tends to infinity, the normalised sum over the

wavenumbers k_+ can be replaced by an integral over a continuous variable:

$$-\beta F = \int_{-\pi}^{\pi} \frac{dk}{2\pi} \ln\left(\sqrt{1 + W_{\|} - W_{\perp}\cos k} + \sqrt{1 - W_{\|} - W_{\perp}\cos k}\right) + \frac{1}{2}\ln\left(\cosh 2\beta J_{\|}\cosh 2\beta J_{\perp}\right). \tag{2.113}$$

This expression provides the logarithm of the partition function, per lattice site, of the Ising model on the infinite square lattice. We can make a transformation to obtain an expression which is symmetric in the two lattice directions. In seeking such a representation, it is helpful to reintroduce the variable μ_k. The argument of the logarithm in the integrand in the expression 2.113 is equal to $\sqrt{2W_{\|}}\mu_k$, so that the expression 2.113 can be written as,

$$-\beta F = \int_{-\pi}^{\pi} \frac{dk}{2\pi}\mu_k + \frac{1}{2}\ln 2W_{\|} + \frac{1}{2}\ln\left(\cosh 2\beta J_{\|}\cosh 2\beta J_{\perp}\right). \tag{2.114}$$

Following Onsager(17), we can now make use of the remarkable identity,

$$\int_{-\pi}^{\pi} \frac{dq}{2\pi}\ln\left(\cosh u - \cos q\right) = u - \ln 2, \tag{2.115}$$

together with the expression for $\cosh 2\mu_k$ in equation 2.82 to represent μ_k as an integral:

$$\begin{aligned}\mu_k = \frac{1}{2}\left(2\mu_k\right) &= \frac{1}{2}\int_{-\pi}^{\pi}\frac{dq}{2\pi}\ln\left(\cosh 2\mu_k - \cos q\right) + \frac{1}{2}\ln 2 \\ &= \frac{1}{2}\int_{-\pi}^{\pi}\frac{dq}{2\pi}\ln\left(1 - W_{\|}\cos q - W_{\perp}\cos k\right) + \frac{1}{2}\ln 2 - \frac{1}{2}\ln W_{\|}.\end{aligned} \tag{2.116}$$

Substituting this expression for μ_k into the expression 2.114, we obtain the well-known formula,

$$-\beta F = \frac{1}{2}\int_{-\pi}^{\pi}\frac{dk}{2\pi}\int_{-\pi}^{\pi}\frac{dq}{2\pi}\ln\left(1 - W_{\|}\cos q - W_{\perp}\cos k\right) + \frac{1}{2}\ln\left(\cosh 2\beta J_{\|}\cosh 2\beta J_{\perp}\right) + \ln 2. \tag{2.117}$$

Upon examination of the integral in this expression, it is clear that the integrand is divergent at the lower limit $k = 0$, $q = 0$ at the critical temperature where the parameters $W_{\|}$ and $W_{\perp}$ satisfy

$$W_{\|} + W_{\perp} = 1. \tag{2.118}$$

The integral itself is perfectly convergent at this temperature and the free energy is a smooth function of temperature, but the divergence in the integrand gives rise to singularities in the thermodynamic

quantities at the level of the second derivative of the free energy.

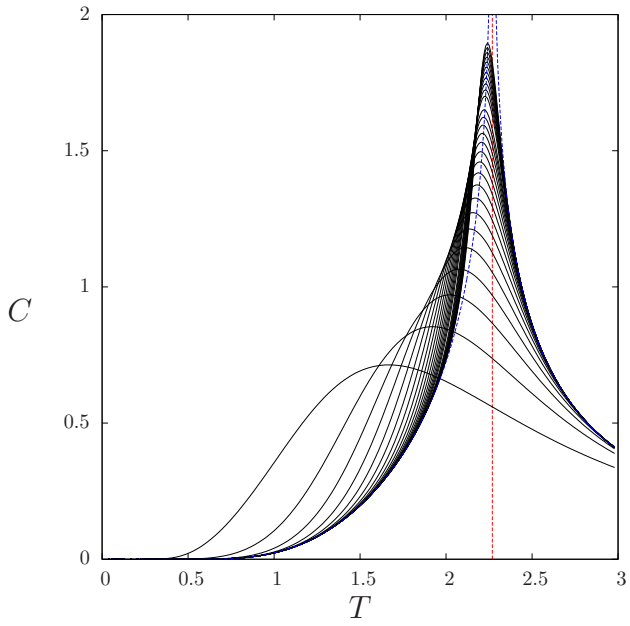

Figure 2.4: The specific heat of the Ising model on the $M = N$ toroidal lattice, for the case $J_{\parallel} = J_{\perp}$, for $M = N =$ 2-30. Also shown is the specific heat for the infinite square lattice (blue dashed line). The critical temperature of the phase transition in the square lattice model is indicated by the vertical red dotted line. Temperature is in units of $J_{\perp} = J_{\parallel}$.

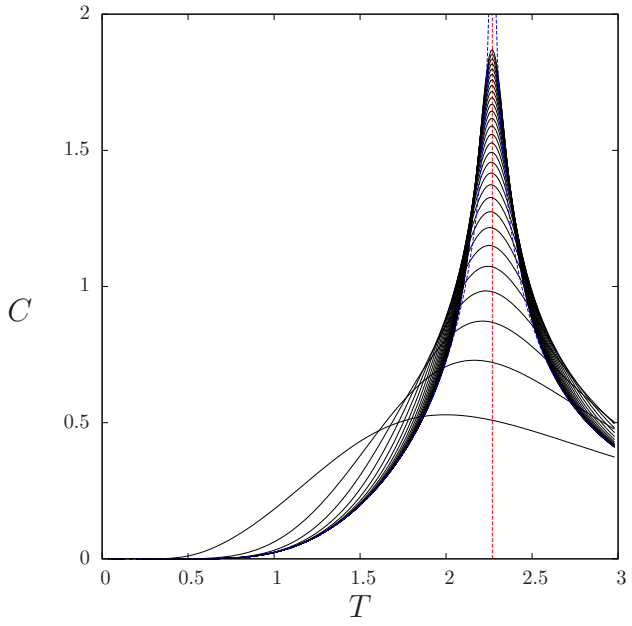

Figure 2.5: The specific heat of the Ising model on the infinite cylindrical lattice of circumference N, for the case $J_{\parallel} = J_{\perp}$, for N = 2-30. Also shown is the specific heat for the infinite square lattice (blue dashed line). The critical temperature of the phase transition in the square lattice model is indicated by the vertical red dotted line. Temperature is in units of $J_{\perp} = J_{\parallel}$.

We shall not pursue the exact solution of the Ising model any further in this thesis. We have shown how to exactly represent the free energy for the Ising model on the finite toroidal lattice, and how to obtain from this both the one-dimensional and two-dimensional limits. We now briefly exhibit some calculations making use of this exact solution. Some examples of the specific heat of the finite systems and the one-dimensional systems are shown in figures 2.4 and 2.5 respectively, together with the specific heat for the infinite square lattice. The curves in these figures have been obtained by calculating the logarithm of the partition function exactly, using the formula 2.103 for the finite system, the formula 2.112 for the one-dimensional system and the formula 2.117 for the infinite square lattice, and then numerically differentiating these data using difference formulae to obtain the specific heat. The use of difference formulae to obtain the derivatives of quantities is discussed more explicitly in section 2.3.

We have only included the results for the case of $J_{\perp} = J_{\parallel}$, because when we come to investigate the planar rotator model in the sections to follow we shall only consider the model where all the interactions have the same strength. The finite-size results in figure 2.4 are all for the case where the two periodicities of the torus are equal, $M = N$, and the two-dimensional system is approached by

making both the parameters larger at the same rate.

The two-dimensional specific heat exhibits a logarithmic divergence at the transition temperature(17). For the case $J_\perp = J_\parallel = J$, the transition temperature is $2J/\ln|1+\sqrt{2}|$(37) and this is indicated in figures 2.4 and 2.5. Although we cannot calculate the specific heat at this point, the data in the vicinity are certainly indicative of a divergence. Both the finite system and one-dimensional specific heat curves exhibit peaks which grow in size and become sharper as the system-size is increased. It is quite convincing from figure 2.4 that as the system-size is made larger and larger, the finite-size specific heat curve will come to overlap with the two-dimensional curve, and the peak will ultimately become a divergence in the limit that the system-size becomes infinite. Similarly it is quite convincing from figure 2.5 that the one-dimensional specific heat curve will come to overlap with the two-dimensional curve as the remaining finite size-parameter is made to tend to infinity.

Figures 2.4 and 2.5 illustrate the relationship between the zero-dimensional and one-dimensional systems and the two-dimensional system, and illustrates graphically how the two-dimensional thermodynamics emerge in the limit that a finite-size parameter tends to infinity. Furthermore, it shows quite convincingly, and indeed we have shown above mathematically, that these two limiting procedures both provide the same two-dimensional behaviour. This is pertinent to the investigation of the planar rotator model which follows in the remainder of this chapter, where we shall target the square lattice as the limit of a one-dimensional system where a scaling parameter tends to infinity.

2.3 One-to-two dimensional crossover

In the previous section, we calculated the specific heat of the Ising model on a finite N by N lattice using the exact expression for the partition function, and illustrated the approach to the two-dimensional limit as N is made to increase. This idea can be utilised to investigate the thermodynamics of two-dimensional and higher dimensional models for which no exact solution has been provided, by examining the trends in the thermodynamics of a finite system as the system size is made to increase. This is an extremely established concept in statistical mechanics under the name finite-size scaling, and is most commonly applied in conjunction with Monte Carlo calculations as the tool to obtain the thermodynamics of the finite systems(22; 23; 24; 25; 26). We shall use the term *zero-to-two dimensional crossover*, provided the target is a two-dimensional system; in our example, the finite N by N lattice is a zero-dimensional system, and becomes a two-dimensional system in the limit that the finite-size scaling parameter N tends to infinity.

One can equally well consider *one-to-two dimensional crossover*, where one deals with a system which is infinite in one direction and finite in another, and examines the trends in the thermodynamics as the length of the system in the finite direction is increased. In the previous section we also illustrated this idea using the exact solution of the Ising model, where we calculated the specific heat of the model on an infinite cylinder of circumference N, and illustrated the effect of increasing N. The utility of one-to-two dimensional crossover is that the thermodynamics of the one-dimensional systems are provided in a particularly straightforward way in terms of transfer operators. As we shall presently show, for an infinite one-dimensional system the partition function is given by the largest eigenvalue of the transfer operator, and consequently can be computed to a considerably higher accuracy than is typically possible using Monte Carlo methods.

This technique is rarely used in statistical mechanics, but is widely-used in quantum mechanics, in which context it is called exact diagonalisation(44). This refers to the study of an infinite quantum system by diagonalising the Hamiltonian for a finite system and examining how the result changes as the system-size is made to increase(45; 46). In the context of one-to-two dimensional crossover, the transfer matrix is the analogue of the Hamiltonian in exact diagonalisation, and the partition function, which is obtained as the *largest* eigenvalue of the transfer matrix, is the analogue of the ground state energy, which is the *smallest* eigenvalue of the Hamiltonian.

We therefore desire a one-dimensional geometry, which is infinite in one principle direction and finite in another, such that if we increase the system size in the finite direction the geometry becomes, in the limit, the square lattice. The most obvious geometry to use is a strip which is infinitely long but which has a finite height. If we use a periodic boundary condition in the finite direction, this geometry is an infinite cylinder. This geometry is that of the torus discussed in section 2.1.2, but where one of the periodicities M has been set equal to infinity. The scaling variable N is here the circumference of the cylinder.

An alternative geometry which one can use is a helix, as depicted in figure 2.6. Here the finite size scaling parameter N is the circumference of the helix. This geometry has a great computational advantage over the cylinder, in that the application of the transfer matrix involves a significantly smaller number of operations. The model of nearest neighbour interactions on the helix is completely equivalent to the model of equal nearest and Nth-nearest neighbour interactions on a linear chain. Therefore the transfer matrix is that described in section 2.1.1, and the application of the transfer matrix involves the summation over one spin-variable in the chain. In contrast, the transfer matrix

for the cylinder is that discussed in section 2.1.2 and involves the summation over N spin variables. An equivalent statement is that the transfer operator for the helix is a sparse matrix in comparison to that for the cylinder.

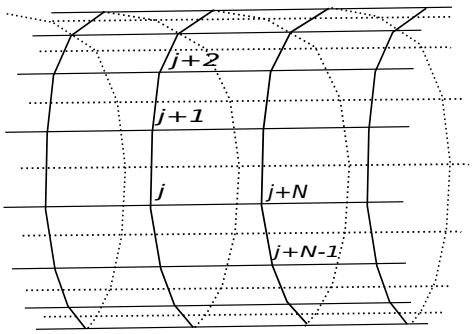

Figure 2.6: Illustration of the J_1-J_N model as a helix.

We now proceed to developing some of the formalism of the one-to-two dimensional crossover theory. This is simply the transfer operator formalism applied to find the thermodynamics of a one-dimensional system, where the crossover to a two-dimensional system is controlled by some scaling parameter N, the two-dimensional system corresponding to the limit $N \to \infty$. We shall go back to the transfer operator theory discussed in sections 2.1.1 and 2.1.2 and consider the case of a one-dimensional system, that is, the limit in which the system size M diverges. In this limit, the partition function is described completely by the largest eigenvalue of the transfer matrix. This is a great simplification of the mathematics, and as a result of this we can obtain extremely simple formulae for thermodynamic quantities up to the first derivative of the partition function, and for certain thermodynamic averages. The formalism has many analogies to quantum mechanics. For example, the role of the largest eigenvalue of the partition function in completely describing the thermodynamics of the one-dimensional system is analogous to the role of the quantum ground state in completely describing the zero-temperature physics of a quantum system.

We shall develop the formalism of one-to-two dimensional crossover for a generic spin-system, where it is understood that there is some scaling variable N as a parameter in the theory. When we apply this theory to the planar rotator model in the next section, we shall always use the helix geometry, and so we shall make use of the formalism developed in section 2.1.1 for the linear chain. For this reason, we shall here use the formalism for the linear chain, and work with the formalism of section 2.1.1 in the limit that the length of the spin-chain M tends to infinity.

We have shown that the partition function for a spin-chain of length M is equal to the sum of the eigenvalues of the transfer matrix raised to the Mth power, equation 2.5. Let z_0 be the largest of the eigenvalues of $\hat{T}$, and let us assume that this eigenvalue is nondegenerate. Now in the limit that $M \gg 1$, the sum in equation 2.5 is dominated by the term $(z_0)^M$, where the corrections from the other terms are exponentially small with increasing M:

$$\mathcal{Z}_M \sim (z_0)^M . \tag{2.119}$$

It is natural to eliminate the system-size M, which we wish to set equal to infinity, by working with the logarithm of the partition function per lattice-site, $\ln \mathcal{Z}_M/M$. From the expression 2.119 we deduce the equation

$$\frac{1}{M} \ln \mathcal{Z}_M = \ln z_0. \tag{2.120}$$

The eigenvalue z_0 can be regarded as the partition function *per spin*. This eigenvalue controls the thermodynamics of the one-dimensional system. The calculation of the partition function is reduced in this limit from the full diagonalisation of $\hat{T}$ to calculating just the largest eigenvalue. The Helmholtz free energy per lattice site is given by,

$$F = -\frac{1}{\beta} \ln z_0. \tag{2.121}$$

In this work, we have calculated the largest eigenvalue on the computer using the power method, which is simply to repeatedly apply the matrix in question to an arbitrary vector until the result converges to the eigenvector belonging to the largest eigenvalue. The mathematics which underpins this method is as follows. Any arbitrary vector $|f\rangle$ can be written as a linear combination of the eigenvectors $|f_\alpha\rangle$ of the transfer operator,

$$|f\rangle = \sum_\alpha a_\alpha |f_\alpha\rangle, \tag{2.122}$$

and therefore the repeated application of $\hat{T}$ is given by,

$$\left(\hat{T}\right)^L |f\rangle = \sum_\alpha a_\alpha \, (z_\alpha)^L \, |f_\alpha\rangle. \tag{2.123}$$

In the limit that $L \gg 1$, the term in the largest eigenvalue is exponentially larger than the other terms

in this series, and we may write,

$$\left(\hat{T}\right)^{L} |f\rangle \sim a_0 \left(z_0\right)^{L} |f_0\rangle, \tag{2.124}$$

where $|f_0\rangle$ is the eigenvector belonging to z_0. This occurs provided that the initial state $|f\rangle$ has a finite overlap with the eigenvector belonging to the largest eigenvalue, which amounts to the statement that the coefficient a_0 is non-zero. The procedure which we employ is to repeatedly apply the transfer operator to some initial state. The resulting vector is normalised at each iteration, which provides a number which converges to the largest eigenvalue of the transfer matrix with successive iterations. In this way the largest eigenvalue of the transfer matrix can be obtained to machine accuracy.

The calculation is computationally expensive in two ways, firstly in the number of operations required to multiply the vector by the transfer matrix, and secondly in the size of the vector, which must be stored in the computer's memory. Both of these expenses are worsened with the increase of the scaling parameter N, and as a result there is some value of this parameter above which the calculation cannot be performed. For the J_1-J_N models, the vector is represented on the computer as p^N numbers, where p is the number of allowed spin states. For models with continous spins, such as the planar rotator model, the vector is infinitely large, and therefore some scheme must be employed to discretise the spin variables in order to apply the technique to such models. This is discussed at great length in the context of the planar rotator model in section 2.4.

Thermodynamic quantities which involve up to the first derivative of the partition function can be expressed in simple formulae involving the eigenvalue z_0 and the corresponding eigenvector $|f_0\rangle$. These formulae follow from the fact that the derivatives of the eigenvalue z_0 can be calculated by means of perturbation theory. If λ is some parameter in the transfer matrix $\hat{T}$, then for an infinitesimal change in this parameter we can write,

$$\hat{T}(\lambda + d\lambda) = \hat{T}(\lambda) + d\lambda \frac{d}{d\lambda} \hat{T}(\lambda). \tag{2.125}$$

If the second term in this equation is regarded as a pertubation of the transfer operator, perturbation theory provides the corresponding leading order change in the eigenvalue of $\hat{T}$ to be

$$z_0(\lambda + d\lambda) = z_0(\lambda) + d\lambda \frac{\langle f_0(\lambda) | \frac{d}{d\lambda} \hat{T}(\lambda) | f_0(\lambda) \rangle}{\langle f_0(\lambda) | f_0(\lambda) \rangle}, \tag{2.126}$$

where $|f_0(\lambda)\rangle$ is the "unperturbed" eigenvector belonging to $z_0(\lambda)$. The derivative of z_0 can therefore

be deduced to be

$$\frac{dz_0}{d\lambda} = \frac{z_0(\lambda + d\lambda) - z_0(\lambda)}{d\lambda} = \frac{\langle f_0(\lambda)|\frac{d}{d\lambda}\hat{T}(\lambda)|f_0(\lambda)\rangle}{\langle f_0(\lambda)|f_0(\lambda)\rangle}. \tag{2.127}$$

Among the thermodynamic quantities which we can write down using this formula are the internal energy,

$$E = -\frac{1}{z_0}\frac{\partial z_0}{\partial \beta} = -\frac{1}{z_0}\frac{\langle f_0|\frac{\partial}{\partial \beta}\hat{T}|f_0\rangle}{\langle f_0|f_0\rangle}, \tag{2.128}$$

and the magnetisation,

$$M = -\frac{\partial F}{\partial B} = \frac{1}{\beta z_0}\frac{\langle f_0|\frac{\partial}{\partial B}\hat{T}|f_0\rangle}{\langle f_0|f_0\rangle}. \tag{2.129}$$

In order to obtain such quantities to machine accuracy, in our calculations of z_0 we ensure that both the eigenvalue and the eigenvector have converged to machine accuracy; this in general requires a larger number of iterations than the calculation of the eigenvalue alone.

In principle, higher order derivatives may be calculated by applying perturbation theory to higher orders. The formulae for the higher derivatives involve the rest of the eigenvalue spectrum of $\hat{T}$. For example, under the stronger assumption that none of the eigenvalues of $\hat{T}$ are degenerate, for the second derivative one obtains,

$$\frac{d^2 z_0}{d\lambda^2} = \frac{\langle f_0(\lambda)|\frac{d^2}{d\lambda^2}\hat{T}(\lambda)|f_0(\lambda)\rangle}{\langle f_0(\lambda)|f_0(\lambda)\rangle} + 2\sum_{\alpha\neq 0}\frac{\left(\langle f_0(\lambda)|\frac{d}{d\lambda}\hat{T}(\lambda)|f_\alpha(\lambda)\rangle\right)^2}{(z_0(\lambda) - z_\alpha(\lambda))\,\langle f_0(\lambda)|f_0(\lambda)\rangle\langle f_\alpha(\lambda)|f_\alpha(\lambda)\rangle}. \tag{2.130}$$

This formula can in principle be used to calculate such quantities as the specific heat,

$$C = \frac{\partial E}{\partial T} = \beta^2\left[\frac{1}{z_0}\frac{\partial^2 z_0}{\partial \beta^2} - \left(\frac{1}{z_0}\frac{\partial z_0}{\partial \beta}\right)^2\right], \tag{2.131}$$

and the magnetic susceptibility,

$$\chi = \frac{\partial M}{\partial B} = -\frac{1}{\beta}\left[\frac{1}{z_0}\frac{\partial^2 z_0}{\partial B^2} - \left(\frac{1}{z_0}\frac{\partial z_0}{\partial B}\right)^2\right]. \tag{2.132}$$

Although the formula 2.130 is of some mathematical interest, the application of it in practice requires one to have calculated the entire eigenvalue spectrum of the transfer operator, and this is a task of much greater computational expense than the calculation of the largest eigenvalue. It is more practical to calculate the higher derivatives of the partition function from the computed values of the first derivative with the use of difference formulae. To obtain the second and higher derivatives of z_0

with respect to λ, we calculate the first derivative to machine accuracy at the five evenly spaced points lying symmetrically around the relevant value of the parameter, and we write,

$$\begin{pmatrix} \frac{dz_0}{d\lambda}(\lambda-2\Delta\lambda)-\frac{dz_0}{d\lambda}(\lambda) \\ \frac{dz_0}{d\lambda}(\lambda-\Delta\lambda)-\frac{dz_0}{d\lambda}(\lambda) \\ \frac{dz_0}{d\lambda}(\lambda+\Delta\lambda)-\frac{dz_0}{d\lambda}(\lambda) \\ \frac{dz_0}{d\lambda}(\lambda+2\Delta\lambda)-\frac{dz_0}{d\lambda}(\lambda) \end{pmatrix} = \begin{pmatrix} -2\Delta\lambda & 2(\Delta\lambda)^2 & -\frac{4}{3}(\Delta\lambda)^3 & \frac{2}{3}(\Delta\lambda)^4 \\ -\Delta\lambda & \frac{1}{2}(\Delta\lambda)^2 & -\frac{1}{6}(\Delta\lambda)^3 & \frac{1}{24}(\Delta\lambda)^4 \\ \Delta\lambda & \frac{1}{2}(\Delta\lambda)^2 & \frac{1}{6}(\Delta\lambda)^3 & \frac{1}{24}(\Delta\lambda)^4 \\ 2\Delta\lambda & 2(\Delta\lambda)^2 & \frac{4}{3}(\Delta\lambda)^3 & \frac{2}{3}(\Delta\lambda)^4 \end{pmatrix} \begin{pmatrix} \frac{d^2z_0}{d\lambda^2}(\lambda) \\ \frac{d^3z_0}{d\lambda^3}(\lambda) \\ \frac{d^4z_0}{d\lambda^4}(\lambda) \\ \frac{d^5z_0}{d\lambda^5}(\lambda) \end{pmatrix} + O\left((\Delta\lambda)^5\right),$$

which follows simply from the Taylor expansion of $\frac{dz_0}{d\lambda}$ about the value λ. These relations can be inverted to provide approximate formulae for the derivatives of z_0 up to the fifth order,

$$\frac{d^2z_0}{d\lambda^2}(\lambda) \approx \frac{1}{\Delta\lambda}\left[\frac{1}{12}\frac{dz_0}{d\lambda}(\lambda-2\Delta\lambda)-\frac{2}{3}\frac{dz_0}{d\lambda}(\lambda-\Delta\lambda)+\frac{2}{3}\frac{dz_0}{d\lambda}(\lambda+\Delta\lambda)-\frac{1}{12}\frac{dz_0}{d\lambda}(\lambda+2\Delta\lambda)\right], \quad (2.133)$$

$$\frac{d^3z_0}{d\lambda^3}(\lambda) \approx \frac{1}{(\Delta\lambda)^2}\left[-\frac{1}{12}\frac{dz_0}{d\lambda}(\lambda-2\Delta\lambda)+\frac{4}{3}\frac{dz_0}{d\lambda}(\lambda-\Delta\lambda)+\frac{4}{3}\frac{dz_0}{d\lambda}(\lambda+\Delta\lambda)-\frac{1}{12}\frac{dz_0}{d\lambda}(\lambda+2\Delta\lambda)-\frac{5}{2}\frac{dz_0}{d\lambda}(\lambda)\right],$$

$$\frac{d^4z_0}{d\lambda^4}(\lambda) \approx \frac{1}{(\Delta\lambda)^3}\left[-\frac{1}{2}\frac{dz_0}{d\lambda}(\lambda-2\Delta\lambda)+\frac{1}{3}\frac{dz_0}{d\lambda}(\lambda-\Delta\lambda)-\frac{1}{3}\frac{dz_0}{d\lambda}(\lambda+\Delta\lambda)+\frac{1}{2}\frac{dz_0}{d\lambda}(\lambda+2\Delta\lambda)\right],$$

$$\frac{d^5z_0}{d\lambda^5}(\lambda) \approx \frac{1}{(\Delta\lambda)^4}\left[\frac{dz_0}{d\lambda}(\lambda-2\Delta\lambda)-4\frac{dz_0}{d\lambda}(\lambda-\Delta\lambda)-4\frac{dz_0}{d\lambda}(\lambda+\Delta\lambda)+\frac{dz_0}{d\lambda}(\lambda+2\Delta\lambda)+6\frac{dz_0}{d\lambda}(\lambda)\right].$$

We have assumed that the largest eigenvalue z_0 is nondegenerate. This is found to always be the case for the finite N system, and degeneracy of the largest eigenvalue is only seen to occur in the two dimensional limit $N \to \infty$. This is well-known in the context of exact-diagonalisation, where the groundstate of the finite system is always non-degenerate, and degeneracy is seen to emerge as the size of the system is increased. Exact diagonalisation studies frequently consider precisely the question of whether in the infinite system the groundstate is degenerate, and this is done by assessing the rate at which the separation of the groundstate energy to the first excitation energy decreases as the system is made larger(45; 46). In the context of one-to-two dimensional crossover, the degeneracy of certain eigenvalues of the transfer matrix with the largest eigenvalue occur at a critical point The calculation of other eigenvalues of the transfer matrix in addition to z_0 is therefore, just as in exact diagonalisation, an important facet of the technique.

Let z_1 be the next-largest eigenvalue after z_0 and let $|f_1\rangle$ be the corresponding eigenstate. In principle, this state can be obtained using the power method in exactly the manner described in the

calculation for $|f_0\rangle$, provided that one chooses an initial state $|f\rangle$ which has no overlap with $|f_0\rangle$ but a finite overlap with $|f_1\rangle$. In this case we would have after many iterations,

$$\left(\hat{T}\right)^L |f\rangle \sim a_1 \left(z_1\right)^L |f_1\rangle, \tag{2.134}$$

in place of the expression 2.124. The initial state can be first orthogonalised with respect to $|f_0\rangle$ by the procedure

$$|f\rangle \rightarrow |f\rangle - \frac{\langle f_0|f\rangle}{\langle f_0|f_0\rangle}|f_0\rangle. \tag{2.135}$$

In practice, even if the intitial state is orthogonal to $|f_0\rangle$, any numerical error which occurs in the calculation of each application of the transfer matrix will build up over a large number of iterations to generate a $|f_0\rangle$-component in the state, and one must continually orthogonalise the state with respect to $|f_0\rangle$ in order for it to converge to $|f_1\rangle$. This method can be generalised to calculate any number of eigenstates, in the order of decreasing modulus of the corresponding eigenvalues, by simply orthogonalising with respect to the previously calculated eigenstates. For example, the eigenstate belonging to the third-largest eigenvalue is obtained by continually applying the procedure

$$|f\rangle \rightarrow |f\rangle - \frac{\langle f_0|f\rangle}{\langle f_0|f_0\rangle}|f_0\rangle - \frac{\langle f_1|f\rangle}{\langle f_1|f_1\rangle}|f_1\rangle. \tag{2.136}$$

A striking analogy between the one-to-two dimensional crossover theory and quantum mechanics emerges relating to the calculation of thermodynamic averages of quantities which are functions of contiguous sets of spins. Consider a function of N neighbouring spins in the chain, $Q(\vec{S}_1, \vec{S}_2, ..., \vec{S}_N)$. The thermodynamic average of this quantity is, from first principles,

$$\langle Q(\vec{S}_1, \vec{S}_2, ..., \vec{S}_N)\rangle = \frac{1}{\mathcal{Z}_M}\left(\prod_{j=1}^{M}\int d\Omega_j\right)\left(Q(\vec{S}_1, \vec{S}_2, ..., \vec{S}_N)e^{-\beta H_M}\right). \tag{2.137}$$

Now, in section 2.1.1, in our consideration of the partition function as a summation over all the M spin-variables in the chain, we have seen that $(M - N)$ of these summations provide the diagonal elements of $\hat{T}^M$, and the remaining N summations provide the trace of this operator. In the present calculation, we can identify the N spins which are the arguments of $Q(\vec{S}_1, \vec{S}_2, ..., \vec{S}_N)$ with the trace,

and consequently we may write,

$$\langle Q(\vec{S}_1, \vec{S}_2, ..., \vec{S}_N)\rangle = \frac{1}{\mathcal{Z}_M}\mathrm{tr}\left(\hat{Q}\hat{T}^M\right), \tag{2.138}$$

where the operator $\hat{Q}$ is constructed to provide the factors $Q(\vec{S}_1, \vec{S}_2, ..., \vec{S}_N)$:

$$\langle \vec{S}_N, ..., \vec{S}_1|\hat{Q}|\vec{S}'_1, ..., \vec{S}'_N\rangle = Q(\vec{S}_1, \vec{S}_2, ..., \vec{S}_N)\prod_{j=1}^{M}\delta_{\vec{S}_j,\vec{S}'_j}. \tag{2.139}$$

Expanding the trace using the eigenbasis of the transfer matrix provides

$$\begin{aligned}\langle Q(\vec{S}_1, \vec{S}_2, ..., \vec{S}_N)\rangle &= \frac{1}{\mathcal{Z}_M}\sum_\alpha \frac{\langle f_\alpha|\hat{Q}\hat{T}^M|f_\alpha\rangle}{\langle f_\alpha|f_\alpha\rangle} \\ &= \frac{1}{\mathcal{Z}_M}\sum_\alpha (z_\alpha)^M \frac{\langle f_\alpha|\hat{Q}|f_\alpha\rangle}{\langle f_\alpha|f_\alpha\rangle}.\end{aligned} \tag{2.140}$$

In the limit $M \to \infty$ only the term involving the largest eigenvalue is relevant, and substituting in the expression for the partition function in this limit, we obtain,

$$\langle Q(\vec{S}_1, \vec{S}_2, ..., \vec{S}_N)\rangle = \frac{\langle f_0|\hat{Q}|f_0\rangle}{\langle f_0|f_0\rangle}. \tag{2.141}$$

Using the expression for the inner product 2.10, this is given explicitly by

$$\langle Q(\vec{S}_1, ..., \vec{S}_N)\rangle = \frac{1}{\langle f_0|f_0\rangle}\left(\prod_{j=1}^{N}\int d\Omega_j\right) f_0(\vec{S}_N, ..., \vec{S}_1)Q(\vec{S}_1, ..., \vec{S}_N)f_0(\vec{S}_1, ..., \vec{S}_N). \tag{2.142}$$

It is clear from this expression that the quantity

$$\frac{1}{\langle f_0|f_0\rangle}f_0(\vec{S}_N, ..., \vec{S}_1)f_0(\vec{S}_1, ..., \vec{S}_N)$$

is the probability distribution for the configuration of the N contiguous spins. These results are perfectly analogous to quantum mechanics, where the expectation value of some observable $\hat{O}$ is given by,

$$\langle\hat{O}\rangle = \frac{\langle\Psi|\hat{O}|\Psi\rangle}{\langle\Psi|\Psi\rangle},$$

and the quantum mechanical wavefunction provides the analogous probability density as,

$$\frac{\Psi^*(\{x_i\})\Psi(\{x_i\})}{\langle\Psi|\Psi\rangle}.$$

The formula for the ensemble average of a function of N contiguous spins has a very simple form because we can identify the N spin-variables which form the argument of the function with the trace. For completeness, we now deal with the more complicated case of functions of a larger number of contiguous spins. The ensemble average of a function of $(N+l)$ contiguous spins, $Q(\vec{S}_1, ..., \vec{S}_{N+l})$, is of course,

$$\langle Q(\vec{S}_1, \vec{S}_2, ..., \vec{S}_{N+l})\rangle = \frac{1}{\mathcal{Z}_M}\left(\prod_{j=1}^{M}\int d\Omega_j\right)\left(Q(\vec{S}_1, \vec{S}_2, ..., \vec{S}_{N+l})e^{-\beta H_M}\right). \tag{2.143}$$

In comparison to the case of the function of N contiguous spins, in this case there are an "extra" l spin variables whose summation cannot be included in the trace and which are not equivalent to the repeated application of $\hat{T}$, owing to the presence of the function Q; the summation over these l spins cannot be simplified, and we must simply define a new operator so as to account for these summations. We introduce the new transfer operator $\hat{V}$ and write,

$$\langle Q(\vec{S}_1, ..., \vec{S}_{N+l})\rangle = \frac{1}{\mathcal{Z}_M}\mathrm{tr}\left(\hat{V}^l\hat{T}^{M-l}\right), \tag{2.144}$$

where $\hat{V}$ is defined to simply include the summation over l spin-variables including the function Q in the summand via,

$$\left((\hat{V})^l f\right)(\vec{S}_{1+l}, ..., \vec{S}_{N+l}) = \left(\prod_{j=1}^{l}\int d\Omega_j\right) Q(\vec{S}_1, ..., \vec{S}_{N+l})e^{\beta K(\vec{S}_1,...,\vec{S}_{N+1})+...+\beta K(\vec{S}_l,...,\vec{S}_{N+l})} f(\vec{S}_1, ..., \vec{S}_N). \tag{2.145}$$

Proceeding in the same manner as in the former case, the trace in equation 2.144 can be represented in the eigenbasis of $\hat{T}$ as,

$$\langle Q(\vec{S}_1, ..., \vec{S}_{N+l})\rangle = \frac{1}{\mathcal{Z}_M}\sum_\alpha (z_\alpha)^{M-l}\,\frac{\langle f_\alpha|(\hat{V})^l|f_\alpha\rangle}{\langle f_\alpha|f_\alpha\rangle}, \tag{2.146}$$

and for any finite l, the term in the largest eigenvalue dominates in the limit that $M \to \infty$ and we

obtain in this limit,

$$\langle Q(\vec{S}_1, ..., \vec{S}_{N+l})\rangle = \frac{1}{(z_0)^l} \frac{\langle f_0|(\hat{V})^l|f_0\rangle}{\langle f_0|f_0\rangle}. \tag{2.147}$$

A particularly important example is the spin-spin correlation function, $\langle \vec{S}_1 \cdot \vec{S}_{1+r}\rangle$. For the short-range spin correlations, with $r < N$, we have,

$$\langle \vec{S}_1 \cdot \vec{S}_{1+r}\rangle = \frac{1}{\langle f_0|f_0\rangle} \left(\prod_{j=1}^{N} \int d\Omega_j \right) \left(\vec{S}_1 \cdot \vec{S}_{1+r} \right) f_0(\vec{S}_N, ..., \vec{S}_1) f_0(\vec{S}_1, ..., \vec{S}_N), \tag{2.148}$$

while for $r \geq N$ we have the representation,

$$\langle \vec{S}_1 \cdot \vec{S}_{1+r}\rangle = \left(\frac{1}{z_0} \right)^{r+1-N} \frac{\langle f_0|(\hat{V})^{r+1-N}|f_0\rangle}{\langle f_0|f_0\rangle}, \tag{2.149}$$

where the new transfer operator $\hat{\tilde{T}}$ is defined by

$$\begin{aligned} &\left((\hat{V})^{r+1-N} f \right) (\vec{S}_{1+r-N}, ..., \vec{S}_r) \\ &\quad = \left(\prod_{j=1}^{N+1-r} \int d\Omega_j \right) \left(\vec{S}_1 \cdot \vec{S}_{1+r} \right) e^{\beta K(\vec{S}_1, ..., \vec{S}_{N+1}) + ... + \beta K(\vec{S}_{r+1-N}, ..., \vec{S}_{r+1})} f(\vec{S}_1, ..., \vec{S}_N). \end{aligned} \tag{2.150}$$

Any of the quantities discussed, which may be calculated to a high accuracy for the finite N system by the formalism outlined above, can be extrapolated to the two-dimensional limit $N \to \infty$. This is the only part of the application of the one-to-two dimensional crossover theory that is not on a sound mathematical footing. One fits a function of $1/N$ to the finite N data and reads off the value of the fitted function at the point $1/N = 0$. In this thesis, the only function which we have fitted to the data is the Lagrange interpolating polynomial, this being the unique lowest-order polynomial which passes through the data points(47). This extrapolation is often seen to fail, in that it predicts behaviour which is certainly not that of the two-dimensional system.

We close this section by applying the one-to-two dimensional crossover to the Ising model, in order to show how the theory predicts the existence of a phase transition. We exhibit calculations of the specific heat, the correlation length and the magnetic susceptibility.

The specific heat of the J_1-J_N Ising model is shown in figure 2.7, and the transition temperature of the square lattice Ising model is indicated. There is a pronounced peak, which increases as N is increased and which appears to be precisely at the transition temperature. In the square lattice Ising model, the specific heat exhibits a logarithmic divergence at the transition temperature. It seems that

in the limit $N \to \infty$ the peak in the one-to-two dimensional crossover calculation continues to grow and ultimately becomes this very divergence.

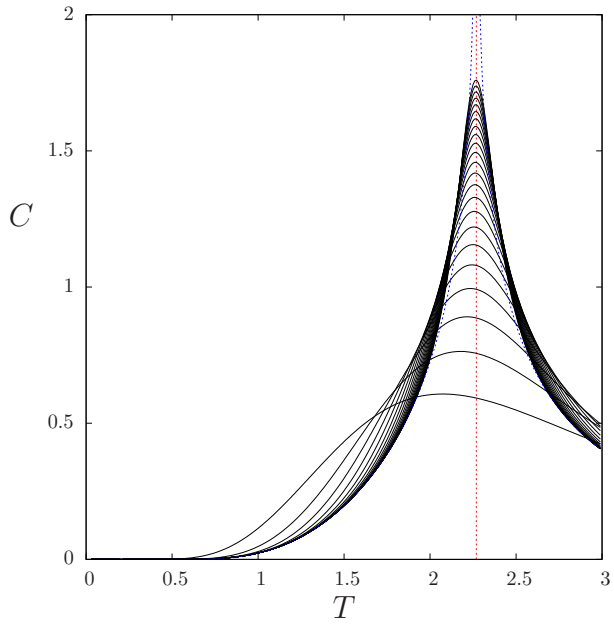

Figure 2.7: Specific heat of the J_1-J_N Ising model for N = 2-24. Also shown is the specific heat of the square lattice Ising model (dotted blue line). The red dotted line marks the transition temperature of the square lattice Ising model.

The derivatives of the specific heat with respect to the temperature are shown in figures 2.8 to 2.10. In the square lattice model, the specific heat is logarithmically divergent at the transition temperature, and each successive temperature derivative of the specific heat must exhibit a stronger divergence at this temperature. For finite N, each successive derivative of the specific heat takes larger absolute values in the vicinity of the transition temperature; the size of the peaks and troughs in these derivatives increases with N, and the increase with N is greater in the higher derivatives. It is quite convincing that each of these quantities is becoming divergent in the limit $N \to \infty$, and it appears that higher and higher derivatives are becoming divergent faster as N is increased, in agreement with the known behaviour of the square lattice model.

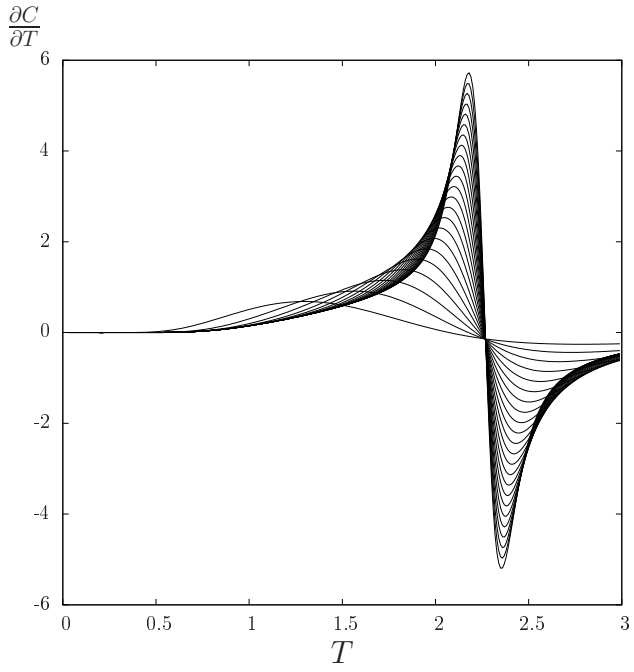

Figure 2.8: First derivative of the specific heat with respect to T for the Ising model for N = 2-24.

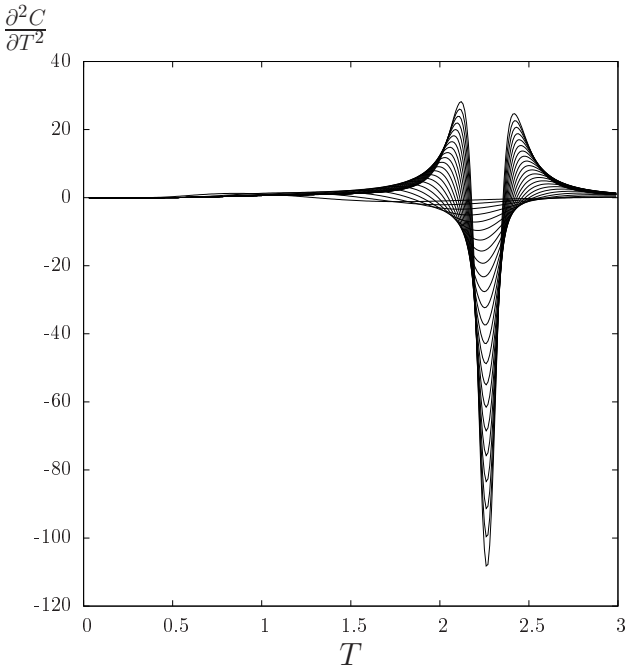

Figure 2.9: Second derivative of the specific heat with respect to T for the Ising model for N = 2-24.

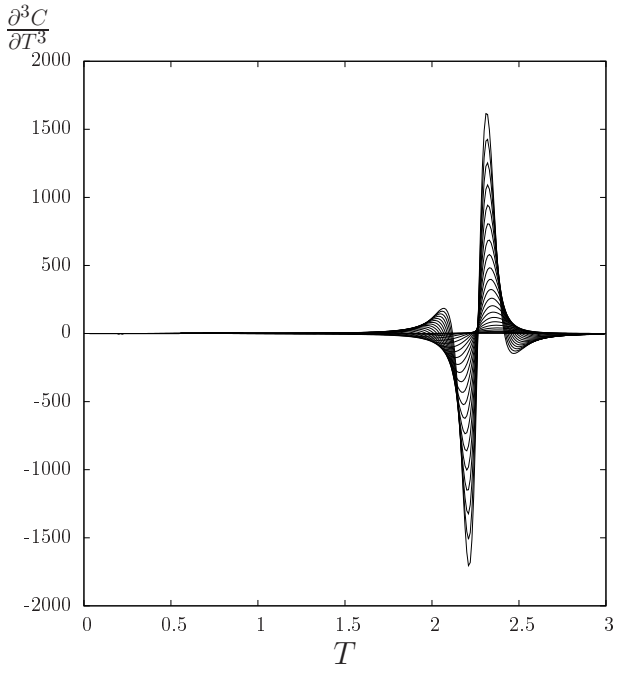

Figure 2.10: Third derivative of the specific heat with respect to T for the Ising model for $N = 2$-24.

The correlation length ξ and magnetic susceptibility χ provide a means to estimate the corresponding critical exponents. In the square lattice Ising model, just above the transition temperature these quantities have the form,

$$\xi \sim (T - T_C)^{-\nu},$$

$$\chi \sim (T - T_C)^{-\gamma},$$

where the critical exponents have the values $\nu = 1$ and $\gamma = 7/4(6)$.

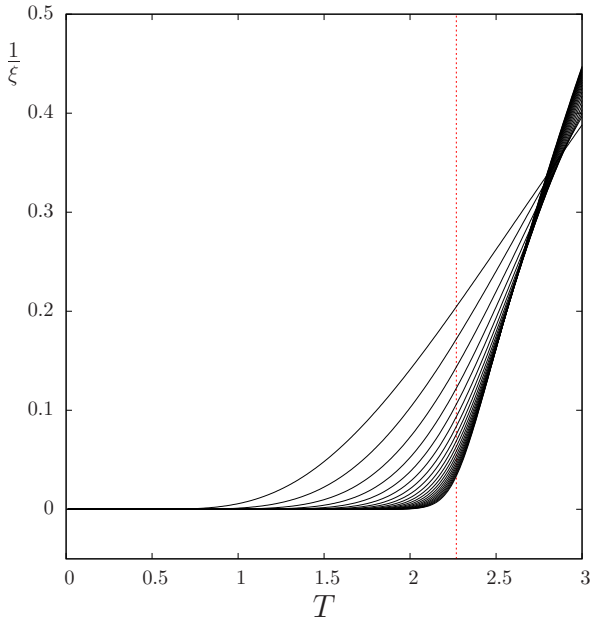

Figure 2.11: The inverse correlation length of the J_1-J_N Ising model, for N = 2-22. The vertical dotted line marks the transition temperature of the square lattice Ising model.

The calculations of $1/\xi$ are shown in Figure 2.11. In the square lattice model, the correlation length diverges at the transition temperature, and is equal to infinity in the long-range ordered phase below the transition. The one-to-two dimensional crossover calculations certainly predict that the correlation length should be infinite for the limit $N = \infty$ for all temperatures below, with the possible exception of the very near-vicinity of, the transition temperature. The value of the correlation length in the region below the phase transition is increasing with N, and for the biggest calculation, $N = 22$, the correlation length is calculated to be greater than 10^5 for all temperatures $0 < T < 2$ and greater than 10^{16} for $0 < T < 1$.

In addition, $1/\xi$ shows a linear form in the vicinity of the transition temperature, in accord with the critical exponent having the value $\nu = 1$. The functional form of the correlation length can be investigated further by calculating the derivatives with respect to temperature of $1/\xi$. The first and second derivatives are shown in figures 2.12 and 2.13 respectively. The first temperature derivative of the known critical temperature-dependence of $1/\xi$ is a step function, where the step occurs at the transition temperature, and the second derivative is a Dirac delta-function centred at the transition temperature. The prediction for the $N \to \infty$ limit of the one-to-two dimensional crossover calculations

is certainly an abrupt step-like change in the first derivative, and a very large peak or a divergence in the second derivative, the position of the peak in the second derivative lying very close to the transition temperature. As it happens, the second derivative of $1/\xi$ with respect to the logarithm of temperature, shown in figure 2.14, reveals the emerging divergence at the transition temperature most clearly, the peak in this quantity being even closer to the transition temperature.

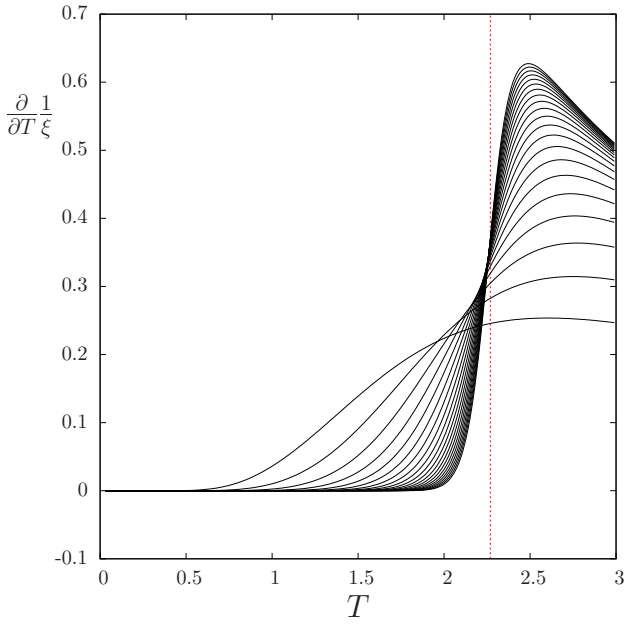

Figure 2.12: Derivative of the reciprocal correlation length with respect to temperature for $N = 2$-22.

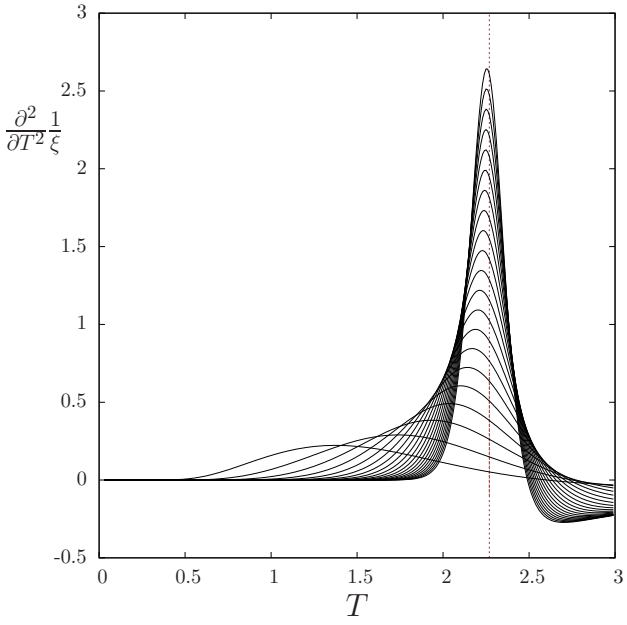

Figure 2.13: Second derivative of the reciprocal correlation length with respect to temperature for $N = 2$-22. The vertical dotted line marks the transition temperature of the square lattice Ising model.

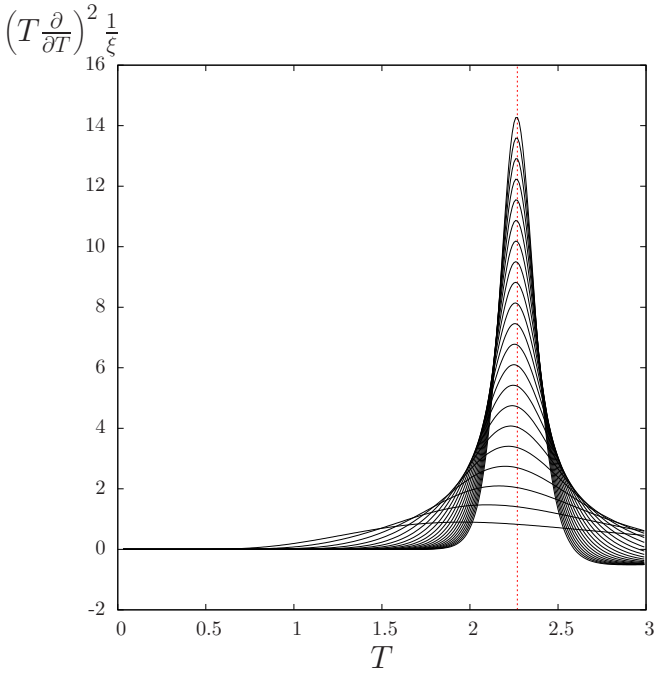

Figure 2.14: Second derivative of the reciprocal correlation length with respect to $\ln T$ for $N = 2$-22. The vertical dotted line marks the transition temperature of the square lattice Ising model.

The situation is much the same for the magnetic susceptibility. The square lattice model has χ also equal to infinity below the phase transition. The calculations of $1/\chi$ are shown in figure 2.15, and again suggest that the susceptibility should be infinite in the low-temperature region in the $N \to \infty$ limit, the value for the largest calculation, $N = 18$, being larger than 10^4 for temperatures below $T = 1.5$. The first temperature derivative of the known two-dimensional critical form of $1/\chi$ is a power law with the exponent $3/4$, and the second temperature derivative is a power law with exponent $-1/4$, and the latter function diverges at the transition temperature. The calculations of the first and second temperature derivatives of $1/\chi$ are shown in figures 2.16 and 2.17 respectively. While there is apparently little to be deduced from the calculation of the first derivative, a very clear peak appears in the second derivative, in accord with the expectation that this quantity should diverge in the $N \to \infty$ limit, although the position of this peak is still substantially displaced from the transition temperature in the biggest calculation. In this instance the *third* derivative of $1/\chi$ with respect to the logarithm of temperature shows a peak in very close proximity to the transition temperature, and it is extremely convincing the in the $N \to \infty$ limit the peak will lie precisely on top of the transition temperature. Concerning the critical exponent γ, the hard prediction of the one-to-two dimensional

crossover calculations, based on the number of temperature-derivatives of $1/\chi$ which must be taken before a peak emerges, is that the exponent lies in the range $1 \leq \gamma < 2$.

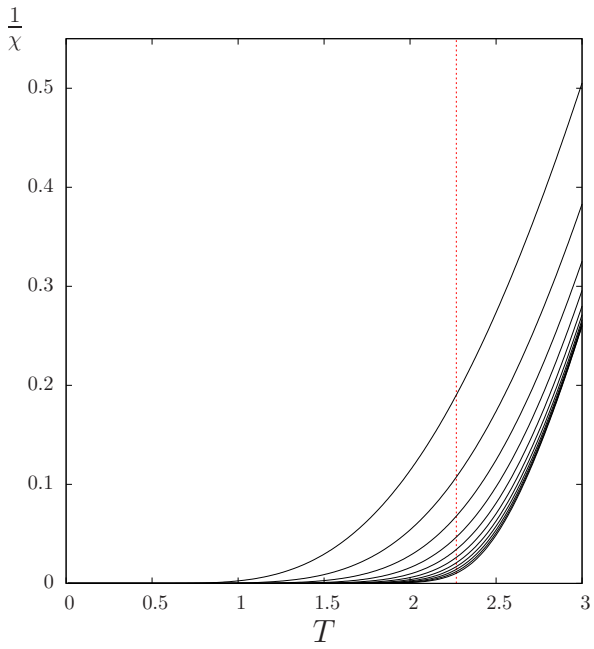

Figure 2.15: Reciprocal of the magnetic susceptibility of the Ising model for N = 2-12. The vertical dotted line marks the transition temperature of the square lattice Ising model.

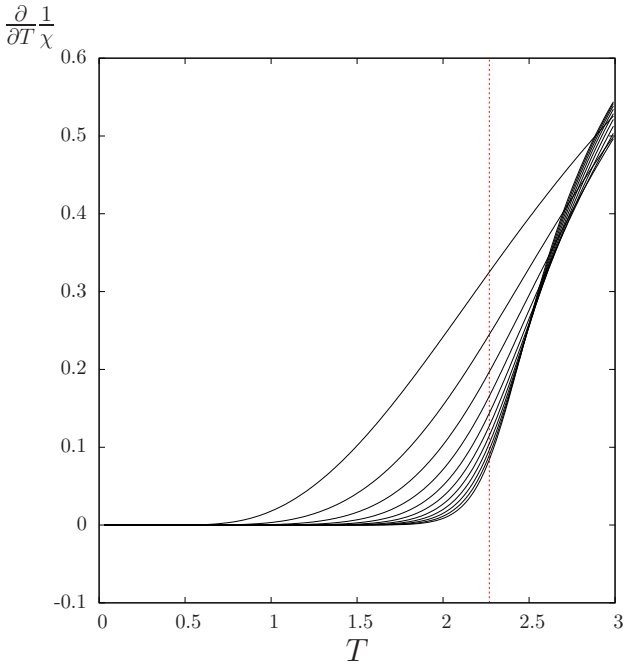

Figure 2.16: First derivative of the reciprocal magnetic susceptibility with respect to temperature for $N = 2$-12. The vertical dotted line marks the transition temperature of the square lattice Ising model.

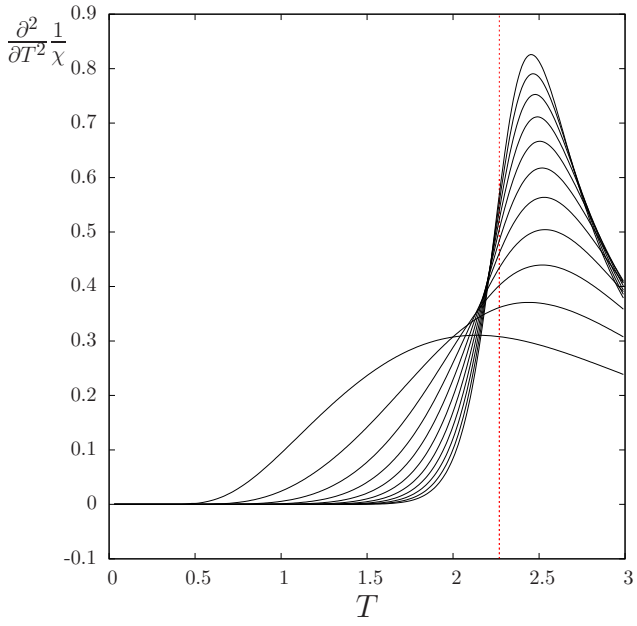

Figure 2.17: Second derivative of the reciprocal magnetic susceptibility with respect to temperature for N = 2-12. The vertical dotted line marks the transition temperature of the square lattice Ising model.

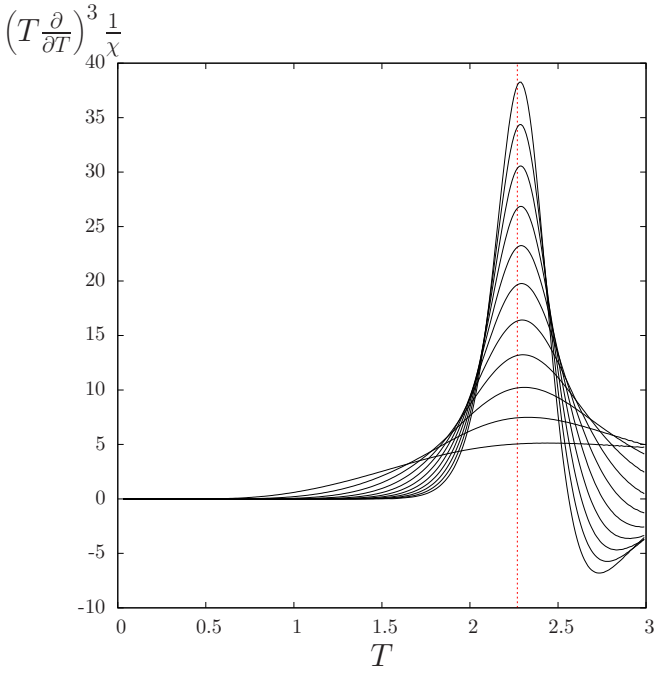

Figure 2.18: Third derivative of the reciprocal magnetic susceptibility with respect to $\ln T$ for $N = 2$-12. The vertical dotted line marks the transition temperature for the square lattice Ising model.

2.4 One-to-two dimensional crossover of the planar rotator model

2.4.1 Introductory remarks

In this section we shall apply the one-to-two dimensional crossover to the planar rotator model. The scheme which we shall use is the J_1-J_N spiral geometry, and therefore we consider the Hamiltonian,

$$H_N = -J \sum_j \left[\cos(\phi_j - \phi_{j+1}) + \cos(\phi_j - \phi_{j+N})\right] \tag{2.151}$$

where the index j labels the sites on an infinite spin-chain. The spiral circumference N is the finite-size scaling parameter, and we shall be concerned with how the results of our calculations change as N is increased, ultimately appealing to the limit that N tends to infinity. The question which we aim to address is the style of phase transition which occurs in the square lattice planar rotator model.

The technique, as discussed in the previous section, is to construct the transfer operator and then

to find the largest eigenvalue on a computer. The planar rotator model has continuous degrees of freedom, and in order to represent the transfer operator on a computer, some discretisation procedure must be employed. One scheme is simply to discretise the spin-angles ϕ_j, that is to only allow them to take an integer number q of discrete evenly spaced values in the range 0 to 2π. The model which results from performing this discretisation is known as the q-state clock model, owing to a resemblence of the equally-spaced spin-directions to a clock face. A thorough investigation of the one-to-two dimensional crossover of the clock model has been carried out previously and is reported in the thesis of A. M. Cave(29).

The clock model is not isotropic, and as a result long-range order must occur on the square lattice at low temperature. This discretisation therefore drastically changes the low temperature physics of the model. The $q = 2$, $q = 3$ and $q = 4$ clock models are equivalent to the Ising model, the three-state Potts model(48) and two independent Ising models respectively, and all these models undergo a single second order phase transition from a long-range ordered phase to a disordered phase, and the transition temperatures are known exactly(49). For $q > 4$, the clock model undergoes two phase transitions(14): a low temperature transition from a long-range ordered state into a power-law correlated phase, and a high temperature transition from the power-law correlated phase into a disordered phase. The latter transition corresponds to the phase transition in the planar rotator model.

The clock model can be thought of as an approximation to the planar rotator model, with erroneous low temperature behaviour resulting from this approximation, or thought of as an interesting model in its own right. It is also equivalent to the planar rotator model with an additional strong crystal field interaction, which forces the isotropic planar spins to point in the evenly spaced discrete directions. From this viewpoint, the long-range order transition is associated with the crystal field interaction, while the upper transition is associated with the underlying planar spins, and the investigations into the clock model have indicated that these should be thought of as quite independent(29).

In this thesis we shall present the results of using a different discretisation scheme based on parameterising the continuous spin-angles in terms of Fourier series. The Fourier indices provide mathematically natural discrete degrees of freedom to describe the transfer matrix, but in doing this one obtains a matrix which is infinitely large. We *truncate* the Fourier series to simply ignore the high Fourier components. This results in a finite matrix whose eigenvalue is equal to that of the transfer matrix to machine accuracy for a sufficient truncation. In this scheme, the error is introduced into the calculation not with the discretisation, which is the exact representation of periodic functions as

Fourier series, but with the truncation of the Fourier series. As we shall come to discuss, the number of Fourier components which it is necessary to include in the calculation in order to achieve machine accuracy is larger at lower temperatures. The low temperature corruption present in the clock model is therefore still present in the truncated Fourier series scheme, but it surfaces in a different way.

In the thesis of A. M. Cave, the clock models were discussed in large part as interesting models in their own right, rather than only approximations to the planar rotator model. This thesis is concerned with the planar rotator model exclusively. The calculations have been performed with the philosophy that the number of Fourier components should be actively adjusted as a function of the temperature in order to ensure that the thermodynamics of the pure planar rotator model are calculated to a high accuracy. The low temperature error resulting from the truncation will be present in some calculations, but this will always be regarded as an irritation. By contrast, the low temperature "error" in the clock models is of great physical interest, in that it describes a second phase transition associated with a crystal field interaction.

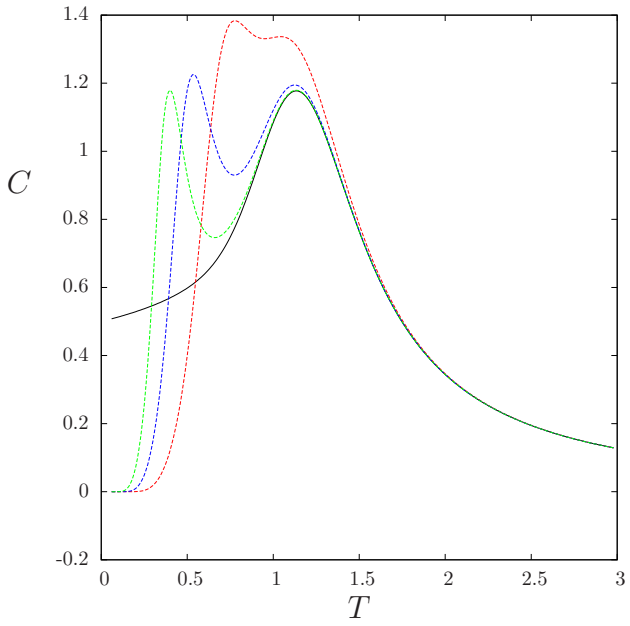

Figure 2.19: The specific heat of the J_1-J_5 planar rotator model (solid black line), and the J_1-J_5 q-state clock model for $q = 5$ (red line), $q = 6$ (blue line) and $q = 7$ (green line). The clock model calculations were provided by A. M. Cave.

Figure 2.19 shows transfer function calculations of the specific heat of the J_1-J_5 q-state clock model for $q = 5$, $q = 6$ and $q = 7$ which were completed by A. M. Cave, together with a calculation of the

specific heat of the J_1-J_5 planar rotator model completed as part of the present investigation. We shall come to discuss the calculations of the specific heat for the planar rotator model in much more detail in section 2.4.4, but at this stage simply offer this calculation in order to compare it with the clock model calculations. The clock model calculations clearly provide a good approximation to the planar rotator specific heat at sufficiently high temperatures, and the second peak which occurs at low temperature is a sympton caused by the discretisation of the spin-angles, and is taken by A. M. Cave to mark the long-range-order transition which occurs in the square lattice clock models. Increasing the number of discrete spin-directions q provides a better approximation to the planar rotator model, evidenced in the calculations by a closer match between the specific heat curves down to lower temperatures, and the shift of the low temperature peak towards the origin.

In addition, the calculations allow us to make a much stronger statement regarding the relationship between the two models. Figure 2.20 shows the ratio of each of the three clock model specific heat curves to the planar rotator curve. Strikingly, while the low temperature peak is clearly visible in the ratio of the specific heats, the high temperature peak is entirely absent. This shows quite convincingly that the peak in the planar rotator specific heat and the upper peak in the clock model specific heats are identical. A. M. Cave has interpreted the two peaks in the clock model specific heats as being associated with the two phase transitions which occur in the square lattice clock model, and has provided evidence that these are both regular phase transitions, and either the specific heat itself or some higher temperature derivative of the specific heat will exhibit a divergence at these points in the two-dimensional limit. Figure 2.20 shows quite convincingly that any of the behaviour associated with the upper peak in the clock model should be identical in the planar rotator model. One can therefore target the peak in the specific heat of the planar rotator model by examining a clock model calculation.

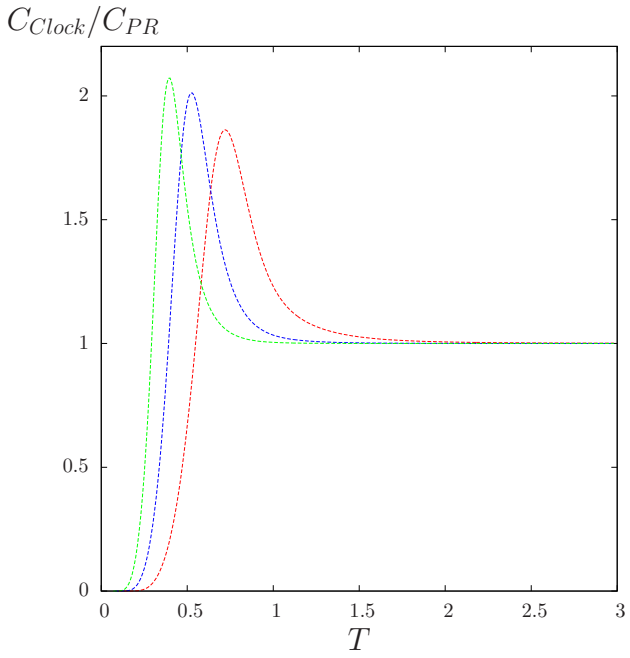

Figure 2.20: The data of figure 2.19, but plotted as the ratio of the specific heat of the J_1-J_5 q-state clock model to that of the J_1-J_5 planar rotator for $q = 5$ (red line), $q = 6$ (blue line) and $q = 7$ (green line). The clock model calculations were provided by A. M. Cave.

The desire to calculate the thermodynamics of the pure planar rotator model to a high accuracy limits the scope of the calculations in the present investigation to smaller values of N than in A. M. Cave's work. Concerning the style of phase transition which occurs in the planar rotator model, the clock model calculations therefore constitute the best evidence on this matter which can be provided using the one-to-two dimensional crossover technique. However, in order to establish the relationship between the two models it has been necessary to calculate the thermodynamics of the pure planar rotator model to a high accuracy, and this has led to the investigations reported in the present thesis. It is also arguably worthwhile to be able to present the evidence for the nature of the phase transition in the planar rotator model which is apparent in the bare thermodynamics of this model, without the need to consider the smooth additions to the thermodynamics which occur in clock model calculations.

Both the clock model investigations and the present planar rotator investigations provide consistent evidence that the phase transition in the square lattice planar rotator model is a regular phase transition with ordinary critical exponents. This is a very different picture to the widely-held view that the model should exhibit a Kosterlitz-Thouless transition which does not show up in the thermodynamics. The evidence in the pure planar rotator calculations is cleaner and therefore easier to interpret, but is

limited to smaller values of the scaling parameter N. The evidence provided in the clock model calculations is less clean because of the smooth additions to the planar rotator thermodynamics, but it is stronger evidence because one has access to larger values of N.

We begin, in section 2.4.2, by describing how the transfer operator for the planar rotator model is represented in terms of Fourier series; one finds that in this representation the transfer operator is cast as a matrix whose elements are products of Bessel functions. We devote some space to discussing the properties of these functions, in order to justify the truncation of the Fourier indices which we make for the purposes of computation. In section 2.4.3 we then describe a symmetry of the planar rotator model, namely with respect to the angle with respect to which the spin-angles are measured. We extract this symmetry in order to divide the N-dimensional space of the transfer operator into a discrete, independent set of $(N-1)$-dimensional subspaces which are labelled by a single index m. In terms of the computational expense of the one-to-dimensional crossover, this reduction in the size of the transfer operator increases by one the largest value of N for which we may perform the calculations.

In the subsequent sections we shall discuss a number of specific calculations of different quantities. The first set of quantities are the specific heat and higher temperature derivatives of the entropy, and these are dealt with in section 2.4.4. These calculations are both the most straightforward application of the one-to-two dimensional crossover technique and those whose results are easiest to understand. Ultimately one finds smooth curves for these quantities which show increasingly violent behaviour as N is increased, suggestive that a divergence will occur in one of the derivatives in the limit $N \to \infty$.

We shall then discuss the correlation length, the magnetic susceptibility and the helical stiffness in sections 2.4.5, 2.4.6 and 2.4.7 respectively. Each of these calculations requires some additional mathematical formalism, and the calculations of the magnetic susceptibility and the helical stiffness require one to modify the Hamiltonian. We shall present detailed discussions of each of the quantities in turn, in which we shall introduce whatever additional mathematics is pertinent to that particular calculation. In particular, the correlation length is closely associated with the eigenvalue spectrum of the transfer operator, and in section 2.4.5 we will also discuss a number of calculations of other eigenvalues in addition to the largest eigenvalue. The correlation length and magnetic susceptibility calculations allow some estimation of the relevant critical exponents for those quantities, and probably constitute the most striking indication of a regular phase transition in the square lattice model.

2.4.2 Fourier space representation

The equation 2.8, which defines the transfer operator, for the planar rotator model takes the form,

$$\left(\hat{T}f\right)(\phi_1,\phi_2,...,\phi_N)=\int_{-\pi}^{\pi}\frac{d\phi_1}{2\pi}e^{\beta K(\phi_0,\phi_1,...,\phi_N)}f(\phi_0,\phi_1,...,\phi_{N-1}). \tag{2.152}$$

Throughout this section, we shall assume that the transfer operator has been chosen to be self-adjoint, in the sense described in section 2.1.1, that is that the exponent $K(\phi_0,\phi_1,...)$ is symmetric under the operation of reversing the order of its arguments,

$$K(\phi_0,\phi_1,...,\phi_N)=K(\phi_N,\phi_{N-1},...,\phi_0). \tag{2.153}$$

As indicated above, we adopt the mathematically natural discretisation scheme of Fourier series; we write for a general state,

$$f(\phi_1,...,\phi_N)=\sum_{m_1=-\infty}^{\infty}\sum_{m_2=-\infty}^{\infty}...\sum_{m_N=-\infty}^{\infty}f_{m_1,m_2,...,m_N}e^{i(m_1\phi_1+m_2\phi_2+...+m_N\phi_N)}. \tag{2.154}$$

This is equivalent to representing the underlying vector $|f\rangle$ using the basis states $|m_1,...,m_N\rangle$, where

$$\langle\phi_N,...,\phi_1|m_1,...,m_N\rangle=e^{i(m_1\phi_1+m_2\phi_2+...+m_N\phi_N)}, \tag{2.155}$$

and these states have the orthogonality property,

$$\langle m_1,...,m_N|m'_1,...,m'_N\rangle=\prod_{j=1}^{N}\delta_{m_j+m'_{N+1-j}}. \tag{2.156}$$

The Fourier coefficients of the function $f(\phi_1,...,\phi_N)$ are the components of $|f\rangle$ in this basis, and are given explicitly by

$$f_{m_1,m_2,...,m_N}=\langle -m_N,-m_{N-1},...,-m_1|f\rangle. \tag{2.157}$$

To find the Fourier-space form of the transfer operator, we must write down the Fourier coefficients of the function $e^{\beta K(\phi_0,\phi_1,...,\phi_N)}$ in equation 2.152. Whatever choice is made for the function $K(\phi_0,\phi_1,...,\phi_N)$, it is always a sum of cosine angles of the spin functions. We must therefore consider

the expansion,

$$e^{x\cos\theta} = \sum_{s=-\infty}^{\infty} I_s(x) e^{is\theta}, \tag{2.158}$$

where $I_s(x)$ is the modified Bessel function of the first kind of order s. The Fourier components of $e^{\beta K}$, and therefore the matrix elements of the transfer operator in the Fourier basis, are given by products of these functions.

Given the utmost importance of the functions $I_s(x)$ in the calculations, we now briefly discuss their properties. Equation 2.158 can be regarded as a definition of these functions, and from this definition one can immediately deduce the integral representation,

$$I_s(x) = \int_{-\pi}^{\pi} \frac{d\theta}{2\pi} e^{is\theta} e^{x\cos\theta}. \tag{2.159}$$

By replacing the factor $e^{x\cos\theta}$ in the integrand by its power series in the variable x, and integrating out the variable θ term by term, one obtains the following series representation for $I_s(x)$,

$$I_s(x) = \sum_{n=0}^{\infty} \frac{1}{(|s|+n)!n!} \left(\frac{x}{2}\right)^{2n+|s|}. \tag{2.160}$$

The series in equation 2.160 converges extremely rapidly, and can consequently be used to calculate the functions $I_s(x)$ to a high accuracy for all values of x. It is this series representation which we have used to calculate the functions using the computer.

In the limit that x is small, the functions are given by the first term of the power series 2.160, providing the small-x limit of

$$I_s(x) \sim \frac{1}{|s|!} \left(\frac{x}{2}\right)^{|s|}. \tag{2.161}$$

The zeroth order function $I_0(x)$ takes the value one at $x = 0$, and all the higher order functions take the value zero at $x = 0$. This limit of small x corresponds to the limit where the temperature is large.

The large-x limit, which corresponds to the case of low temperature, may be obtained from the integral representation in equation 2.159. In this limit the integrand in equation 2.159 is extremely large in the vicinity of $\theta = 0$, and this region dominates the integral. One can therefore replace the integral in this limit by

$$I_s(x) \sim \frac{1}{2\pi} \int_{-\infty}^{\infty} e^{is\theta} e^{x\left(1-\frac{\theta^2}{2}\right)}, \tag{2.162}$$

and evaluating the Gaussian integral provides the large x limit to be

$$I_s(x) \sim \frac{e^{x-s^2/2x}}{\sqrt{2\pi x}}. \tag{2.163}$$

All of the functions ultimately increase without bound as x is increased.

All of the coefficients in the power series 2.160 are positive, and consequently in the domain $0 \leq x < \infty$, these functions are monotonically increasing functions of x. The functions also have the property that, excluding the points $x = 0$ and $x = \infty$, the higher-order functions are always smaller for the same value of x:

$$I_s(x) < I_{s'}(x) \quad \text{if} \quad |s| > |s'|. \tag{2.164}$$

In addition, for any finite value of x, the sufficiently high-order functions become exponentially small. The ratio of the second to the first term in the power series 2.160 is equal to $\frac{1}{|s|+1}\left(\frac{x}{2}\right)^2$. If this number is taken to be small, then to a good approximation $I_s(x)$ is given by only the first term in the series. This is the case if x is taken to be small, and this is of course precisely the small-x limit in 2.161. This is also the case if the order $|s|$ is very large. Precisely, if $|s| \gg \left(\frac{x}{2}\right)^2$ then we may approximate $I_s(x)$ by the first term. In addition, if $|s| \gg 1$ we may employ the Stirling limit,

$$|s|! \sim \sqrt{2\pi|s|}\left(\frac{|s|}{e}\right)^{|s|},$$

to replace the factorial in the first term, so that for sufficiently high orders we find the asymptotic form,

$$I_s(x) \sim \frac{1}{\sqrt{2\pi|s|}}\left(\frac{ex}{2|s|}\right)^{|s|}. \tag{2.165}$$

The implication of the exponential decay of the larger-order functions, described by the relation 2.165, is that, at any finite temperature, the transfer matrix can always be truncated to be finite, and the error resulting from the truncation can be made arbitrarily small by enlarging the truncated matrix. The size of the matrix that is required to provide the largest eigenvalue to a given accuracy is larger at lower temperatures, and this corresponds to a computationally more expensive calculation. The low temperature limit therefore presents an inherent difficulty in these calculations.

We truncate the transfer matrix by truncating the Fourier indices, $m_1, m_2, ..., m_N$, which we let take integer values in the range,

$$-M \leq m_i \leq +M$$

for some positive integer M, which we regard as an active parameter that describes the truncation. The number of degrees of freedom, per spin-variable, is therefore given by $p = 2M+1$. The eigenvector is represented by p^N numbers, and this effectively changes as a function of temperature.

2.4.3 Rotational symmetry

In the absence of an additional term such as a magnetic field, the Hamiltonian 2.151 depends only on the differences in the spin-angles for different sites, and is therefore symmetric with respect to a global rotation of the axis with respect to which the spins are measured. This symmetry is also present in the transfer operator, and can be extracted to effectively reduce the number of degrees of freedom in the eigenvalue problem from N to $N-1$. In quantum mechanical problems, a symmetry can be associated with some operator which commutes with the Hamiltonian, and consequently the eigenstates of the Hamiltonian can be chosen to be eigenstates of this operator also, which has the effect of splitting the problem into a number of independent subspaces. In the context of one-to-two dimensional crossover, a symmetry corresponds to an operator which commutes with the transfer operator $\hat{T}$. The rotational symmetry of the spin-variables is described by the operator $\hat{R}_\alpha$, which we define to rotate each of the spin-variables through an angle α,

$$(\hat{R}_\alpha f)(\phi_1, \phi_2, ..., \phi_N) = f(\phi_1 + \alpha, \phi_2 + \alpha, ..., \phi_N + \alpha). \tag{2.166}$$

This operator has the matrix elements,

$$\langle \phi_N, ..., \phi_1 | \hat{R}_\alpha | \phi'_1, ..., \phi'_N \rangle = \prod_{j=1}^{N} 2\pi\delta(\phi_j - \phi'_j - \alpha), \tag{2.167}$$

and it is straightforward to formally prove that $\hat{R}_\alpha$ commutes with the transfer operator $\hat{T}$.

Any exponential function of the spin-angles is an eigenfunction of the operator $\hat{R}_\alpha$. The Fourier states $|m_1, ..., m_N\rangle$ are a complete basis of such states, with corresponding eigenvalues given by $e^{i(m_1+m_2+...+m_N)\alpha}$. The Fourier states with distinct values for this eigenvalue therefore comprise independent subspaces. Each subspace is spanned by all the Fourier modes where the sum of the Fourier indices has a certain value,

$$m_1 + m_2 + ... + m_N = m, \tag{2.168}$$

and the integer values of the variable m label the subspaces. This equation effectively acts as a constraint on the N Fourier indices, so that the number of degrees of freedom required to describe one of the subspaces is reduced to $N-1$. We may define a projection operator $\hat{P}_m$ which acts to project a state onto the m-subspace,

$$\hat{P}_m = \sum_{\substack{m_1+m_2+...+m_N \\ = m}} |m_1, m_2, ..., m_N\rangle\langle -m_N, -m_{N-1}, ..., -m_1|, \tag{2.169}$$

and in general any state can be split up into its components in the different subspaces,

$$|f\rangle = \sum_{m=-\infty}^{\infty} |f^{(m)}\rangle, \tag{2.170}$$

where

$$|f^{(m)}\rangle = \hat{P}_m|f\rangle. \tag{2.171}$$

We shall consistently use the notation that a superscript in brackets indicates that a state lies entirely within the corresponding subspace.

We shall take advantage of this symmetry to reduce the size of the transfer matrix. There remains a large amount of choice in how we choose to parameterise the states in the m-subspace. The fact that the interactions in the Hamiltonian depend only on the differences in spin-angles suggests that the floating variables

$$\psi_j = \phi_j - \phi_{j+1}, \text{ for } j = 1, 2, ..., (N-1) \tag{2.172}$$

are a natural parameterisation, and we may regard the function $K(\phi_1, ...)$ as a function of these variables:

$$K(\phi_1, ..., \phi_N) \to K(\phi_1 - \phi_2, ..., \phi_{N-1} - \phi_N).$$

The Fourier state can be written as

$$e^{i(m_1\phi_1+...+m_N\phi_N)} = e^{im\phi_1} e^{i(n_1(\phi_1-\phi_2)+n_2(\phi_2-\phi_3)+...+n_{N-1}(\phi_{N-1}-\phi_N))}, \tag{2.173}$$

where the newly introduced indices are implicitly given by the equations,

$$\begin{aligned} m_1 &= m + n_1, \\ m_2 &= n_2 - n_1, \\ m_3 &= n_3 - n_2, \\ &\vdots \\ m_{N-1} &= n_{N-1} - n_{N-2}, \\ m_N &= -n_{N-1}. \end{aligned} \tag{2.174}$$

Within the m-subspace, these equations effectively relate the Fourier components of the function of N variables $f^{(m)}(\phi_1, ..., \phi_N)$ to the Fourier components of a function of the $N-1$ floating variables, $F^{(m)}(\psi_1, ..., \psi_{N-1})$, where

$$f^{(m)}(\phi_1, ..., \phi_N) = e^{im\phi_1} F^{(m)}(\phi_1 - \phi_2, \phi_2 - \phi_3, ..., \phi_{N-1} - \phi_N). \tag{2.175}$$

We shall throughout indicate the functions of the floating variables with the capital of the symbol used for the corresponding function of the original spin-angles. Expressed in this way, one is effectively making a change of variables from the N original spin-angles ϕ_j to a parameterisation in terms of the $N-1$ floating variables plus one of the original angles, in this case ϕ_1, which provides the axis with respect to which the other degrees of freedom are measured. For a function which may span the entire N-dimensional space, one has in general,

$$f(\phi_1, ..., \phi_N) = \sum_{m=-\infty}^{\infty} e^{im\phi_1} F^{(m)}(\phi_1 - \phi_2, ..., \phi_{N-1} - \phi_N), \tag{2.176}$$

and the functions of the floating variables are the resulting coefficients of writing the full function f as a Fourier series in ϕ_1.

We may completely describe a state in the m-subspace entirely using the function $F^{(m)}(\psi_1, ..., \psi_{N-1})$. To connect this description with the underlying vector-formalism, we introduce the states $|m; \psi_1, ..., \psi_{N-1}\rangle$, where

$$\langle \phi_N, ..., \phi_1 | m; \psi_1, ..., \psi_{N-1} \rangle = e^{im\phi_1} \prod_{j=1}^{N-1} 2\pi\delta(\psi_j - \phi_j + \phi_{j+1}). \tag{2.177}$$

From this definition, it follows that these states obey the orthogonality condition,

$$\langle m';\psi'_1,...,\psi'_{N-1}|m;\psi_1,...,\psi_{N-1}\rangle = e^{im(\psi_1+\psi_2+...+\psi_{N-1})}\delta_{m+m'}\prod_{j=1}^{N-1}2\pi\delta(\psi_j+\psi'_{N-j}), \tag{2.178}$$

and the completeness condition for these states takes the form,

$$\sum_{m=-\infty}^{\infty}\prod_{j=1}^{N-1}\int_{-\pi}^{\pi}\frac{d\psi_j}{2\pi}e^{-im(\psi_1+\psi_2+...+\psi_{N-1})}|m;\psi_1,...,\psi_{N-1}\rangle\langle -m;-\psi_{N-1},...,-\psi_1| = \hat{I}. \tag{2.179}$$

This basis relates to the description in terms of the floating angles according to,

$$F^{(m)}(\psi_1,...,\psi_{N-1}) = e^{-im(\psi_1+\psi_2+...+\psi_{N-1})}\langle -m;-\psi_{N-1},...,-\psi_1|f\rangle. \tag{2.180}$$

The matrix elements of the transfer operator in this basis are given by,

$$\langle -m;-\psi_N,...,-\psi_2|\hat{T}|m';\psi'_1,...,\psi'_{N-1}\rangle = e^{\beta K(\psi'_1,\psi_2,...,\psi_N)}e^{im(\psi'_1+\psi_2+...+\psi_{N-1}+\psi_N)}\delta_{m,m'}\prod_{j=2}^{N-1}2\pi\delta(\psi_j-\psi'_j). \tag{2.181}$$

There is no nonzero matrix element connecting distinct m-subspaces, as we expect. The transformation of the function $F^{(m)}(\psi_1,...)$ by the transfer operator is described by,

$$e^{-im(\psi_2+...+\psi_N)}\langle -m;-\psi_N,...,-\psi_2|\hat{T}|f\rangle = \int_{-\pi}^{\pi}\frac{d\psi_1}{2\pi}e^{im\psi_1}e^{\beta K(\psi_1,\psi_2,...,\psi_N)}F^{(m)}(\psi_1,...,\psi_{N-1}). \tag{2.182}$$

This provides an integral representation for the transfer operator in the m-subspace. This expression is extremely similar to the representation of the full transfer operator in the original spin-variables, equation 2.152, but with the addition of the Fourier factor $e^{im\psi_1}$. We introduce the notation that $\hat{T}_m$ denotes the part of the transfer operator which acts on this subspace,

$$\hat{T}_m = \hat{P}_m\hat{T}\hat{P}_m. \tag{2.183}$$

In practice, equation 2.182 is the starting point for our calculations, with the exception of the calculations of the magnetic susceptibility for which the rotational symmetry must be broken and one cannot employ the floating basis. One can apply the power method on each of the operators $\hat{T}_m$ to obtain its own eigenvalues and eigenvectors. It is found that the largest eigenvalue of the full transfer operator, the partition function, is always found in the $m = 0$ subspace. Consequently, the one-to-two

dimensional crossover theory for most quantities, apart from those relating to the response to a magnetic field and certain correlation functions, can be carried out by simply working with $\hat{T}_0$ in place of the full transfer operator $\hat{T}$. For the most part we have proceeded in this way. The calculations of the correlation functions require the inclusion of eigenvalues of other subspaces in addition to $m = 0$, and the calculations of quantities related to the magnetic susceptibility cannot be performed using the floating basis.

For representing the transfer operator on the computer, we work in Fourier space and parameterise the eigenfunction $F^{(m)}$ with the Fourier indices $n_1, ..., n_{N-1}$ in equation 2.173, and write,

$$F^{(m)}(\psi_1, ..., \psi_{N-1}) = \sum_{n_1=-\infty}^{\infty} ... \sum_{n_{N-1}=-\infty}^{\infty} F^{(m)}_{n_1,n_2,...,n_{N-1}} e^{i(n_1\psi_1+n_2\psi_2+...+n_{N-1}\psi_{N-1})}. \tag{2.184}$$

We use a variety of representations for the transfer function which follow from different choices of the function $K(\psi_1, \psi_2, ..., \psi_N)$. The simplest choice for which the transfer function is self-adjoint for any N is

$$K(\psi_1, \psi_2, ..., \psi_N) = \frac{1}{2}\cos\psi_1 + \cos(\psi_1 + \psi_2 + ... + \psi_{N-1} + \psi_N) + \frac{1}{2}\cos\psi_N \tag{2.185}$$

for which the explicit eigenvalue equation which we solve is,

$$\sum_{r=-\infty}^{\infty}\sum_{s=-\infty}^{\infty} I_{s+r+m}\left(\tfrac{\beta J}{2}\right) I_s(\beta J) I_{s+n_{N-1}}\left(\tfrac{\beta J}{2}\right) F^{(m)}_{r,n_1-s,...,n_{N-2}-s} = z^{(m)}_\alpha F^{(m)}_{n_1,n_2,...,n_{N-1}}. \tag{2.186}$$

The transfer matrix is truncated to be finite by truncating the Fourier indices in exactly the manner previously explained. The size of the eigenvector is then $(2M+1)^{N-1}$ where M is the highest Fourier mode included.

As an extremely important aside, we note that in taking the approach of representing the transfer matrix with the floating basis, and regarding the function $F^{(m)}$ as the object of primary importance, the inner product is in fact nontrivial expressed in this representation; one has the addition of a Fourier factor in the integral representation of the inner product,

$$\langle g^{(m')} | f^{(m)} \rangle = \delta_{m+m'} \prod_{j=1}^{N-1} \int_{-\pi}^{\pi} \frac{d\psi_j}{2\pi} G^{(-m)}(-\psi_{N-1}, -\psi_{N-2}, ..., -\psi_1) F^{(m)}(\psi_1, \psi_2, ..., \psi_{N-1}) \times e^{im(\psi_1+\psi_2+...+\psi_{N-1})}. \tag{2.187}$$

Finally, we note that there is a second, independent symmetry of the transfer operator, which

corresponds to changing the sign of all of the floating variables:

$$F^{(m)}(\psi_1, \psi_2, ..., \psi_{N-1}) \to F^{(m)}(-\psi_1, -\psi_2, ..., -\psi_{N-1}).$$

In terms of the spin-state described by the floating variables, this operation is a reversal of the chirality of the spins: the first spin ϕ_1 is not changed, but the spiralling of the following spins up to ϕ_N is inverted. All of the eigenfunctions of the reduced transfer operator $\hat{T}_m$ are either chiral-symmetric,

$$F^{(m)}(\psi_1, \psi_2, ..., \psi_{N-1}) = F^{(m)}(-\psi_1, -\psi_2, ..., -\psi_{N-1}),$$

or chiral-antisymmetric,

$$F^{(m)}(\psi_1, \psi_2, ..., \psi_{N-1}) = -F^{(m)}(-\psi_1, -\psi_2, ..., -\psi_{N-1}).$$

It is found that the eigenfunction belonging to the largest eigenvector in each of the m-subspaces is always symmetric.

2.4.4 Thermal derivatives of the entropy

We now come to the first set of calculations which we have to discuss. These quantities are the derivatives of the entropy S of the system with respect to the logarithm of temperature,

$$\left(T\frac{\partial}{\partial T}\right)^n S,$$

the first of these derivatives being the specific heat C. To obtain these quantities, we have calculated the largest eigenvalue and corresponding eigenvector of the operator $\hat{T}_0$ using the power method, and from these determined the internal energy according to the formula 2.128. The specific heat and higher temperature derivatives of the entropy up to the third order have been calculated by numerically differentiating the internal energy using the difference formulae 2.133.

The calculations of the specific heat of the J_1-J_N planar rotator model are depicted in figure 2.21. The specific heat exhibits a clear peak, which becomes more pronounced as the scaling parameter N is increased. This is quantitatively very much like the specific heat of the J_1-J_N Ising model shown in figure 2.7. By comparison with the Ising case, this data alone would appear to be suggestive of a

second order phase transition in the two-dimensional limit, where the position of the peak marks the transition temperature.

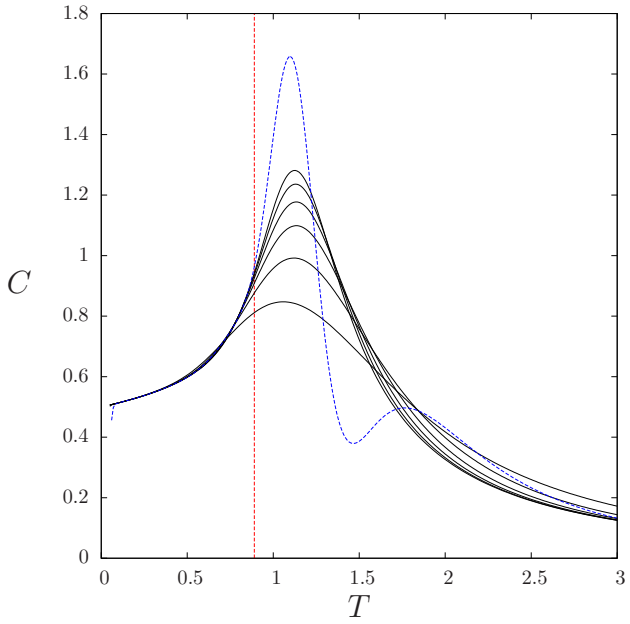

Figure 2.21: The specific heat of the J_1-J_N planar rotator model for N = 2-7 (solid lines), with a polynomial extrapolation to the case of $N = \infty$ (blue dotted line). The vertical dotted line indicates the estimated Kosterlitz-Thouless transition temperature, $T = 0.89$.

If a second order phase transition did occur in the square lattice planar rotator model, the peak in the specific heat would be expected to grow as N is increased and ultimately become a divergence in the limit $N \to \infty$. In the Kosterlitz-Thouless transition the specific heat exhibits a large finite peak at some temperature higher than the transition temperature(19). Since we have only calculated the specific heat for finite values of the scaling parameter N, we cannot definitively conclude that the peak in the specific heat does not converge to be finite in the two-dimensional limit. However, the calculations for the J_1-J_N planar rotator model indicate that such a convergence does not occur up to the value $N = 7$. In addition, the calculations presented in the thesis of A. M. Cave with clock models show that this peak does not converge up to the value $N = 12$(29).

A better indication of whether the specific heat is converging to have a finite peak can be obtained from the higher derivatives of the entropy with respect to the logarithm of temperature. The second, third and fourth derivatives are depicted in figures 2.22, 2.23 and 2.24. In the vicinity of the peak in the specific heat, the derivatives of the specific heat take large values, are seen to increase as the scaling

parameter N is increased, and the rate of this increase is greater in the higher derivatives. It is clear from these calculations that none of these derivatives are converging up to the value $N = 7$. In addition, A. M. Cave has shown that the same quantities are not converging up to the value $N = 12(29)$. Given that each successive derivative appears to be diverging at a faster rate, this is suggestive that one of the derivatives, or a higher derivative which we have not calculated, will be divergent in the two-dimensional limit. The calculations therefore suggest that, even if the specific heat does converge to exhibit a finite peak, one of the higher derivatives of the entropy is still likely to exhibit a divergence, corresponding to a higher order regular phase transition. It is important to note that a divergence in any derivative of the entropy is in complete contradiction with the picture of the Kosterlitz-Thouless transition, which predicts that there should be no divergences in any thermodynamic quantity.

We conclude our discussion of these quantities by briefly touching upon the value of the critical temperature of the phase transition. In the interpretation that the peak in the specific heat becomes a divergence in the two-dimensional limit, then the position of the divergence in this limit marks the transition temperature, and the position of the peak in the specific heat in our calculations must converge to sit at the transition temperature as the peak diverges. The estimated transition temperature of the Kosterlitz-Thouless transition, $T_{KT} = 0.89J$, is marked in figure 2.21, and is always fairly well-separated from the position of the peak. This is consistent with the picture that the specific heat converges to a finite peak where the peak is at a higher temperature than the Kosterlitz-Thouless transition, but conversely, assuming a second order phase transition, the calculations strongly suggest that the transition temperature does not agree with the estimated value of T_{KT}.

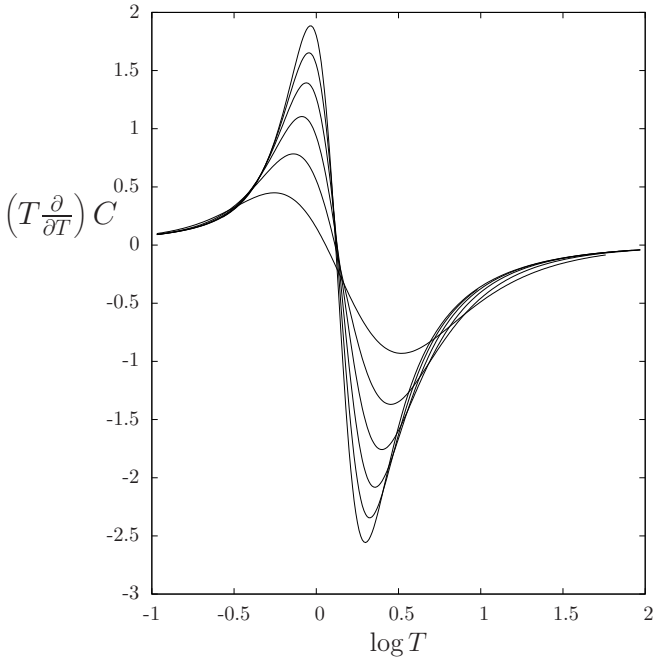

Figure 2.22: First derivative of specific heat with respect to $\ln T$ for $N = 2$-7.

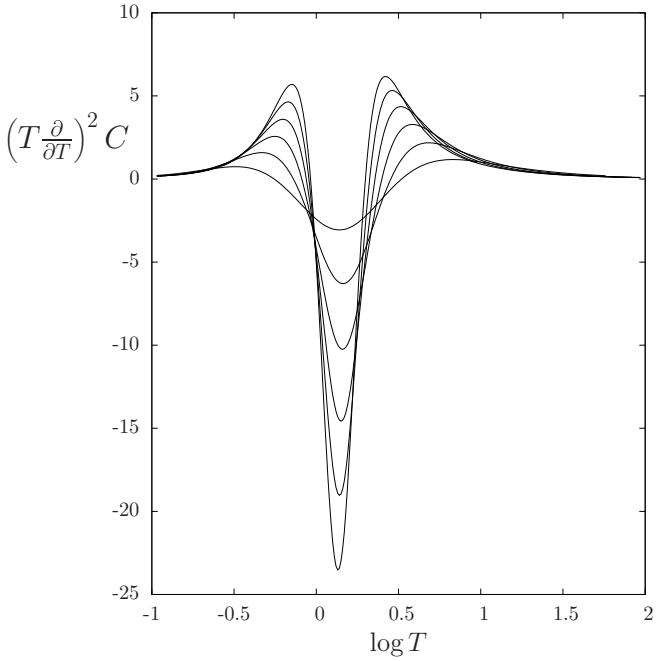

Figure 2.23: Second derivative of specific heat with respect to $\ln T$ for $N = 2$-7.

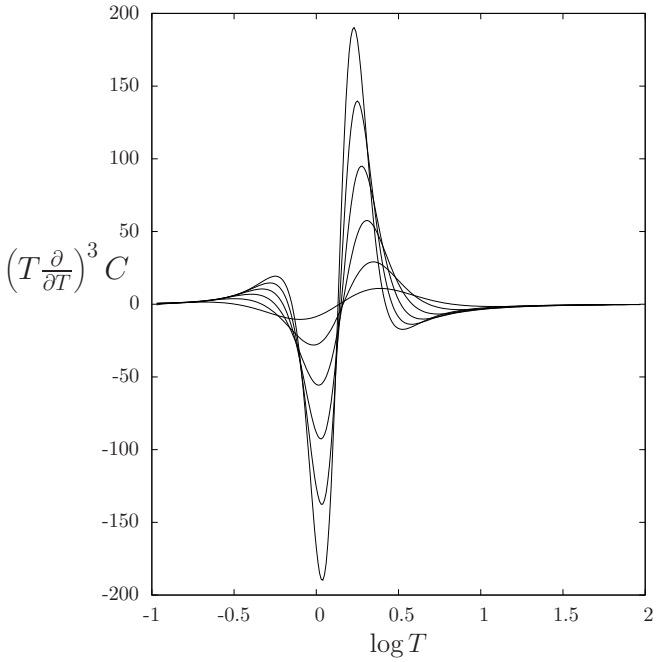

Figure 2.24: Third derivative of specific heat with respect to $\ln T$ for $N = 2$-7.

2.4.5 Correlation lengths and eigenvalues

We now come to the second set of quantities to be discussed, which relates to the correlation length ξ, which is defined as the length characterising the long-range decay of the spin-spin correlation function. For the square lattice planar rotator model, in the disordered phase we would write

$$\langle \cos(\phi_j - \phi_{j'}) \rangle \sim e^{-r_{jj'}/\xi},$$

where $r_{jj'}$ is the distance between the lattice sites j and j', and where this expression is understood to apply in the case that this distance is very large. We consider the correlation $\langle e^{iq(\phi_1 - \phi_{1+r})} \rangle$ as a function of r, where q is an integer. This essentially corresponds to the correlation above in the case $q = 1$. Each of these correlation functions decays exponentially at long range, and therefore has an associated correlation length, which we denote ξ_q. This quantity is given by the simple formula,

$$\frac{1}{\xi_q} = \ln|z_0| - \ln|z_0^{(q)}|, \tag{2.188}$$

where z_0 is the largest eigenvalue of the transfer operator, which as detailed above is essentially the partition function, and $z_0^{(q)}$ is the largest eigenvalue in the $m = q$ subspace. The correlation length is therefore directly related to the separation of these eigenvalues. As discussed in section 2.188, the eigenvalues are not degenerate for finite N, but their separation decreases as N is increased. We expect to see degeneracy occur in the two-dimensional limit $N \to \infty$, corresponding to the phase transition in the square lattice model.

Concerning this limit, there is a subtlety in relating the correlation length which we calculate to the relevant one for the square lattice model. For the finite N system, in calculating the correlation $\langle e^{iq(\phi_1 - \phi_{1+r})} \rangle$ and taking the range r to be very large, we are considering the correlation between lattice sites which are separated a large distance along the axial direction of the helix depicted in figure 2.6. In the limit $N \to \infty$, this must correspond to the correlation between lattice sites separated along one of the principal axes of the square lattice, the separation being the number of intermittent lattice sites along that direction. In our correlation functions for the finite system the distance between nearest neighbour lattice sites in this direction is measured as N, and consequently the range r is N times larger than the physical distance between the two lattice points. One must therefore divide the correlation length of the finite-N system by N to obtain the quantity which corresponds to the square lattice correlation length.

We now present a formal derivation of equation 2.188. We shall throughout take the eigenvectors of the transfer operator to be normalised, $\langle f_\alpha^{(m)} | f_\alpha^{(m)} \rangle = 1$. From equation 2.149, this can be represented as

$$\langle e^{iq(\phi_1 - \phi_{1+r})} \rangle = \left(\frac{1}{z_0} \right)^{r+1-N} \langle f_0^{(0)} | (\hat{V}_q)^{r+1-N} | f_0^{(0)} \rangle, \tag{2.189}$$

where $|f_0^{(0)}\rangle$ is the eigenvector belonging to the largest eigenvector in the $m = 0$ subspace, which is the largest of all the eigenvalues of the transfer operator z_0, and where the modified transfer operator $\hat{V}_q$ is defined by

$$\begin{aligned} &\left((\hat{V}_q)^{r+1-N} f \right) (\phi_{r+2-N}, ..., \phi_{r+1}) \\ &\qquad = \prod_{j=1}^{r+1-N} \int_{-\pi}^{\pi} \frac{d\phi_j}{2\pi} e^{iq(\phi_1 - \phi_{1+r})} \prod_{l=1}^{r+1-N} e^{\beta K(\phi_l - \phi_{l+1}, ..., \phi_{l+N-1} - \phi_{l+N})} f(\phi_1, ..., \phi_N). \end{aligned} \tag{2.190}$$

From this definition it follows that the matrix elements of this operator in the basis of the spin-variables

are

$$\langle \phi_{r+1}, ..., \phi_{r+2-N} | (\hat{V}_q)^{r+1-N} | \phi_1, ..., \phi_N \rangle$$
$$= \prod_{j=1}^{r+1-N} \int_{-\pi}^{\pi} \frac{d\phi_j}{2\pi} e^{iq(\phi_1 - \phi_{1+r})} \prod_{j=N+1}^{r+1-N} \int_{-\pi}^{\pi} \frac{d\phi_j}{2\pi} \prod_{l=1}^{r+1-N} e^{\beta K(\phi_l - \phi_{l+1}, ..., \phi_{l+N-1} - \phi_{l+N})}. \tag{2.191}$$

This is the same expression as for the matrix elements of $(\hat{T})^{r+1-N}$, with the modification of the extra factor of $e^{iq(\phi_1 - \phi_{1+r})}$. The effect of this factor in the matrix element is to move from the m-subspace to the $(m+q)$-subspace. This is most cleanly demonstrated in formal terms by considering the matrix elements in the Fourier basis:

$$\begin{aligned}
&\langle -m_N, ..., -m_1 | (\hat{V}_q)^{r+1-N} | m'_1, ..., m'_N \rangle \\
&\quad = \prod_{j=1}^{N} \int_{-\pi}^{\pi} \frac{d\phi_j}{2\pi} \prod_{j'=r+2-N}^{r+1} \int_{-\pi}^{\pi} \frac{d\phi_{j'}}{2\pi} \langle \phi_{r+1}, ..., \phi_{r+2-N} | (\hat{V}_q)^{r+1-N} | \phi_1, ..., \phi_N \rangle \\
&\qquad\qquad \times \langle -m_N, ..., -m_1 | \phi_{r+2-N}, ..., \phi_{r+1} \rangle \langle \phi_1, ..., \phi_N | m'_1, ..., m'_N \rangle \\
&\quad = \prod_{j=1}^{N} \int_{-\pi}^{\pi} \frac{d\phi_j}{2\pi} \prod_{j'=r+2-N}^{r+1} \int_{-\pi}^{\pi} \frac{d\phi_{j'}}{2\pi} \langle \phi_{r+1}, ..., \phi_{r+2-N} | (\hat{V}_q)^{r+1-N} | \phi_1, ..., \phi_N \rangle \\
&\qquad\qquad \times e^{-i(m_1 \phi_{r+2-N} + ... + m_N \phi_{r+1})} e^{i(m'_1 \phi_1 + ... + m'_N \phi_N)}.
\end{aligned} \tag{2.192}$$

The factor $e^{iq(\phi_1 - \phi_{1+r})}$ in the matrix element of $(\hat{V}_q)^{r+1-N}$ may be absorbed into the other Fourier factors to obtain,

$$\begin{aligned}
&\langle -m_N, ..., -m_1 | (\hat{V}_q)^{r+1-N} | m'_1, ..., m'_N \rangle \\
&\quad = \prod_{j=1}^{N} \int_{-\pi}^{\pi} \frac{d\phi_j}{2\pi} \prod_{j'=r+2-N}^{r+1} \int_{-\pi}^{\pi} \frac{d\phi'_j}{2\pi} \langle \phi_{r+1}, ..., \phi_{r+2-N} | (\hat{T})^{r+1-N} | \phi_1, ..., \phi_N \rangle \\
&\qquad\qquad \times e^{-i(m_1 \phi_{r+2-N} + ... + (m_N + q)\phi_{r+1})} e^{i((m'_1 + q)\phi_1 + ... + m'_N \phi_N)} \\
&\quad = \prod_{j=1}^{N} \int_{-\pi}^{\pi} \frac{d\phi_j}{2\pi} \prod_{j'=r+2-N}^{r+1} \int_{-\pi}^{\pi} \frac{d\phi'_j}{2\pi} \langle \phi_{r+1}, ..., \phi_{r+2-N} | (\hat{T})^{r+1-N} | \phi_1, ..., \phi_N \rangle \\
&\qquad\qquad \times \langle -(m_N + q), -m_{N-1}, ..., -m_1 | \phi_{r+2-N}, ..., \phi_{r+1} \rangle \\
&\qquad\qquad \times \langle \phi_1, ..., \phi_N | (m'_1 + q), m'_2, ..., m'_N \rangle \\
&\quad = \langle -(m_N + q), -m_{N-1}, ..., -m_1 | (\hat{T})^{r+1-N} | (m'_1 + q), m'_2, ..., m'_N \rangle.
\end{aligned} \tag{2.193}$$

Now, this matrix element is only finite between states in the same subspace, for which the index must be $(m+q)$ if m is equal to the sum of the indices $m_1, ..., m_N$. In this case the matrix element can be expanded in terms of the eigenvalues of the transfer operator in this subspace, $|f_\alpha^{(m+q)}\rangle$, to obtain,

$$\begin{aligned}
&\langle -(m_N+q), -m_{N-1}, ..., -m_1|(\hat{T})^{r+1-N}|(m_1'+q), m_2', ..., m_N'\rangle \\
&\qquad = \sum_\alpha \sum_{\alpha'} \langle -(m_N+q), ..., -m_1|f_\alpha^{(q)}\rangle\langle f_\alpha^{(m+q)}|(\hat{T})^{r+1-N}|f_{\alpha'}^{(m+q)}\rangle\langle f_{\alpha'}^{(q)}|(m_1'+q), ..., m_N'\rangle \\
&\qquad\qquad \times \delta_{m_1+...+m_N=m_1'+...+m_N'=m} \\
&\qquad = \sum_\alpha \left(z_\alpha^{(m+q)}\right)^{r+1-N} \langle -(m_N+q), ..., -m_1|f_\alpha^{(m+q)}\rangle\langle f_\alpha^{(m+q)}|(m_1'+q), ..., m_N'\rangle \\
&\qquad\qquad \times \delta_{m_1+...+m_N=m_1'+...+m_N'=m}. \qquad (2.194)
\end{aligned}$$

Therefore expanding the quantity $\langle f_0^{(0)}|(\hat{V}_q)^{r+1-N}|f_0^{(0)}\rangle$ in the Fourier basis provides,

$$\begin{aligned}
\langle f_0^{(0)}|(\hat{V}_q)^{r+1-N}|f_0^{(0)}\rangle &= \sum_{\substack{m_1+...+m_N \\ =0}} \sum_{\substack{m_1'+...+m_N' \\ =0}} \langle f_0^{(0)}|m_1, ..., m_N\rangle\langle -m_N', ..., -m_1'|f_0^{(0)}\rangle \\
&\qquad \times \langle -(m_N+q), -m_{N-1}, ..., -m_1|(\hat{T})^{r+1-N}|(m_1'+q), m_2', ..., m_N'\rangle \\
&= \sum_\alpha \left(z_\alpha^{(q)}\right)^{r+1-N} \sum_{\substack{m_1+...+m_N \\ =0}} \langle f_0^{(0)}|m_1, ..., m_N\rangle\langle -(m_N+q), ..., -m_1|f_\alpha^{(q)}\rangle \\
&\qquad \times \sum_{\substack{m_1'+...+m_N' \\ =0}} \langle -m_N', ..., -m_1'|f_0^{(0)}\rangle\langle f_\alpha^{(q)}|(m_1'+q), ..., m_N'\rangle. \qquad (2.195)
\end{aligned}$$

If we now consider the long-range limit $r \to \infty$, we may simplify this expression using the same argument as we have employed previously, that the sum over the eigenstates is exponentially dominated by the largest eigenvalue, which we indicate with the label α having the value zero. We therefore find in this limit,

$$\begin{aligned}
\langle e^{iq(\phi_1-\phi_{1+r})}\rangle \sim \left(\frac{z_0^{(q)}}{z_0}\right)^{r+1-N} &\sum_{\substack{m_1+...+m_N \\ =0}} \langle f_0^{(0)}|m_1, ..., m_N\rangle\langle -(m_N+q), ..., -m_1|f_0^{(q)}\rangle \\
&\times \sum_{\substack{m_1'+...+m_N' \\ =0}} \langle -m_N', ..., -m_1'|f_0^{(0)}\rangle\langle f_0^{(q)}|(m_1'+q), ..., m_N'\rangle. \qquad (2.196)
\end{aligned}$$

This expression is made up of an exponential decay with an associated decay length given by equation 2.188, together with multiplicative factors which do not depend upon the range.

In the finite N system, the eigenvalues z_0 and $z_0^{(q)}$ are always non-degenerate, but they may become degenerate in the two-dimensional limit $N \to \infty$. As indicated in section 2.3, this emerging degeneracy is associated with a critical point in the square lattice model. It is known that below the phase transition in the square lattice planar rotator model the long-range correlations have a power law form, corresponding to an infinite correlation length. In terms of the eigenvalues, this indicates that the eigenvalues z_0 and $z_0^{(q)}$ become degenerate at the phase transition and remain degenerate at all temperatures below the phase transition.

The reciprocal of the correlation lengths have been calculated using the formula 2.188, the eigenvector $z_0^{(q)}$ being obtained by applying the power method to $\hat{T}_q$. The calculations of the reciprocal of the regular correlation length (the case $q = 1$) are shown in figure 2.25, together with a polynomial extrapolation to the case of $N = \infty$. The extrapolated correlation length exhibits the features that we would expect for the two-dimensional system, where the correlation length is infinite below the phase transition. The extrapolation predicts the value zero for the reciprocal correlation length to several decimal places for the reciprocal of the correlation length for a large low temperature region, apparently down to zero-temperature. It is rather striking that the extrapolation so strongly predicts the value zero at temperatures where the values of $1/\xi$ for the finite systems are relatively large and have clearly not converged to any limit. This agreement with the behaviour which is known for the two-dimensional system provides strong evidence that the limit $N \to \infty$ does indeed provide the square lattice model.

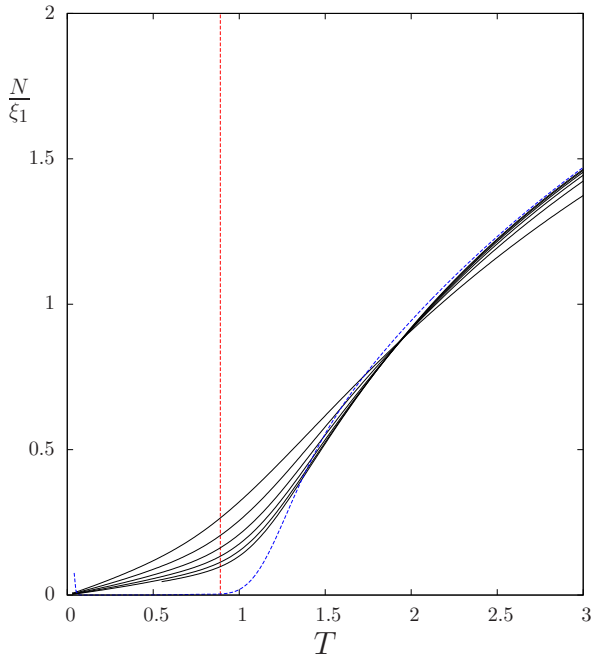

Figure 2.25: The inverse correlation length of the J_1-J_N planar rotator model for $N = 2$-7 (solid lines), with a polynomial extrapolation to the case of $N = \infty$(blue dotted line). The $N = 7$ calculation has not been completed at low temperature; the extrapolation is obtained from just the $N = 2$ to $N = 6$ curves. The upturn in the extrapolation close to the origin can be attributed to the reduced accuracy of the calculations close to $T = 0$. The vertical dotted line indicates the estimated Kosterlitz-Thouless transition temperature, $T = 0.89$.

The predicted critical temperature of the Kosterlitz-Thouless transition is also indicated in figure 2.25. In the Kosterlitz-Thouless picture, the reciprocal of the correlation length would be expected to vanish at this temperature. A stronger prediction than the place at which the quantity should vanish is the form of the function close to this point, which is predicted to be,

$$\frac{1}{\xi} \sim e^{-a/\sqrt{T-T_{KT}}},$$

which is smooth and infinitely differentiable. The extrapolated correlation length is in good agreement with the Kosterlitz-Thouless picture. However, the polynomial extrapolation of a series of smooth functions will always itself be a smooth function, and for this reason this quantity cannot by itself be used to exclude the possibility of the non-analytic power law behaviour which would accompany a regular phase transition,

$$\frac{1}{\xi} \sim (T - T_C)^{\nu}.$$

We have investigated the functional form of the correlation length by calculating the thermal derivatives of $1/\xi$. These derivatives have been calculated numerically from the values of the correlation length, which have been calculated to machine accuracy, in exactly the same way that the derivatives of the entropy are obtained by numerically differentiating the internal energy as previously discussed. The first derivative of $1/\xi$ is shown in figure 2.26 and the second derivative is shown in figure 2.27. If one has the power law behaviour, each successive derivative of $1/\xi$ in the vicinity of the transition will also have a power law behaviour, where the exponent is reduced by one. After a certain number of differentiations, the resulting quantity will be divergent at the transition temperature, when the exponent becomes negative. If one finds that one of the derivatives of $1/\xi$ appears to be divergent, this indicates that the critical behaviour of the correlation length is a power law. In addition the number of derivatives required to produce this divergence provides a range, from this number to the next smallest integer, within which the critical exponent ν must lie.

The first derivative of the inverse correlation length shows an abrupt, step-like feature in the vicinity of the transition temperature. The features are qualitatively similar to the calculation for the Ising model discussed in the previous section (figure 2.12), for which in the two-dimensional limit the form is known to be a theta-function in the vicinity of the phase transition. The second derivative exhibits a sharp peak, which grows as the scaling parameter N is increased. It certainly appears that this quantity is diverging. Again, the features are qualitatively similar to the Ising model calculation (figure 2.13), which is known to be a delta-function singularity in the two-dimensional limit. A divergence in this quantity for the planar rotator model, or any higher temperature derivative of $1/\xi$, is in complete contradiction with the Kosterlitz-Thouless picture. These calculations indicate that the temperature dependence of the correlation length is of the power-law type close to the transition, with a critical exponent ν which lies somewhere between the values 1 and 2.

If the second derivative of $1/\xi$ is indeed divergent in the two-dimensional limit, the position of the divergence marks the critical temperature of the phase transition. The estimated Kosterlitz-Thouless transition temperature is indicated in figure 2.27. The peak in the second derivative of $1/\xi$ appears to be converging to a position which is well-separated from the estimated value of T_{KT}, suggesting a different critical temperature. The position of the peak for $N = 7$ is in close proximity to the position of the peak in the specific heat (figure 2.21). The calculations of the specific heat and the correlation length are both suggestive of a regular phase transition, and suggest a consistent approximate value for the transition temperature, which is not the same as the estimated critical temperature of the

Kosterlitz-Thouless transition temperature.

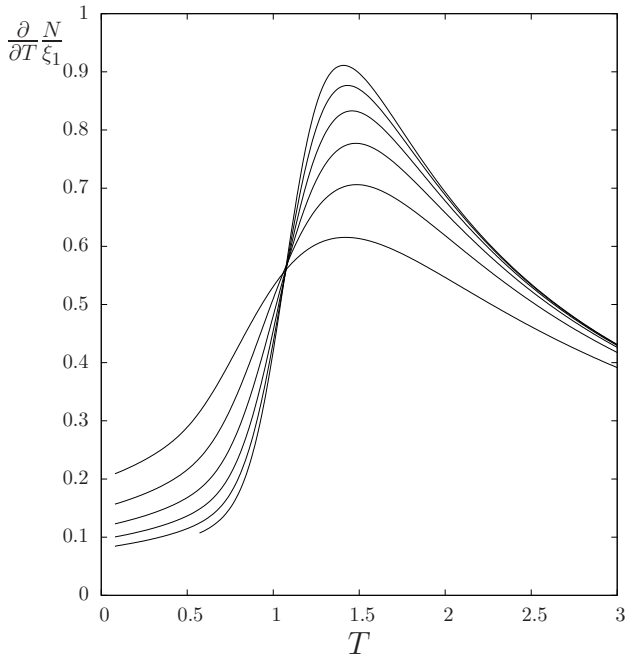

Figure 2.26: First derivative of the reciprocal correlation length with respect to T for $N = 2$-7.

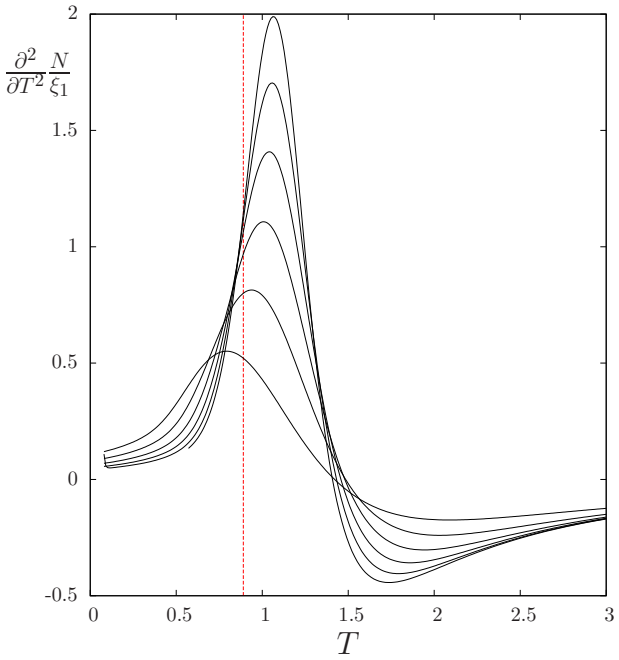

Figure 2.27: Second derivative of the reciprocal correlation length with respect to T for $N = 2$-7.

We have also calculated the correlation lengths associated with the correlation functions for $q = 2$ and $q = 3$ in equation 2.188. These calculations are exhibited in figures 2.28 and 2.29, together with polynomial extrapolations to the case $N = \infty$. The temperature dependence is qualitatively similar to that of the regular correlation length, but the scale is altered as the correlation functions with higher q decay more rapidly. In terms of the eigenvalues, this corresponds to the largest eigenvalue $|z_0^{(q)}|$ in each subspace decreasing with increasing q. In the square lattice model, the reciprocal of each of the correlation lengths must be equal to zero in the power-law correlated phase. For both the $q = 2$ and $q = 3$ cases the polynomial extrapolation predicts this behvaviour. It appears that all of the eigenvalues $z_0^{(q)}$ become degenerate below the phase transition in the two-dimensional limit $N \to \infty$.

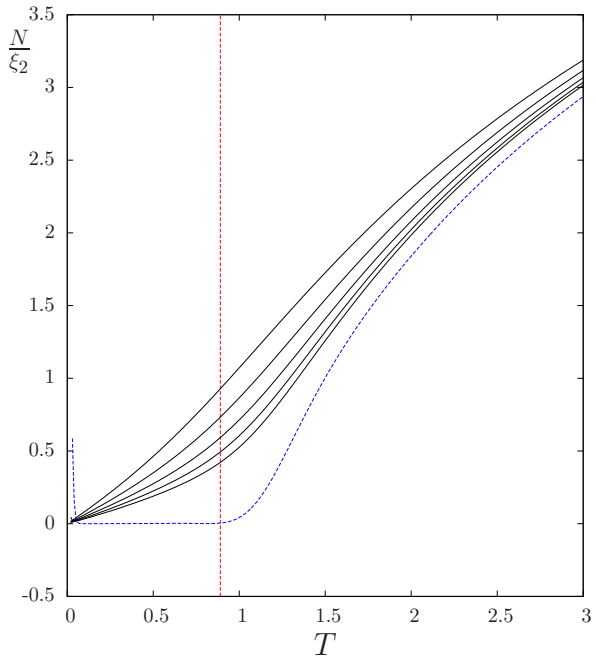

Figure 2.28: Reciprocal correlation length corresponding to $q = 2$ for N = 2-6 (solid lines) together with an extrapolation to $N = \infty$. The upturn in the extrapolation close to the origin can be attributed to the reduced accuracy of the calculations close to $T = 0$.

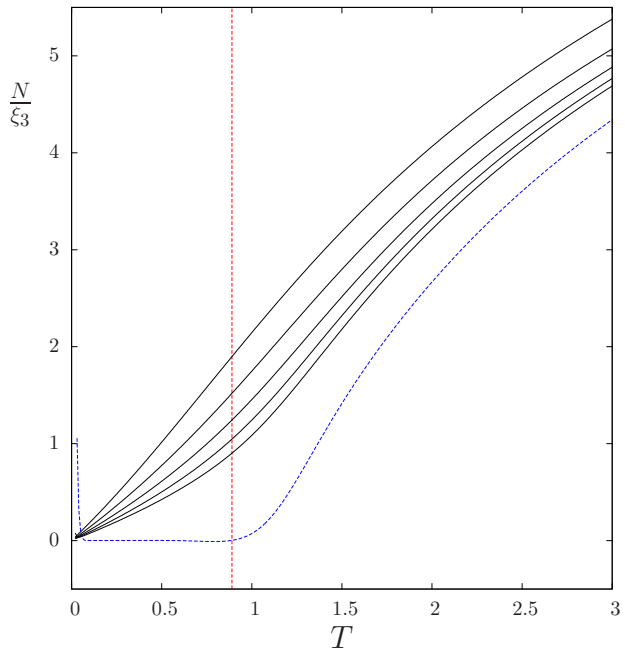

Figure 2.29: Reciprocal correlation length corresponding to $q = 3$ for N = 2-6 (solid lines) together with an extrapolation to $N = \infty$. The upturn in the extrapolation close to the origin can be attributed to the reduced accuracy of the calculations close to $T = 0$.

In the scaling hypothesis, it is assumed that close to the phase transition there is only a single length scale, the correlation length $\xi(4)$. We therefore expect that in the square lattice model all of the correlation lengths ξ_q have the same critical behaviour. The derivatives of $1/\xi_2$ and $1/\xi_3$ with respect to temperature are exhibited in figures 2.30 to 2.33. The temperature dependence is qualitatively similar to that found in the derivatives of the ordinary correlaton length; although any emergence of a sharp step in the first derivative is certainly far less apparent, particularly in the $q = 3$ case, the second derivative shows a pronouced peak in both the $q = 2$ and $q = 3$ cases. The data is indicative that the correlation lengths for higher q have a power law form close to the phase transition; the $q = 2$ and $q = 3$ cases appear to have critical exponents which are either the same as or close to the value of the exponent for the ordinary correlation length indicated by the calculations in figures 2.25 to 2.27, in agreement with the scaling hypothesis.

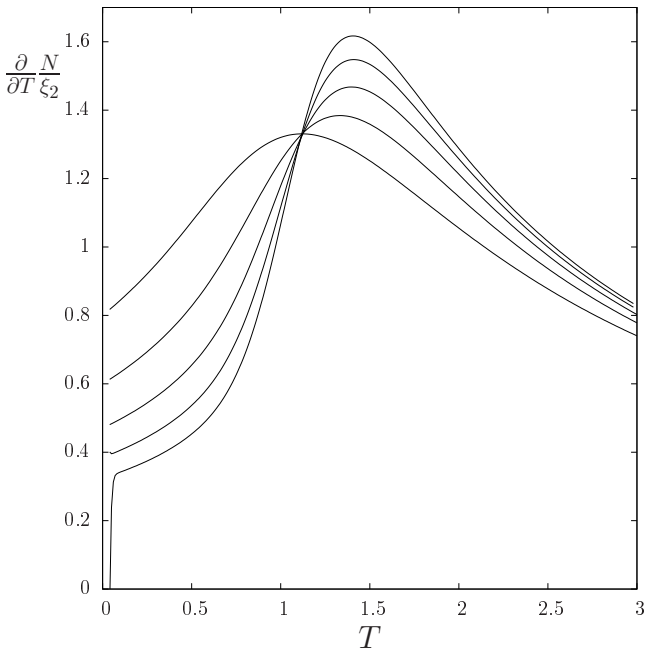

Figure 2.30: First derivative of the $q = 2$ reciprocal correlation length with respect to T for $N = 2$-6.

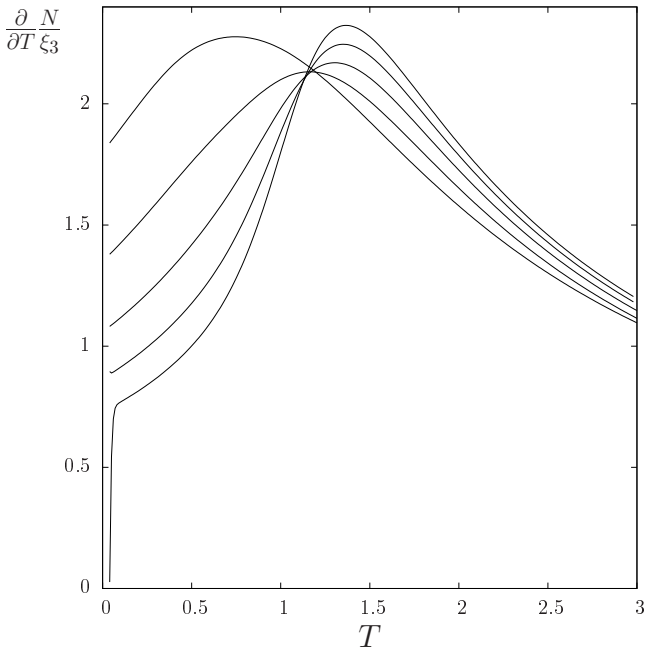

Figure 2.31: First derivative of the $q = 3$ reciprocal correlation length with respect to T for $N = 2$-6.

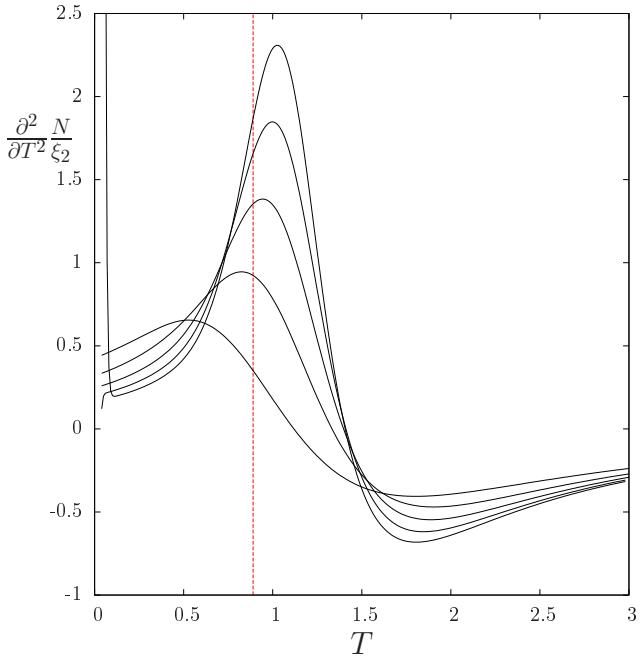

Figure 2.32: Second derivative of the $q = 2$ reciprocal correlation length with respect to T for $N = 2$-6.

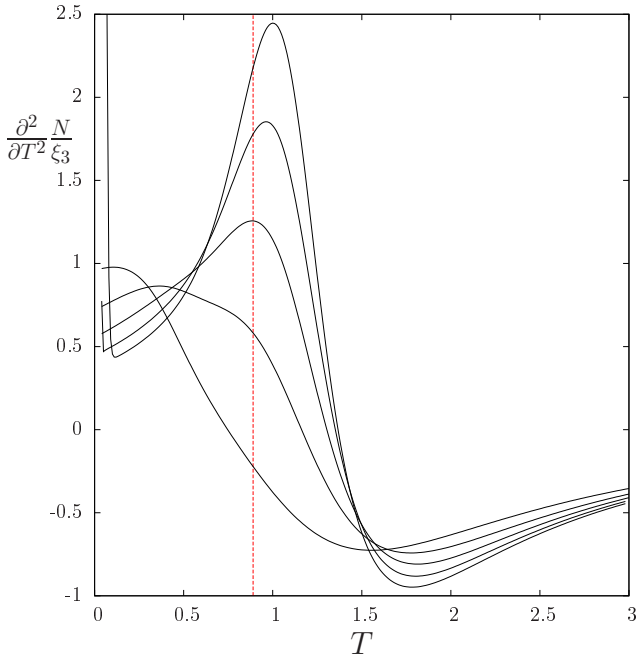

Figure 2.33: Second derivative of the $q = 3$ reciprocal correlation length with respect to T for $N = 2$-6.

Of course, one can associate an analogue of the correlation lengths ξ_q with any eigenvalue of the

transfer operator. We have calculated this quantity for the two next largest-modulus eigenvalues in the $m = 0$ subspace; these calculations are exhibited in figure 2.34. Of these two eigenvalues, one is symmetric and the other antisymmetric with respect to reversing the chirality of the spins, and in the finite N system these eigenvalues cross each other at an N-dependent temperature.

We have calculated polynomial extrapolations to the case $N = \infty$ of the correlation length for the chiral-symmetric and chiral-antisymmetric eigenvalues independently; the results of the extrapolations are shown in 2.35. The extrapolations suggest that both of these correlation lengths are zero in the low temperature region below the phase transition, and therefore that the eigenvalues $|z_1^{(0)}|$ and $|z_2^{(0)}|$ become degenerate with z_0 in this phase.

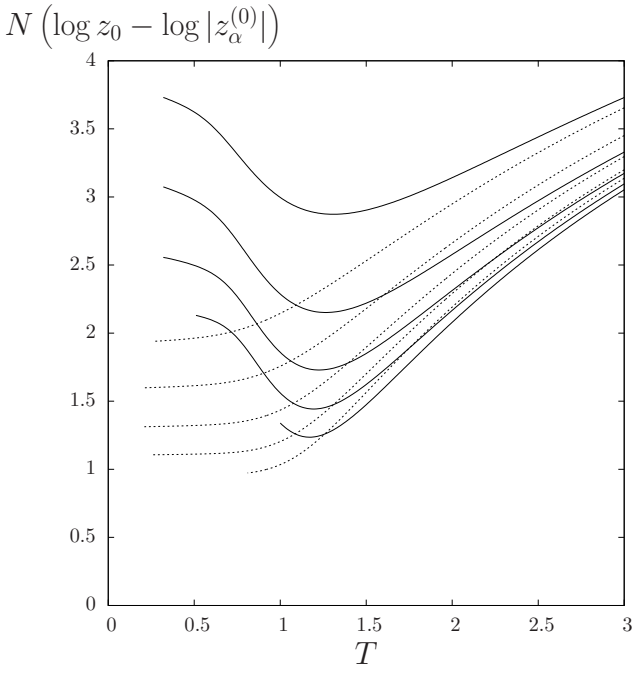

Figure 2.34: The correlation length corresponding to the second and third largest-modulus eigenvalues in the $m = 0$ subspace, for N = 2-6. Of these two eigenvalues, one is chiral-symmetric (solid lines) and the other is chiral-antisymmetric (dotted lines).

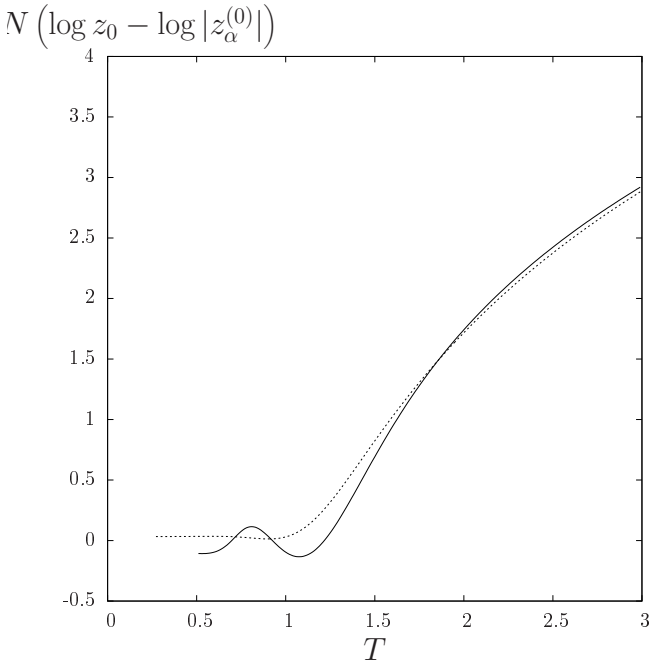

Figure 2.35: The polynomial extrapolations of the correlation length corresponding to the chiral-symmetric eigenvalue (solid line) and the chiral-antisymmetric eigenvalue (dotted line) obtained from the $N = 2$ to $n = 5$ calculations.

2.4.6 Magnetic susceptibility

We now come to the calculations of the magnetic susceptibility, χ. To obtain this quantity we must consider the situation where a magnetic field is applied to the system. We therefore consider the Hamiltonian,

$$H = -J \sum_j \left[\cos\left(\phi_j - \phi_{j+1}\right) + \cos\left(\phi_j - \phi_{j+N}\right)\right] - B \sum_j \cos\phi_j. \tag{2.197}$$

The addition of the magnetic field term to the Hamiltonian breaks the rotation symmetry of the model, and consequently we can no longer extract this symmetry and represent the transfer operator in the floating basis. This has the effect that the transfer matrix is significantly larger for the calculations of the magnetisation than in other calculations. Because the use of the floating basis effectively reduces the number of spin-parameters by one, the size of the matrix in the calculation for the finite-field system of size N is essentially the same as that for the zero-field system of size $N + 1$. This alone effectively restricts us to performing calculations to systems which are one smaller than for the previously discussed calculations, which in practice means that we have only performed calculations of the magnetic susceptibility up to the value $N = 6$. In addition, it is found that the power method requires

a large number of iterations to converge for the small values of the magnetic field which are necessary in order to calculate the susceptibility accurately; this is an indpendent source of computational expense in comparison to the previous calculations, which has in practice limited us to calculations of the magnetic susceptibility for up to $N = 5$, and even these calculations have not been completed at low temperatures.

We use the power method to obtain the largest eigenvalue and corresponding eigenvector for particular values of the temperature and magnetic field, and these provide the magnetisation to machine accuracy via the formula,

$$M = \frac{1}{\beta z_0} \frac{\langle f_0 | \frac{\partial}{\partial B} \hat{T} | f_0 \rangle}{\langle f_0 | f_0 \rangle}. \tag{2.198}$$

The magnetic susceptibility is calculated as the derivative of the magnetisation with respect to the applied field,

$$\chi = \frac{\partial M}{\partial B},$$

evaluated at zero-field. We calculate this derivative using similar difference formulae to those which we have used to calculate the derivatives of the entropy or the derivatives of the inverse correlation length. We calculate the magnetisation at the three values of the applied field $B = h$, $B = 2h$ and $B = 3h$, where h is a small number. The taylor expansion of the magnetisation about $B = 0$ provides,

$$\begin{pmatrix} M(h) \\ M(2h) \\ M(3h) \end{pmatrix} = \begin{pmatrix} h & \frac{1}{2}h^2 & \frac{1}{6}h^3 \\ 2h & 2h^2 & \frac{4}{3}h^3 \\ 3h & \frac{9}{2}h^2 & \frac{9}{2}h^3 \end{pmatrix} \begin{pmatrix} \chi \\ \frac{\partial \chi}{\partial B} \\ \frac{\partial^2 \chi}{\partial B^2} \end{pmatrix} + O(h^4),$$

from which we can deduce the approximate formula for the susceptibility,

$$\chi \approx \frac{1}{h} \left(3M(h) - \frac{3}{2} M(2h) + \frac{1}{3} M(3h) \right). \tag{2.199}$$

The calculation of the reciprocal of the magnetic susceptibility is shown in figure 2.36, together with the polynomial extrapolation to the limit of $N = \infty$.

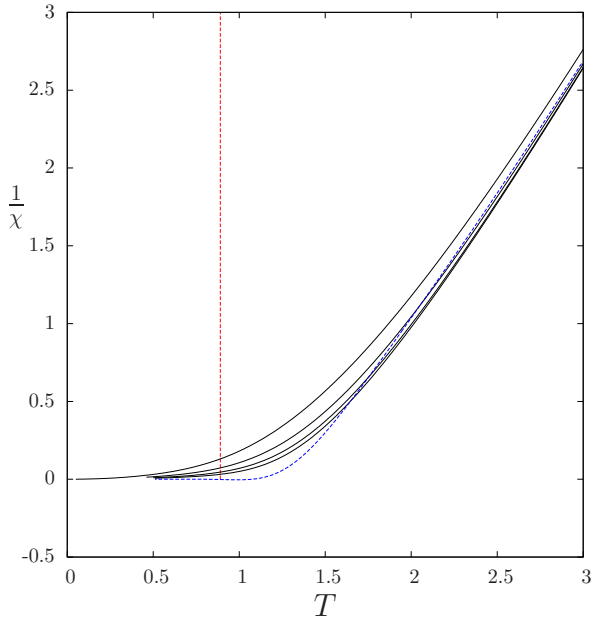

Figure 2.36: The inverse magnetic susceptibility of the J_1-J_N planar rotator model for $N = 2$-5 (solid lines), with a polynomial extrapolation to the case of $N = \infty$(blue dotted line). The vertical dotted line indicates the estimated Kosterlitz-Thouless transition temperature, $T = 0.89$.

Much like with the correlation length, we can attempt to answer the question of whether the magnetic susceptibility in the square lattice model exhibits the critical behaviour associated with a regular phase transition,

$$\frac{1}{\chi} \sim (T - T_C)^{\gamma} ,$$

by calculating its temperature derivatives. The first and second derivatives of $1/\chi$ with respect to temperature are shown in figures 2.37 and 2.38. The data are qualitatively similar to the first and second temperature derivatives of $1/\xi$ (figures 2.26 and 2.27). The first derivative of $1/\chi$ shows a steep rise close to the transition temperature, and the second derivative exhibits a peak which grows as N is increased. As in the case of the correlation length, this is evidence for the susceptibility having the power law form close to the transition, with the critical exponent lying somewhere in the range $1 \leq \gamma < 2$. Again, the peak appears to be well-separated from the estimated value of the Kosterlitz-Thouless transition temperature T_{KT}, but is in close proximity to the peak in the second derivative of $1/\xi$, and both of these quantities, together with the derivatives of the entropy, suggest a consistent picture of a regular phase transition.

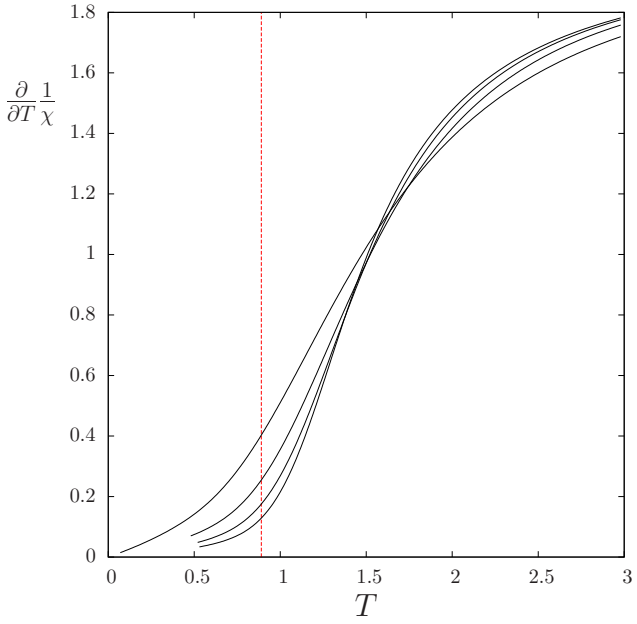

Figure 2.37: First derivative of the reciprocal magnetic susceptibility with respect to T for $N = 2$-5.

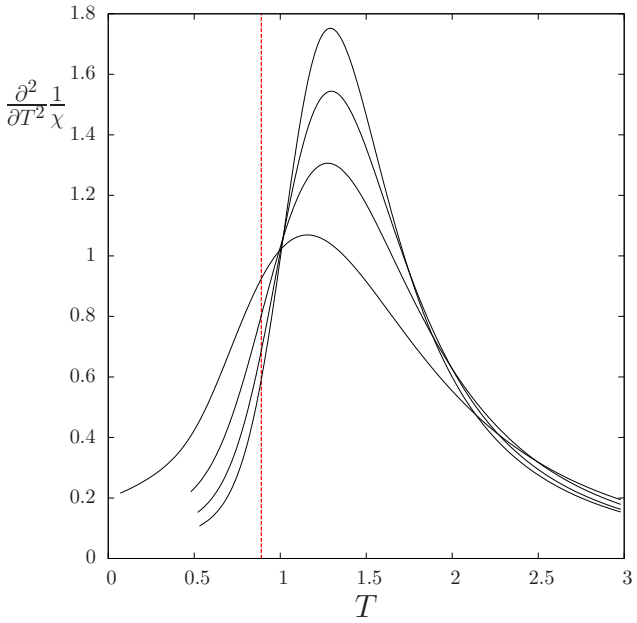

Figure 2.38: Second derivative of the reciprocal magnetic susceptibility with respect to T for $N = 2$-5.

2.4.7 Helical stiffness

We now come to the calculations of the helical stiffness. This quantity is the free energy cost incurred by imposing an infinitesimal twisting of the spin-variables in the model. For the helical geometry which we work with, we may impose a phase-twist in both the nearest-neighbour and Nth-nearest-neighbour bonds, and we must consider the Hamiltonian,

$$H = -J \sum_{j} \left[\cos\left(\phi_j - \phi_{j+1} - \chi_1\right) + \cos\left(\phi_j - \phi_{j+N} - \chi_N\right) \right]. \tag{2.200}$$

The helical stiffness tensor is

$$\underline{\underline{Y}} = \begin{pmatrix} \dfrac{\partial^2 F}{\partial \chi_1^2} & \dfrac{\partial^2 F}{\partial \chi_1 \partial \chi_N} \\ \dfrac{\partial^2 F}{\partial \chi_1 \partial \chi_N} & \dfrac{\partial^2 F}{\partial \chi_N^2} \end{pmatrix}, \tag{2.201}$$

where all of the derivatives are evaluated for $\chi_1 = 0 = \chi_N$.

There is a gauge symmetry in the J_1-J_N planar rotator model which reduces the helical stiffness tensor to a single scalar. By making the gauge transformation $\phi_j \to \phi_j - j\chi_1$ in the Hamiltonian 2.200, one arrives at the Hamiltonian,

$$H = -J \sum_{j} \left[\cos\left(\phi_j - \phi_{j+1}\right) + \cos\left(\phi_j - \phi_{j+N} + N\chi_1 - \chi_N\right) \right]. \tag{2.202}$$

From this form, one can immediately observe that the case $N\chi_1 = \chi_N$ provides the original Hamiltonian without any phase-twisting; this combination of phase-twisting is a gauge symmetry of the Hamiltonian and the corresponding helical stiffness is equal to zero in this instance. Moreover, it is clear that

$$\frac{\partial^2 F}{\partial \chi_N^2} = \frac{1}{N^2} \frac{\partial^2 F}{\partial \chi_1^2}, \tag{2.203}$$

$$\frac{\partial^2 F}{\partial \chi_1 \partial \chi_N} = -\frac{1}{N} \frac{\partial^2 F}{\partial \chi_1^2}, \tag{2.204}$$

and therefore the helical stiffness tensor is effectively reduced to $Y = \frac{\partial^2 F}{\partial \chi_1^2}$:

$$\underline{\underline{Y}} = \begin{pmatrix} 1 & -\dfrac{1}{N} \\ -\dfrac{1}{N} & \dfrac{1}{N^2} \end{pmatrix} Y. \tag{2.205}$$

The eigenvalues of the helical stiffness are $Y_{\parallel} = 0$, which corresponds to the gauge symmetry for $N\chi_1 = \chi_N$, and the non-trivial $Y_{\perp} = (1 + \frac{1}{N^2})Y$. In the two-dimensional limit $N \to \infty$, $Y_{\perp} = Y$, the meaning of which is that the eigenvalue of the helical stiffness corresponds to imposing a phase-twist along one of the principal directions of the square lattice.

The calculations of the helical stiffness eigenvalue $Y_{\perp}$ are shown in figure 2.39. At zero temperature, the spin-configuration of lowest energy is to have the spins spiral, where the pitch of the spiral, or the angle between neighbouring spins, is given by,

$$q = \frac{\chi}{N^2 + 1}. \tag{2.206}$$

This corresponds to the eigenvalue $Y_{\perp}$ taking the value one. It can be seen that the transfer matrix calculations of $Y_{\perp}$ are all aiming at the value one at low temperature. The curves are not continued to the point $T = 0$ because the calculations cannot be performed using the transfer matrix method at low temperature.

The helical stiffness has a steep drop in the vicinity of the phase transition, and this feature becomes more abrupt as N is increased. In the picture of the Kosterlitz-Thouless transition, the helical stiffness is predicted to discontinuously drop from the finite value $2JT_{KT}/\pi$, where T_{KT} is the Kosterlitz-Thouless transition temperature, to zero at the phase transition. In a regular phase transition, a quantity which is identified as an order parameter continuously goes to zero at the critical temperature with a power law temperature dependence.

The derivative of the helical stiffness eigenvalue $Y_{\perp}$ with respect to temperature is shown in figure 2.40. If the helical stiffness jumps discontinuously to zero, then the derivative of the helical stiffness with respect to temperature must exhibit a delta-function divergence at the point of the jump. For finite N, the derivative shows a sharp trough in the vicinity of the phase transition which becomes more pronounced with increasing N. The position of the trough in the derivative is always at a substantially higher temperature than the estimated T_{KT}, and for the values of N for which the calculation has been performed the peak moves to still higher temperatures as N is increased. In the picture of the Kosterlitz-Thouless transition, the position of the peak is expected to converge to sit on top of the estimated value of T_{KT}.

The posititon of the peak in $\frac{\partial Y_{\perp}}{\partial T}$ for the largest value of N for which the calculation has been performed is similar to the positions of the peaks in the second derivative of $1/\xi$ and the second derivative of $1/\chi$; if one were to interpret the calculations as indicating a regular phase transition,

these quantities are broadly consistent in indicating the corresponding critical temperature.

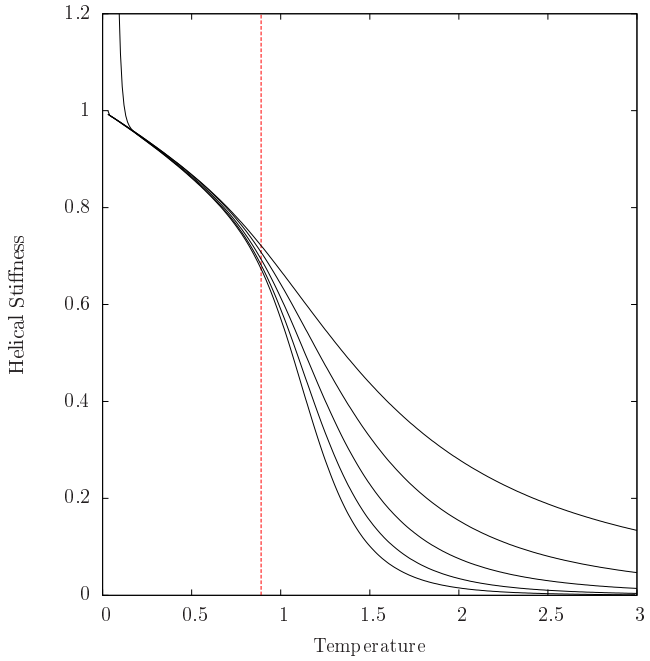

Figure 2.39: The helical stiffness of the J_1-J_N planar rotator model for N = 2-6 (solid lines), with a polynomial extrapolation to the case of $N = \infty$ (blue dotted line). The vertical dotted line indicates the estimated Kosterlitz-Thouless transition temperature, $T = 0.89$.

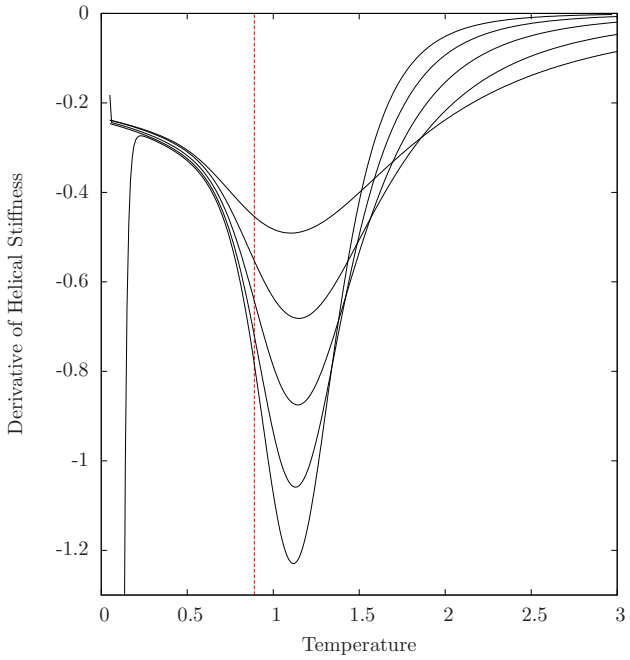

Figure 2.40: The temperature derivative of the helical stiffness of the J_1-J_N planar rotator model for N = 2-6 (solid lines), with a polynomial extrapolation to the case of $N = \infty$(blue dotted line). The vertical dotted line indicates the estimated Kosterlitz-Thouless transition temperature, $T = 0.89$.

2.4.8 Summary and Discussion

We have investigated the square lattice planar rotator model using the one-to-two dimensional crossover technique. We have calculated the specific heat and the correlation length of the J_1-J_N planar rotator model up to $N = 7$, the helical stiffness for up to $N = 6$ and the magnetic susceptibility for up to $N = 5$. Although we have only calculated the thermodynamics for finite systems, the trends in the data as the scaling parameter is increased consistently indicate that a regular phase transition will occur in the square lattice model.

The features in the specific heat close to the transition become sharper with increasing N, and this is seen much more dramatically in the derivatives of the specific heat with respect to temperature; the data certainly indicate that some temperature derivative of the specific heat will become divergent in the limit $N \to \infty$. The strongest evidence for a regular phase transition with ordinary critical exponents is found in the calculations of the correlation length and the magnetic susceptibility. The first few derivatives of these quantities with respect to temperature very much appear to be tending towards the form that would be associated with power law critical behaviour. From this viewpoint,

the lowest order derivative of $1/\xi$ or $1/\chi$ at which a strong peak is observed in the data provides a bound on the associated critical exponents, and these are found to be $1 \leq \nu < 2$ and $1 \leq \gamma < 2$. The calculations of the specific heat, the correlation length and the magnetic susceptibility all suggest a consistent picture of a regular phase transition with a transition temperature slightly higher than J. The Kosterlitz-Thouless transition is predicted to occur at the lower temperature $0.89J$.

The helical stiffness is predicted to exhibit a discontinuous jump from the value $2JT_{KT}/\pi$ to zero at the Kosterlitz-Thouless transition. Our calculations show that the helical stiffness does exhibit an abrupt drop in this vicinity, but we are not able to ascertain whether this is a discontinuity or the smooth change associated with a regular order parameter. The derivative of the helical stiffness with respect to temperature appears to show that the decrease in the helical stiffness coincides with the sharp features in the thermodynamics and not the Kosterlitz-Thouless transition temperature.

We have performed polynomial extrapolations of the data to attempt to estimate the two-dimensional solution. At temperatures removed from the phase transition, this produces the behaviour we expect of the square lattice model; this is most evident in the low-temperature extrapolation of the correlation length. In the vicinity of the transition however the extrapolation fails and this failure is most emphatic in the case of the specific heat, which shows features that are surely unphysical.

This work is complementary to the investigations of the clock models reported in A. M. Cave's thesis(29). The results of his calculations are entirely consistent with the present planar rotator calculations regarding the nature of the planar rotator phase transition; furthermore his work actually constitutes stronger evidence for the same conclusion, as the calculations have been performed for larger systems, up to $N = 11$.

The only aspect of the one-to-two dimensional crossover technique that is not under control is the extrapolation to the two-dimensional limit. It is possible that there is some large value of N which we cannot reach with the computing power currently available to us at which the trends in the quantities we have calculated change and the thermodynamics do not diverge in the two-dimensional limit. In this scenario, if we could perform the calculation at this value of N we would see the Kosterlitz-Thouless transition emerge in the calculations. This of course raises the question of how big this value of N would have to be, and at present we have no ideas regarding how to guess this.

We are of course aware of the degree of consensus that the square lattice planar rotator model exhibits a Kosterlitz-Thouless transition and the fact that our calculations show evidence of a quite different picture puts us in a rather difficult position. To exacerbate this, the literature which deals

with the lattice model itself, rather than related continuum models, is actually rather limited and in many cases these works are consistent with either a Kosterlitz-Thouless transition or a regular phase transition(28; 26).

Even if the implications of our work were to be taken at face value, we do not regard this as contradictory to Kosterlitz-Thouless per se. The implication would be that the thermodynamic functions in the square lattice model simply have an ordinary singularity, with an associated set of ordinary critical exponents, and that this supercedes the Kosterlitz-Thouless mechanism which would control the physics in the absence of this singularity, as it does in the Gaussian model which is obtained as the continuum limit. One could say that Kosterlitz-Thouless is simply not relevant to this particular model.

The implication of our interpretation that a regular phase transition occurs in the model is that ordinary power law singularities can occur in systems in which long range order is forbidden by the Mermin-Wagner theorem. We briefly mention some physical ideas by M. W. Long concerning this. He suggests that the question that should be asked of a spin system is whether the number of spins parallel to a given spin j on average,

$$\sum_{j'} \langle \vec{S}_j \cdot \vec{S}_{j'} \rangle,$$

is divergent. This may be approximated by

$$\sum_{j'} \langle \vec{S}_j \cdot \vec{S}_{j'} \rangle \sim \int_{r_0}^{R} r\mathcal{K}(r) dr$$

where $\mathcal{K}(r)$ is the asymptotic form of the spin-spin correlation function at long range and R is the system size, and this is understood to be in the limit $R \to \infty$. r_0 is some nonzero length that is included to prevent the integral diverging at the lower limit. For exponential correlations $\mathcal{K}(r) = e^{-r/\xi}$ the integral is always finite, for any finite nonzero correlation length ξ. Conversely, for power law correlations $\mathcal{K}(r) = r^{-\eta}$ the integral diverges in the limit $R \to \infty$ for $\eta \leq 2$. M. W. Long suggests therefore, that there is in fact a spontaneously broken symmetry in the power-law phase of the planar rotator model, and there are a divergent number of spins pointing in the symmetry-broken direction on average. The physical suggestion then is that there can be spontaneously broken symmetry, and corresponding to this an ordinary phase transition, associated with the behaviour of a divergent number of spins across the entire system, even in the absence of a finite magnetisation.

Appendix A

Supplementary remarks on the Ising model exact solution

In this appendix we provide some discussion of the inequality 2.111,

$$\prod_{k_+} \left(\sqrt{1 + W_\parallel - W_\perp \cos k_+} + \sqrt{1 - W_\parallel - W_\perp \cos k_+} \right) > \prod_{k_-} \left(\sqrt{1 + W_\parallel - W_\perp \cos k_-} + \sqrt{1 - W_\parallel - W_\perp \cos k_-} \right).$$

We believe this equality to always hold, although we are only aware of how to prove this mathematically for the special case $J_\parallel = J_\perp = J$. Here we present numerical calculations of the ratio of the two terms in the inequality, and we give the mathematical proof of the inequality for $J_\parallel = J_\perp = J$.

Figure A.1 shows some examples of the ratio of the two terms in the inequality evaluated on the computer. In these calculations, one never finds the product over k_- to be larger than the product over k_+, but frequently the two quantities are found to be equal to machine accuracy. We conjecture that in such cases the separation of the two quantities is extremely small but still finite, and that the inequality always holds.

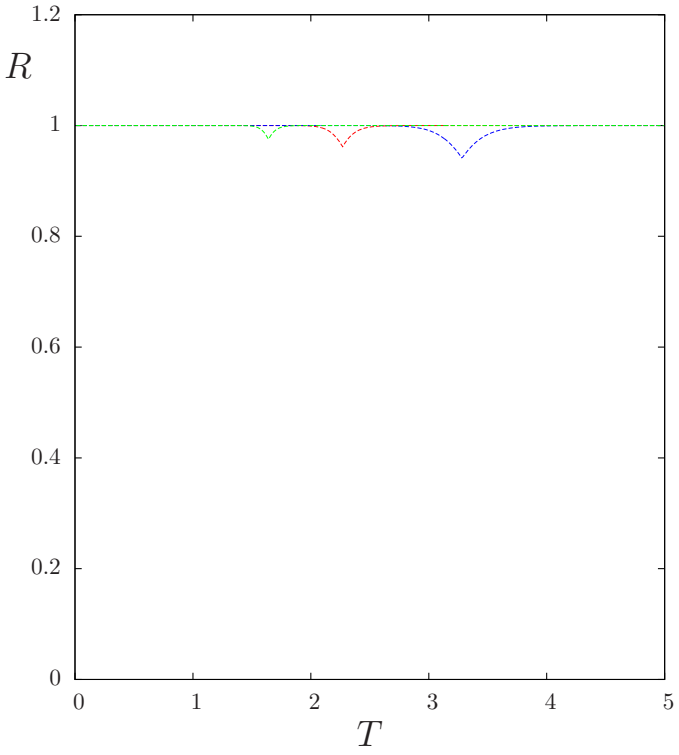

Figure A.1: The ratio of the right hand side of the inequality 2.111 to the left hand side, as a function of temperature (in units of $J_{\|}$) for $N = 20$, for the cases $J_{\perp}/J_{\|} = 1$ (red line), $J_{\perp}/J_{\|} = 2$ (blue line) and $J_{\perp}/J_{\|} = 1/2$ (green line).

We have constructed a proof of the inequality 2.111 in the particular case that $J_{\|} = J_{\perp} = J$. In this instance, we consider the quantity,

$$R(W) = \frac{\prod_{k_-} \left(\sqrt{1 + W - W\cos k_-} + \sqrt{1 - W - W\cos k_-} \right)}{\prod_{k_+} \left(\sqrt{1 + W - W\cos k_+} + \sqrt{1 - W - W\cos k_+} \right)}, \tag{A.1}$$

where

$$W = \frac{\sinh 2\beta J}{\cosh^2 2\beta J},$$

and we seek to prove that this quantity is less than unity for finite temperatures, which corresponds to the parameter W lying in the range $0 < W \leq 1/2$. The lower limit $W = 0$ corresponds either to the case of zero or infinite temperature, and the upper limit $W = 1/2$ corresponds to the transition temperature. We shall show that the derivative of R with respect to W is always less than zero; in conjunction with the clear result that R is equal to one for $W = 0$, this completes the proof.

It is most convenient to describe the derivative of R with respect to W in terms of the logarithm of R: one finds the rather simple formula,

$$\frac{\partial}{\partial W} \ln R = \frac{1}{2W} \left(\Gamma_+ - \Gamma_- \right), \tag{A.2}$$

where

$$\Gamma_\pm = \sum_{k_\pm} \frac{1}{\sqrt{1 + W - W \cos k_\pm} \sqrt{1 - W - W \cos k_\pm}}. \tag{A.3}$$

We shall represent the various factors in the summands as expansions in the variable $e^{ik_\pm}$, so that the sums over the sets of wavenumbers can then be evaluated using the property,

$$\sum_{k_\pm} e^{imk_\pm} = N \sum_{r=-\infty}^{\infty} (\mp 1)^r \, \delta_{m+rN}. \tag{A.4}$$

Now, the two factors in the denominator of the summand in the expression A.3 can be written as,

$$\begin{aligned} 1 + W - W \cos k &= \frac{W}{2\xi} (1 - \xi e^{ik})(1 - \xi e^{-ik}), \\ 1 - W - W \cos k &= \frac{W}{2\eta} (1 - \eta e^{ik})(1 - \eta e^{-ik}), \end{aligned} \tag{A.5}$$

where the variables ξ and η satisfy the quadratic equations,

$$\begin{aligned} \xi^2 - 2 \left(\frac{1}{W} + 1 \right) \xi + 1 = 0, \\ \eta^2 - 2 \left(\frac{1}{W} - 1 \right) \eta + 1 = 0. \end{aligned} \tag{A.6}$$

For $0 < W \leq 1/2$, both of these equations always have a solution which lies between zero and unity, except for the upper limit at which the latter quadratic has the repeated root of unity. For all points other than at the phase transition, therefore, we may safely assume that the variables ξ and η have values which are between zero and unity, and consequently we are permitted to expand the factors in the denominator as infinite power series, employing the result,

$$\frac{1}{\sqrt{1 - t}} = \sum_{m=0}^{\infty} \frac{(2m)!}{\left(2^m m!\right)^2} t^m \qquad \text{for} \qquad |t| < 1. \tag{A.7}$$

However, it is found that the mathematics is greatly simplified by instead first removing the square

root entirely by making use of the identity,

$$\int_{-\pi}^{\pi} \frac{d\phi}{2\pi} \left(\frac{1}{1 - t\cos^2\phi} \right) = \frac{1}{\sqrt{1-t}}. \tag{A.8}$$

If one now expands the integrand in this expression in powers of t, one obtains the result,

$$\frac{1}{\sqrt{1-t}} = \int_{-\pi}^{\pi} \frac{d\phi}{2\pi} \sum_{m=0}^{\infty} \left(t\cos^2\phi \right)^m. \tag{A.9}$$

Writing the factors in the summand in equation A.3 in this way, one can perform the summation over the set of wavenumbers, and one can then proceed to re-sum the resulting expression. The utility of making use of the expansion A.9 is that all of the terms that shall occur are geometric series, allowing the resummation to be performed trivially. Applying the factorisations A.5 and the expansion A.9, one obtains the expansion of the denominator to be,

$$\begin{aligned} &\frac{1}{\sqrt{(1+W-W\cos k_{\pm})(1-W-W\cos k_{\pm})}} \\ &\quad = \frac{2}{W}\sqrt{\xi\eta} \int_{-\pi}^{\pi} \frac{d\phi}{2\pi} \int_{-\pi}^{\pi} \frac{d\theta}{2\pi} \int_{-\pi}^{\pi} \frac{d\phi'}{2\pi} \int_{-\pi}^{\pi} \frac{d\theta'}{2\pi} \sum_{m=0}^{\infty} \sum_{n=0}^{\infty} \sum_{m'=0}^{\infty} \sum_{n'=0}^{\infty} \Big\{ \\ &\qquad \left(\xi\cos^2\phi\right)^m \left(\xi\cos^2\theta\right)^n \left(\eta\cos^2\phi'\right)^{m'} \left(\eta\cos^2\theta'\right)^{n'} e^{i(m+m'-n-n')k_{\pm}} \Big\}. \end{aligned} \tag{A.10}$$

It is useful to introduce the new summation indices $l = m + m'$ and $l' = n + n'$ in place of the indices m' and n'. Performing the summation over the wavenumbers using the result A.4, one then obtains the result,

$$\begin{aligned} \Gamma_{\pm} = \frac{2N}{W}\sqrt{\xi\eta} &\int_{-\pi}^{\pi} \frac{d\phi}{2\pi} \int_{-\pi}^{\pi} \frac{d\theta}{2\pi} \int_{-\pi}^{\pi} \frac{d\phi'}{2\pi} \int_{-\pi}^{\pi} \frac{d\theta'}{2\pi} \sum_{l=0}^{\infty} \sum_{m=0}^{l} \sum_{l'=0}^{\infty} \sum_{n=0}^{l'} \\ &\left(\xi\cos^2\phi\right)^m \left(\xi\cos^2\theta\right)^n \left(\eta\cos^2\phi'\right)^{l-m} \left(\eta\cos^2\theta'\right)^{l'-n} \sum_{r=-\infty}^{\infty} (\mp 1)^r \, \delta_{l-l'+rN}. \end{aligned} \tag{A.11}$$

Using the delta function in this expression to eliminate the summation over l' provides,

$$\Gamma_{\pm} = \frac{2N}{W}\sqrt{\xi\eta}\int_{-\pi}^{\pi}\frac{d\phi}{2\pi}\int_{-\pi}^{\pi}\frac{d\theta}{2\pi}\int_{-\pi}^{\pi}\frac{d\phi'}{2\pi}\int_{-\pi}^{\pi}\frac{d\theta'}{2\pi}\sum_{r=-\infty}^{\infty}(\mp 1)^r\sum_{l=\max(0,-rN)}^{\infty}\sum_{m=0}^{l}\sum_{n=0}^{l+rN}$$
$$\left(\xi\cos^2\phi\right)^m\left(\xi\cos^2\theta\right)^n\left(\eta\cos^2\phi'\right)^{l-m}\left(\eta\cos^2\theta'\right)^{l+rN-n}, \tag{A.12}$$

which we may re-write in the form,

$$\Gamma_{\pm} = \frac{2N}{W}\sqrt{\xi\eta}\int_{-\pi}^{\pi}\frac{d\phi}{2\pi}\int_{-\pi}^{\pi}\frac{d\theta}{2\pi}\int_{-\pi}^{\pi}\frac{d\phi'}{2\pi}\int_{-\pi}^{\pi}\frac{d\theta'}{2\pi}\sum_{l=0}^{\infty}\sum_{m=0}^{l}\left(\frac{\xi\cos^2\phi}{\eta\cos^2\phi'}\right)^m\left(\eta\cos^2\phi'\right)^l\left(\eta\cos^2\theta'\right)^l$$
$$\times\left\{\sum_{n=0}^{l}\left(\frac{\xi\cos^2\theta}{\eta\cos^2\theta'}\right)^n+2\sum_{r=1}^{\infty}(\mp 1)^r\left(\eta\cos^2\theta'\right)^{rN}\sum_{n=0}^{l+rN}\left(\frac{\xi\cos^2\theta}{\eta\cos^2\theta'}\right)^n\right\}. \tag{A.13}$$

It is now trivial to evaluate each of the geometric sums in this expression to provide,

$$\Gamma_{\pm} = \frac{2N}{W}\sqrt{\xi\eta}\int_{-\pi}^{\pi}\frac{d\phi}{2\pi}\int_{-\pi}^{\pi}\frac{d\theta}{2\pi}\int_{-\pi}^{\pi}\frac{d\phi'}{2\pi}\int_{-\pi}^{\pi}\frac{d\theta'}{2\pi}\frac{1}{\eta\cos^2\theta'-\xi\cos^2\theta}$$
$$\times\left\{\frac{\eta\cos^2\theta'}{(1-\eta^2\cos^2\phi'\cos^2\theta')(1-\xi\eta\cos^2\phi\cos^2\theta')}\frac{1\mp(\eta\cos^2\theta')^N}{1\pm(\eta\cos^2\theta')^N}\right.$$
$$\left.-\frac{\xi\cos^2\theta}{(1-\xi\eta\cos^2\phi'\cos^2\theta)(1-\xi^2\cos^2\phi\cos^2\theta)}\frac{1\mp(\xi\cos^2\theta)^N}{1\pm(\xi\cos^2\theta)^N}\right\}. \tag{A.14}$$

The integrals over ϕ and ϕ' can be performed using the identity A.8 to obtain the form,

$$\Gamma_{\pm} = \frac{2N}{W}\sqrt{\xi\eta}\int_{-\pi}^{\pi}\frac{d\theta}{2\pi}\int_{-\pi}^{\pi}\frac{d\theta'}{2\pi}\frac{F_{\pm}(\xi\cos^2\theta)-F_{\pm}(\eta\cos^2\theta')}{\xi\cos^2\theta-\eta\cos^2\theta'}, \tag{A.15}$$

where

$$F_{\pm}(z) = \frac{1}{\sqrt{(1-\eta z)(1-\xi z)}}\frac{1\mp z^N}{1\pm z^N}. \tag{A.16}$$

Finally, we obtain,

$$\frac{\partial}{\partial W}\ln R = \frac{N}{W^2}\sqrt{\xi\eta}\int_{-\pi}^{\pi}\frac{d\theta}{2\pi}\int_{-\pi}^{\pi}\frac{d\theta'}{2\pi}\frac{F(\xi\cos^2\theta)-F(\eta\cos^2\theta')}{\xi\cos^2\theta-\eta\cos^2\theta'}, \tag{A.17}$$

where

$$F(z) = F_+(z)-F_-(z) = -\frac{1}{\sqrt{(1-\eta z)(1-\xi z)}}\frac{4z^N}{1-z^{2N}}. \tag{A.18}$$

The integrand in the double integral in equation A.17 is always equal to the derivative of the functon

$F(z)$ evaluated for some value of z in the range $0 < z < \max(\xi, \eta)$, and is therefore always less than or equal to zero because $F(z)$ is a monotonic decreasing function in the range $0 < z < 1$. Therefore the integral itself is always less than zero, and consequently the derivative of the quantity R is always less than zero. This completes the proof of the inequality 2.111 for the particular case of $J_\perp = J_\parallel$.

References for Part 1

[1] L. D. Landau and E. M. Lifshitz, *Statistical Physics* (Pergamon, London, 1958).

[2] M. Buckingham and W. Fairbank, The nature of the λ-transition in liquid helium, in *Progress in Low Temperature Physics, Volume III*, edited by C. Gorter, chap. 3, pp. 80–112, North-Holland Publishing Company, Amsterdam, 1961.

[3] J. A. Lipa, D. R. Swanson, J. A. Nissen, T. C. P. Chui, and U. E. Israelsson, Heat capacity and thermal relaxation of bulk helium very near the lambda point, Phys. Rev. Lett. **76**, 944 (1996).

[4] J. M. Yeomans, *Statistical Mechanics of Phase Transitions* (Oxford University Press, Oxford, 1992).

[5] M. E. Fisher, Renormalization group theory: Its basis and formulation in statistical physics, Rev. Mod. Phys. **70**, 653 (1998).

[6] R. J. Baxter, *Exactly Solved Models in Statistical Mechanics* (Academic Press, London, 1982).

[7] J. Cardy, *Scaling Theory and Renormalisation in Statistical Physics* (Cambridge University Press, Cambridge, 1996).

[8] C. D. Castro and G. Jona-Lasinio, On the microscopic foundation of scaling laws, Physics Letters A **29**, 322 (1969).

[9] K. G. Wilson, Renormalization group and critical phenomena. i. renormalization group and the kadanoff scaling picture, Phys. Rev. B **4**, 3174 (1971).

[10] R. Peierls, On ising's model of ferromagnetism, Mathematical Proceedings of the Cambridge Philosophical Society **32**, 477–481 (1936).

[11] N. D. Mermin and H. Wagner, Absence of ferromagnetism or antiferromagnetism in one- or two-dimensional isotropic heisenberg models, Phys. Rev. Lett. **17**, 1133 (1966).

[12] A. Altland and B. Simons, *Condensed Matter Field Theory* (Cambridge University Press, Cambridge, 2010).

[13] N. D. Mermin, Absence of ordering in certain classical systems, J. Math. Phys. **8**, 1061 (1967).

[14] J. V. José, L. P. Kadanoff, S. Kirkpatrick, and D. R. Nelson, Renormalization, vortices, and symmetry-breaking perturbations in the two-dimensional planar model, Phys. Rev. B **16**, 1217 (1977).

[15] V. L. Berezinskii, Destruction of Long-range Order in One-dimensional and Two-dimensional Systems Possessing a Continuous Symmetry Group. II. Classical Systems, Soviet Journal of Experimental and Theoretical Physics **32**, 493 (1971).

[16] F. Spitzer, *Principles of Random Walk* (Springer-Verlag, New York, 1976).

[17] L. Onsager, Crystal statistics. i. a two-dimensional model with an order-disorder transition, Phys. Rev. **65**, 117 (1944).

[18] P. Butera and M. Comi, Perturbative renormalization group, exact results, and high-temperature series to order 21 for the n-vector spin models on the square lattice, Phys. Rev. B **54**, 15828 (1996).

[19] P. M. Chaikin and T. C. Lubensky, *Principles of Condensed Matter Physics* (Cambridge University Press, Cambridge, 1995).

[20] J. M. Kosterlitz and D. J. Thouless, Ordering, metastability and phase transitions in two-dimensional systems, Journal of Physics C: Solid State Physics **6**, 1181 (1973).

[21] J. M. Kosterlitz, The critical properties of the two-dimensional xy model, Journal of Physics C: Solid State Physics **7**, 1046 (1974).

[22] H. Betsuyaku, Monte carlo investigation of magnetic properties of a two-dimensional plane-rotator model, Solid State Communications **25**, 829 (1978).

[23] P. Olsson and P. Minnhagen, On the helicity modulus, the critical temperature and monte carlo simulations for the two-dimensional xy-model, Physica Scripta **43**, 203 (1991).

[24] P. Olsson, Monte carlo analysis of the two-dimensional xy model. ii. comparison with the kosterlitz renormalization-group equations, Phys. Rev. B **52**, 4526 (1995).

[25] M. Hasenbusch, The two-dimensional xy model at the transition temperature: a high-precision monte carlo study, Journal of Physics A: Mathematical and General **38**, 5869 (2005).

[26] O. Borisenko, G. Cortese, R. Fiore, M. Gravina, and A. Papa, Numerical study of the phase transitions in the two-dimensional $z(5)$ vector model, Phys. Rev. E **83**, 041120 (2011).

[27] H. E. Stanley, Dependence of critical properties on dimensionality of spins, Phys. Rev. Lett. **20**, 589 (1968).

[28] C.-O. Hwang, Six-state clock model on the square lattice: Fisher zero approach with wang-landau sampling, Phys. Rev. E **80**, 042103 (2009).

[29] A. M. Cave, *The Statistical Physics of the 1D to 2D Crossover Using Transfer Function Techniques*, PhD thesis, University of Birmingham, 2015.

[30] V. G. Vaks and A. I. Larkin, On phase transitions of second order, Soviet Phys.- JETP **22**, 678 (1966).

[31] R. G. Bowers and G. S. Joyce, Lattice model for the λ transition in a bose fluid, Phys. Rev. Lett. **19**, 630 (1967).

[32] A. J. Leggett, *Quantum Liquids: Bose condensation and Cooper pairing in condensed-matter systems* (Oxford University Press, Oxford, 2006).

[33] B. D. Hughes, *Random Walks and Random Environments; Volume 1: Random Walks* (Oxford University Press, Oxford, 1995).

[34] J. Frohlich and T. Spencer, The kosterlitz-thouless transition in two-dimensional abelian spin systems and the coulomb gas, Communications in Mathematical Physics **81**, 527 (1981).

[35] R. J. Mason, *Transfer Function Approaches to the One-Dimensional Thermodynamics of Classical Magnets and the Long-Range Dipole Interaction in Rare-Earth Pyrochlores*, PhD thesis, University of Birmingham, 2015.

[36] M. W. Long, unpublished.

[37] H. A. Kramers and G. H. Wannier, Statistics of the two-dimensional ferromagnet. part i, Phys. Rev. **60**, 252 (1941).

[38] B. Kaufman, Crystal statistics. ii. partition function evaluated by spinor analysis, Phys. Rev. **76**, 1232 (1949).

[39] R. J. Baxter, Onsager and kaufman's calculation of the spontaneous magnetization of the ising model: Ii, Journal of Statistical Physics **149**, 1164 (2012).

[40] C. N. Yang, The spontaneous magnetization of a two-dimensional ising model, Phys. Rev. **85**, 808 (1952).

[41] T. D. Schultz, D. C. Mattis, and E. H. Lieb, Two-dimensional ising model as a soluble problem of many fermions, Rev. Mod. Phys. **36**, 856 (1964).

[42] N. N. Bogoliubov, On a new method in the theory of superconductivity, Il Nuovo Cimento (1955-1965) **7**, 794 (1958).

[43] J. G. Valatin, Comments on the theory of superconductivity, Il Nuovo Cimento (1955-1965) **7**, 843 (1958).

[44] H. Q. Lin, Exact diagonalization of quantum-spin models, Phys. Rev. B **42**, 6561 (1990).

[45] S. Tang and J. E. Hirsch, Long-range order without broken symmetry: Two-dimensional heisenberg antiferromagnet at zero temperature, Phys. Rev. B **39**, 4548 (1989).

[46] M. W. Long, A bipartite spin 1/2 heisenberg model with a gap to excitations, Journal of Physics: Condensed Matter **3**, 1741 (1991).

[47] Wolfram Mathworld: Lagrange Interpolating Polynomial, `http://mathworld.wolfram.com/LagrangeInterpolatingPolynomial.html`, Portions of the entry submitted by Brendan Archer;
Accessed: 2017-07-24.

[48] R. B. Potts, Some generalised order-disorder transformations, Proc. Camb. Phil. Soc. **48**, 106 (1952).

[49] F. Y. Wu, The potts model, Rev. Mod. Phys. **54**, 235 (1982).

Part II

Metamagnetism in Bilayer Strontium Ruthenate $Sr_3Ru_2O_7$

We have investigated the metallic compound $Sr_3Ru_2O_7$ using mean field theory. This compound is a paramagnetic metal on the edge of a ferromagnetic instability, and the system can be driven to itinerant ferromagnetism with the application of a magnetic field. This transition takes the form of metamagnetism, an abrupt jump in the curve of magnetisation versus field. The ferromagnetic instability is an example of a quantum critical point, and $Sr_3Ru_2O_7$ has received a great deal of interest because it provides an experimental realisation of quantum criticality. In particular, it is one of the archetypal exhibitions of the formation of a novel electronic phase in the vicinity of a quantum critical point. In the region of the metamagnetic transition, there occurs an electron nematic phase characterised by large anisotropy in the electronic transport, and this is accompanied by an incommensurate spin density wave ordering.

We have constructed a Hubbard-type model for the Ru conduction electrons, and we have shown that a Hartree-Fock mean field theory solution of this model produces a metamagnetic transition which agrees quantitatively with what is observed in the real material. The electronic structure of the material consists of both two-dimensional and one-dimensional Fermi surfaces. Our work points to the conclusion that the metamagnetic transition is associated with the disappearance of one of the one-dimensional Fermi surfaces. This is in contrast to some existing literature which puts forth the view that the transition is associated with the logarithmic singularity in the density of states in the two-dimensional band-structure. In the near-vicinity of the transition, the mean field theory predicts that the system will phase-separate into low-magnetisation regions, where all of the Fermi surfaces are present, and high-magnetisation regions where one of the one-dimensional Fermi surfaces has vanished. We suggest that this phase separation corresponds to the nematic phase.

Chapter 3

Background

This part of the thesis concerns work on modelling the metamagnetism that occurs in the metallic perovskite ruthenate $Sr_3Ru_2O_7$. This compound is a member of the Ruddlesden-Popper series of layered perovskites $Sr_{n+1}Ru_nO_{3n+1}$; the crystal structure of this series consists of stackings of n RuO_2 planes interspersed with planes of SrO; this structure is repeated in the c-axis direction with the neighbouring n-fold stackings separated by two SrO layers. The members of this series to have been successfully synthesised are the single-layer $n = 1$, the bilayer $n = 2$, the triple-layer $n = 3$ and the ideal perovskite $SrRuO_3$ which corresponds to $n = \infty$. The single-layer compound is a metal and exhibits p-wave superconductivity below about 1K(50; 51), while the the $n = 3$ and $n = \infty$ compounds are also metallic and exhibit itinerant ferromagnetism(52; 53; 54; 55). The bilayer compound is a metal sitting on the edge of a ferromagnetic instability, and a transition in to the ferromagnetic state can be induced with the application of a magnetic field. This takes the form of a metamagnetic transition, wherein the magnetisation exibits an abrupt jump at some critical applied field(56; 57). The metamagnetism in $Sr_3Ru_2O_7$ has been the subject of much interest because it occurs in the vicinity of a quantum critical point: the metamagnetic transition is first order, and the critical point which terminates the line of metamagnetic transitions in phase space occurs at a temperature close to zero, and is therefore a quantum critical point(58; 59; 60; 61). This material also exemplifies the phenomenon of the appearance of a novel electronic phase in the vicinity of a quantum critical point. In the region of the metamagnetism, there occurs a so-called electronic nematic phase characterised by large anisotropy in the transport properties in the basal plane, together with the existence of an incommensurate spin density wave ordering(62; 63).

The actual modelling will be described in the next chapter. This chapter provides the necessary background for this work, of which there are three kinds of material: key aspects of $Sr_3Ru_2O_7$, such as its crystal structure, which are a pre-requisite to the modelling; the particular experimental results which we aim to model, namely the metamagnetic jump exhibited in the plot of magnetisation versus applied magnetic field; and an overview of a whole set of experimental results which have attracted attention towards $Sr_3Ru_2O_7$ as an interesting system, which provide the motivation for our work. The latter includes signatures of quantum criticality in form of deviations in the temperature dependence of bulk quantities from the Fermi liquid form, and the signatures of the electronic nematic phase, the most notable of which are dramatic step-like changes in the in-plane resistivity, and large anisotropy in this quantity when the magnetic field has an in-plane component.

The order of topics to be dealt with is as follows. In section 3.1 we describe the crystal structure of $Sr_3Ru_2O_7$. Section 3.2 covers the Fermi surface and the density of states. The $Sr_3Ru_2O_7$ Fermi surface is quasi two-dimensional, but in addition the electronic structure has features which are strongly one-dimensional. This is discussed by means of exhibiting angle-resolved photoemission spectroscopy, quantum oscillations experiments, scanning tunnelling microscopy and density functional theory calculations. The electronic structure of the single-layer compound Sr_2RuO_4 is also discussed, as this provides a way of introducing features in the more complicated electronic structure of $Sr_3Ru_2O_7$ very clearly. Sections 3.1 and 3.2 both contain essential pre-requisites for our modelling of $Sr_3Ru_2O_7$ in the next chapter.

In section 3.3 we deal with the experiments relating to metamagnetism and quantum criticality. We begin by exhibiting the magnetisation itself, which shows metamagnetism, which is an abrupt jump in the magnetisation with field. This plot, of magnetisation versus applied field, is the primary behaviour that we seek to emulate with our model in the next chapter. Conversely, the remainder of this section is not directly related to the modelling, as the experiments dealt with concern effects which we simply do not include in our model, such as the effect of finite temperature. We discuss how the metamagnetism is related to a quantum critical point, and place $Sr_3Ru_2O_7$ in the context of a phase diagram which applies to a variety of systems which exhibit itinerant magnetism. We discuss the effects of applying pressure to the system and of changing the orientation of the applied magnetic field, both of which act as tuning parameters which can be used to drive the system towards quantum criticality. We conclude this section with a series of experiments which show evidence of quantum criticality in the vicinity of the metamagnetism, which amounts to the apparent divergence of some

bulk quantity, or a deviation from normal metallic behaviour. We discuss the electrical resistivity, the nuclear spin relaxation time as measured by nuclear magnetic resonance, the coefficient of thermal expansion, the specific heat, effective masses measured in quantum oscillations experiments and the Gruneisen parameter.

In section 3.4 we deal with experiments relating to the nematic phase which occurs in proximity to the underlying QCP in sufficiently clean $Sr_3Ru_2O_7$ samples. We first deal with the signatures of the nematic phase for magnetic fields applied in the c-axis direction, these being the occurrence of two first order phase transitions, which mark the boundaries of the nematic phase, and the in-plane electrical resistivity which shows step-like jumps $\sim 50\%$ of its value on entering and leaving the nematic phase. We then move on to experiments which apply a field at a small angle to the c-axis so as to produce a small field component along one of the in-plane principal crystal axes. This produces dramatic anisotropy between the two in-plane directions, which is exhibited in the electrical resistivity and the thermal expansion. Our modelling will not directly address any of these experiments. However, the result of our modelling will imply the existence of a phase-separated state in the vicinity of the metamagnetism, which we postulate to correspond to the nematic phase.

Section 3.5 concerns the incommensurate spin density wave that is observed in the vicinity of the metamagnetism. We exhibit neutron scattering data which reveals the presence of the spin density wave and discuss the effect of the direction of the applied magnetic field. For the fields parallel to the c-axis, spin density waves are found propagating along both of the in-plane principal axes, but introducing a small field component along one of the in-plane axes eliminates the propagation in the perpendicular in-plane direction. Again, these experiments do not directly relate to our modelling.

Finally, in section 3.6 we discuss the results of an experiment which dopes the material with electrons by substituting a small number of Sr atoms with La atoms. The principal experimental measurements are the specific heat, which is found to be highly sensitive to the doping, and the electrical resistivity. The effect of doping the system with electrons is something which we have direct access to in our modelling, and we shall devote some space to discussing this in the next chapter.

3.1 Crystal Structure

The crystal structure of $Sr_3Ru_2O_7$ is shown in figure 3.1. This compound is one of the Ruddlesden-Popper series of layered perovskites $Sr_{n+1}Ru_nO_{3n+1}$. The Ruddlesden-Popper series is a series of crystal structures found for materials with chemical formulae $A_{n+1}B_nO_{3n+1}$, where B is very often

a transition metal. The leading order crystal structure is composed of stackings of BO_2 planes and AO planes which are both structured on underlying square lattices of the same lattice constant. The BO_2 plane has B atoms at the lattice points of the underlying square lattice and O atoms sat halfway between each nearest neighbour pair of B atoms; the AO plane has O atoms at the lattice points of the underlying square lattice and A atoms at the lattice points of the dual square lattice, which are in the centre of the squares formed by four closest lattice points. The Ruddlesden-Popper structure has n BO_2 planes stacked on top of each other interspersed with AO planes, with the O atoms in the AO planes lying on top of the B atoms in the adjacent plane, so that there is an O atom lying half-way between all nearest neighbour pairs of B atoms. The n-fold stackings of BO_2 planes are bookended by *spacer layers* of two AO planes which are out of phase with each other, that is the A atoms in the top plane sit on top of the O atoms in the bottom plane, following which there is another n-fold stacking of phase shifted BO_2 planes and the structure is repeated in the c-direction. As emphasised in figure 3.1, the B atoms sit in an octahedron of neighbouring O atoms. The $n = \infty$ member of the Ruddlesden-Popper series has the simplified chemical formula ABO_3 and consists of in-phase stacked BO_2 planes with interspersed AO planes repeated up the z-axis; this is known as the ideal perosvskite crystal structure. $Sr_3Ru_2O_7$ is the $n = 2$ member of the Ruddlesden-Popper series, and so has *bilayers* of RuO_2 repeated in the c-axis direction.

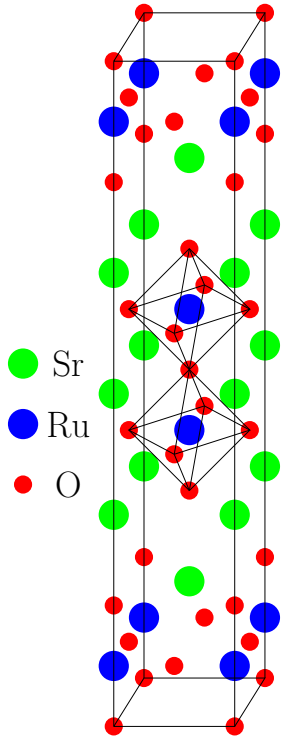

Figure 3.1: Crystal structure of $Sr_3Ru_2O_7$

In real materials, structural distortions of this simple crystal structure arise in the form of rotations and deformations of the O octahedra. In $Sr_3Ru_2O_7$, the octahedra are rotated about the c-axis through an angle of approximately 6.8 degrees, with the sense of rotation of each octahedra being opposite to that of all its neighbouring octahedra(64). The structure of the RuO_2 planes resulting from this distortion is shown in figure 3.2.

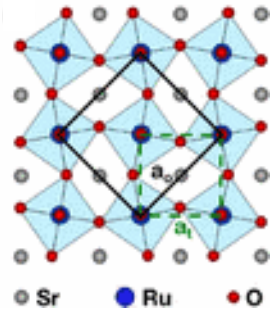

Figure 3.2: Illustration of the 6.8 degrees rotation of the O octahedra in one of the RuO_2 planes. (Taken from reference (65)).

3.2 Fermi Surface and Density of States

The neighbouring n-fold stackings of RuO_2 layers in the crystal structure $Sr_{n+1}Ru_nO_{3n+1}$ are largely isolated from each other due to the intermediate SrO spacer layer and because the positioning of the neighbouring stackings is out of phase. The electronic structure of the low-n members of the series is therefore strongly two-dimensional. We regard the $Sr_3Ru_2O_7$ Fermi surface as a two-dimensional object throughout this thesis.

In addition, the electronic structure also has strongly one-dimensional characteristics due to weak hybridisation of the relevant Ru orbital states in certain crystallographic directions. We discuss this in more detail in the context of building a model for $Sr_3Ru_2O_7$ in the next chapter in section 4.3, but for the present we wish to focus on the experiments and so merely state the important points. The relevant electron states are the t_{2g} cubic harmonic wavefunctions, d_{xy}, d_{yz} and d_{zx}, which are three mutually perpendicular orientations of the same orbital aligned with the three crystallographic directions. The symmetry of the wavefunctions is such that hybridisation between neighbouring Ru sites in one of the three crystallographic directions is strongly suppressed; the d_{xy} electrons are mobile in the x and y directions but not in the z direction, and so on. The d_{yz} and d_{xz} electrons are only mobile in one of the in-plane directions and therefore are essentially one-dimensional.

We introduce the $Sr_3Ru_2O_7$ Fermi surface by way of the Fermi surface for the single-layer compound Sr_2RuO_4(66). Observe figure 3.3 which shows a measurement of the Sr_2RuO_4 Fermi surface obtained using Angle Resolved Photoemission Spectroscopy (ARPES). To leading order, the image shows lines of Fermi surface intersecting the k_x and k_y axes at $(\pm k^*, 0)$ and $(0, \pm k^*)$, which are the d_{yz} and d_{zx} Fermi surfaces, and a quasi-circular Fermi surface associated with the d_{xy} orbital; there is a qualitative correction to this simple picture in the form of band reconstruction where these Fermi surfaces cross, close to the four corners in figure 3.3. To get from this picture to the $Sr_3Ru_2O_7$ Fermi surface there are primarily two modifications. Firstly the mobility of the d_{yz} and d_{zx} electrons between the upper and lower RuO_2 layers results in each of their Fermi surfaces being split - this is often referred to as bilayer splitting(66) - so that there are twice as many horizontal and vertical Fermi surface sheets. Secondly, the twisting of the O-octahedra discussed above has the effect of doubling the size of the unit cell in the RuO_2 plane, and corresponding to this there is a backfolding of the Fermi surface, in the form of a reflection in the diagonal lines connecting the points $(\pm\pi, 0)$, $(0, \pm\pi)$. This provides a decent description of the $Sr_3Ru_2O_7$ Fermi surface; an ARPES measurement of the Fermi surface is shown in figure 3.4.

The experimental Fermi surface is one of the most relevant ingredients for our modelling of $Sr_3Ru_2O_7$, and in the next chapter much attention is given to how to make the Fermi surface in our model agree qualitatively with the experiments. We will not include the effect of the twisting of the octahedra and the associated Fermi surface reconstruction, but apart from this facet our model does provide a Fermi surface much like the real material.

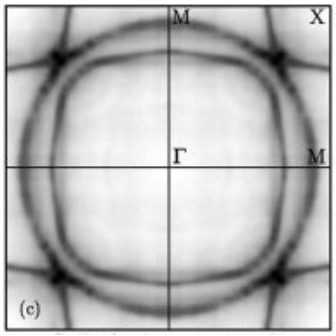

Figure 3.3: ARPES image of the single layer compound Sr_2RuO_4 Fermi surface. (Taken from reference (67)).

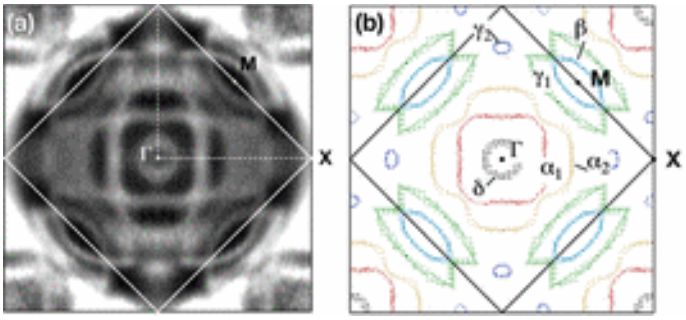

Figure 3.4: Angle-resolved photon emission spectrography image of the Fermi surface of $Sr_3Ru_2O_7$. (Taken from reference (65)).

A great deal of information regarding the Fermi surface is obtained in quantum oscillation experiments. There have been a number of quantum oscillations studies of $Sr_3Ru_2O_7$(68; 66); there are five distinct Fermi surface sheets observed in $Sr_3Ru_2O_7$ associated with the Ru t_{2g} orbitals(66), but the effect of backfolding due to the lattice distortion and the reconnections that occur at the crossing points of distinct Fermi surfaces has the effect of making it difficult to associate the sheets seen in quantum oscillation experiments with the individual bands which we deal with at the level of our modelling. These issues are far less severe if one examines the single layer compound Sr_2RuO_4. Here quantum oscillations finds just three distinct Fermi surface sheets, two of which are essentially mixtures of the d_{yz} and d_{zx} orbitals, and the third of which is attributed almost entirely to the d_{xy} orbitals(69). The

most significant observation from the point of view of our modelling is that the effective mass deduced for the d_{xy}-associated Fermi surface sheet is approximately double the size of that for the d_{yz}/d_{zx} bands (see figure 3.5). It is a straightforward matter to incorporate the d_{xy} particles having a larger effective mass than the the d_{yz} and d_{zx} particles into our modelling, and section 4.6.4 in the next chapter is devoted to investigating this.

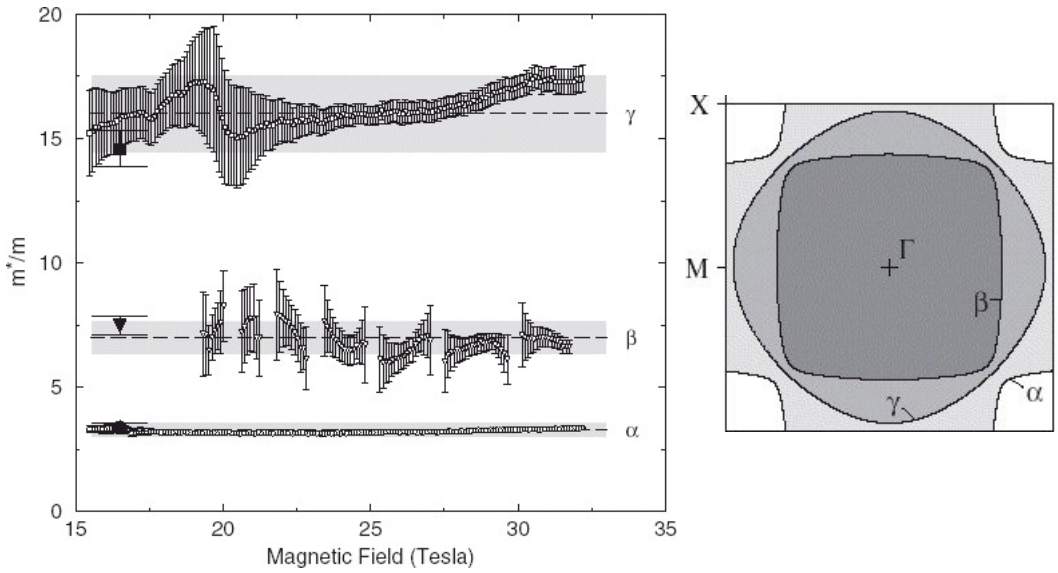

Figure 3.5: Left: The effective masses associated with each of the three distinct Fermi surface sheets in the single layer compound Sr_2RuO_4 as functions of an applied magnetic field.
Right: Illustration of the Sr_2RuO_4 Fermi surface with key to the labelling of the three sheets.
(Both figures taken from reference (69)).

The densities of states of one- and two-dimensional systems exhibit singularities, which are known as van Hove singularities. There are therefore associated with the quasi-one- and quasi-two-dimensional character of the d_{yz}/d_{zx} and d_{xy} bands respectively sharp peaks in the $Sr_3Ru_2O_7$ density of states. In particular, measurements of the density of states by both scanning tunnelling microscopy (STM)(70) (shown in figure 3.6) and ARPES(65) show the presence of peaks within a few meV of the chemical potential. The presence of a van Hove singularity in proximity to the chemical potential is a well-known scenario in which a metallic system can be driven to an itinerant ferromagnetic state, this mechanism famously being known as Stoner ferromagnetism. The implication is that $Sr_3Ru_2O_7$ is close to such a magnetic instability, and this provides a possible explanation for the exhibition of metamagnetism by this material, which we describe below.

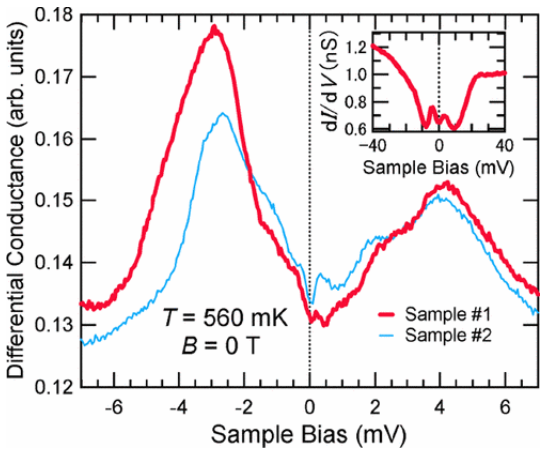

Figure 3.6: Scanning Tunnelling Microscopy differential conductance as a function of bias voltage; this quantity is proportional to the electronic density of states where the bias voltage in V corresponds to the distance from the Fermi level in eV. The figure clearly shows peaks at $-3meV$ and $+4meV$. (Both figures taken from reference (70)).

Another important component of the literature regarding the Fermi surface of $Sr_3Ru_2O_7$ is density functional theory (DFT). The calculations that are the easiest to interpret are the calculations of the density of states. These calculations support the picture of quasi-one- and quasi-two-dimensional electronic structure arising from the d_{yz}/d_{zx} and the d_{xy} orbitals respectively. As in the case of the experimental Fermi surface, this is seen much more easily in the single layer compound Sr_2RuO_4. Figure 3.7 shows the density of states associated with individual Ru orbitals for Sr_2RuO_4. The d_{yz}/d_{zx} density of states has the qualitative from associated with a one-dimensional linear chain with nearest neighbour hybridisation. The d_{xy} density of states has the qualitative form expected from a tight-binding model on a square lattice (see appendix B).

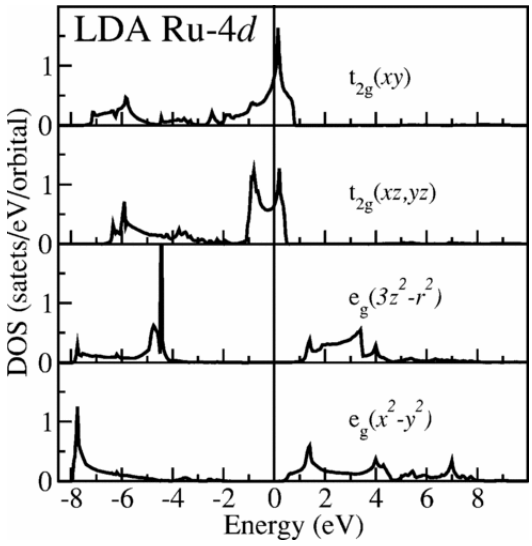

Figure 3.7: Density functional theory calculations of the density of states for the single layer compound Sr_2RuO_4. (Taken from reference (71)).

A DFT calculation of the individual orbital components of the $Sr_3Ru_2O_7$ density of states is shown in figure 3.8. The hybridisation of d_{yz}/d_{zx} orbitals between the upper and lower part of the bilayer renders their density of states more complicated, but the d_{xy} density of states is qualitatively the same as seen in the single layer compound as we would expect. The feature of this calculation that is particularly relevant to our modelling is that the van Hove singularity in the d_{xy} density of states is found in close proximity to the chemical potential. This is line with the ARPES and STM experiments which show van Hove singularities close to the chemical potential in $Sr_3Ru_2O_7$. Because this is consistently observed in DFT works(72; 73), it has been suggested by a number of authors that the metamagnetism in $Sr_3Ru_2O_7$ is controlled by the d_{xy} band in a picture of Stoner ferromagnetism(74; 75; 65). We suggest a picture of a Stoner ferromagnetic instability that is rather controlled by the d_{yz}/d_{zx} bands. This issue of which of these bands is dominant in the metamagnetism is one of the major issues which we attempt to address in our modelling in the next chapter.

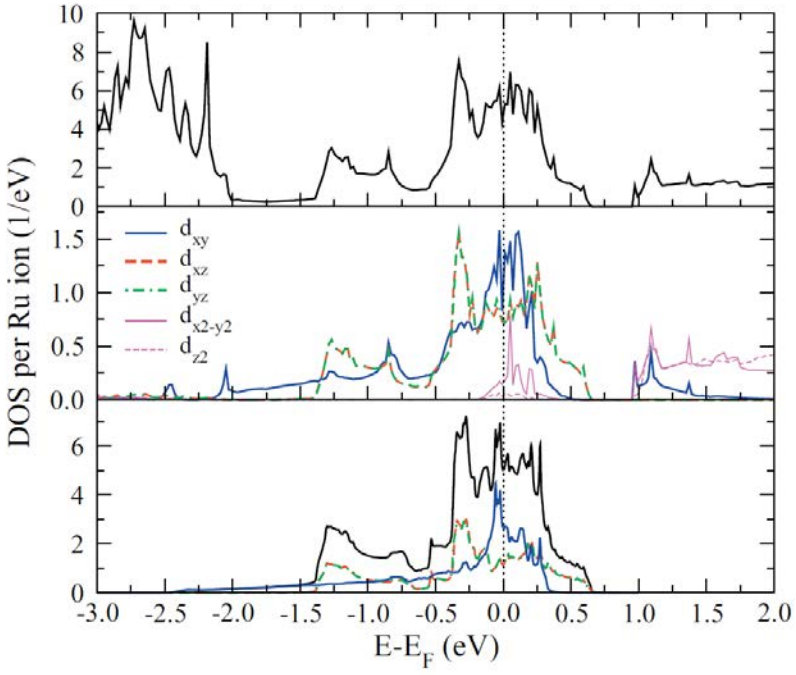

Figure 3.8: Density of states for different bands in $Sr_3Ru_2O_7$ calculated using density functional theory. The important features for our modelling in the next chapter are the densities of states of associated with the individual d_{xy}, d_{yz} and d_{zx} in the middle and bottom sections of the figure. The middle and bottom sections show two different DFT calculations. (Taken from reference (73)).

3.3 Metamagnetism and Quantum Criticality

Measurements of the magnetisation of $Sr_3Ru_2O_7$ versus applied magnetic field are shown in figure 3.9. At low temperatures, the magnetisation induced by an externally applied magnetic field exhibits an abrupt increase at a field of approximately 8 Tesla if the field is applied in the c-axis direction and approximately 5 Tesla if the field is applied in the in-plane direction. This phenomenon is the main target of our modelling in the next chapter. Our model can exhibit a metamagnetic jump, where the increase in the magnetisation matches the experiments quite well, although we shall not be able to predict the magnetic field at which the metamagnetic jump occurs, or the dependence on the direction of the applied field.

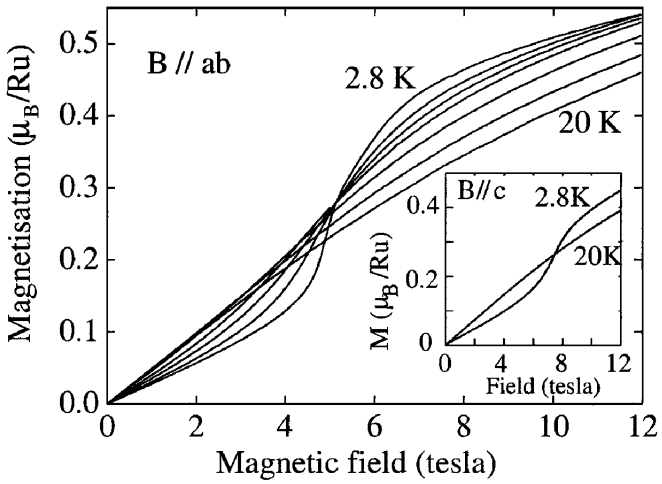

Figure 3.9: Measurements of the magnetisation of $Sr_3Ru_2O_7$ as a function of applied magnetic field showing the metamagnetism. Main figure: field applied in the in-plane direction. Inset: field applied in the *c*-axis direction. The metamagnetism is exhibited in both cases but occurs at a smaller field for the in-plane field than for the *c*-axis field. (Taken from reference (56)).

$Sr_3Ru_2O_7$ is positioned in the Ruddlesden-Popper series $Sr_{n+1}Ru_nO_{3n+1}$ between the single layer compound, which is nonmagnetic, and the ideal perovskite $SrRuO_3$ which is an itinerant ferromagnet. It therefore seems reasonable that one should think of the metamagnetism as being the manifestation of $Sr_3Ru_2O_7$ being "almost ferromagnetic": the system is on the edge of the ferromagnetic instability, and can be pushed ferromagnetic with the application of a magnetic field. The triple layer compound $Sr_4Ru_3O_{10}$ also exhibits metamagnetic transitions in response magnetic fields applied in the in-plane direction, and these occur at lower fields than for the bilayer compound, suggesting a consistent picture of the whole series with the triple-layer compound lying in even closer proximity to the ferromagnetic instability. With regard to this last point, it should be noted that the magnetic characteristics of the triple-layer compound are significantly more complicated than the bilayer system: there is an ordered ferromagnetic moment in the *c*-axis direction at zero-field, and the metamagnetic transitions only occur for in-plane fields(76).

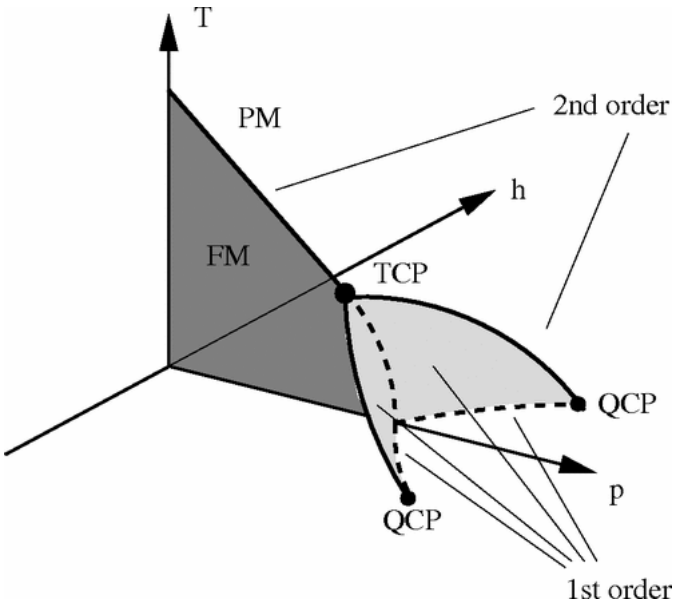

Figure 3.10: The phase diagram generic to a number of systems which exhibit itinerant ferromagnetism in the space of temperature (T), magnetic field (h) and pressure (p). For smaller values of the pressure p, there is a second order phase transition between paramagnetic (PM) and itinerant ferromagnetic (FM) states. Increasing p reduces the transition temperature. The line of second order phase transitions bifurcates at the tricritical point (TCP) into two lines of first order transitions. A line of first order transitions must always end at a critical point; for the case depicted both critical points lie at zero temperature and are therefore quantum critical points (QCP). (Taken from reference (77)).

$Sr_3Ru_2O_7$ is viewed in the context of the phase diagram shown in Figure 3.10. A large number of materials which exhibit itinerant ferromagnetism are thought to have phase diagrams of this form. $ZrZn_2$, for example, undergoes a second order phase transition, at a transition temperature 28.5 Kelvin, from a paramagnetic phase to an itinerant ferromagnetic phase(78): this paradigm corresponds to the left hand side of the phase diagram. By applying pressure to the system, the transition temperature is reduced, and there is a corresponding line of second order phase transitions in the $h = 0$ plane on the phase diagram. At a pressure of 16.5kbar, below the line of second order phase transitions the magnetic moment is found to disappear discontinuously(79). The line of second order transitions splits, at what is called the *tricritical point*, into *two* lines of critical points which move away from the $h = 0$ plane. There are associated *surfaces* of first order transitions, which are accompanied by metamagnetic jumps in the magnetisation. The surfaces, often described as "wings", are the surfaces which join the lines of second order transitions to the $T = 0$ plane perpendicular to that plane(77). Any crossing of one of the wings in the T-p-h space corresponds to a first order transition and a metamagnetic jump(80). It is to be expected that the system in question has an inversion symmetry along some axis, and therefore

that provided the magnetic field is applied along this axis, the two wings in the phase diagram are reflections of each other in the $h = 0$ plane. At a given fixed pressure, cutting through one of the wings produces a line of first order transitions in the T-h space which end in a critical point, and this critical point is pushed to lower temperatures with increasing pressure. In principal the critical point can be pushed to zero temperature; the behaviour in its vicinity is then governed by quantum fluctuations rather than thermal fluctuations and it is said to be a *quantum critical point* (QCP).

The behaviour of $Sr_3Ru_2O_7$ can be viewed as an example of this same phase diagram, where at ambient pressure, the system is positioned past the tricritical point and in the vicinity of the QCP. The situation is slightly different for the cases where the magnetic field is in the c-axis direction or in the ab-plane. The situation for fields in the c-axis is that is there is a line of first order transitions in the T-h space which ends at a critical point which lies below 0.05 Kelvin(81), and at a field of approximately 7.9 Tesla. The situation for fields in the ab-plane has the critical endpoint at approximately 1.25 Kelvin(81) and 6.5 Tesla. The angle of the field direction with respect to the c-axis can therefore be thought of as acting as a tuning parameter, in an analogous fashion to the pressure in figure 3.10. The tuning of the end-point by the angle of the field, determined from measurements of the ac magnetic susceptibilty(81), is shown in figure 3.11.

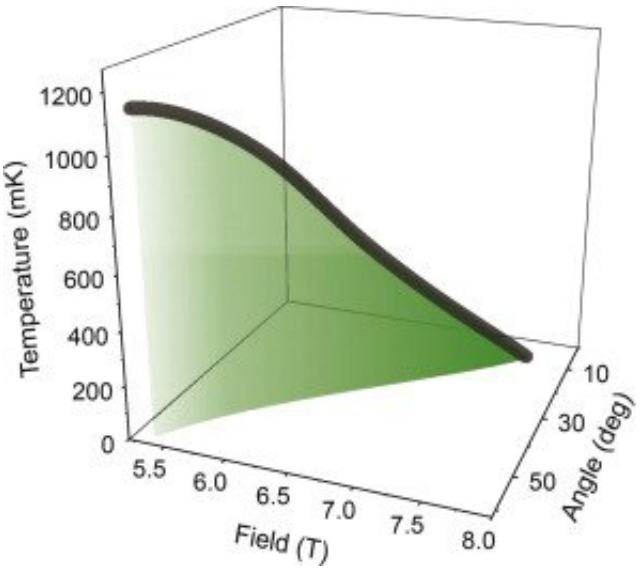

Figure 3.11: The surface of first order transitions exhibited by a sample of $Sr_3Ru_2O_7$ in the phase space of temperature, magnetic field modulus, and the angle of the field direction to the c-axis. The positions of the phase transitions were determined by measurements of the ac magnetic susceptibility. (Taken from reference (81)).

The picture of $Sr_3Ru_2O_7$ in terms of the phase diagram in figure 3.10 is largely borne out by

experiments on the result of applying pressure to the system. In the situation of the magnetic field applied in the *ab*-plane, measurements of the ac magnetic susceptibility(80) indicate that the endpoint at 1.25 Kelvin can be tuned to close to zero temperature with the application of hydrostatic pressure. This is illustrated in figure 3.12. This is also consistent with measurements of the resistivity(59) and the dc magnetic susceptibility(82) for fields in the *ab*-plane. It should be noted that the application of uniaxial pressure in the *c*-axis direction can actually drive the system ferromagnetic at zero field(83), which is clearly some other effect which is not to be explained by the picture of figure 3.10.

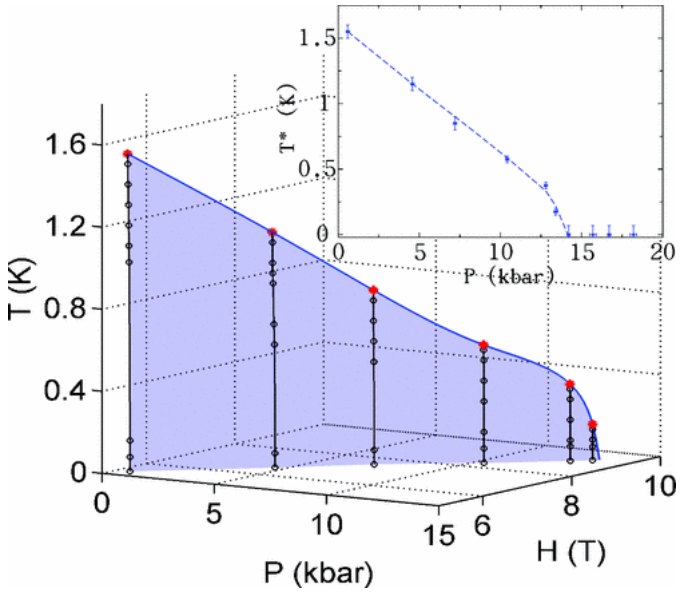

Figure 3.12: The pushing of the end-point to zero-temperature by application of pressure, determined from measurements of the ac magnetic susceptibility. (Taken from reference (80)).

Quantum phase transitions are fundamentally different from classical phase transitions, arising from the fundamental differences between quantum and classical fluctuations. Field theoretic treatments of quantum criticality, analogous to the well established field theories of classical criticality, predict that, even at finite temperature, close to the quantum critical point quantum fluctuations can influence the physics, and cause the behaviour of the system to deviate from ordinary metallic physics(84; 85). Therefore quantum criticality is closely associated with exotic electronic behaviour. In addition to this deviation from Fermi liquid behaviour as the QCP is approached, in real systems the QCP is often masked on the phase diagram by a small region of some distinct phase, such as superconductivity(86). In $Sr_3Ru_2O_7$ a *nematic* electronic phase occurs, and this is discussed in the following section.

We now turn our attention to various experiments which show direct evidence that $Sr_3Ru_2O_7$ lies

in proximity to a QCP for fields in the c-axis direction. We begin with the electrical resistivity. In an ordinary metal, at low temperature the temperature-dependence of the resistivity is given by the law $\rho = \rho_{\rm res} + AT^2$ where $\rho_{\rm res}$ and A do not depend on temperature; quantum criticality is often seen in the temperature dependence being a power law which deviates from the quadratic. Figure 3.13, taken from a study by Grigera *et al*(58), shows the results of fitting measurements of the resistivity to the function $\rho = \rho_{\rm res} + AT^{\alpha}$, where the $\rho_{\rm res}$ is determined as the zero-temperature resistance for each applied field, A is calculated as the low-temperature limit of $(\rho - \rho_{\rm res})/T^2$ for each applied field, and the exponent α is allowed to vary with both temperature and field. The colour plot of the exponent is an example of one of the archetypal plots which shows signatures of quantum criticality: the exponent is seen to deviate from the value 2 in the vicinity of the metamagnetism. The parameters $\rho_{\rm res}$ and A are shown in the right hand side of the figure. Both exhibit a strong rise and possibly a divergence as the metamagnetic field is approached; Grigera *et al* make the comment that this is very good evidence for quantum criticality(58).

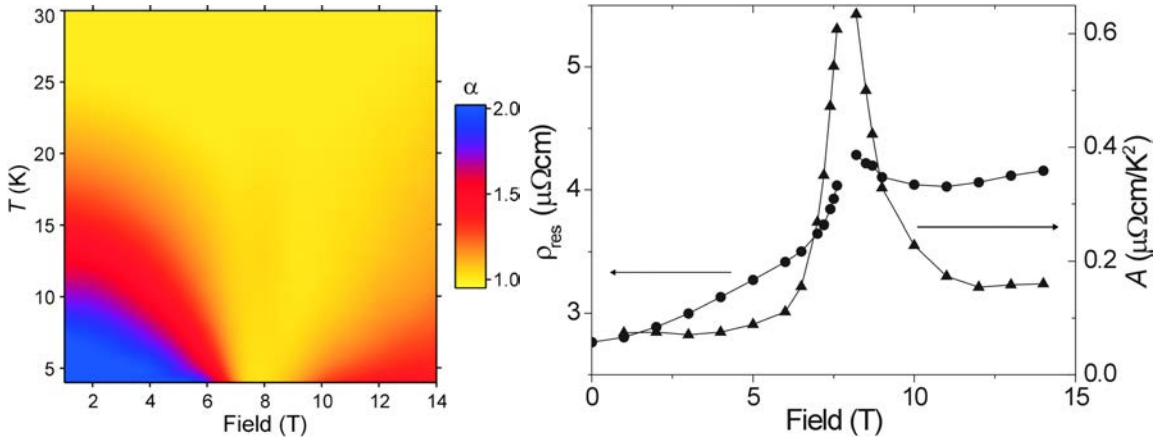

Figure 3.13: Results of fitting measurements of the electrical resisitvity to the function $\rho = \rho_{\rm res} + AT^{\alpha}$. Left: Colour plot of the exponent α, which is allowed to vary with both temperature and field. Right: Plot of the temperature-independent parameters $\rho_{\rm res}$ and A as a function of field. (Taken from reference (58)).

We next mention a Nuclear Magnetic Resonance (NMR) study of $Sr_3Ru_2O_7$ by Kitagawa *et al*(87). In a Fermi liquid, the NMR relaxation rate is proportional to temperature, and the coefficient of proportionality is closely related to the parameter A, the coefficient of T^2 in the low temperature expansion of the specific heat. Figure 3.14 overlays measurements of the relaxation rate divided by temperature as a function of magnetic field for a number of isotherms, together with the very same measurements of A as in figure 3.13; in the low and high-field regions the relaxation rate over

temperature is independent of temperature as expected of a Fermi liquid, but in the metamagnetic region the Fermi liquid behaviour breaks down.

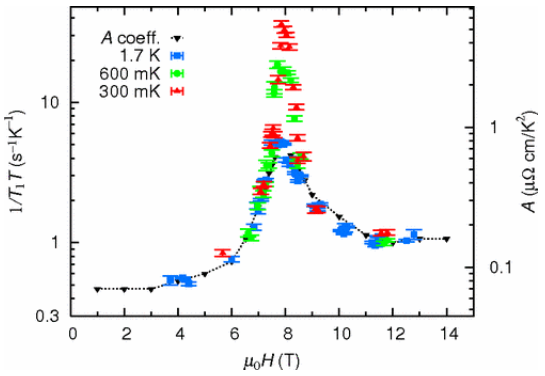

Figure 3.14: The NMR relaxation rate divided by temperature plotted as a function of magnetic field for three different temperatures, together with the parameter A plotted in figure 3.13. (Taken from reference (87)).

Another quantity sensitive to the QCP is the thermal expansion. Figure 3.15 shows the linear coefficient of thermal expansion in the c axis direction, which is the quantity(88)

$$\frac{d}{dT}\left(\frac{\Delta L_c}{L_c}\right),$$

where L_c is the length of a single crystal of $Sr_3Ru_2O_7$ in the c-axis direction and ΔL_c the change in this length, and the figure plots this quantity divided by the temperature versus magnetic field. This quantity is expected to change sign near a QCP; this is observed, with the expansion coefficient over temperature displaying peaks which become more pronounced as the temperature is reduced. The functional form of this quantity as a function of field matches the field theory prediction for a QCP, apart from in the close proximity to the QCP itself where the nematic phase occurs.

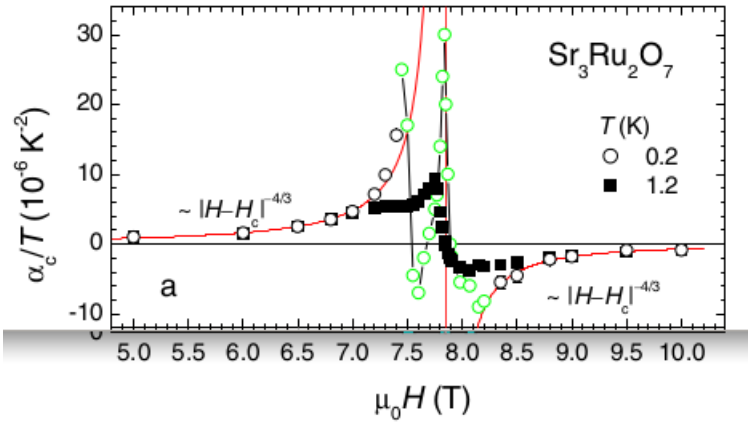

Figure 3.15: The coefficient of linear thermal expansion, symbol α_c, divided by temperature as a function of field for $T = 0.2K$ (open circles) and $T = 1.2K$ (filled squares). The green open circles indicate $T = 0.2K$ measurements for which $\frac{\partial^2 \alpha_c}{\partial T^2} \neq 0$, which indicates non-Fermi liquid behaviour. The red curve is a fit to the field theory prediction of the field-dependence of α_c/T. (Taken from reference (88)).

Signatures of quantum criticality can be seen in the specific heat. For a Fermi liquid, at low temperatures the specific heat is proportional to temperature, and the coefficient of proportionality, which is often given the symbol γ, is linear in the effective mass of the system. A large value of γ is indicative that the system has strong correlations, and γ is predicted to diverge at a quantum critical point. This parameter is found experimentally as where the curve of the specific heat divided by temperature versus temperature intercepts the vertical axis. An example of this plot is shown in the left hand side of figure 3.16, both in the zero-field case and for fields close to the metamagnetism. At zero field, the γ value is approximately 100 in units of mJK^{-2} per mole of Ru. This value is slightly more than twice as large as the values seen in Sr_2RuO_4 and $SrRuO_3$(89), which is symptomatic of the bilayer compound lying in proximity to quantum criticality, and places $Sr_3Ru_2O_7$ as a moderate strongly correlated system. By comparison, the strongly correlated heavy fermion materials are usually categorised as such if their gamma value is greater than 400(90). The γ value is measured to roughly double in the vicinity of the metamagnetism. The right hand panel of figure 3.16 plots the specific heat divided by temperature versus magnetic field for a set of fixed temperatures. Sharp behaviour occurs as the metamagnetic region is approached, and this becomes more pronounced as the temperature is reduced. The data for 0.2 Kelvin are certainly broadly suggestive that the γ value diverges.

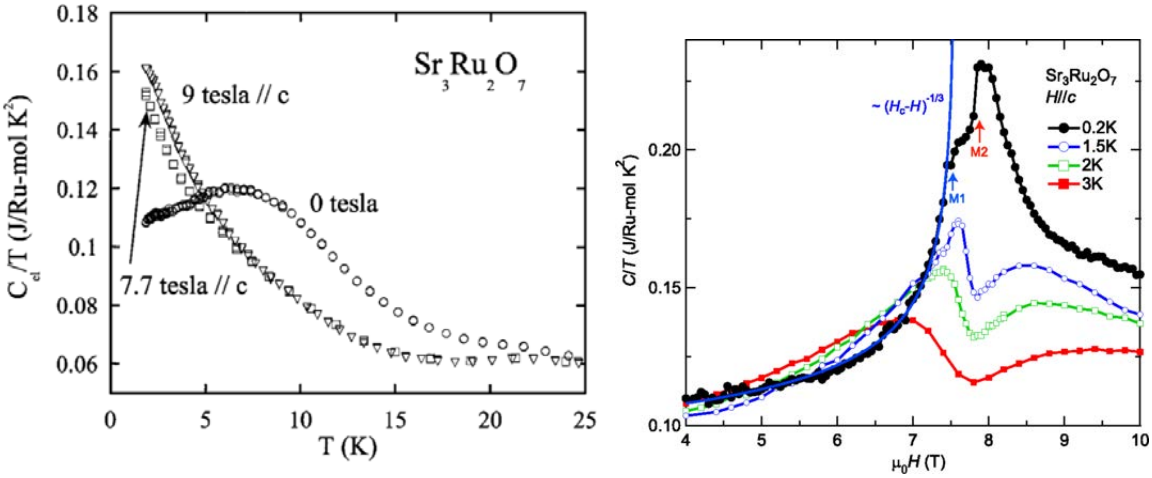

Figure 3.16: The γ-factor of specific heat divided by temperature as an indicator of quantum criticality. Left: C/T versus T for different fields. (Taken from reference (56)).
Right: C/T versus magnetic field for different isotherms. The solid blue curve is a fit to the field theory prediction of the asymptotic form of C/T. (Taken from reference (61)).

The effective mass can also be targeted with quantum oscillations experiments, and one sees essentially the same thing as indicated by the specific heat. Figure 3.17 shows the effective mass associated with two particular $Sr_3Ru_2O_7$ Fermi surface sheets obtained from de Haas-van Alphen oscillations. These quantities appear to diverge in the vicinity of the metamagnetism. This is broadly consistent with the picture indicated by the specific heat measurements; the effective masses diverge, and this is a signature of the underlying quantum critical point.

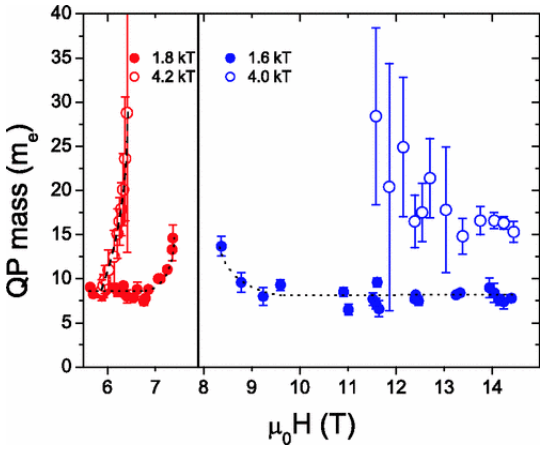

Figure 3.17: The effective masses associated with two particular Fourier components of de Haas-van Alphen oscillations as a function of a magnetic field applied in the c-axis direction. The two components are indicated by filled and unfilled circles respectively. The divergence of the effective masses in the vicinity of the metamagnetic transition is an indicator of the underlying quantum critical point. (Taken from reference (91)).

Finally, we mention measurements of the Gruneisen parameter Γ, which is given by(92),

$$\Gamma = -\frac{1}{C}\frac{dM}{dT},$$

where the quantities on the right hand side are to be evaluated with the magnetic field held constant. This quantity is predicted to change sign and to diverge close to a QCP(61). Measurements of the Gruneisen parameter are shown in Figure 3.18; the lefthand panel shows an isotherm of Γ as a function of magnetic field which is strongly peaked at the metamagnetic jump. The right hand panel shows a colour plot of Γ as a function of temperature and field, which shows that Γ changes sign crossing over the metamagnetic region.

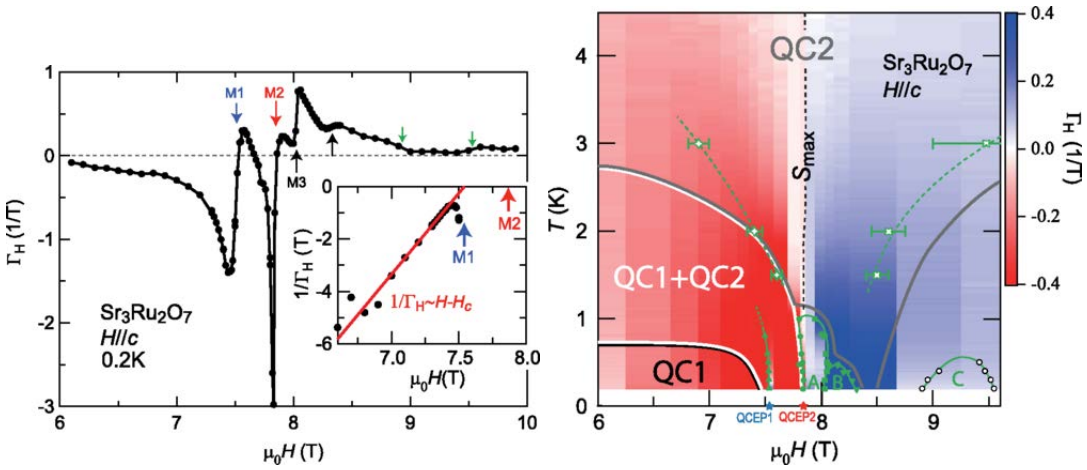

Figure 3.18: Left: Main figure: Gruneisen parameter as function of magnetic field for $T = 0.2K$. Inset: Reciprocal of the Gruneisen parammeter; the red curve shows a linear fit.
Right Colour plot of the Gruneisen parameter in the phase space of temperature and field. Solid green symbols indicate features in the Gruneisen parameter and empty green symbols indicate features in curves of specific heat versus field. (Taken from reference (61)).

3.4 Electron Nematic Phase

For the case of a magnetic field in the c-axis direction, in the vicinity of the metamagnetism there occurs a variety of exotic behaviour quite unique to this material. This includes sharp changes in the electron transport as a function of the applied field, large anisotropy in the electron transport for applied fields with an in-plane component, and the occurrence of spin-density waves. This is usually interpreted in terms of the formation of some distinct electronic phase which occurs in close proximity to the QCP in sufficiently clean samples of $Sr_3Ru_2O_7$ and masks the close approach of the QCP: this is

a familiar scenario in systems which have a QCP(86). Because this novel phase is chiefly characterised by strong anisotropy, this phase has been called a *nematic phase* in analogy to the behaviour of certain liquid crystals(93).

Our modelling, which is discussed in the next chapter, is not sophisticated enough to reproduce any of the experimental results which empirically define the nematic phase. However, it does make a prediction regarding the fundamental nature of this phase. Our model predicts that the system will exhibit a metamagnetic jump and that in the vicinity of the metamagnetic jump, the system will adopt a phase separated mixture of low- and high-magnetisation phases. We therefore postulate that this mixed phase corresponds to the nematic phase observed in $Sr_3Ru_2O_7$. This is discussed at great length in the next chapter.

The occurrence of the nematic phase in $Sr_3Ru_2O_7$ is manifested in the splitting of the first order transition associated with that QCP into *two* first order phase transitions, which mark the boundaries of the nematic phase. This is illustrated in figure 3.19 which shows the components of magnetic field in the *c*-axis and in-plane directions at which first order phase transitions occur, for two samples of $Sr_3Ru_2O_7$ with differing levels of disorder. The dirtier sample always undergoes a single first order transition, but the cleaner sample shows a single transition for the field in the *ab*-plane, which splits into two closely positioned transitions as the field is tilted towards the *c*-axis. Figure 3.20 shows the corresponding picture of the transitions in the phase space of temperature, field, and the angle of the field to the *c*-axis; this is to be compared with figure 3.11 and is a version of that figure for a cleaner sample of $Sr_3Ru_2O_7$ which shows two phase transitions and the nematic phase. Figure 3.20 reveals a quite complicated picture: whereas in the case of only a single transition the angle of the field essentially acts as a tuning parameter which monotonically pushes the endpoint to zero temperature, the appearance of the second transition in the cleaner system marks a change in the trajectory of the endpoint, and the angle appears to push the endpoints corresponding to both transitions to *higher* temperatures.

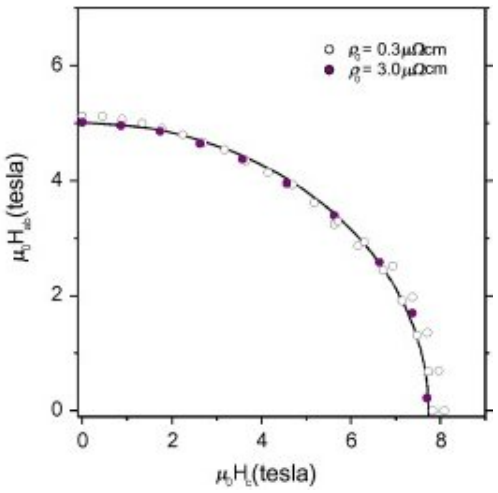

Figure 3.19: The positions of first order phase transitions plotted against the components of the applied magnetic field in the *c*-axis direction and in the *ab*-plane, for two different $Sr_3Ru_2O_7$ samples, at a fixed temperature of 0.1 Kelvin. The two samples are labelled by their resistivities, which are given in the top right of the figure; the high-resistivity (and therefore high-disorder) sample always exhibits a single transition, but for the low-resistivity (and therefore low-disorder) sample there is a single transition for the field in the *ab*-plane which splits into two closely positioned positions as the field is tilted towards the *c*-axis direction. (Taken from reference (93)).

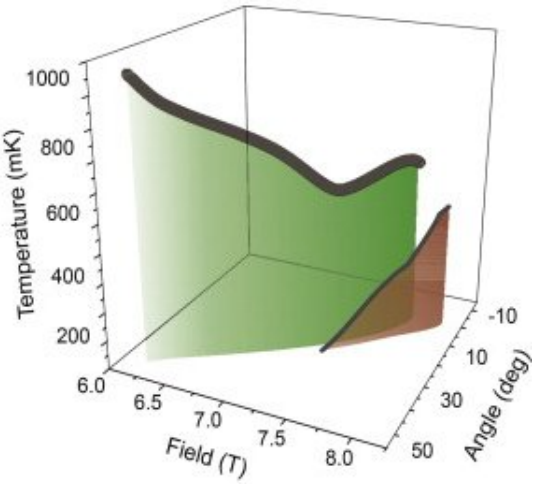

Figure 3.20: Two surfaces of first order transitions observed in a sample of $Sr_3Ru_2O_7$ from ac magnetic susceptibility measurements. Compare with figure 3.11 and see its caption; the present figure applies to a $Sr_3Ru_2O_7$ sample with less disorder than the sample in figure 3.11. (Taken from reference (94)).

The dramatic increase in the resistivity in the vicinity of the metamagnetism is exhibited in figure 3.21. The resistivity approximately doubles from a flat value in a step-like change at approximately 7.9 Tesla, and drops to a different flat value in a second step at approximately 8.1 Tesla. The flat resistivity in the high-magnetisation state is larger than that in the low-magnetisation state. In addition, a curious

feature of this figure is that the resistivity actually slightly descreases before the first step-like jump. Figure 3.22 overlays another example of this same plot with plots of the real and imaginary parts of the AC susceptibility. The susceptibility shows sharp peaks which match up extremely well with the features in the resistivity. The two peaks in the imaginary part of the susceptibility, which occur in concord with the two step-like changes in the resistivity, are interpreted as indicating two first order phase transitions. The additional peak which is exhibited in the real part of the susceptibility occurs with the small decrease in resistivity to the left of the metamagnetism and is interpreted as a crossover(60).

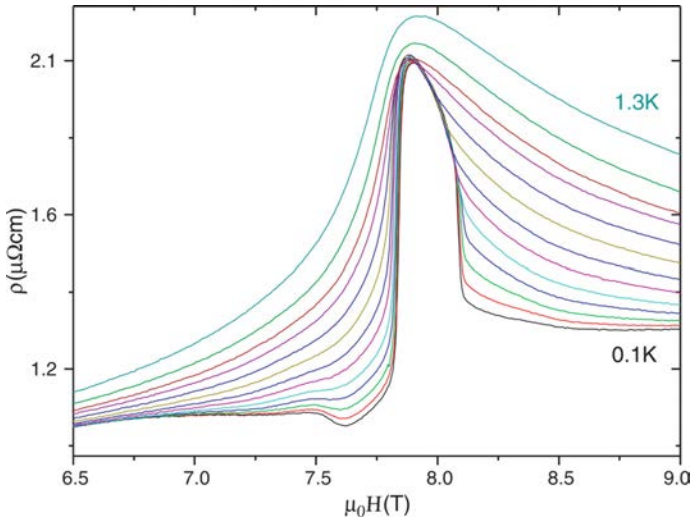

Figure 3.21: Measurements of the in-plane resistivity as a function of a magnetic field applied in the c-axis direction for temperatures ranging from 1.3K to 0.1K in steps of 0.1K. (Taken from reference (95)).

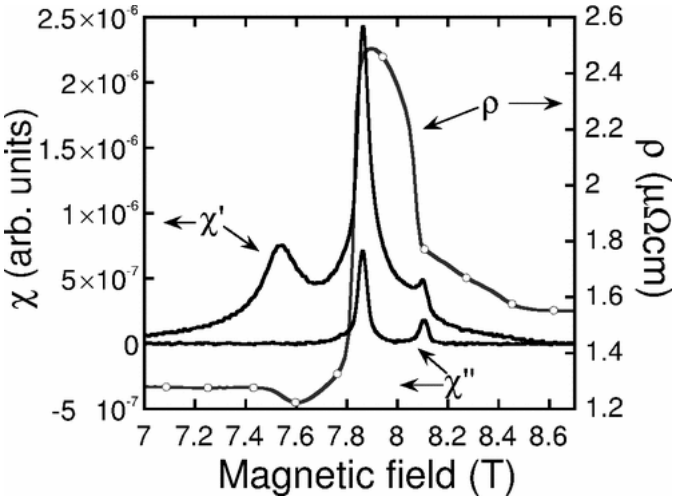

Figure 3.22: The real and imaginary parts of the AC magnetic susceptibility, χ' and χ'' respectively, as a function of a static applied field in the c axis direction, for fields in the vicinity of the metamagnetism, overlayed with the resistivity ρ which is to be compared with figure 3.21. These measurements were made at a fixed temperature of 0.02K. The peaks in the imaginary part χ'', which coincide with the step-like changes in the resistivity, indicate first order phase transitions. The real part χ' also shows coincident peaks, with an additional peak which coincides with the slight low-field descrease in the resistivity. (Taken from reference (60)).

The experiment which reveals the anisotropy if the magnetic field has an in-plane component is illustrated in figure 3.23. The direction of the magnetic field is tilted a small angle away from the c axis direction to generate a small in-plane component, and the resistivity is separately measured for two perpendicular in-plane directions, one of which coincides with the in-plane field. If the field coincides with the c-axis, then the two in-plane directions are equivalent, and both resistivities show the step-like changes depicted in figure 3.21. Upon tilting the field, the feature is shifted towards lower fields for the resistivity parallel to the field, which is consistent with the finding that the metamagnetism occurs at a lower field for in-plane fields (see figure 3.9). The anisotropy is the fact that the abrupt changes are almost entirely absent in the resistivity perpendicular to the field, which instead shows a much smaller abrupt shift between the flat low- and high-field values.

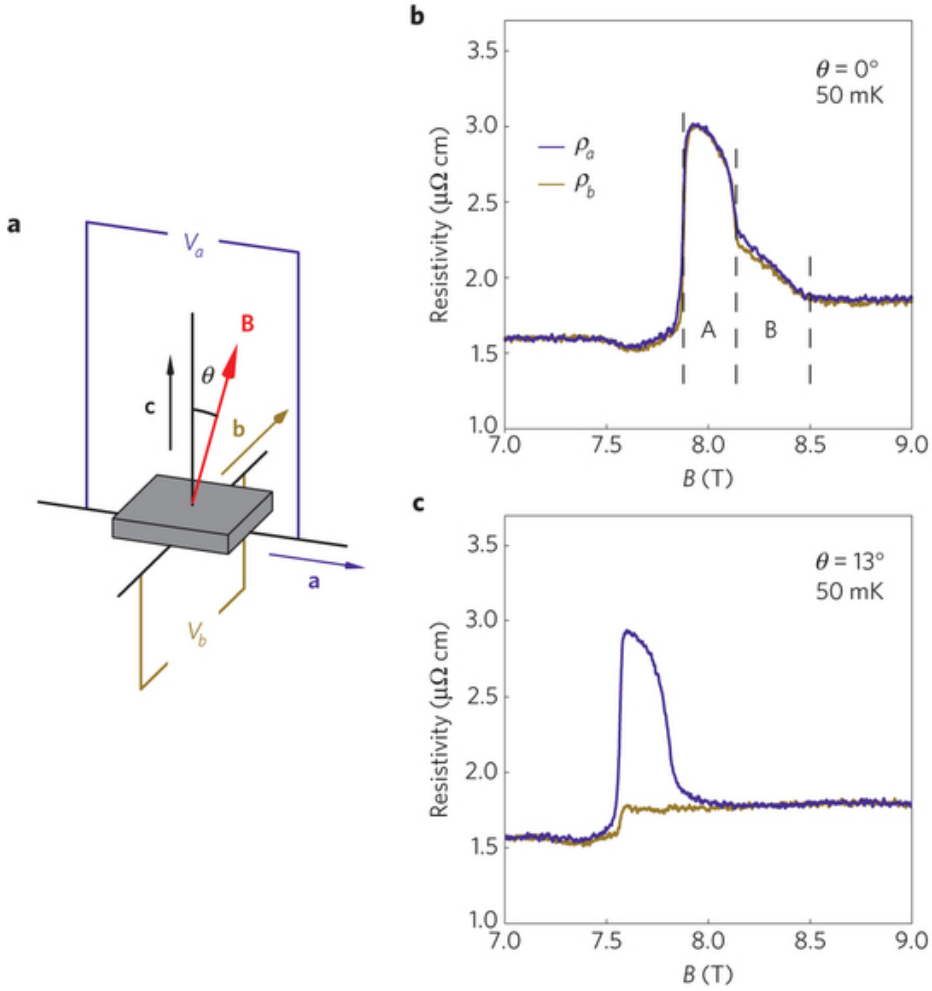

Figure 3.23: Measurements of resistivity showing the anistropy in the vicinity of the metamagnetism. Left: illustration of the experiment; a magnetic field is applied which as a small angle to the c-axis to generate a small in-plane component, and the resistivity is separately measured for two in-plane directions, the field direction and its perpendicular. Top Right: the resistivities in the two perpendicular in-plane directions as functions of field when the field is parallel to the c-axis; in this case the two in-plane directions are equivalent and both resistivities show the same step-like features. Bottom Right: the resistivities parallel and perpendicular to the in-plane field as functions of modulus of the total applied field when it is made to make an angle of 13 degrees with the c-axis; the step-like features remain in the resistivity parallel to the field but are absent in the resistivity perpendicular to the field. (Taken from reference (63)).

The anisotropy in the resistivity is accompanied by lattice distortions which break the symmetry between the two in-plane principal axes. This is revealed in anisotropy in the in-plane thermal expansion, which is shown as a function of temperature in figure 3.24. With the magnetic field parallel to the c-axis, the relative length change caused by an incremental change in temperature is the same in both the in-plane directions. Giving the field a small component in one of the in-plane directions,

anisotropy occurs at low temperatures, apparently coinciding precisely with where the anisotropy in the resistivity occurs (lefthand panel of figure 3.24). The relative length change in the field direction is smaller than that in the perpendicular direction, and is actually *negative* close to zero temperature. Increasing the angle between the magnetic field and the c axis to $\sim$ 10 degrees, one finds that the relative length changes in the two in-plane directions are of similar magnitude but opposite sign (right hand panel of figure 3.24).

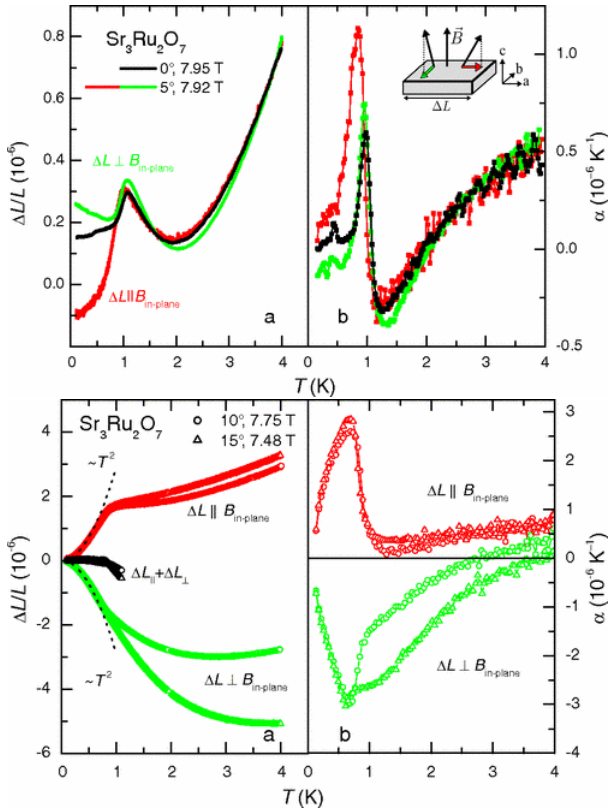

Figure 3.24: Anisotropy of the thermal expansion. Both plots show both the relative length change in the in-plane direction $\frac{\Delta L}{L}$ on the left axis and the corresponding thermal expansion coefficient $\frac{d}{dT}\left(\frac{\Delta L}{L}\right)$ and the right axis.
Left: Relative length changes and thermal expansion coefficients in both principal in-plane directions for a small tilt of the magnetic field in one of the principal directions.
Right: Relative length changes and thermal expansion coefficients in both principal in-plane directions for a larger tilt of the magnetic field in one of the principal directions.
(Both plots are taken from reference (96)).

Figure 3.25 shows how the emergence of the nematic phase masks the approach of the underlying quantum critical point. Compare with figure 3.16 in the previous section, which shows the apparent divergence of the specific heat gamma factor for fields in the metamagnetic region. Figure 3.25 shows measurements at lower temperature which reveal that this divergence is cut off, at approximately 1.2

Kelvin. This corresponds to entering the nematic phase, in which the specific heat has a an asymptotic form proportional to T^2.

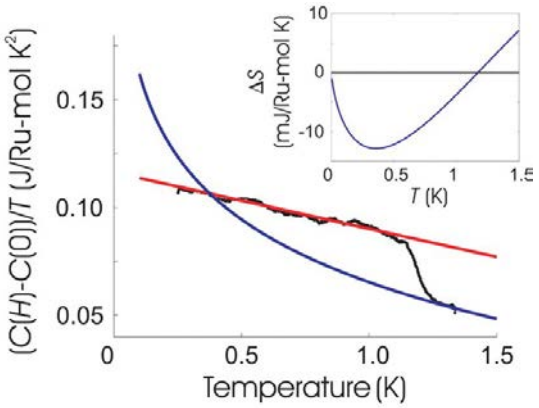

Figure 3.25: The cutoff of the diverging specific heat γ factor by the emergence of the nematic phase. Compare with figure 3.16 which shows data recorded at higher temperatures. The black curve shows C/T at a fixed field of 7.9 Tesla, which exhibits a jump upon entering the nematic phase; this corresponds to the ceiling of the region indicated in figures 3.26 and 3.27. The blue curve is an extrapolation to of the data recorded above the ceiling of the nematic phase which is consistent with the measurements exhibited in figure 3.16, showing the divergence of the γ factor associated with the underlying QCP. The red curve is a linear fit to the low temperature data, showing the specific heat is proportional to T^2 in the nematic phase. (Taken from reference (97)).

Figure 3.26 shows the quantity $\frac{\partial}{\partial B}\left(\frac{S}{T}\right)$ in the temperature-field phase space, which shows up the phase boundaries as sharp features in this quantity; figure 3.27 shows the same phase boundaries determined from features in the electrical resistivity, the ac magnetic susceptibility and the thermal expansion measured in a number of works(95). All these experiments consistently indicate that the left- and righthand boundaries of the nematic phase, beneath the red arrows in figure 3.27, are marked by first order phase transitions, but that the upper boundary of the phase is marked by a second order transition. Figure 3.28 shows how the nematic phase moves on this plot as the field is tilted a small angle away from the c-axis.

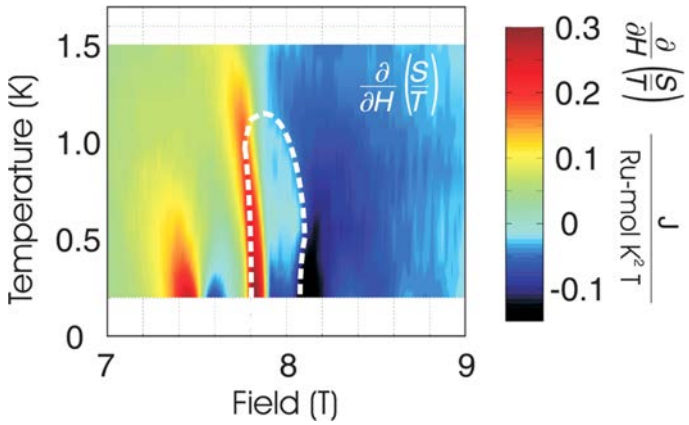

Figure 3.26: Colour plot of the derivative with respect to field of the entropy divided by temperature, as a function of temperature and field. Features in this quantity mark out a distinct equilibrium phase, outlined in the figure, which corresponds to the nematic phase. (Taken from reference (97)).

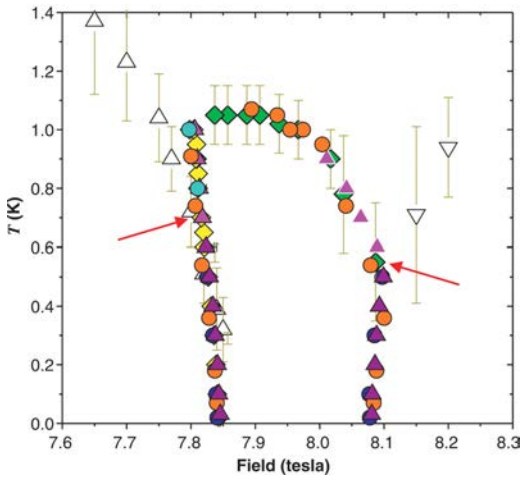

Figure 3.27: A compilation of the positions, in the phase space of temperature and field, of sharp features observed in the resistivity and the AC susceptibility. This is to be interpreted as tracing out the boundaries of the nematic phase. Below the positions marked by the red arrows, the two boundaries indicate first order phase transitions, while above these points the features indicate crossovers. (Taken from reference (95)).

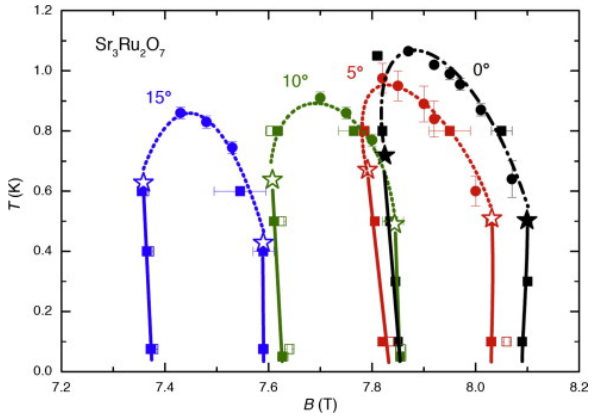

Figure 3.28: The position of the electron nematic phase in the phase space of temperature and magnetic field strength for different angles of the magnetic field; tilting the magnetic field away from the *c*-axis pushes the nematic phase towards smaller fields. (Taken from reference (96)).

The landscape of the specific heat and entropy in the vicinity of the nematic phase has been thoroughly investigated by Rost *et al*(97), and their data is exhibited in figure 3.29. These clearly show the specific heat and the entropy to be peaked in the nematic phase, showing a symmetrical shape in field. On the basis of this survey of the entropy landscape, the authors report that the nematic phase is indeed a distinct thermodynamic phase of $Sr_3Ru_2O_7$, bordered by first and second order phase transitions as described above, rather than a metastable state of some kind. This is further indicated by the lack of observed hysteretic behaviour in the nematic phase(98). Furthermore, the phase diagram is not seen to show any dependence relating to the crystal size and shape(99).

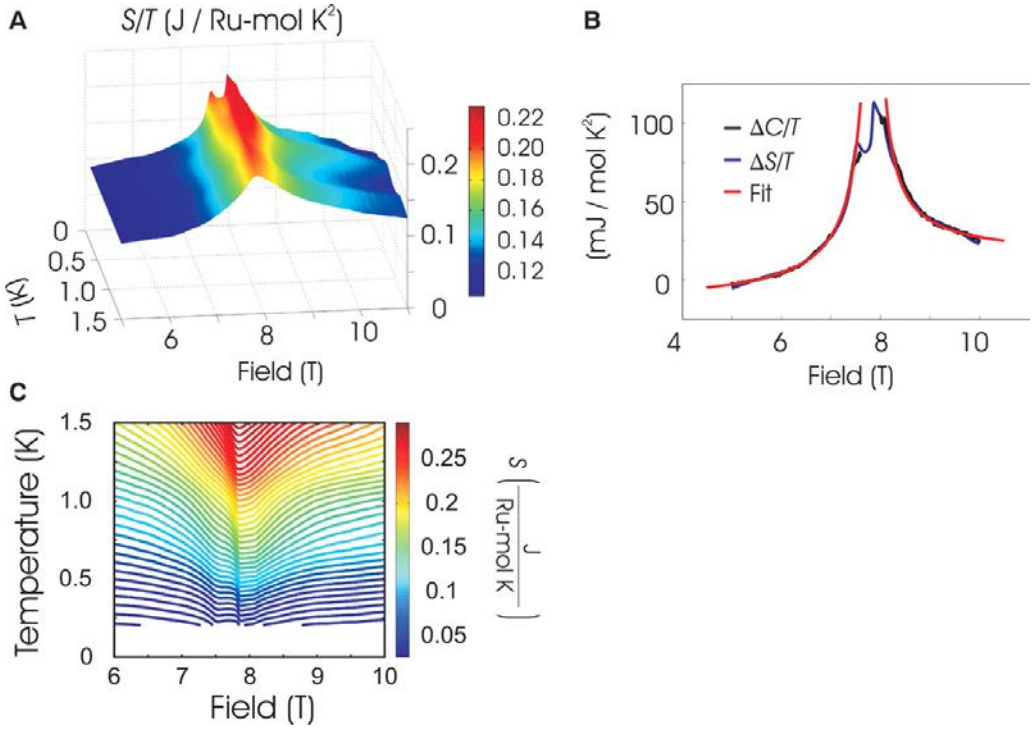

Figure 3.29: Measurements showing the entropy landscape in the region of the nematic phase.
Panel A: Entropy divided by temperature as a function of temperature and field.
Panel B: The entropy divided by temperature and specific heat divided by temperature versus field, overlayed with a fit of the form $A/|B - B_c|$.
Panel C: Contours of constant entropy plotted against temperature and field.
(Taken from reference (97)).

Suggestions regarding the nature of the nematic phase rely on one of two underlying ideas, that it is related to the formation of domains of low- and high-magnetisation phase associated with Stoner ferromagnetism(75; 96), or that it is associated with an intrinsic anisotropy in the Fermi surface itself(100; 101; 102). Our modelling in the next chapter is of the former type. Our work differs from previous domain-based explanations which have associated the Stoner magnetic instability with the d_{xy} orbital in that we advocate a magnetic instability associated with the d_{yz} and d_{zx} orbitals. The more sophisticated modelling in references (101) and (102) associate the metamagnetism with the d_{yz} and d_{zx} orbitals; it is possible that our work is consistent with the findings of those works, and that the main contribution of our work is a simple picture of the nematic phase which is obfuscated in the more sophisticated approaches.

The formation of domains in the system is quite an attractive explanation for the nematic phase: the abrupt increase in the resistivity is interpreted as due to scattering from domain walls, and the anisotropy in the resistivity for small in-plane fields is then associated with the domains running

perpendicular to the field direction, so that only the in-plane current in the field direction is required to cross domain walls. Moreover, the formation of domains is implied by low-level attempts to model the metamagnetism with Stoner ferromagnetism. Our modelling in the next chapter is based on precisely this idea. It must be pointed out that the observed lack of hysteresetic behaviour or dependence on sample size do not support the existence of domains. We simply suggest that these contradictions can be resolved if the domains in question are on extremely short length scales.

3.5 Incommensurate Spin Density Wave

In the vicinity of the metamagnetism, $Sr_3Ru_2O_7$ shows incommensurate spin density waves (SDWs) along the two orthogonal principal axes in the *ab*-plane. Figure 3.30 shows elastic neutron scattering measurements which show the SDW wave as a peak in the scattering intensity(63). For magnetic fields applied parallel to the *c*-axis, peaks are observed at the scattering vectors $(\pm 0.233, 0, 0)$, $(0, \pm 0.233, 0)$, $(\pm 0.218, 0, 0)$ and $(0, \pm 0.218, 0)$ at low temperature in the vicinity of the metamagnetism. The region in which the 0.233 wavevector is oberved appears to roughly coincide with the nematic phase; the 0.218 wavevector occurs at in slightly higher region of applied field, although there is some region of overlap where both wavelengths are observed (see righthand panel of figure 3.30). The 0.218 wavevector appears to coincide with a linear feature in the resistivity which borders the second abrupt jump in the resistivity (see figure 3.30 and the inset showing the resistivity). These two coincident phenomena, the 0.218 wavelength SDW and this feature in the resistivity, characterise a distinct region of the phase diagram; the situation is illustrated in figure 3.31.

If the applied magnetic field is given a small component along one of the in-plane principal directions, the SDW in the perpendicular in-plane direction is suppressed(63). This implies that the SDW is intimately connected with the dramatic features in the resistivity discussed above in connection with the nematic phase.

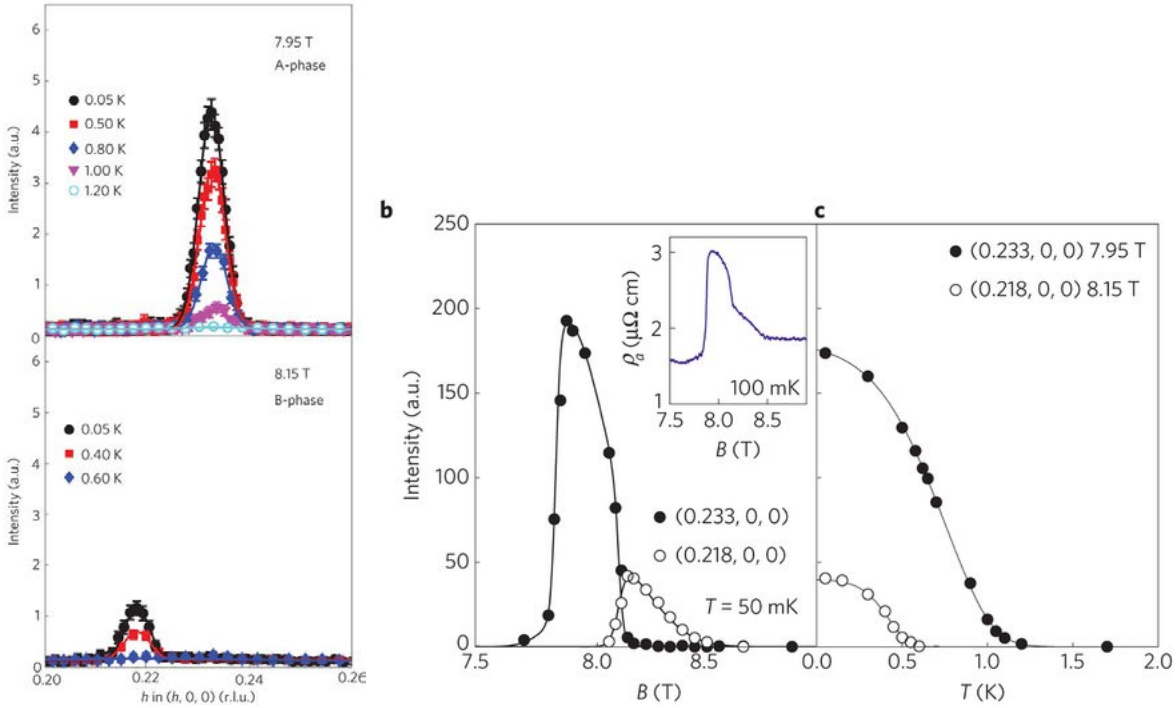

Figure 3.30: Neutron scattering measurements of the SDW.
Left: Scan of intensity observed for scattering vectors $(h, 0, 0)$.
Right: SDW intensities measured at the centre of the observed scattering peaks plotted against both magnetic field and temperature.
(Taken from reference (63)).

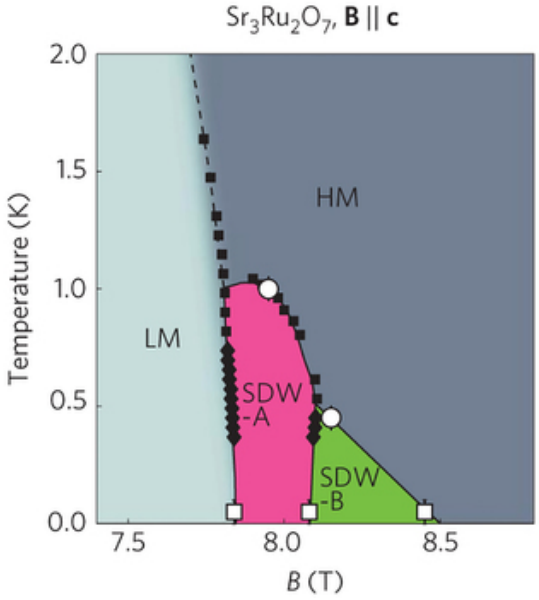

Figure 3.31: Depiction of the regions of SDW phases on the temperature-field phase space. (Taken from reference (63)).

3.6 Effect of electron doping

We finally mention a study by by Farrell *et al*(103) on the effect of electron-doping $Sr_3Ru_2O_7$. These authors investigated the effect of substituting a small fraction of the Sr atoms with La atoms; they parameterise the system with a variable y according to $Sr_{3-y}La_yRu_2O_7$. Sr has two valence electrons and La has three valence electrons, so the effect of this substitution is to dope the system with an additional y electrons per formula unit. Figure 3.32 shows the specific heat divided by temperature for differenct doping levels (compare with figure 3.16). Electron-doping the system reduces the γ value significantly, implying that the system is becoming less strongly-correlated.

This particular experiment is something that we have direct access to in our modelling: we are quite able to perform calculations varying the number of electrons in the system as an independent parameter. A section is devoted to this in the next chapter.

Figure 3.33 shows the in-plane resistivity for different doping levels (compare with figure 3.21). The disorder that is introduced into the system in substituting a small number of Sr atoms with La atoms greatly increases the resistivity, and the effect of this additional resistivity is to largely obscure the distinctive features of the resistivity associated with the nematic phase. However, Farrell *et al* argue that the position of the metmagnetic jump can still be identified in the data in figure 3.33 as the kink of inflexion in the curve of resistivity versus field(103), and with this interpretation the data show that the effect of the electron-doping is clearly to push the metamagnetism to higher fields.

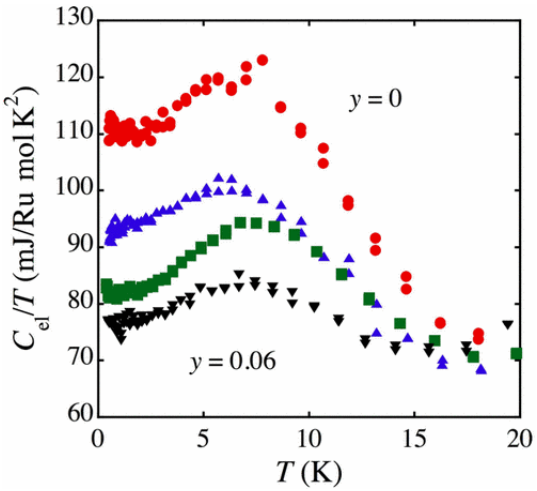

Figure 3.32: The specific heat divided by temperature of $Sr_{3-y}La_yRu_2O_7$ versus temperature for $y = 0$ (red), $y = 0.02$ (blue), $y = 0.04$ (green) and $y = 0.06$ (black). (Taken from reference (103)).

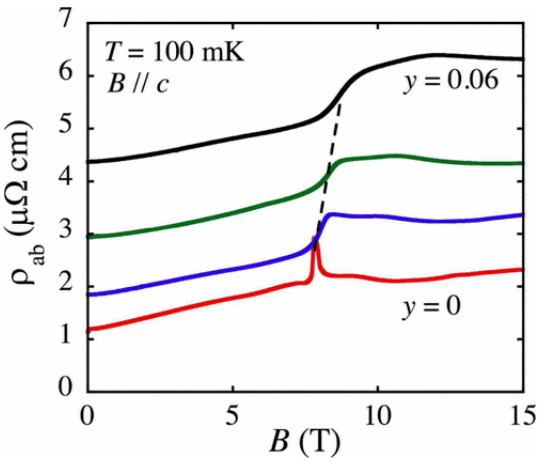

Figure 3.33: The in-plane resistivity of $Sr_{3-y}La_yRu_2O_7$ versus magnetic field, for field parallel to the c-axis, for $y = 0$ (red), $y = 0.02$ (blue), $y = 0.04$ (green) and $y = 0.06$ (black). (Taken from reference (103)).

Chapter 4

Modelling and Mean Field Theory

In this chapter we model the metamagnetism in $Sr_3Ru_2O_7$. We build a 3-band Hubbard type model for the Ru t_{2g} orbitals d_{xy}, d_{yz} and d_{zx}, which for notational convenience we shall from now on label Z, X and Y respectively; our model consists of a hybridisation term with no matrix elements between different orbital species, and an onsite interaction term. A Hartree-Fock mean field solution to the model displays a metamagnetic jump which can be made to agree with the experimental magnetisation curves. The metamagnetism is associated with the X and Y bands, both of whose band structure is one-dimensional at the level of our modelling, and consists of two non-degenerate bands. The metamagnetic jump is associated with the top-lying X/Y band being pushed past the chemical potential, and corresponding to this the disappearance of one of the Fermi surfaces. In the metamagnetic region itself, that is the region of steep rise of magnetisation with field, the mean field solution is a phase separated mixture of a low-magnetisation phase, in which all the X/Y Fermi surfaces are present, and a high-magnetisation phase where one of the X/Y Fermi surfaces has vanished. We postulate this mixed phase to correspond to the nematic phase in $Sr_3Ru_2O_7$.

The connection between the metamagnetism and singularities in the density of states has previously been considered, from a modelling perspective, by a number of authors. A picture essentially the same as ours has been proposed(75; 96), including the prediction of phase separation, but with a transition mediated by the Z bands, which are two-dimensional at the level of our modelling. In this scenario the metamagnetic jump is associated with the van Hove singularity in the Z band density of states being pushed past the chemical potential. We can obtain Z-mediated metamagnetism in our own modelling, but its sensitive dependence on the parameters in the model, particularly the size of the

second-neighbour hybridisation, suggests that this is unlikely to be the metamagnetism that occurs in $Sr_3Ru_2O_7$.

There have also been studies that present a picture of X/Y mediated metamagnetism, but these have dealt with more sophisticated models which include the spin-orbit interaction, and have in addition modelled the nematic phase itself as being associated with an anisotropic Fermi surface(101; 102). Our work uses a much simpler model and does not model any of the experimental features of the nematic phase itself. However, our own approach provides the picture of the nematic phase as a phase-separated picture of the low- and high-magnetisation phases; we presume that essentially the same phase occurs in the more sophisticated modelling, but these more sophisticated approaches, although they are more powerful, have the effect of obfuscating this simple picture.

The chapter is essentially divided into two halves: sections 4.1 to 4.3 deal with building the model and introduce some important physical ideas, such as the Stoner criterion for the susceptibility of metals to ferromagnetism which is covered in section 4.2; sections 4.4 to 4.6 present analysis of the behaviour of the model.

In the first part of the chapter, the aim is to build our model for $Sr_3Ru_2O_7$ from the ground up. In this mindset, section 4.1 acts as an introduction to how one models electrons in crystalline solids in general, and is very much textbook material. This section introduces the two key concepts of Wannier orbitals, which are mutually orthogonal single-particle states localised at sites of the crystalline lattice, and the second quantised representation, which is the use of the Fermi operators $c^\dagger_{\gamma\sigma}$ to represent the electron states. At the end of section 4.1 we will have essentially derived the Hubbard model, which is the famous elementary model of interacting electrons in crystalline solids.

In section 4.2 we discuss Stoner ferromagnetism as applied to the Hubbard model, and we derive the Stoner criterion. In essence, Stoner ferromagnetism is the idea that, in the mean field approximation, a large repulsion between particles can drive a metallic system ferromagnetic, but this is strongly dependent on the properties of the single-particle density of states at the Fermi surface. Systems are strongly susceptible to ferromagnetism if the Fermi level is in close proximity to large peaks or singularities in the density of states. This is precisely the case in $Sr_3Ru_2O_7$, where the density of states contains a number of singularities. In addition to introducing the key physical idea that also applies to our model of $Sr_3Ru_2O_7$, the derivation of the Stoner criterion also serves to introduce the tool which we shall use to tackle that model, namely Hartree-Fock mean field theory.

We build our model of $Sr_3Ru_2O_7$ in section 4.3. We begin with discussions which apply to modelling

transition metal oxides in general, the crystal field interaction and Hund's rules. We thereby arrive at the picture that to leading order the energetically relevant Ru degrees of freedom are the three approximately degenerate t_{2g} states, each of which wavefunctions are mutually orthogonal orientations of the same shape associated with the three principal crystal axes. The model which we are building will then consist of three bands, or six when a magnetic field is included.

Our model consists of a hybridisation term and an onsite interaction term. The essential physics is contained in just two energy scales, t which is associated with hybridisation, and U which is associated with the interaction. The situation of a metal on the verge of a ferromagnetic instability in a mean field picture is that t is the largest energy scale, but not greatly so, that is zt is slightly larger than U, where z is the co-ordination number. We begin with the hybridisation term, and we show how effective Ru-Ru hopping arises perturbatively from miscroscopic calculations in which the intervening O is occupied in a virtual state. We then discuss the on-site interaction term. We calculate the complete on-site Coulomb interaction between electrons in the t_{2g} states, which can be parameterised with two energy scales U and J. This then provides the model which we shall study in the remainder of the chapter. We give some discussion to rather important effects which we do not include in the model, which we regard as vital to an attempt to model the details of the nematic phase in $Sr_3Ru_2O_7$, the long-range Coulomb interaction and the spin-orbit interaction. We finally conclude section 4.3 with some remarks concerning how the mean field solution of our model actually relates to the microscopic physics of the real material; our viewpoint is that, since $Sr_3Ru_2O_7$ is an itinerant ferromagnet, and this is precisely the kind of state that mean field theory predicts, it is valid to model the material in this way, despite the limitations of mean field theory.

In the latter half of the chapter, we exhibit calculations using the model which we have built. In section 4.4, we consider only the pure tight binding model which does not include the interaction term. The tight binding Fermi surface can be made to qualitatively agree with the experimental Fermi surface. In addition, the tight binding theory provides much of the framework for later calculations. Applying a magnetic field raises the energy of the spin-$\downarrow$ particles and lowers the energy of the spin-$\uparrow$ particles, and at some field the top-lying spin-$\downarrow$ X/Y band is pushed past the chemical potential. The transition from the full 6-band state to the state where the top-lying spin-$\downarrow$ X/Y band is missing occurs with a kink in the curve of magnetisation versus field, but when interactions are included this kink can be made to be a steep jump: metamagnetism.

We then finally come to dealing with our full model including onsite interactions. We solve the

model approximately using Hartree Fock mean field theory. In section 4.5 we provide the formalism of the theory and describe how the mean field calculations are actually performed. The calculations are then exhibited in section 4.6. These calculations show that, if large enough interactions are included, the magnetisation exhibits a metamagnetic jump between the 6-band state and the 5-band state where the top-lying spin-$\downarrow$ X/Y band is absent, and the size of this jump can be made to agree quantitatively with the experiments. In the region of the jump, the lowest energy mean field solution is a phase separated mixture of 6-band and 5-band solutions, which we postulate to correspond to the nematic phase in $Sr_3Ru_2O_7$.

In the remainder of section 4.6 we provide more mean field calculations in which we make various alterations to the model. A large number of these calculations are related to the possibility of the Z bands playing a role in the $Sr_3Ru_2O_7$ metamagnetism. We alter the model in the following ways that might be expected to result in the Z bands playing a role: we tune the value of the second neighbour hopping in order to place the Z band van Hove singularity close to the Fermi surface at zero field; we increase the Z density of states while leaving the X/Y density of states unaltered; we include a crystal field splitting which reduces the energy of the Z bands relative to the X/Y bands. The former two alterations can force Z metamagnetism to occur, but in the case of changing the second neighbour hopping fine tuning of this parameter is required and the size of the magnetisation jump is smaller than the one in $Sr_3Ru_2O_7$, and in the case of reducing the Z bandwidth the size of the magnetisation jump is much larger than the one in $Sr_3Ru_2O_7$. Imposing the crystal field splitting does not promote Z metamagnetism and the X/Y bands remain dominant. The final calculations deal with the effect of doping the system by a small amount. Electron-doping reduces, and hole doping increases, the field at which the X/Y metamagnetism occurs; puzzlingly the relevant experiments reveal the opposite trend.

4.1 Fundamentals

In this section we introduce some of the underlying concepts of modelling condensed matter systems. We firstly introduce the framework of modelling electrons moving in a crystal lattice. We show how one can build a picture of the electron as sitting on one of the lattice sites; one can construct a localised wavefunction centred on one of the lattice sites, such that this state is orthogonal to the wavefunction centred on any other lattice site. We describe separately the second quantised representation of many-body systems. This description naturally incorporates both the requirement that systems of identical fermions exhibit antisymmetry under the exchange of two particles, and the possibility of fluctuations

in the number of particles.

4.1.1 Single-particle states on a lattice: Wannier orbitals

In this section we introduce how one describes the wavefunction of a single particle in a crystalline solid. The physical picture is that of a metal, in which the electron moves about a lattice of positive ions. We consider a single electron which is moving in a periodic potential which is formed by the underlying positive ions. Let the potential due to a single ion be placed at the origin of the co-ordinate system be $-V(|\vec{r}|)$. For the hydrogen atom, one would take this to be the bare Coulomb interaction,

$$V(|\vec{r}|) = \frac{e^2}{|\vec{r}|},$$

while for larger atoms one typically regards the nucleus and the core electrons as a point charge which provides a field for the valence electrons, and so one still considers the Coulomb potential. The Hamiltonian of an electron in this field is

$$\frac{\hat{p}^2}{2m} - V(|\vec{r}|). \tag{4.1}$$

Let $\psi(\vec{r})$ be the groundstate wavefunction of this system, and let E_0 be the groundstate energy:

$$\left[\frac{\hat{p}^2}{2m} - V(|\vec{r}|)\right]\psi(\vec{r}) = E_0\psi(\vec{r}). \tag{4.2}$$

We now consider a regular $\mathcal{N}$-site lattice, with periodic boundary conditions, of these ions, for which the single-electron Hamiltonian is

$$H = \frac{\hat{p}^2}{2m} - \sum_j V(|\vec{r} - \vec{R}_j|), \tag{4.3}$$

where the index j labels the lattice sites and $\vec{R}_j$ is the position of the site j. Now, if ions are infinitely far apart, the electron is simply bound around one of the sites in the state ψ; there are therefore $\mathcal{N}$ degenerate states which have the particle localised around each of the sites,

$$\psi_j(\vec{r}) = \psi(\vec{r} - \vec{R}_j). \tag{4.4}$$

As the ions are made to approach each other, the degeneracy is lifted and for $\mathcal{N} \gg 1$ the non-degenerate eigenstates states can be regarded as a continuous *band* of states. The width of the band increases as the ions are brought closer together, this being effectively the energy that is gained in having the particle move around the lattice. The states on each of the individual atoms are said to *hybridise* with one another to produce the delocalised states.

A difficulty in describing this problem is that the states ψ_j on different lattice sites are not orthogonal to one another, but have a finite overlap which is a function of the separation of the sites,

$$\langle \psi_j | \psi_{j'} \rangle = \mathcal{O}(|\vec{R}_j - \vec{R}_{j'}|). \tag{4.5}$$

However, one can always construct a wavefunction such that states on different sites are orthogonal. The states that result from this construction are called *Wannier orbitals*, and we shall now indicate how they should be constructed out of the states ψ_j. One introduces the states,

$$|\psi_{\vec{k}}\rangle = \frac{1}{\sqrt{\mathcal{N}}} \sum_j e^{i\vec{k}\cdot\vec{R}_j} |\psi_j\rangle, \tag{4.6}$$

where the so-called Bloch wavevector $\vec{k}$ takes $\mathcal{N}$ values which are the dual set to the vectors $\vec{R}_j$. The expression 4.6 is the Bloch transform of the state $|\psi_j\rangle$. It is easily verified that these states are orthogonal, and we have,

$$\langle \psi_{\vec{k}} | \psi_{\vec{k}'} \rangle = \delta_{\vec{k},\vec{k}'} \mathcal{O}_{\vec{k}}, \tag{4.7}$$

where

$$\mathcal{O}_{\vec{k}} = \sum_j e^{i\vec{k}\cdot\vec{R}_j} \mathcal{O}(|\vec{R}_j|) = \sum_j e^{i\vec{k}\cdot\vec{R}_j} \int \psi^*(\vec{r}) \psi(\vec{r} - \vec{R}_j) d^3r. \tag{4.8}$$

Now we define

$$|\psi^W_{\vec{k}}\rangle = \frac{1}{\sqrt{\mathcal{O}_{\vec{k}}}} |\psi_{\vec{k}}\rangle \tag{4.9}$$

to obtain an orthonormal basis. The Wannier states $|\psi^W_j\rangle$ are then obtained by performing the inverse Bloch transform to return to a real-space description,

$$|\psi^W_j\rangle = \frac{1}{\sqrt{\mathcal{N}}} \sum_{\vec{k}} e^{-i\vec{k}\cdot\vec{R}_j} \frac{1}{\sqrt{\mathcal{O}_{\vec{k}}}} |\psi_{\vec{k}}\rangle. \tag{4.10}$$

It is easily verified directly that the Wannier states are orthonormal. They are given in terms of the

original states $|\psi_j\rangle$ by

$$|\psi_j^W\rangle = \sum_{j'} u(\vec{R}_j - \vec{R}_{j'})|\psi_{j'}\rangle, \tag{4.11}$$

where

$$u(\vec{R}_j - \vec{R}_{j'}) = \frac{1}{\mathcal{N}} \sum_{\vec{k}} e^{-i\vec{k}\cdot(\vec{R}_j - \vec{R}_{j'})} \frac{1}{\sqrt{\mathcal{O}_{\vec{k}}}}. \tag{4.12}$$

The wavefunction of the Wannier state, centered on the origin, is given by

$$\psi^W(\vec{r}) = \sum_j u(\vec{R}_j)\psi(\vec{r} - \vec{R}_j). \tag{4.13}$$

The amplitude $u(\vec{R}_j)$ is largest for the onsite orbital $\psi(\vec{r})$, and decreases with range. The Wannier orbital is approximately the original onsite wavefunction, with corrections from the offsite wavefunctions which become increasingly small at long range.

The eigenstates of the system are precisely the states $|\psi_{\vec{k}}^W\rangle$ which are obtained as the Bloch transform of the Wannier states. The Bloch tranform in general provides the eigenstates for periodic Hamiltonians at the single particle level. The Bloch states are the eigenstates of precisely the translations under which the Hamiltonian is symmetric. The formalism which underpins this is that, for an operator $\hat{S}$ which commutes with the Hamiltonian,

$$[\hat{S}, H] = 0, \tag{4.14}$$

there can be no nonzero matrix elements of H between eigenstates of $\hat{S}$ belonging to different eigenvalues, and therefore the eigenstates of $\hat{S}$ break up the full Hilbert space of H into a set of disconnected subspaces which can be separately diagonalised. The Bloch transform, in the context we have described, breaks the problem into $\mathcal{N}$ disconnected subspaces which are labelled by the Bloch wavevectors $\vec{k}$. In general the dimension of the $\vec{k}$ subspace is precisely the number of degrees of freedom per lattice site of the Hamiltonian. In the above we have chosen to include only a single degree of freedom per lattice site, the orbital ψ_j.

4.1.2 Second quantised description of many-body systems

A system of many particles can be described by a wavefunction which depends upon the co-ordinates of each of the particles, $\Psi(\vec{r}_1, \vec{r}_2, ...)$. In general this wavefunction can be written in terms of single

particle states. Let $\psi_\gamma(\vec{r})$ be some complete linearly independent set of single particle states. The general N-particle wavefunction can then be written as

$$\Psi(\vec{r}_1, \vec{r}_2, ..., \vec{r}_N) = \sum_{\gamma_1,\gamma_2,...,\gamma_N} a_{\gamma_1,\gamma_2,...,\gamma_N} \psi_{\gamma_1}(\vec{r}_1) \times \psi_{\gamma_2}(\vec{r}_2) \times ... \times \psi_{\gamma_N}(\vec{r}_N). \tag{4.15}$$

The indistinguishability of identical particles places some restrictions on the coefficients $a_{\gamma_1,\gamma_2,...,\gamma_N}$ in this expansion. For describing a system of fermions, the wavefunction must be antisymmetric with respect to the exchange of any pair of particles. For two particles, this leads to the general form,

$$\Psi(\vec{r}_1, \vec{r}_2) = \sum_{\gamma_1 \neq \gamma_2} b_{\gamma_1,\gamma_2} \left[\psi_{\gamma_1}(\vec{r}_1)\psi_{\gamma_2}(\vec{r}_2) - \psi_{\gamma_1}(\vec{r}_2)\psi_{\gamma_2}(\vec{r}_1)\right]. \tag{4.16}$$

The general antisymmetric form becomes increasingly complicated for larger and larger numbers of particles. Note that the property of antisymmetry under the exchange of any pair of particles forbids wavefunctions which have more than one particle in the same single-particle state, which is the principle of Pauli exclusion.

The complicated structure which is demanded by the antisymmetry makes the wavefunction a rather unwieldy description of a many-particle state. In addition, the many-body wavefunction is not well-constructed for systems for which the number of particles is not fixed. In regard to both of these concerns, a more convenient description of many-body systems is the second-quantised form. One introduces the vaccuum state $|0\rangle$ which corresponds to there being no particles in the system. One associates with each of the single-particle states ψ_γ a so-called creation operator $c^\dagger_\gamma$, the operation of which is defined to provide a particle in the state ψ_γ. So, the state $c^\dagger_\gamma|0\rangle$ corresponds to the single-particle state $\psi_\gamma(\vec{r})$. A many body state is created by acting multiple creation operators on the vaccuum. The antisymmetry with respect to the exchange of any pair of particles is incorporated into the definition of the creation operators, in the additional enforced condition that any two creation operators anticommute with each other,

$$\{c^\dagger_\gamma, c^\dagger_{\gamma'}\} = 0. \tag{4.17}$$

The states $c^\dagger_{\gamma_1} c^\dagger_{\gamma_2} ... c^\dagger_{\gamma_N}|0\rangle$ form a basis set, with the proviso that, as a consequence of the anticommutability, a consistent ordering of the creation operators must be used in the basis states, for example the order that operators with a smaller index always appear to the left of operators with a larger index

$\gamma_1 < \gamma_2 < ... < \gamma_N$. Note that putting $\gamma' = \gamma$ in expression 4.17 implies

$$\left(c_\gamma^\dagger\right)^2 = 0, \tag{4.18}$$

which expresses Pauli exclusion because acting $c_\gamma^\dagger$ on any state which already has a particle in the state ψ_γ gives zero. The Hermitian conjugate operators c_γ are called annihilation operators because they have the effect of removing a particle in the state ψ_γ. The annihilation operators produce zero acting on the vaccuum,

$$c_\gamma|0\rangle = 0. \tag{4.19}$$

The final part of the description is the anticommutation relation between the annihilation operators and the creation operators, the anticommutator being given by the overlap of the corresponding single particle states $|\psi_\gamma\rangle$,

$$\{c_\gamma, c_{\gamma'}^\dagger\} = \langle\psi_\gamma|\psi_{\gamma'}\rangle. \tag{4.20}$$

If the single particle states are orthogonal, then the creation and annihilation operators for different states anticommute; as an aside, note that it follows from this that c_γ acting on any state which does not have a particle in the state ψ_γ, and not only the vaccuum, gives zero. Throughout this chapter, it will be assumed that one is working with the Wannier states which are orthonormal, so that this condition is simplified to,

$$\{c_\gamma, c_{\gamma'}^\dagger\} = \delta_{\gamma,\gamma'}. \tag{4.21}$$

We are now in a position to write down a many-particle Hamiltonian in the second quantised form. We begin with the non-interacting Hamiltonian; consider the periodic lattice of ions described in the previous section, but where we now allow more than one particle in the system:

$$H = \sum_{i=1}^{N} \frac{\hat{p}_i^2}{2m} - \sum_{i=1}^{N}\sum_{j} V(\vec{r}_i - \vec{R}_j). \tag{4.22}$$

Let the $c_j^\dagger$ be the creation operator for a Wannier state $\psi(\vec{r})$ on the site j. In this representation the non-interacting Hamiltonian is written as

$$H = -\sum_{j,j'} t_{j,j'} c_j^\dagger c_{j'}, \tag{4.23}$$

where

$$-t_{j,j'} = \int d^3r \psi_j^*(\vec{r}) \left[\frac{\hat{p}^2}{2m} - \sum_j V(\vec{r} - \vec{R}_j) \right] \psi_{j'}(\vec{r}). \tag{4.24}$$

The terms in the Hamiltonian with $j \neq j'$ are often referred to as "hopping" terms, in that they move the particle from the site j' to the site j. This Hamiltonian is diagonalised by the Bloch transform,

$$c_{\vec{k}}^\dagger = \frac{1}{\sqrt{\mathcal{N}}} \sum_j e^{i\vec{k}\cdot\vec{R}_j} c_j^\dagger, \tag{4.25}$$

and the band structure is given by

$$\epsilon_{\vec{k}} = -\sum_j t_{0,j} e^{i\vec{k}\cdot\vec{R}_j}. \tag{4.26}$$

The lowest energy state with N particles in the system is to occupy the N $\vec{k}$-states with the lowest energy; one therefore has in the thermodynamic limit a continuous region of $\vec{k}$-space which is occupied, up to some level $\epsilon_{\vec{k}} = \epsilon_F$ which is called the Fermi surface. If the number of particles is not fixed, one introduces the chemical potential μ and one instead minimises $H - \mu N$ at constant μ; this produces a Fermi surface $\epsilon_F = \mu$.

This touches on an important point regarding the calculations to follow in this chapter, which is that in most instances we wish to perform calculations at constant particle number N, but we instead have access to calculations at constant chemical potential μ. This leads to a scheme where one uses the chemical potential as the independent variable and calculates the particle number as a function of μ, and then one adjusts the input μ to obtain the desired value of N.

Of course, all of the interesting physics in condensed matter systems arises out of the interactions between electrons. The many-particle Hamiltonian with the same pairwise interaction between all pairs of particles,

$$H = \sum_{i=1}^N \frac{\hat{p}_i^2}{2m} - \sum_{i=1}^N \sum_j V(\vec{r}_i - \vec{R}_j) + \sum_{i=i'+1}^N \sum_{i'=1}^N U(\vec{r}_i - \vec{r}_{i'}), \tag{4.27}$$

in the second quantised form gives again the hopping terms with additional two-particle terms which describe the interactions,

$$H = -\sum_{j,j'} t_{j,j'} c_j^\dagger c_{j'} + \sum_{j_1,j_2,j_1',j_2'} U_{j_1,j_2;j_1'j_2'} c_{j_1}^\dagger c_{j_2}^\dagger c_{j_2'} c_{j_1'}. \tag{4.28}$$

The interaction parameters are given by,

$$U_{j_1,j_2;j_1',j_2'} = \int d^3r \int d^3r' \psi^*_{j_1}(\vec{r})\psi^*_{j_2}(\vec{r'})U(\vec{r}-\vec{r'})\psi_{j_2'}(\vec{r'})\psi_{j_1'}(\vec{r}). \tag{4.29}$$

The electron spin degree of freedom can be included by using the creation operators,

$$c_j^\dagger \rightarrow c_{j\sigma}^\dagger$$

where σ labels the two spin-states. Neither the hybridisation nor the Coulomb interaction (which we are treating as a classical field) can act to change the electron spin, and so the Hamiltonian 4.28 including spin becomes,

$$H = -\sum_{j,j'}\sum_{\sigma} t_{j,j'} c^\dagger_{j\sigma} c_{j'\sigma} + \sum_{j_1,j_2,j_1',j_2'} \sum_{\sigma_1,\sigma_2} U_{j_1,j_2;j_1'j_2'} c^\dagger_{j_1\sigma_1} c^\dagger_{j_2\sigma_2} c_{j_2'\sigma_2} c_{j_1'\sigma_1}, \tag{4.30}$$

where $t_{j,j'}$ and $U_{j_1,j_2;j_1',j_2'}$ are as previously defined.

The largest conributions are those which involve orbitals on neighbouring sites; a first approximation is therefore to include only the onsite parameters, in which case one obtains,

$$H = -t \sum_{\langle jj'\rangle\sigma} c^\dagger_{j\sigma} c_{j'\sigma} + U \sum_j c^\dagger_{j\uparrow} c_{j\uparrow} c^\dagger_{j\downarrow} c_{j\downarrow}, \tag{4.31}$$

which is the Hubbard model. We have written the interaction term explicitly in terms of the operators $c^\dagger_{j\sigma} c_{j\sigma}$ which correspond to the number of spin-σ particles on site j; this makes clear the physical meaning of this term, which is to impose an energy penalty $+U$ if there are two particles on the site j.

4.2 Mean field theory of the Hubbard model: Stoner ferromagnetism

The purpose of this section is to show how the itinerant ferromagnetic state, which is the style of state we intend to model in $Sr_3Ru_2O_7$, arises in the mean field solution of an interacting model. To this end, we consider the simplest interacting model, the Hubbard model. We apply Hartree-Fock mean field theory to the Hubbard model, and investigate the susceptibility to magnetism by attempting to

minimise the mean field energy written as a power series in the magnetisation. The coefficients of the series are functions of the single-particle density of states and its derivatives; consideration of the properties of these coefficients for which a finite magnetisation minimises the energy provide criteria in terms of the density of states for when the system is predicted to be ferromagnetic, and whether the transition to ferromagnetism is first or second order.

This mean field picture of itinerant ferromagnetism arising from the repulsive interaction between particles is referred to as Stoner ferromagnetism(104). It is important to discuss this because in our modelling of $Sr_3Ru_2O_7$ we shall obtain metamagnetism arising from this very same physics, and therefore the content of this section effectively underpins our work on $Sr_3Ru_2O_7$. In addition to the physical arguments, we also make use of this section to describe the Hartree-Fock mean field method, which is the method we shall apply to our Hubbard-type model for $Sr_3Ru_2O_7$.

The Hubbard model is given by,

$$H = -t \sum_{\langle jj' \rangle \sigma} c^{\dagger}_{j\sigma} c_{j'\sigma} + U \sum_{j} c^{\dagger}_{j\uparrow} c_{j\uparrow} c^{\dagger}_{j\downarrow} c_{j\downarrow}. \tag{4.32}$$

In the non-interacting case $U = 0$, the Hamiltonian is diagonalised by the Bloch transform

$$c^{\dagger}_{\vec{k}\sigma} = \frac{1}{\sqrt{\mathcal{N}}} \sum_{j} e^{-i\vec{k}\cdot\vec{R}_j} c^{\dagger}_{j\sigma}, \tag{4.33}$$

providing the single-particle spectrum

$$\epsilon_{\vec{k}} = -tz\gamma_{\vec{k}}, \tag{4.34}$$

where z is the number of nearest neighbour sites on the lattice and $\gamma_{\vec{k}}$ is the structure factor,

$$\gamma_{\vec{k}} = \frac{1}{z} \sum_{\vec{\tau}} e^{i\vec{k}\cdot\vec{\tau}}, \tag{4.35}$$

where τ is the displacement vector from a lattice site to one of its nearest neighbours. The density of states per spin-species is given by

$$\rho(\epsilon) = \frac{1}{\mathcal{N}} \sum_{\vec{k}} \delta(\epsilon - \epsilon_{\vec{k}}), \tag{4.36}$$

providing the number of particles as

$$n = \int d\epsilon \rho(\epsilon) f(\epsilon - \mu) = \frac{1}{\mathcal{N}} \sum_{\vec{k}} f(\epsilon_{\vec{k}} - \mu) \tag{4.37}$$

where $f(x)$ is the Fermi function,

$$f(x) = \frac{1}{e^{x/T} + 1}, \tag{4.38}$$

where T is the temperature. The groundstate has the particles occupying the lowest-energy states possible, so that all of the single-particle states for which $\epsilon_{\vec{k}} < \mu$ are occupied and all of the higher-lying states are empty. The occupancy in reciprocal space is described by the Fermi surface,

$$\epsilon_{\vec{k}} = \mu. \tag{4.39}$$

We apply the well-known Hartree-Fock mean field theory, which is a prescription for obtaining the variationally optimised non-interacting state for approximating the ground state of a many-body system. Explicitly, one calculates the so-called mean field energy $E^{mf} = \langle H \rangle$, which for a non-interacting state can be expressed entirely in terms of single-particle correlations (this is essentially the content of Wick's theorem(105)). From this, the Hartree-Fock mean field Hamiltonian is constructed in terms of a set of single particle operators $\hat{\eta}_\alpha$ and the corresponding correlations $\eta_\alpha = \langle \hat{\eta}_\alpha \rangle$ according to(106),

$$H^{mf} = \sum_\alpha \frac{\partial E^{mf}}{\partial \eta_\alpha} \hat{\eta}_\alpha - \sum_\alpha \frac{\partial E^{mf}}{\partial \eta_\alpha} \eta_\alpha + E^{mf}. \tag{4.40}$$

The groundstate of this single-particle Hamiltonian provides precisely the variationally optimised non-interacting approximation to the real groundstate(106). The physical picture is that the interactions are being approximated by coupling the particles to the *mean fields* $\partial E^{mf}/\partial \eta_\alpha$, which describe the effect of the interactions on average.

For a non-interacting state, we have,

$$\langle c^\dagger_{j\uparrow} c_{j\uparrow} c^\dagger_{j\downarrow} c_{j\downarrow} \rangle = \langle c^\dagger_{j\uparrow} c_{j\uparrow} \rangle \langle c^\dagger_{j\downarrow} c_{j\downarrow} \rangle - \langle c^\dagger_{j\uparrow} c_{j\downarrow} \rangle \langle c^\dagger_{j\downarrow} c_{j\uparrow} \rangle + \langle c^\dagger_{j\uparrow} c^\dagger_{j\downarrow} \rangle \langle c_{j\downarrow} c_{j\uparrow} \rangle. \tag{4.41}$$

We make the assumption that there are no pairing correlations, $\langle c^\dagger_{j\uparrow} c^\dagger_{j\downarrow} \rangle = 0 = \langle c_{j\downarrow} c_{j\uparrow} \rangle$, and so the last term in this expression vanishes. Furthermore, we can express this expectation value in terms of

the average number of particles on the site,

$$n_j = \langle c_{j\uparrow}^\dagger c_{j\uparrow} + c_{j\downarrow}^\dagger c_{j\downarrow} \rangle, \tag{4.42}$$

and the onsite magnetisation $\vec{M}_j$, whose components are simply related to the single-particle correlations by,

$$M_j^x = \langle c_\uparrow^\dagger c_\downarrow + c_\downarrow^\dagger c_\uparrow \rangle, \tag{4.43}$$

$$M_j^y = i\langle c_\downarrow^\dagger c_\uparrow - c_\uparrow^\dagger c_\downarrow \rangle, \tag{4.44}$$

$$M_j^z = \langle c_\uparrow^\dagger c_\uparrow - c_\downarrow^\dagger c_\downarrow \rangle. \tag{4.45}$$

We find,

$$\begin{aligned} \langle c_{j\uparrow}^\dagger c_{j\uparrow} c_{j\downarrow}^\dagger c_{j\downarrow} \rangle &= \langle c_{j\uparrow}^\dagger c_{j\uparrow} \rangle \langle c_{j\downarrow}^\dagger c_{j\downarrow} \rangle - \langle c_{j\uparrow}^\dagger c_{j\downarrow} \rangle \langle c_{j\downarrow}^\dagger c_{j\uparrow} \rangle \\ &= \frac{1}{4} \left((n_j)^2 - \vec{M}_j \cdot \vec{M}_j \right), \end{aligned} \tag{4.46}$$

According to the Hartree-Fock prescription, the interaction term is replaced in the mean field Hamiltonian with,

$$\begin{aligned} U \sum_j c_{j\uparrow}^\dagger c_{j\uparrow} c_{j\downarrow}^\dagger c_{j\downarrow} \to U \sum_j \left[\langle c_{j\downarrow}^\dagger c_{j\downarrow} \rangle c_{j\uparrow}^\dagger c_{j\uparrow} + \langle c_{j\uparrow}^\dagger c_{j\uparrow} \rangle c_{j\downarrow}^\dagger c_{j\downarrow} - \langle c_{j\downarrow}^\dagger c_{j\uparrow} \rangle c_{j\uparrow}^\dagger c_{j\downarrow} - \langle c_{j\uparrow}^\dagger c_{j\downarrow} \rangle c_{j\downarrow}^\dagger c_{j\uparrow} \right] \\ - U \sum_j \left[\langle c_{j\downarrow}^\dagger c_{j\downarrow} \rangle \langle c_{j\uparrow}^\dagger c_{j\uparrow} \rangle - \langle c_{j\downarrow}^\dagger c_{j\uparrow} \rangle \langle c_{j\uparrow}^\dagger c_{j\downarrow} \rangle \right]. \end{aligned} \tag{4.47}$$

We assume that the noninteracting state has the same translational symmetry as the original Hamiltonian, and therefore that the correlations are the same for every lattice site,

$$n_j = n, \tag{4.48}$$

$$\vec{M}_j = \vec{M}, \tag{4.49}$$

and therefore the interaction term becomes,

$$U\sum_j c^\dagger_{j\uparrow}c_{j\uparrow}c^\dagger_{j\downarrow}c_{j\downarrow} \to \frac{U}{2}\sum_j \Big[(n-M_z)c^\dagger_{j\uparrow}c_{j\uparrow} + (n+M_z)c^\dagger_{j\downarrow}c_{j\downarrow} + (M_x - iM_y)c^\dagger_{j\uparrow}c_{j\downarrow} + (M_x+iM_y)c^\dagger_{j\downarrow}c_{j\uparrow}\Big] - \frac{U}{4}\mathcal{N}\left(n^2 - \vec{M}\cdot\vec{M}\right). \tag{4.50}$$

The full mean field Hamiltonian is therefore,

$$H^{mf} = \sum_{\vec{k}} \begin{pmatrix} c^\dagger_{\vec{k}\uparrow} & c^\dagger_{\vec{k}\downarrow}\end{pmatrix} \begin{pmatrix} -tz\gamma_{\vec{k}} + \frac{U}{2}(n-M_z) & \frac{U}{2}(M_x - iM_y) \\ \frac{U}{2}(M_x+iM_y) & -tz\gamma_{\vec{k}} + \frac{U}{2}(n+M_z)\end{pmatrix}\begin{pmatrix} c_{\vec{k}\uparrow} \\ c_{\vec{k}\downarrow}\end{pmatrix} - \frac{U}{4}\mathcal{N}\left(n^2 - \vec{M}\cdot\vec{M}\right), \tag{4.51}$$

where we have utilised the Bloch transform.

The spectrum is given by the eigenvalues of the 2 by 2 matrix in equation 4.51, which are given by

$$\epsilon^{mf}_{\vec{k}} = -tz\gamma_{\vec{k}} + \frac{Un}{2} \pm \frac{U}{2}|\vec{M}|. \tag{4.52}$$

The magnetisation $\vec{M}$ provides an effective magnetic field which couples to the spin of the particles; the two single-particle eigenstates are precisely the two spin-species resolved in the direction of the magnetisation. We can, without loss of generality, take the symmetry-broken direction to be the z-axis; there are then only two independent non-zero onsite correlations, $n_\uparrow = \langle c^\dagger_{j\uparrow}c_{j\uparrow}\rangle$ and $n_\downarrow = \langle c^\dagger_{j\downarrow}c_{j\downarrow}\rangle$, which provide the number of particles and magnetisation per site as

$$n = n_\uparrow + n_\downarrow, \tag{4.53}$$

$$M = n_\uparrow - n_\downarrow. \tag{4.54}$$

The dispersion is given by

$$\begin{aligned}\epsilon^{mf}_{\vec{k}\sigma} &= -tz\gamma_{\vec{k}} + \frac{U}{2}(n - \sigma M) \\ &= -tz\gamma_{\vec{k}} + Un_{\bar{\sigma}}.\end{aligned} \tag{4.55}$$

and the mean field can be written in the form,

$$H^{mf} - \mu N = \sum_{\vec{k}\sigma} \left(-tz\gamma_{\vec{k}} + Un_{\bar{\sigma}} - \mu\right) c^{\dagger}_{\vec{k}\sigma} c_{\vec{k}\sigma} - \mathcal{N} U n_{\uparrow} n_{\downarrow} \tag{4.56}$$

One can consider a mean field density of states for each spin-species,

$$\rho^{mf}_{\sigma}(\epsilon) = \frac{1}{\mathcal{N}} \sum_{\vec{k}} \delta(\epsilon - \epsilon^{mf}_{\vec{k}\sigma}). \tag{4.57}$$

This provides the following self-consistent equations for the two occupation numbers,

$$n_{\sigma} = \int d\epsilon \rho^{mf}_{\sigma}(\epsilon) f(\epsilon - \mu) = \frac{1}{\mathcal{N}} \sum_{\vec{k}} f(\epsilon^{mf}_{\vec{k}\sigma} - \mu). \tag{4.58}$$

Because one has a term in $n_{\bar{\sigma}}$ in the mean field spectrum $\epsilon^{mf}_{\vec{k}\sigma}$, the equations for $n_{\uparrow}$ and $n_{\downarrow}$ are coupled. However, in the case that the total particle number n is constant, the constraint

$$n_{\uparrow} + n_{\downarrow} = n \tag{4.59}$$

reduces the theory to a single self-consistent equation. Even in the case that the particle number is not fixed, the self-consistent equations can still be rendered independent from each other by redefining the chemical potential. The mean field dispersion can be written as

$$\epsilon^{mf}_{\vec{k}\sigma} = -tz\gamma_{\vec{k}} + Un - Un_{\sigma}. \tag{4.60}$$

Now, the term Un can be absorbed into the chemical potential. We define an *internal* chemical potential $\tilde{\mu}$ by

$$\tilde{\mu} = \mu - Un, \tag{4.61}$$

so that we can write the mean field Hamiltonian in the form

$$H^{mf} - \mu N = \sum_{\vec{k}\sigma} \left(-tz\gamma_{\vec{k}} - Un_{\sigma} - \tilde{\mu}\right) c^{\dagger}_{\vec{k}\sigma} c_{\vec{k}\sigma} - \mathcal{N} U n_{\uparrow} n_{\downarrow} \tag{4.62}$$

and we redefine the mean field dispersion to be

$$\epsilon^{mf}_{\vec{k}\sigma} = -tz\gamma_{\vec{k}} - Un_\sigma. \tag{4.63}$$

One can simply consider this newly defined dispersion whose occupancy is controlled by $\tilde{\mu}$:

$$\langle c^\dagger_{\vec{k}\sigma} c_{\vec{k}\sigma}\rangle = f(\epsilon^{mf}_{\vec{k}\sigma} - \tilde{\mu}) \tag{4.64}$$

With these definitions, the self-consistent equations become

$$n_\sigma = \frac{1}{\mathcal{N}}\sum_{\vec{k}} f(\epsilon^{mf}_{\vec{k}\sigma} - \tilde{\mu}). \tag{4.65}$$

We will use this idea in the mean field calculations which are to follow in this thesis. In practice, we shall make use of it even in the cases where we are working at fixed particle number, since this is found to lead to more straightforward computation in models which involve particles of more than one orbital species.

The energy of the system per site is given by,

$$E = \frac{\langle H^{mf}\rangle}{\mathcal{N}} = \frac{1}{\mathcal{N}}\sum_{\vec{k}\sigma} \epsilon^{mf}_{\vec{k}\sigma} f(\epsilon^{mf}_{\vec{k}\sigma} - \tilde{\mu}) - \frac{U}{4}(n^2 - M^2) \tag{4.66}$$

$$= \sum_\sigma \int \epsilon \rho^{mf}_\sigma(\epsilon) f(\epsilon - \tilde{\mu}) d\epsilon - \frac{U}{4}(n^2 - M^2). \tag{4.67}$$

Now, with the current definition of $\epsilon^{mf}_{\vec{k}\sigma}$, the mean-field density of states is related to the non-interacting density of states $\rho(\epsilon)$ of the pure tight binding model by

$$\rho^{mf}_{\vec{k}\sigma}(\epsilon) = \rho(\epsilon + Un_\sigma). \tag{4.68}$$

In the low-temperature limit, we have $f(\epsilon - \tilde{\mu}) \to \Theta(\tilde{\mu} - \epsilon)$, and consequently,

$$E = \sum_\sigma \int_{-\infty}^{\tilde{\mu}} \epsilon\rho\left(\epsilon + \tfrac{U}{2}(n + \sigma M)\right) d\epsilon - \frac{U}{4}(n^2 - M^2). \tag{4.69}$$

We regard M as a small quantity and write the energy as an expansion in M. The coefficients of the expansion are written in terms of the density of states and its derivatives evaluated at the Fermi

surface.

Let $\tilde{\mu}_0$ be the value of $\tilde{\mu}$ where the magnetisation is zero, and write,

$$\tilde{\mu} = \tilde{\mu}_0 + \delta\tilde{\mu}. \tag{4.70}$$

Now, expanding the expression for the energy about the point $\tilde{\mu} = \tilde{\mu}_0$, $M = 0$ we have,

$$\begin{aligned} E = 2\int_{\infty}^{\tilde{\mu}_0} \epsilon\rho(\epsilon + \tfrac{Un}{2})d\epsilon + 2\sum_{l=1}^{\infty} \frac{1}{(2l)!}\left[\tilde{\mu}_0\rho^{(2l-1)}(\tilde{\mu}_0 + \tfrac{Un}{2}) - \rho^{(2l-2)}(\tilde{\mu}_0 + \tfrac{Un}{2})\right]\left(\frac{UM}{2}\right)^{2l} \\ + 2\sum_{l=0}^{\infty}\sum_{k=1}^{\infty} \frac{1}{k!(2l)!}\left[\tilde{\mu}_0\rho^{(2l+k-1)}(\tilde{\mu}_0 + \tfrac{Un}{2}) + (k-1)\rho^{(2l+k-2)}(\tilde{\mu}_0 + \tfrac{Un}{2})\right]\left(\frac{UM}{2}\right)^{2l}(\delta\tilde{\mu})^k \\ - \frac{U}{4}(n^2 - M^2) \end{aligned} \tag{4.71}$$

The dependence of the chemical potential on the magnetisation can be deduced from the constraint on the number of particles. Written in terms of the density of states, the sum of the spin-↑ and spin-↓ particle numbers is

$$n = \int_{\infty}^{\tilde{\mu}} \left[\rho(\epsilon + \tfrac{Un}{2} + \tfrac{UM}{2}) + \rho(\epsilon + \tfrac{Un}{2} - \tfrac{UM}{2})\right] d\epsilon. \tag{4.72}$$

By repeatedly differentiating this equation with respect to M at constant n, we obtain a set of equations which relate the derivatives of the chemical potential $\tilde{\mu}$ to the density of states and its derivatives. This provides the expansion of $\delta\tilde{\mu}$ in M to be

$$\begin{aligned} \delta\tilde{\mu} = -\frac{1}{2!}\frac{\rho'}{\rho}\left(\frac{UM}{2}\right)^2 - \frac{1}{4!}\left[\frac{\rho'''}{\rho} + 3\left(\frac{\rho'}{\rho}\right)^2 - 6\frac{\rho'\rho''}{\rho^2}\right]\left(\frac{UM}{2}\right)^4 \\ - \frac{1}{6!}\left[\frac{\rho^{\mathrm{v}}}{\rho} + 45\left(\frac{\rho'}{\rho}\right)^5 + 60\left(\frac{\rho'}{\rho}\right)^2\frac{\rho''}{\rho} + 90\frac{\rho'}{\rho}\left(\frac{\rho''}{\rho}\right)^2 \right. \\ \left. -150\left(\frac{\rho'}{\rho}\right)^3\frac{\rho'''}{\rho} - 15\frac{\rho''\rho''' + \rho'\rho^{\mathrm{v}}}{\rho^2}\right]\left(\frac{UM}{2}\right)^6 + ... \end{aligned} \tag{4.73}$$

where all terms in the density of states and its derivatives are evaluated with the argument $\tilde{\mu}_0 + \frac{Un}{2}$.

This provides the expansion of the energy in M at constant n, up to the sixth order, to be,

$$E = 2\int_{-\infty}^{\tilde{\mu}} (\epsilon - \tilde{\mu})\rho(\epsilon + \tfrac{Un}{2})d\epsilon - \frac{Un^2}{4} + \frac{U}{4}\left[1 - U\rho\right]M^2 + \frac{1}{12}\left(\frac{U}{2}\right)^4 \rho\left[3\left(\frac{\rho'}{\rho}\right)^2 - \frac{\rho''}{\rho}\right]M^4 + \frac{1}{360}\left(\frac{U}{2}\right)^6 \frac{1}{\rho}\left[15\left(\frac{\rho'}{\rho}\right)^4 + 15\frac{\rho'\rho''}{\rho^2} - 45\left(\frac{\rho'}{\rho}\right)^2\frac{\rho''}{\rho} - \frac{\rho'^{\mathrm{v}}}{\rho}\right]M^6 + ..., \tag{4.74}$$

Note that it comes as no surpise that this expansion includes only even powers of M, as this reflects the symmetry of the underlying Hamiltonian with respect to the direction of magnetisation.

The magnetisation is predicted to be such as to minimise the energy. Now, the absence of a linear term in the expansion indicates that the state with no magnetisation, $M = 0$, always corresponds to a stationary point of E. In the simplest scenario, if the coefficient of the quadratic term is negative, this indicates that the stationary point at $M = 0$ is unstable and the system should go magnetic, the magnetic state corresponding to a minimum in the energy at finite M. The coefficient of the quadratic term is negative if

$$U\rho(\tilde{\mu}_0 + \tfrac{Un}{2}) > 1, \tag{4.75}$$

which is known as the Stoner criterion. If one envisages varying the Coulomb energy U from zero, the mean field theory predicts that the system will go ferromagnetic at the point $U\rho = 1$, and that this will be a second order phase transition. Alternatively, if the coefficient of the quadratic term is positive, but the coefficient of the quartic term is negative, for which the criterion is(104),

$$\frac{\rho''}{\rho} > 3\left(\frac{\rho'}{\rho}\right)^2, \tag{4.76}$$

there must be two local minima in the free energy, one located at $M = 0$ and one at a finite M. This corresponds to the transition to ferromagnetism being first order: for $U\rho < 1$ there is a unique free energy minimum at $M = 0$; for $U\rho > 1$ the $M = 0$ point remains a minimum but there occurs a second minimum which provides a lower energy. In summary, the Stoner criterion 4.75 indicates whether ferromagnetism is predicted in the system, and the condition 4.76 indicates whether this transition is first or second order.

Let the density of states have a singularity at $\epsilon = \epsilon_0$ such that in the vicinity of the singularity it has the form,

$$\rho(\epsilon) \sim \frac{\lambda}{(\epsilon - \epsilon_0)^K}.$$

Substituting this expression into 4.76 provides,

$$\frac{\rho''(\epsilon)}{\rho(\epsilon)} - 3\left(\frac{\rho'(\epsilon)}{\rho(\epsilon)}\right)^2 = \frac{K(1-2K)}{(\epsilon-\epsilon_0)^2} \tag{4.77}$$

and the inequality 4.76 is satisfied provided $0 < K < 1/2$. The upper and lower limits of this range correspond to the square-root and logarithmic van Hove singularities that are found in one-dimensional and two-dimensional band structures respectively. This indicates that first order ferromagnetic transitions can be expected to occur in systems with either one- or two-dimensional electronic structure if the chemical potential lies in the vicinity of an associated van Hove singularity.

Because the electronic structure of $Sr_3Ru_2O_7$ contains both quasi-one-dimensional and quasi-two-dimensional features, the Stoner argument provides a picture to apply to the $Sr_3Ru_2O_7$ metamagnetism. It has been suggested that the metamagnetism is associated with a logarithmic van Hove singularity(96); in this work we argue that it is associated with a different feature in the electronic structure, a square-root singularity arising from a quasi-one-dimensional band.

4.3 Building a model of the Ruthenate system

In this section we shall describe in detail how one builds a second quantised model for the Ruthenate system. We first deal with two topics that are germane to the modelling of the transition metal oxide materials in general, the topics of the crystal field interaction and Hund's rules. The crystal field interaction is the external potential in which the Ru ion sits in the material; the effect of the crystal field interaction is to lift the five-fold degeneracy of the Ru $4d$-shell into a high energy doublet and a low energy triplet; the energy of this splitting is such that only the three low-energy states are relevant. Hund's rules are concerned with how the electron-electron interaction affects the collective onsite magnetic moment of the Ru valence electrons. The key piece of physics is the exchange interaction, which provides an effective ferromagnetic interaction between electrons on the same site. This acts as a more aggressive promotion of an initinerant ferromagnetic state in concert with the Stoner magnetism we have discussed above.

We then move on to building a model for the Ru electrons. Our model consists of a hybridisation term and an onsite interaction term. Because $Sr_3Ru_2O_7$ is a paramagnetic metal, the hybridisation is the dominant term, although the proximity of a ferromagnetic instability is modelled by the energy scale for the interactions being comparable to the hybridisation. We begin with the hopping terms.

Hybridisation between pairs of Ru sites occurs, where the underlying process sees the Ru electron hop onto the neighbouring O, briefly occupying the onsite p orbital and then hopping onwards onto the next Ru. We show from first principles how the effective hopping arises from perturbation theory, although the precise hybrisation terms we include are arrived at by attempting to match the experimental Fermi surface and density functional theory calculations discussed in the previous chapter. The interaction term which we use is the general onsite Coulomb interaction for the t_{2g} orbitals, which we derive. This interaction term is parameterised by the two parameters U, which corresponds to the Coulomb energy in the Hubbard model, and J which is closely associated with the first Hund rule.

This reaches the level to which we are going to model $Sr_3Ru_2O_7$. In the remainder of this section, we shall describe caveats to this level of description in the form of other effects which have not so far been included. There are two effects which would have to be included in order to model the behaviour of the nematic phase in $Sr_3Ru_2O_7$. The first of these is the long-range Coulomb interaction, which will control the arrangement of the charged domains in the phase-separated solution which is predicted by our mean field theory. The second is the spin-orbit interaction, which is the lowest-level microscopic interaction which provides a dependence on the direction of the magnetic field and we regard this as being primarily responsible for the dependence on the field direction in $Sr_3Ru_2O_7$.

Finally, we frame the modelling of the material from the viewpoint of strongly-correlated physics; from this viewpoint, the hybridisation energies and onsite Coulomb repulsions are merely *effective* parameters which describe the collective behaviour of the system, which is governed by the correlated physics of all the electrons in the system, and the effective parameters are not directly related to any single-particle or two-particle energy scales that exist in the material.

4.3.1 Crystal Field splitting

The chemistry of the transition metal oxide compounds is dominated by the large electronegativity of Oxygen. The neutral O atom has two holes in the $2p$ shell, and in molecules the O atoms almost always acquire extra electrons to form the ion O^{2-} with the $2p$ shell full. In transition metal oxides, therefore, the O sites are centres of negative charge. The Coulomb interaction due to these charge centres on the transition metal valence electrons is called a *crystal field*, and has the effect of altering the atomic states of the valence electrons from those of a transition metal ion in free space.

Now, for the ion in free space the relevant wavefunctions are the spherical harmonics $Y_m^l(\theta, \phi)$, which are labelled by the orbital angular momentum quantum number l which is an integer, and the

quantum number m which takes the integer values from $-l$ to $+l$ and provides the component of orbital angular momentum along the z-axis of the co-ordinate system. In transition metals the valence electrons are in the d-shell which has $l = 2$; disregarding normalisation, we have

$$\begin{aligned} Y_2^2 &= \sin^2\theta e^{2i\phi} \\ Y_1^2 &= \sin\theta\cos\theta e^{i\phi} \\ Y_0^2 &= 3\cos^2\theta - 1 \\ Y_{-1}^2 &= \sin\theta\cos\theta e^{-i\phi} \\ Y_{-2}^2 &= \sin^2\theta e^{-2i\phi} \end{aligned} \tag{4.78}$$

The crystal field potential is usually cubic symmetric to a good approximation, that is, it is mapped onto itself by the transformations of the cubic symmetry group. The effect of the crystal field is to split the degeneracy of the d-shell according to the subspaces which are closed under this same set of operations. There are two closed subspaces, the three states,

$$\begin{aligned} d_{xy} &= \frac{xy}{r^2} = \sin^2\theta\sin\phi\cos\phi \propto i(Y_2^2 - Y_{-2}^2) \\ d_{yz} &= \frac{yz}{r^2} = \sin\theta\cos\theta\sin\phi \propto -i(Y_1^2 + Y_{-1}^2) \\ d_{zx} &= \frac{zx}{r^2} = \sin\theta\cos\theta\cos\phi \propto -(Y_1^2 - Y_{-1}^2) \end{aligned} \tag{4.79}$$

which is called the t_{2g} subspace, and the two states

$$\begin{aligned} d_{3z^2-1} &\propto Y_0^2 \\ d_{x^2-y^2} &\propto Y_2^2 + Y_{-2}^2 \end{aligned} \tag{4.80}$$

which is called the e_g subspace. In the ideal Ruddlesden-Popper structure for $Sr_{n+1}Ru_nO_{3n+1}$, and for a large number of transition metal oxides, the transition metal ion sits in an octahedral cage of O ions. For this crystal field, the e_g states have a higher energy than the t_{2g} states: the d-shell is split into a low energy triplet and a high energy doublet. In characterising the electronic states of transition metal oxide compounds, one pictures filling up the crystal field-split d-shell with the number of particles that are indicated by the valency of the transition metal ion: in the case of $Sr_3Ru_2O_7$ the valency is Ru^{4+}, corresponding to four electrons in the $4d$ shell. The nature of the groundstate configuration of the

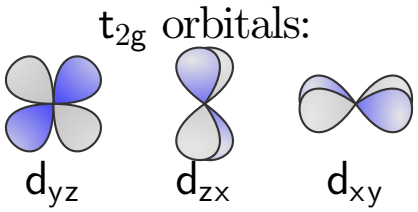

Figure 4.1: Cartoon of the t_{2g} orbitals. The three orbitals are three mutually perpendicular orientations of the same shape.

crystal field-split d-shell requires the consideration of Hund's rules which are discussed below, but it is found that to a good approximation in $Sr_3Ru_2O_7$ the e_g states can be ignored so that the t_{2g} orbitals are the only relevant degrees of freedom.

The t_{2g} orbitals are depicted in Figure 4.1. These orbitals are three mutually perpendicular rotations of the same shape, the orientations characterised by the three mutually perpendicular axes along which the wavefunction vanishes coinciding with the directions of the nearest neighbour O sites. Two of these directions are equivalent, and it shall be shown below that hybridisation occurs in these two directions, while no hybridisation occurs in the third direction. Because the Ru valence electrons are to a good approximation only mobile on the two-dimensional geometry of the bilayer, this results in strongly one-dimensional characteristics in the electronic structure.

Note that all the t_{2g} and e_g states have zero orbital angular momentum: the angular momentum is said to be *quenched* by the crystal field. With regard to our modelling, we therefore regard the magnetisation as being entirely due to electron spin and not orbital angular momentum, and we shall calculate the magnetisation as the difference in the number of spin-$\uparrow$ and spin-$\downarrow$ holes per Ru site. However, an orbital angular momentum can be generated in the the t_{2g} subspace through the states $d_{yz} + id_{zx}$ and $d_{yz} - id_{zx}$ which are eigenstates of orbital angular momentum; as we discuss in section 4.3.6 this is the state that is relevant in the spin-orbit interaction, which we do not incorporate into our modelling but which we do regard as highly relevant to the nematic phase in $Sr_3Ru_2O_7$.

4.3.2 Hund's rules

Hund's rules concern the effects of spin- and orbital-angular momentum on the electronic state of ions. The first Hund's rule is the largest effect and concerns the exchange interaction. This interaction arises out of the fundamental property that the fermion many-body state be antisymmetric with respect to the exchange of two indistinguishable particles. The effect can be explained at the level of two particles. The full wavefunction of two indistinguishable spin-$\frac{1}{2}$ fermions constists of both their

spatial wavefunction and their spin wavefunction; a basis for the spin wavefunction is given by the antisymmetric singlet,

$$|\sigma_1\sigma_2\rangle = \frac{1}{\sqrt{2}}\left(|\uparrow\downarrow\rangle - |\downarrow\uparrow\rangle\right)$$

which corresponds to the spins of the particles being antiparallel, and the symmetric triplet

$$\begin{aligned}
|\sigma_1\sigma_2\rangle &= |\uparrow\uparrow\rangle \\
|\sigma_1\sigma_2\rangle &= \frac{1}{\sqrt{2}}\left(|\uparrow\downarrow\rangle + |\downarrow\uparrow\rangle\right) \\
|\sigma_1\sigma_2\rangle &= |\downarrow\downarrow\rangle
\end{aligned}$$

which constitutes a spin-1 state, with the spins of the particles being parallel. The requirement that the full wavefunction be antisymmetric with respect to the exchange of the particles means that if the spin wavefunction is symmetric then the spatial wavefunction must be antisymmetric and vice versa. It is found that the Coulomb interaction between the two electrons leads to an antisymmetric spatial wavefunction, and therefore the parallel spin state, being energetically preferred. This can be intuitively guessed by examining the Coulomb energy for a two-particle state with the spatial wavefunction $\Psi(\vec{r}_1, \vec{r}_2)$, which is given by

$$\int dr_1 \int dr_2 |\Psi(\vec{r}_1, \vec{r}_2)|^2 U(\vec{r}_1 - \vec{r}_2)$$

where $U(\vec{r}_1 - \vec{r}_2)$ is the electron-electron interaction, which is the Coulomb interaction. The interaction is largest when the electrons are in close proximity to one another, and this conincides with a node in the antisymmetric wavefunction, since an antisymmetric function must vanish at $\vec{r}_1 = \vec{r}_2$. This integral is therefore smaller for the antisymmetric spatial wavefunction.

A similar effect which takes place on a smaller energy scale concerns the orbital angular momentum. States which find the particles with a large z-component of orbital angular momentum, and with the orbital angular momentum of multiple particles parallel, are energetically preferred due to the electron-electron interaction. This can also be understood on an intuitive level by a picture of the electrons as particles in classical orbits; in configurations which have the particles orbiting in the same sense and with large angular momentum, the particles spend less time in close proximity to one another and so the interaction energy is reduced on average. This is encompassed in Hund's second rule, which states that the valence electron states are occupied so as to maximise the total orbital angular momentum in

the z-direction, except where this is in conflict with Hund's first rule. In transition metal oxides, the second Hund's rule is rendered moot by the crystal field interaction, which enforces that the valence electron states have zero net angular momentum. On a yet smaller energy scale is the spin-orbit coupling effect, which is often dealt with in the form of a third Hund's rule, but we will discuss spin orbit coupling separately below.

In dictating the electronic state of the transition metal ion, the first Hund rule is in direct conflict with the crystal field interaction. For up to three d-electrons, the t_{2g} states are occupied and the electrons have their spins parallel in accord with the Hund rule. When occupying with the fourth electron the Hund rule suggests that the e_g level is occupied and the spin be parallel to the first three electrons, but this configuration must pay the crystal field splitting as a penalty. If the crystal field splitting is larger than the energy to be gained from the Hund coupling, then the fourth electron goes into the t_{2g} band, with its spin antiparallel to the other electrons. It is found that for ions of transition metals which lie before Cobalt in the periodic table, the Hund coupling is the larger energy scale, while for elements past Cobalt the crystal field energy is dominant. Ru is a case of the latter, and so to leading order only the t_{2g} states are regarded as relevant.

4.3.3 Effective hybridisation mediated by O sites

We here consider the single particle Hamiltonian for the Ruthenate system. We will argue for a tight binding model involving only the Ru electron states, which includes nearest neighbour and second nearest neighbour hopping between Ru sites. We describe how this arises as an effective model starting from a model which includes the O electron states. We then determine the precise hybridisation terms which we include in our model, and the size of the energy-scales, by comparison with the experimental Fermi surfaces and the density functional theory calculations discussed in the previous chapter.

In our remarks on crystal field effects, we have indicated that the chemistry of the system forces the picture that only the Sr^{2+} and O^{2-} ions occur in the material. These ions correspond to entirely closed orbital shells. This leaves the Ru-4d shell partially occupied, with four 4d electrons per site on average, which occupy only the t_{2g} states. This is illustrated in figure 4.2. The natural choice of a vaccuum state is that which finds the t_{2g} states empty. However, we choose to use as degrees of freedom holes instead of particles. Because the t_{2g} level can accomodate up to six electrons, the average of four electrons per site is equivalent to two holes per site. With this picture, we take the *filled* t_{2g} band as the vaccuum, and we shall fill up the t_{2g} levels with holes to achieve two per site on

average.

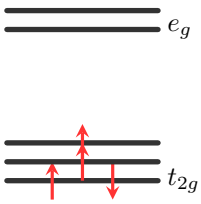

Figure 4.2: Cartoon showing the onsite occupancy of the crystal-field-split Ru $4d$-shell. Four electrons are found in the t_{2g} level. In our modelling we regard the filled t_{2g} level as the vaccuum state; the onsite configuration therefore has two holes in the t_{2g}. The e_g level is not included in our modelling.

In building a noninteracting Hamiltonian of the generic form 4.23 to describe the hybridisation, one must include the relevant orbitals for the both the Ru and the O sites. The relevant Ru orbitals are the three t_{2g} states, the Z, X and Y. The relevant O orbitals are the three states in the $2p$ shell, which we label p_x, p_y and p_z. These are clearly the relevant states, because moving a hole from a Ru atom onto a neighbouring O ion is equivalent to removing an electron from the O, and this electron must come from the $2p$ shell which is filled for the ion O^{2-}. In principle one can proceed to calculate all of the matrix elements between these orbitals on different sites. We do not perform any such calculations; we are simply working towards a form for an effective model for the Ru degrees of freedom, and the parameters in this model will then be deduced from comparison with density functional theory calculations and experiments.

Recall that there is a O site intermediate between each nearest pair of Ru sites. We immediately neglect all matrix elements between states on sites farther separated than the next-nearest neighbours. Of the offsite matrix elements, this leaves the matrix elements between the Ru states and the O states on neighbouring sites, and the matrix elements between states on nearest pairs of O atoms. Now, consideration of the symmetry of these orbitals under the inversion of one of the coordinate axes shows that the majority of these matrix elements are identically zero. The nonzero Ru-O hybridisations are indicated in figure 4.3. The Ru states only hybridise with the neighbours in two of the three Cartesian directions, and only with one of the $2p$ orbitals; all of these matrix elements have the same value which we label u. There are several nonzero matrix elements between nearest pairs of O sites and these are indicated in figure 4.4.

The large electronegativity of Oxygen, which demands the closed shell O^{2-} ion, corresponds to a large onsite energy Δ for a hole occupying the $2p$ states. We can regard the off-site matrix elements

as perturbations to the case where Δ is the only energy scale. If we measure the energy relative to the onsite Ru energy, we can regard the Hamiltonian in the form

$$H = H_0 + \delta H \tag{4.81}$$

where

$$H_0 = \Delta \sum_{i\alpha\sigma} p^\dagger_{i\alpha\sigma} p_{i\alpha\sigma}, \tag{4.82}$$

where the i labels the O sites in the lattice, α labels the three $2p$ species and $p^\dagger_{i\alpha\sigma}$ is the creation operator for a spin-σ hole in the corresponding state, and δH contains all of the hybridisation matrix elements indicated in figures 4.3 and 4.4. The unperturbed system $H = H_0$ has the onsite Ru t_{2g} orbitals as a triply degenerate groundstate.

The standard theory of degenerate perturbation theory prescribes that the effect of including δH is given order by order by an effective Hamiltonian of the form,

$$P\delta HP + P\delta H\frac{1-P}{H_0}\delta HP + ... \tag{4.83}$$

where P is the projection operator which projects onto the t_{2g} states. We have not determined the third order term, but we expect it to involve the operator,

$$P\delta H\frac{1-P}{H_0}\delta H\frac{1-P}{H_0}\delta HP.$$

The first order term in the expression 4.83 vanishes. The second order term gives an effective hybridisation between nearest pairs of Ru sites. Because each of the t_{2g} states have nonzero matrix elements with neighbouring O sites in only two directions, the effective Ru-Ru hybridisation is also in only two directions. The effective Hamiltonian at second order is given by,

$$\begin{aligned} H^{(2)}_{\text{eff}} = &-\frac{u^2}{\Delta}\sum_{\langle jj'\rangle_{x,y}}\left(Z^\dagger_{j\sigma}Z_{j\sigma} + Z^\dagger_{j\sigma}Z_{j'\sigma}\right) - \frac{u^2}{\Delta}\sum_{\langle jj'\rangle_{y,z}}\left(Y^\dagger_{j\sigma}Y_{j\sigma} + Y^\dagger_{j\sigma}Y_{j'\sigma}\right) \\ &- \frac{u^2}{\Delta}\sum_{\langle jj'\rangle_{z,x}}\left(X^\dagger_{j\sigma}X_{j\sigma} + X^\dagger_{j\sigma}X_{j'\sigma}\right) \end{aligned} \tag{4.84}$$

where j labels the Ru sites, and the notation $\langle jj'\rangle_{...}$ indicates nearest neighbour pairs of Ru sites in the indicated directions. There occur both onsite terms and hopping terms; these correspond to processes

where the hole hops from a Ru site onto a neighbouring O site, and then hops either back to the original Ru site or on to the neighbouring Ru site.

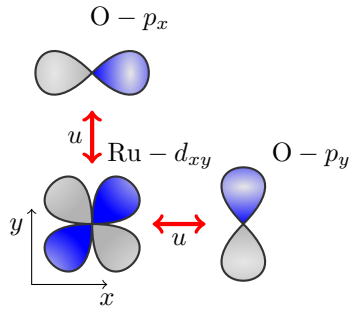

Figure 4.3: Nonzero matrix elements between the Ru d_{xy} orbital and the $2p$ orbitals on neighbouring O sites in the x- and y-directions. There is no hybridisation with any of the $2p$ states on neighbouring O sites in the z-direction. The matrix elements between the d_{yz} and d_{zx} states and the $2p$ states on neighbours in the x-, y- and z-directions are obtained from these by cyclic permutation.

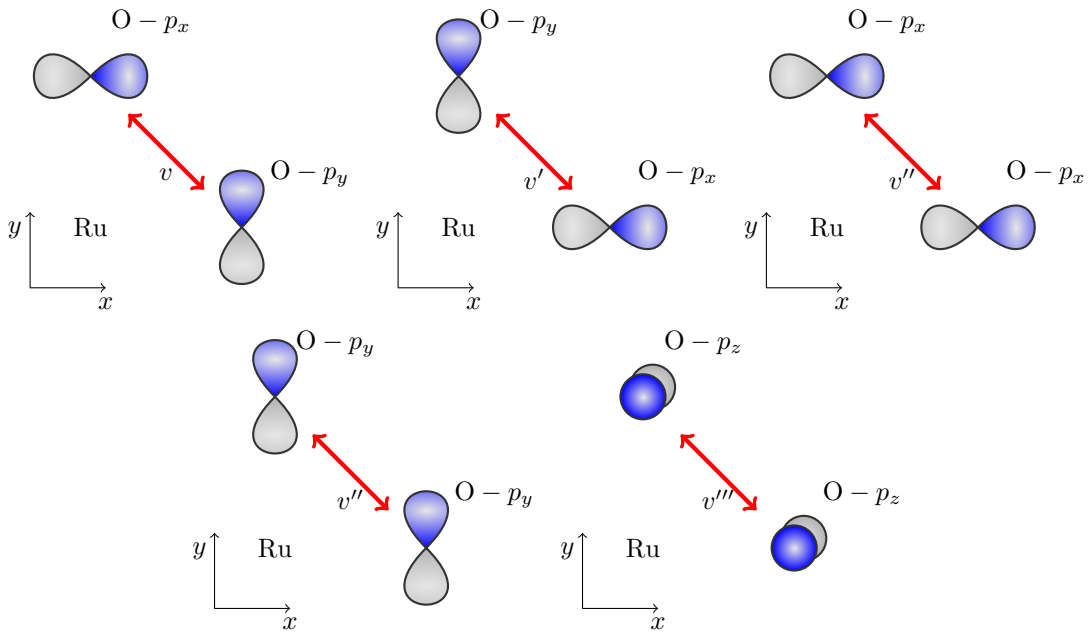

Figure 4.4: The nonzero matrix elements between $2p$ states on neighbouring pairs of O atoms in the x-y plane. The position of the nearest Ru ion is indicated. The matrix elements between neighbouring O atoms in the y-z and z-x planes are obtained from these by cyclic permutation.

Carrying the perturbation theory to third order, the matrix elements between O states become relevant, and there occur both corrections to the onsite energies and nearest neighbour hopping, with an energy scale u^2v/Δ^2, but also more complicated physics. Most importantly there occurs a

hybridisation between *second* nearest neighbour Ru sites via the matrix element v with energy scale u^2v/Δ^2. Secondly, there occurs at this order terms such as $Z^\dagger_{j\sigma}Y_{j\sigma}$ and $Z^\dagger_{j\sigma}Y_{j'\sigma}$ which move the hole between the t_{2g} states either onsite or on nearest neighbour or next nearest neighbour Ru sites, via the matrix element v''' with energy scale u^2v'''/Δ^2.

Now, certainly both the non-interacting model, and the mean field theory which we shall deal with when interactions are included, are much easier to solve when the terms which hybridise the different t_{2g} states are absent, as the occupation numbers for the different t_{2g} orbitals can be calculated independently for a given chemical potential. One might hope to circumvent the complications that arrive in the the third order effective model $H^{(3)}_{\text{eff}}$ by working only with the second order corrections $H^{(2)}_{\text{eff}}$. However, when we come to explicitly describe the implications of a tight binding description for the bilayer ruthenate system, attempting to obtain a Fermi surface that agrees with experiment forces us to include a sizeable second-nearest neighbour Ru-Ru hopping, which we have argued is an effect that only occurs as a third order perturbation. In this light it seems appropriate to work with the full third order effective hopping Hamiltonian $H^{(2)}_{\text{eff}} + H^{(3)}_{\text{eff}}$. However, we will only include the second-nearest-neighbour hopping which preserves the orbital species. There is some justification in this: the terms which change the orbital species almost certainly occur on a somewhat smaller energy scale, based on the intuition that $|v| > |v'''|$.

We have attempted to justify the hybridisation term which we shall use in our model using microscopic calculations. In practice, however, rather than having been devised from first principles, the hybridisation term in our model was arrived at purely by attempting to reproduce the experimental Fermi surface and the DFT calculations of the density of states disussed in the previous chapter in section 3.2. The strong one-dimensional and two-dimensional character of the X/Y and Z bands respectively is evident in the experimental Fermi surface, and particularly in the DFT calculations of the density of states of the single layer compound Sr_2RuO_4. The inclusion of the second neighbour hopping is required to obtain a Z Fermi surface which matches that seen in $Sr_3Ru_2O_7$; we use the value $t_2 = 0.4t$ as this is approximately the smallest value of t_2 which provides the correct topology of the Z Fermi surface for which the occupancies of the three t_{2g} bands are equal. The energy scale t is set by comparing with the DFT calculations. Observe the DFT calculation of the X/Y density of states in figure 3.8, which has bandwidth of approximately 2eV; in the tight-binding description the bandwidth is given by $6t$ (see appendix B and in particular the calculations of the X/Y density of states in figure B.4), from which we deduce the value $t \approx 0.35$eV.

4.3.4 Onsite Coulomb interaction in the t_{2g} subspace

Here we consider the Coulomb interaction between particles (or holes) lying in t_{2g} orbitals on the same Ru site. The onsite interaction is given by,

$$\sum_{\sigma_1\sigma_2}\sum_{\beta_1,\beta_2,\beta_1',\beta_2'} U_{\beta_1,\beta_2;\beta_1'\beta_2'} c^\dagger_{\beta_1\sigma_1} c^\dagger_{\beta_2\sigma_2} c_{\beta_2'\sigma_2} c_{\beta_1'\sigma_1} \tag{4.85}$$

where the labels β_1, β_2, β_3 and β_4 run over the three t_{2g} orbitals X, Y and Z. By considering the symmetry properties of the t_{2g} wavefunctions it can be shown that all of the matrix elements in this expression can be written in terms of just two energy scales. The onsite matrix elements are given by,

$$U_{\beta_1,\beta_2;\beta_1',\beta_2'} = \int d\vec{r} \int d\vec{r}\,' \, \psi^*_{\beta_1}(\vec{r})\psi^*_{\beta_2}(\vec{r}\,')U(|\vec{r}-\vec{r}\,'|)\psi_{\beta_2'}(\vec{r}\,')\psi_{\beta_1'}(\vec{r}).$$

Each of the the t_{2g} wavefunctions is symmetric with respect to the inversion of one of the three co-ordinate axes and antisymmetric with respect to the inversion of the other two. Consider the implications of the following changes of integration variables:

$$x \to -x,\ x' \to -x';$$
$$y \to -y,\ y' \to -y';$$
$$z \to -z,\ z' \to -z'.$$

Because the two-body interaction potential $U(|\vec{r}-\vec{r}\,'|)$ is symmetric under each of these transformations, one finds that the integral must vanish except in the case that there are an even number of factors of each of the t_{2g} orbitals in the integrand. The integral is only nonzero for the following cases:

$$\begin{array}{llllllll}
1) & \beta_1 & = & \beta_2 & = & \beta_1' & = & \beta_2'; \\
2) & \beta_1 & = & \beta_2 & \neq & \beta_1' & = & \beta_2'; \\
3) & \beta_1 & = & \beta_1' & \neq & \beta_2 & = & \beta_2'; \\
4) & \beta_1 & = & \beta_2' & \neq & \beta_2 & = & \beta_1'.
\end{array}$$

Now, because the t_{2g} orbitals are perpendicular orientations of the same orbital shape, it is clear that all of the matrix elements for any one of these cases are the same. We can therefore write the onsite

Coulomb interaction as

$$U_1 \sum_{\beta} c^{\dagger}_{\beta\uparrow} c^{\dagger}_{\beta\downarrow} c_{\beta\downarrow} c_{\beta\uparrow} + U_2 \sum_{\beta\neq\beta'} c^{\dagger}_{\beta\uparrow} c^{\dagger}_{\beta\downarrow} c_{\beta'\downarrow} c_{\beta'\uparrow} + U_3 \frac{1}{2} \sum_{\sigma\sigma'} \sum_{\beta\neq\beta'} c^{\dagger}_{\beta\sigma} c^{\dagger}_{\beta'\sigma'} c_{\beta'\sigma'} c_{\beta\sigma} + U_4 \frac{1}{2} \sum_{\sigma\sigma'} \sum_{\beta\neq\beta'} c^{\dagger}_{\beta\sigma} c^{\dagger}_{\beta'\sigma'} c_{\beta\sigma'} c_{\beta'\sigma} \tag{4.86}$$

where U_1, U_2, U_3 and U_4 are the matrix elements for the cases 1 to 4 respectively. We can simplify this expression further by using the symmetry properties of the t_{2g} wavefunctions to obtain relations between these four matrix elements. Now, we can write the t_{2g} wavefunctions as

$$\psi_Z(\vec{r}) = u(r)\frac{xy}{r^2}, \tag{4.87}$$

with the ψ_Y and ψ_X wavefunctions defined implicitly by cyclic permutation; the factor xy/r^2 contains solely the angular dependence of the wavefunction, and $u(r)$ is the radial dependence which is the same for all the $4d$ orbitals. The integrals for the first matrix element for the first case is

$$U_1 = \int d\vec{r} \int d\vec{r}\,' \, |u(r)u(r')|^2 \frac{(xyx'y')^2}{(rr')^4} U(|\vec{r} - \vec{r}\,'|), \tag{4.88}$$

and for the second case the integral is

$$U_2 = \int d\vec{r} \int d\vec{r}\,' \, |u(r)u(r')|^2 \frac{xy^2zx'y'^2z'}{(rr')^4} U(|\vec{r} - \vec{r}\,'|). \tag{4.89}$$

The third case has the integral,

$$U_3 = \int d\vec{r} \int d\vec{r}\,' \, |u(r)u(r')|^2 \frac{(xyy'z')^2}{(rr')^4} U(|\vec{r} - \vec{r}\,'|), \tag{4.90}$$

and we can relate U_3 to U_1 and U_2 by means of a coordinate transformation. Make the change of variables in the integral U_3 of a rotation through some angle θ about the y- and y'-axes:

$$\begin{pmatrix} x \\ y \\ z \end{pmatrix} \rightarrow \begin{pmatrix} \cos\theta & 0 & \sin\theta \\ 0 & 1 & 0 \\ -\sin\theta & 0 & \cos\theta \end{pmatrix} \begin{pmatrix} x \\ y \\ z \end{pmatrix}, \qquad \begin{pmatrix} x' \\ y' \\ z' \end{pmatrix} \rightarrow \begin{pmatrix} \cos\theta & 0 & \sin\theta \\ 0 & 1 & 0 \\ -\sin\theta & 0 & \cos\theta \end{pmatrix} \begin{pmatrix} x' \\ y\prime \\ z' \end{pmatrix}.$$

With this change of variables the integrand in the integral U_3 becomes,

$$\frac{|u(r)u(r')|^2}{(rr')^4}U(|\vec{r}-\vec{r}'|)\Big\{\sin^2\theta\cos^2\theta\left[(xyx'y')^2+(zyz'y')^2\right] \\ +\cos^4\theta(xyy'z')^2+\sin^4\theta(zyx'y')^2-4\sin^2\theta\cos^2\theta xy^2zx'y'^2z' \\ +2\sin\theta\cos\theta y^2y'^2\left[\cos^2\theta(xzz'^2-x^2x'z')+\sin^2\theta(xzx'^2-z^2x'z')\right]\Big\}. \tag{4.91}$$

When this expression is integrated over $\vec{r}$ and $\vec{r}'$, the result can be written in terms of U_1, U_2 and U_3 as,

$$U_3 = 2\sin^2\theta\cos^2\theta U_1 + (\cos^4\theta+\sin^4\theta)U_3 - 4\sin^2\theta\cos^2\theta U_2, \tag{4.92}$$

which for arbitrary values of θ implies the relation,

$$U_1 - 2U_2 - U_3 = 0. \tag{4.93}$$

Finally, we note that the integral for U_4 is identical to U_2 owing to the fact that the t_{2g} wavefunctions are all purely real,

$$U_4 = U_2. \tag{4.94}$$

Now let us examine the expression 4.86. Consider the third term, which may be written in the form,

$$\frac{U_3}{2}\sum_{\beta\neq\beta'}\left(c^\dagger_{\beta\uparrow}c_{\beta\uparrow}+c^\dagger_{\beta\downarrow}c_{\beta\downarrow}\right)\left(c^\dagger_{\beta'\uparrow}c_{\beta'\uparrow}+c^\dagger_{\beta'\downarrow}c_{\beta'\downarrow}\right). \tag{4.95}$$

The effect of this term is to impose an energy penalty $+U_3$ for each pair of particles on the site in different orbitals; the similarity in the effect of this term in comparison with the Hubbard onsite interaction motivates the use of the notation $U_3 = U$. Next, consider the fourth term in 4.86, which can be written as,

$$\frac{U_4}{2}\sum_{\beta\neq\beta'}\left(c^\dagger_{\beta\uparrow}c_{\beta'\uparrow}c^\dagger_{\beta'\downarrow}c_{\beta\downarrow}+c^\dagger_{\beta'\uparrow}c_{\beta\uparrow}c^\dagger_{\beta\downarrow}c_{\beta'\downarrow}-c^\dagger_{\beta\uparrow}c_{\beta\uparrow}c^\dagger_{\beta'\downarrow}c_{\beta'\downarrow}-c^\dagger_{\beta'\uparrow}c_{\beta'\uparrow}c^\dagger_{\beta\downarrow}c_{\beta\downarrow}\right). \tag{4.96}$$

The last two terms in this expression give an energy gain of $-U_4$ for pairs of particles in different states which have their spins parallel. This is precisely the physics of Hund's rules discussed above. We therefore refer to the matrix element U_4 as the Hund coupling and use the symbol $U_4 = J$. The

full onsite Coulomb interaction written in terms of the two energy scales U and J is,

$$\frac{U}{2}\sum_{\beta\neq\beta'}\sum_{\sigma\sigma'}c^{\dagger}_{\beta\sigma}c_{\beta\sigma}c^{\dagger}_{\beta'\sigma'}c_{\beta'\sigma'}+\frac{J}{2}\sum_{\beta\neq\beta'}\sum_{\sigma\sigma'}c^{\dagger}_{\beta\sigma}c^{\dagger}_{\beta'\sigma'}c_{\beta\sigma'}c_{\beta'\sigma}$$
$$+(U+2J)\sum_{\beta}c^{\dagger}_{\beta\uparrow}c_{\beta\uparrow}c^{\dagger}_{\beta\downarrow}c_{\beta\downarrow}+J\sum_{\beta\neq\beta'}c^{\dagger}_{\beta\uparrow}c^{\dagger}_{\beta\downarrow}c_{\beta'\downarrow}c_{\beta'\uparrow}. \tag{4.97}$$

4.3.5 Long-range Coulomb interaction

We have now established the model which we shall study for $Sr_3Ru_2O_7$. In this and the following two sections we discuss some additional effects which are not incorporated in this model.

The most significant of these is the long-range Coulomb interaction. We have excluded all interactions apart from the largest terms, which are those between particles on the same Ru site. The interaction terms between particles on nearby sites represent a significant correction to the purely onsite terms(107). As shown in section 4.1.2, one can write down the Coulomb interaction between particles in a condensed matter system in second-quantised form in a fully general way as a sum of two-particle operators. The largest contributions of this sum are from those terms involving operators on the same lattice site as one would expect; the off-site terms represent smaller and smaller corrections which decay as the inverse of the separation. However, the sum of all of the offsite terms represents a large correction to the energy, and its omission cannot be justified on the basis that it is a small correction to the on-site interaction. It is in this sense that the Coulomb interaction is said to be long-range.

The physical consequence of the long-range Coulomb interaction is an enormous energetic cost to having mesoscopic regions of the system which are charged, which enforces that the system is charge neutal over microscopic or mesoscopic length-scales. At the level of two particles, if the system is charge-neutral over the scale of the separation of two particles, the Coulomb interaction is screened by the presence of intervening electrons to effectively have a much smaller value. In this scenario one can therefore treat the Coulomb interaction as being effectively short-range, although the restriction to a purely onsite interaction still represents a substantial additional approximation to this(107).

As we discuss in section 4.6.2, however, the long-range Coulomb interaction is extremely relevant to the state which is predicted by our mean field calculations to occur coincident with the metamagnetism, which is a phase-separated mixture of two charged phases. This style of state must occur as domains of the two phases, and the length-scale for the domains is set by the long-range Coulomb interaction. In

our model which contains only onsite interactions, there is nothing to set this length-scale and nothing to provide any information on the domain structure.

4.3.6 Spin-Orbit interaction

The spin-orbit interaction is the lowest level microscopic interaction which provides the model with knowledge of the direction of the applied magnetic field. Consequently, we suggest that it is essentially responsible for the anisotropic behaviour associated with the nematic phase in $Sr_3Ru_2O_7$; this has been suggested by others, and more sophisticated models which include the spin-orbit interaction obtain solutions which exhibit a nematic phase(101; 102). It is therefore one of the most important effects which we do not incorporate into the modelling.

The spin-orbit interaction arises at the single-particle level from including the effects of special relativity perturbatively. The spin and orbital angular momentum of a particle are coupled, and the interaction can be written as,

$$\mathcal{K}\vec{L}\cdot\vec{S} = \mathcal{K}\left[\frac{1}{2}(L^+S^- + L^-S^+) + L^zS^z\right].$$

Because the orbital angular momentum is quenched in the t_{2g} states, one might naively expect the spin-orbit interaction to be irrelevent for these degrees of freedom; however, referring back to equation 4.79 it will be observed that the linear combinations $(d_{yz} + id_{zx})$ and $(d_{yz} - id_{zx})$ are spherical harmonics and therefore have nonzero orbital angular momentum. Written in the t_{2g} subspace the spin-orbit interaction takes the form(108),

$$\begin{aligned}\mathcal{K}\vec{L}\cdot\vec{S} = \frac{\mathcal{K}}{2}\Big[&Z^\dagger_\uparrow(X_\downarrow - iY_\downarrow) - Z^\dagger_\downarrow(X_\uparrow + iY_\uparrow) + (X^\dagger_\downarrow + iY^\dagger_\downarrow)Z_\uparrow - (X^\dagger_\uparrow - iY^\dagger_\uparrow)Z_\downarrow \\ &+ iX^\dagger_\uparrow Y_\uparrow - iY^\dagger_\uparrow X_\uparrow - iX^\dagger_\downarrow Y_\downarrow + iY^\dagger_\downarrow X_\downarrow\Big]. \qquad (4.98)\end{aligned}$$

The size of the energy scale $\mathcal{K}$ in the single-layer compound Sr_2RuO_4 has been estimated as approximately 0.16 eV(109), and the same value can be taken for the bilayer compound because the spin-orbit interaction is an onsite, single-particle effect. This is smaller, albeit not greatly so, than the effect of the second-neighbour hopping, which is to be measured as $zt_2 \approx .8$eV where $z = 4$ is the number of nearest-neighbour Ru sites. However, we shall attempt to fit the experimental magnetisation curves using values of the Hund coupling J that are smaller than $\mathcal{K}$, and from this perspective

the spin-orbit interaction is certainly a relevant energy scale and should be included. Our reasons for not incorporating the spin-orbit interaction are to a great extent to make our calculations easier: the spin-orbit interaction introduces terms which couple the t_{2g} orbital species and this greatly increases the complexity of solving the mean field theory. (See section 4.3.3 where we discuss not including hybridisation terms which couple orbital degrees of freedom.)

Because it contains matrix elements between different t_{2g} species, the spin-orbit interaction will result in reconstructions where the Fermi surfaces of distinct bands cross in tight binding pictures. The resulting Fermi surfaces will more closely resemble the experimental Fermi surface. However, similar effects should in principle also arise purely from the hybridisation energies as we have discussed. We do not anticipate that including the spin-orbit interaction will qualitatively alter the magnetisation curves which we obtain in the mean field solution, although we anticipate a quantitative change between fields in the c-axis and in-plane fields.

4.3.7 The theory as an effective description of correlated physics

The model of $Sr_3Ru_2O_7$, which involves a large degree of simplification as we have discussed above, is still far too difficult to solve exactly. We treat the model using mean field theory and in this section we say something about the inherent limitations of this technique, and how the mean field theory solution corresponds to the true physical situation in the material. Mean field theory approximates the behaviour of an interacting system with a non-interacting state; by its very nature this does not capture the physics of systems in which the correlations between particles play an important role.

In particular, mean field theory vastly over-estimates the tendency of systems to magnetic order. This is seen in the case of the Hubbard model: as we dealt with in section 4.2, mean field theory predicts itinerant ferromagnetism in the Hubbard model by the Stoner argument, but it is known that the Hubbard model is not ferromagnetic in regions of its phase diagram where the Stoner criterion is met(110). Mean field theory overestimates the susceptibilty of systems to magnetic order. Something must therefore be said regarding the itinerant ferromagnetism in the Ruthenate model.

The metamagnetism in $Sr_3Ru_2O_7$ is associated with an instability to itinerant ferromagnetism. In modelling the metamagnetism, we therefore seek an itinerant ferromagnetic solution. This is a style of state which mean field theory can provide and it is possible to tune a mean field theory to match the experiments relatively well. We operate with a mean field theory in which we target itinerant ferromagnetism exclusively, and do not investigate other styles of state which could also be sought

using Hartree-Fock mean field theory, such as antiferromagnetism or superconductivity.

Now, the state of the real material is that of a Fermi liquid, which refers to the idea that the interactions between electrons in the real material act to produce an effective non-interacting state of quasi-particles, where the corresponding energy scales have been renormalised(106, pp. 126-132). The energy scales which are ingredients of the mean field theory, t, t_2, U and J, are reflective of these renormalised energy scales, and not the bare parameters that would be calculated in microscopic calculations. Associated with this is the issue of the sizes and the roles of the interaction energies U and J. The Hund coupling J provides an intrinsic onsite ferromagnetic interaction, and therefore acts to promote ferromagnetism more aggressively than U; we therefore suggest that J is largely responsible for the magnetism which we presume to exist in the groundstate of our model and in the real material. However, including a sizeable value of U with $J = 0$ is sufficient to produce in the mean field solution, a metamagnetic jump only slightly smaller than what is seen in the experiments; the addition of a moderate value of J then results in a metamagnetic jump which matches the experiments quite well. It is possible that the mean field theory provides the correct answer for the wrong reasons here, in that the parameter U provides a susceptibility to ferromagnetism in the mean field solution which it does not in the exact solution, whereas in the exact solution ferromagnetism is due primarily to J.

Finally, a crucial feature of the magnetisation curves which is not well-predicted by the mean field theory is the magnetic field at which the metamagnetic jump takes occurs: the mean field theory predicts magnetic fields which are an order of magnitude larger than what is seen in experiments. This huge discrepancy is a symptom of the energy scales in the mean field theory being reflective of the renormalised energies in the Fermi liquid state, rather than the bare microscopic energies. We include the magnetic field in our model by adding the term,

$$-B \sum_{j\beta\sigma} \sigma c^{\dagger}_{j\beta\sigma} c_{j\beta\sigma}.$$

In the mean field solution, this term is left unaltered, and the parameter B occurs in the solution as a bare parameter; we presume that in the exact solution of the model one would find rather an effective renormalised field. Therefore, in describing the state of the system using mean field theory, the value of the parameter B ought to be reflective of the renormalised Fermi liquid field, and not the bare value of the magnetic field that would be applied in an experiment. We make no statement regarding how to relate the renormalised field to the physical applied field, either in our own model or in the real

material: this simply lies beyond the scope of our calculations.

4.4 Tight binding theory

In this section we deal with a non-interacting model of the Ru $4d$ t_{2g} electrons on a bilayer. We include a hybridisation $-t$ between nearest neighbour Ru sites, and a hybridisation $+t_2$ between second nearest neighbour sites. The choice of definitions to imply that the first and second neighbour hybridisations have opposing signs, and indeed the very inclusion of a second neighbour hybridisation, anticipates the comparison of the tight binding Fermi surface with that of $Sr_3Ru_2O_7$ which we make near the end of this section; this comparison shows that a second-neighbour hybridisation differing in sign to the nearest-neighbour hybridisation and with magnitude approximately $t_2 = 0.4t$ is required to match the experimental Fermi surface.

We do not include any hybridisation between different t_{2g} orbitals and the band structures of the three orbital species are therefore independent. In addition, as we have discussed in the previous section, each of the three orbitals hybridises in only two of the three crystal-axis directions. The X and Y holes are mobile in the y and x directions respectively, and in the z direction so that they can move between the upper and lower part of the bilayer; the sub-geometry on which they are mobile is therefore a ladder, where the two rungs of the ladder correspond to the two bilayers. The Z holes are mobile in both the x and y directions, but cannot move between the bilayers and the corresponding subgeometry is therefore that of a square lattice. Full calculations of the bandstructures are provided in appendix B, where the X/Y orbitals and the Z orbitals are dealt with separately as the t-t_2 tight-binding model applied to the geometries of a ladder and a square lattice respectively.

We calculate the magnetisation of the system as a function of an applied magnetic field. The magnetisation increases essentially linearly with field, but at a certain field the slope abruptly changes. This point marks where the top-lying spin-$\downarrow$ X/Y band is pushed past the chemical potential and is emptied of holes, and the corresponding Fermi surface vanishes. When interactions are included into the model, this will come to cause a jump in the magnetisation - metamagnetism - qualitatively and quantitatively similar to that seen in $Sr_3Ru_2O_7$.

The full tight binding model for all three t_{2g} orbital species is, with the inclusion of an externally

applied magnetic field B, in the basis of Bloch states,

$$H = \sum_{\vec{k}\alpha\sigma} \begin{pmatrix} X^\dagger_{\vec{k},\alpha,\sigma} & Y^\dagger_{\vec{k},\alpha,\sigma} & Z^\dagger_{\vec{k},\alpha,\sigma} \end{pmatrix} \begin{pmatrix} \epsilon^X_{\vec{k}\alpha} - B\sigma & 0 & 0 \\ 0 & \epsilon^Y_{\vec{k}\alpha} - B\sigma & 0 \\ 0 & 0 & \epsilon^Z_{\vec{k}\alpha} - B\sigma \end{pmatrix} \begin{pmatrix} X_{\vec{k},\alpha,\sigma} \\ Y_{\vec{k},\alpha,\sigma} \\ Z_{\vec{k},\alpha,\sigma} \end{pmatrix}. \tag{4.99}$$

The Bloch wavevector $\vec{k}$ is the dual variable to the x- and y- coordinates of the sites. The index α is the dual of the z-coordinate, which takes just two values and the Bloch states are symmetric ($\alpha = +1$) or antisymmetric ($\alpha = -1$) combinations of states on the upper and lower parts of the bilayer. As a result of the property that each of the orbital species only hybridise along two of the three lattice directions, $\epsilon^X_{\vec{k}\alpha}$ is independent of k_x,

$$\epsilon^X_{\vec{k}\alpha} = \epsilon^X_{k_y\alpha} = -2(t - \alpha t_2)\cos k_y - \alpha t, \tag{4.100}$$

$\epsilon^Y_{\vec{k}\alpha}$ is independent of k_y,

$$\epsilon^Y_{\vec{k}\alpha} = \epsilon^X_{k_x\alpha} = -2(t - \alpha t_2)\cos k_x - \alpha t, \tag{4.101}$$

and $\epsilon^Z_{\vec{k}\alpha}$ is independent of α,

$$\epsilon^Z_{\vec{k}\alpha} = \epsilon^Z_{\vec{k}} = -2t\cos k_x - 2t\cos k_y + 4t_2\cos k_x \cos k_y. \tag{4.102}$$

These spectra are derived in appendix B.

The total number of holes per site is

$$n = \frac{1}{2L_xL_y}\sum_{j\alpha\sigma}\left[\langle X^\dagger_{j\alpha\sigma}X_{j\alpha\sigma}\rangle + \langle Y^\dagger_{j\alpha\sigma}Y_{j\alpha\sigma}\rangle + \langle Z^\dagger_{j\alpha\sigma}Z_{j\alpha\sigma}\rangle\right], \tag{4.103}$$

where L_x and L_y are the size of the system in the x and y directions respectively. The number of Z-orbital holes is independent of the index α, and we write,

$$\langle Z^\dagger_{j\alpha\sigma}Z_{j\alpha\sigma}\rangle = n_{Z\sigma}. \tag{4.104}$$

The X- and Y-orbitals have the same occupancy:

$$\langle X^\dagger_{j\alpha\sigma}X_{j\alpha\sigma}\rangle = \langle Y^\dagger_{j\alpha\sigma}Y_{j\alpha\sigma}\rangle = n_{X\alpha\sigma}, \tag{4.105}$$

and the total number of X/Y-orbital spin-σ holes per site of is given by

$$n_{X\sigma} = \frac{1}{2}(n_{X,+,\sigma} + n_{X,-,\sigma}). \tag{4.106}$$

The total number of holes per site can therefore be written as,

$$n = 2n_{X\uparrow} + 2n_{X\downarrow} + n_{Z\uparrow} + n_{Z\downarrow}. \tag{4.107}$$

The bands are populated up to a chemical potential μ which is chosen to provide the correct number of holes per site, that is to satisfy the constraint

$$n = 2. \tag{4.108}$$

We shall refer to the constraint as the *external equation*.

The major difficulty in these tight binding calculations is that one has access to calculations at constant chemical potential, when what is desired is calculations for a constant number of holes. The theory provides the occupation numbers of the individual bands as functions of the chemical potential (see appendix B), from which the total number of holes per site is determined by equation 4.107; one has to then choose the chemical potential to achieve the physical number of holes, that is to satisfy equation 4.108. One must implement some iterative procedure on the computer to search for the correct chemical potential. The same issue must be dealt with in the mean field theory which we discuss later in the chapter, and in practice the tight binding calculations which we shall exhibit in this section were performed by applying the same computational procedures as were used for the mean field calculations, the procedures being provided in the appendix C.

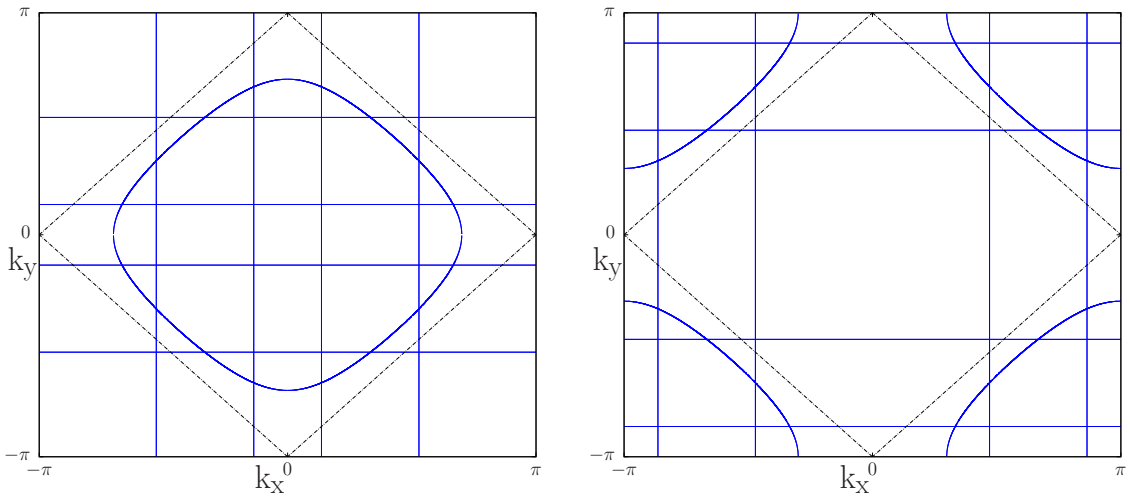

Figure 4.5: Fermi surface for the tight-binding model for the case of nearest neighbour hopping only ($t_2 = 0$) Left: hole picture; Right: electron picture. Comparing the right hand picture with ARPES determinations of the $Sr_3Ru_2O_7$ Fermi surface, the square lattice Fermi surface in the tight binding model is holelike while that of the material is electronlike.

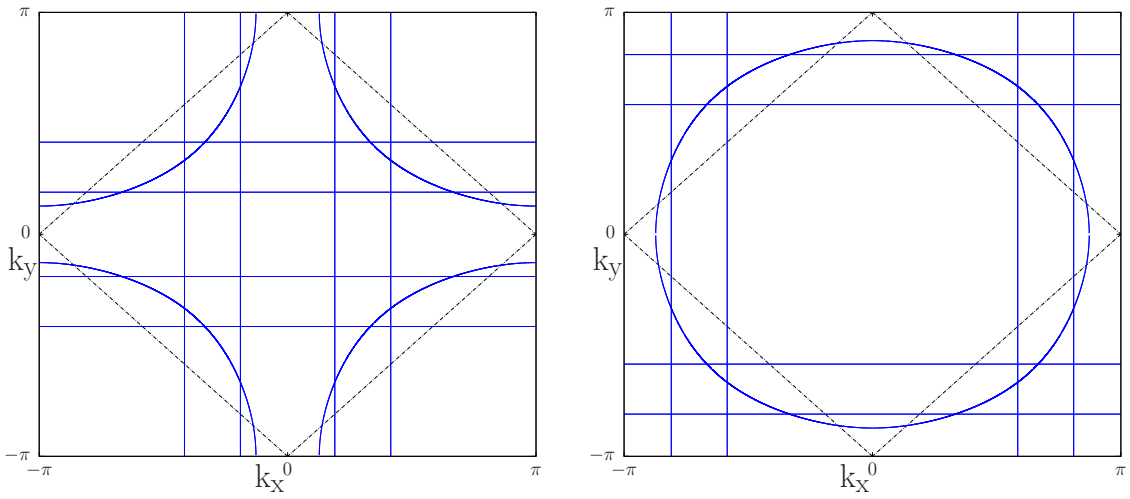

Figure 4.6: Fermi surface for the tight-binding model including a nearest neighbour hopping t and a second-nearest-neighbour hopping $t_2 = 0.4t$. Left: hole picture; Right: electron picture. Comparing the right hand picture with ARPES determinations of the $Sr_3Ru_2O_7$ Fermi surface, the square lattice Fermi surfaces are both electronlike.

The zero-field ($B = 0$) Fermi surface for the tight-binding model is depicted in figures 4.5 and 4.6, for the cases of $t_2 = 0$ and $t_2 = 0.4t$ respectively. Each of the one-dimensional X/Y bands provides two

lines of Fermi surface at the points in reciprocal space where the band crosses the chemical potential. There are therefore four lines in both the k_x- and k_y-directions. The Z band provides a curved Fermi surface.

The right-hand images in figures 4.5 and 4.6 are to be compared with the picture of the $Sr_3Ru_2O_7$ Fermi surface deduced from ARPES experiments in Figure 3.4. The aspect of these pictures to compare is the square lattice Fermi surface, which is centred on the (π, π) point in right hand member of figure 4.5, but is centred on the $(0, 0)$ point in the right hand member of 4.6 and in the ARPES data in figure 3.4. This discrepancy between the $t_2 = 0$ theory and the experiment is precisely what motivates the inclusion of a sizeable second-neighbour hopping into the model.

The topology of the square lattice Fermi surface is associated with whether the Z-van Hove singularity lies above or below the chemical potential, and the position of the singularity in a tight binding description has a sensitive dependence on the size of the second neighbour hopping energy. In order to obtain the same topology as the experimental Fermi surface, a large enough second neighbour hopping must be included to push the van Hove singularity past the chemical potential at zero field; the value $t_2 = 0.4t$ is, approximately speaking, the minimum value which accomplishes this while keeping the occupancy of the Z-bands at the approximate experimental value of $1/3$, which corresponds to the 2 holes per site being equally distributed amongst the three t_{2g} orbitals(66) (see appendix B, figure B.8).

The magnetisation of the system as a function of the applied magnetic field B is depicted in figure 4.7. We have calculated both a *6-band solution*, which includes all the occupation numbers we have discussed, and a *5-band solution*, in which the occupancy of the $X_{-\downarrow}$ band, which is the highest-lying of the X-bands, is set explicitly to zero, $n_{X,-,\downarrow} = 0$. The physical meaning of the plot of magnetisation is that, as the field B is increased, the spin-$\downarrow$ bands are pushed up in energy until the $X_{-\downarrow}$ band is pushed past the chemical potential and is emptied of holes. This point is seen on the figure of magnetisation where the 6-band solution smoothly merges with the 5-band solution and ceases to exist. For fields below this point, the 5-band solution corresponds to a metastable state where all the holes have been removed from the $X_{-\downarrow}$ band and put into the other bands.

The metastability of the 5-band solution at low fields is seen in the accompanying figure which shows the energy of the 6- and 5-band solutions as a function of B. The total energy of the system is

given by,

$$\begin{aligned} E &= 2E_X + E_Z - BM \\ &= \sum_\sigma \Big[-2(t-t_2)\frac{\sin(\pi n_{X,+,\sigma})}{\pi} - 2(t+t_2)\frac{\sin(\pi n_{X,-,\sigma})}{\pi} - tn_{X,+,\sigma} + tn_{X,-,\sigma} \\ &\qquad - 4t\mathcal{Q}_1(\mu + B\sigma) + 4t_2\mathcal{Q}_2(\mu + B\sigma)\Big] - BM, \end{aligned} \tag{4.109}$$

where the functions $\mathcal{Q}_1(\epsilon)$ and $\mathcal{Q}_2(\epsilon)$ are as given in appendix B. The figure clearly shows the energy of the 6-band solution to be lower than that of the 5-band solution for the same field in the low-field region.

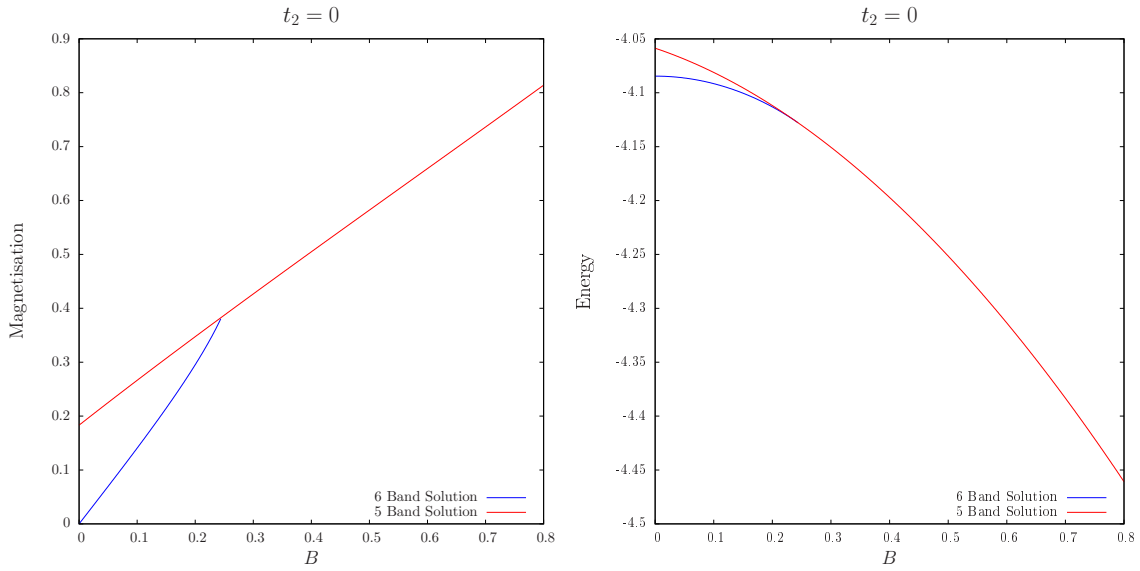

Figure 4.7: Magnetisation and Energy of the tight-binding model as a function of the applied magnetic field B. The 6-band solution includes all of the bands, and the 5-band solution excludes the $X_{-\downarrow}$-band.

4.5 Model with onsite Coulomb interactions: Mean field theory

We now come to consider the model which adds the onsite interaction derived in section 4.3.4 to the tight-binding model of the previous section. We solve this model approximately using Hartree Fock mean field theory. In this section we deal with the formalism of the theory. The calculations themselves are exhibited and discussed in section 4.6.

We approximate the interacting Hamiltonian by a mean field Hamiltonian which is obtained by

the Hartree-Fock prescription which was introduced in section 4.2, where the mean fields which we include in the theory are the occupation numbers of each of the bands in the system. The values of the occupation numbers are determined as the solutions of a set of self-consistent equations, which we term the *internal equations*, which are transcendental and are solved on the computer. The solving of the internal equations is made considerably easier by the introduction of two new parameters $\tilde{\mu}$ and $\tilde{B}$, which are related to the chemical potential μ and the magnetic field B respectively, and treating these as independent variables. The values of $\tilde{\mu}$ and $\tilde{B}$ must then be tuned to satisfy two *external equations* to provide the correct total number of holes in the system and the correct magnetic field B which is the physical independent variable. The computational procedures for solving both the internal equations and the external equations are dealt with in appendix C.

Referring to section 4.3.4, the on-site Coulomb interaction for the t_{2g} orbitals is given by

$$\begin{aligned}\hat{\mathcal{V}} = \frac{U}{2}\sum_{\beta\neq\beta'}\sum_{\sigma\sigma'} c^{\dagger}_{\beta\sigma}c_{\beta\sigma}c^{\dagger}_{\beta'\sigma'}c_{\beta'\sigma'} + \frac{J}{2}\sum_{\beta\neq\beta'}\sum_{\sigma\sigma'} c^{\dagger}_{\beta\sigma}c^{\dagger}_{\beta'\sigma'}c_{\beta\sigma'}c_{\beta'\sigma} \\ + (U+2J)\sum_{\beta} c^{\dagger}_{\beta\uparrow}c_{\beta\uparrow}c^{\dagger}_{\beta\downarrow}c_{\beta\downarrow} + J\sum_{\beta\neq\beta'} c^{\dagger}_{\beta\uparrow}c^{\dagger}_{\beta\downarrow}c_{\beta'\downarrow}c_{\beta'\uparrow}. \qquad (4.110)\end{aligned}$$

We impose

$$\langle c^{\dagger}_{\beta\sigma}c_{\beta'\sigma'}\rangle = \delta_{\beta\beta'}\delta_{\sigma\sigma'}n_{\beta\sigma}, \qquad \langle c^{\dagger}_{\beta\sigma}c^{\dagger}_{\beta'\sigma'}\rangle = 0 \qquad (4.111)$$

and consequently the mean field expectation value of the on-site Coulomb interaction term is given by

$$\begin{aligned}E_C = \langle\hat{\mathcal{V}}\rangle &= \frac{U}{2}\sum_{\sigma\sigma'}\sum_{\beta\neq\beta'} n_{\beta\sigma}n_{\beta'\sigma'} - \frac{J}{2}\sum_{\sigma}\sum_{\beta\neq\beta'} n_{\beta\sigma}n_{\beta'\sigma} + (U+2J)\sum_{\beta} n_{\beta\uparrow}n_{\beta\downarrow} \qquad (4.112)\\ &= \frac{1}{2}(U-J)\Big[n^2 - \Big(\sum_{\beta\sigma} n_{\beta\sigma}\Big)^2\Big] + Jn_{\uparrow}n_{\downarrow} + 2J\sum_{\beta} n_{\beta\uparrow}n_{\beta\downarrow},\end{aligned}$$

where n is the total number of holes per site,

$$n = \sum_{\beta\sigma} n_{\beta\sigma}, \qquad (4.113)$$

and n_{σ} is the total number of spin-σ holes per site,

$$n_{\sigma} = \sum_{\beta} n_{\beta\sigma}. \qquad (4.114)$$

Taking the derivative with respect to the fields $n_{\beta\sigma}$ yields

$$\frac{\partial E_C}{\partial n_{\beta\sigma}} = U(n - n_{\beta\sigma}) - J(n_\sigma - n_{\beta\sigma}) + 2Jn_{\beta\bar{\sigma}}. \tag{4.115}$$

We can represent the number of spin-σ in terms of the magnetisation M:

$$M = n_\uparrow - n_\downarrow \implies n_\sigma = \frac{n + \sigma M}{2}. \tag{4.116}$$

This provides

$$\frac{\partial E_C}{\partial n_{\beta\sigma}} = (U - \frac{J}{2})n - \frac{J}{2}M\sigma - (U - J)n_{\beta\sigma} + 2Jn_{\beta\bar{\sigma}}. \tag{4.117}$$

The interaction $\hat{\mathcal{V}}$ is replaced in the Hartree-Fock mean field theory with the term,

$$\sum_{j\beta\sigma}\left[\frac{\partial E_C}{\partial n_{\beta\sigma}}c^\dagger_{j\beta\sigma}c_{j\beta\sigma} - \frac{\partial E_C}{\partial n_{\beta\sigma}}n_{\beta\sigma} + E_C\right] = \sum_{j\beta\sigma}\left[(U - \frac{J}{2})n - \frac{J}{2}M\sigma - (U - J)n_{\beta\sigma} + 2Jn_{\beta\bar{\sigma}}\right]c^\dagger_{j\beta\sigma}c_{j\beta\sigma} \tag{4.118}$$
$$- \mathcal{N}\left\{\frac{1}{2}(U - J)\Big[n^2 - \Big(\sum_{\beta\sigma} n_{\beta\sigma}\Big)^2\Big] + Jn_\uparrow n_\downarrow + 2J\sum_\beta n_{\beta\uparrow}n_{\beta\downarrow}\right\}.$$

The full mean field Hamiltonian is therefore,

$$
\begin{aligned}
H_{MF} - \mu N = \sum_{\vec{k}\alpha\sigma} \Big\{ & (\epsilon^X_{k_y\alpha} - B\sigma - \mu) X^\dagger_{\vec{k}\alpha\sigma} X_{\vec{k}\alpha\sigma} + (\epsilon^X_{k_x\alpha} - B\sigma - \mu) Y^\dagger_{\vec{k}\alpha\sigma} Y_{\vec{k}\alpha\sigma} \\
& + (\epsilon^Z_{\vec{k}} - B\sigma - \mu) Z^\dagger_{\vec{k}\alpha\sigma} Z_{\vec{k}\alpha\sigma} \Big\} \\
& + \sum_{j\alpha\sigma} \Big\{ \Big((U - \frac{J}{2})n - \frac{J}{2} M\sigma \Big) \Big(X^\dagger_{j\alpha\sigma} X_{j\alpha\sigma} + Y^\dagger_{j\alpha\sigma} Y_{j\alpha\sigma} + Z^\dagger_{j\alpha\sigma} Z_{j\alpha\sigma} \Big) \\
& \qquad + \Big(-(U - J) n_{X\sigma} + 2J n_{X\bar{\sigma}} \Big) \Big(X^\dagger_{j\alpha\sigma} X_{j\alpha\sigma} + Y^\dagger_{j\alpha\sigma} Y_{j\alpha\sigma} \Big) \\
& \qquad + \Big(-(U - J) n_{Z\sigma} + 2J n_{Z\bar{\sigma}} \Big) Z^\dagger_{j\alpha\sigma} Z_{j\alpha\sigma} \Big\} \\
& - \mathcal{N} \Big\{ \frac{1}{2}(U - J) \Big[n^2 - \Big(\sum_{\beta\sigma} n_{\beta\sigma} \Big)^2 \Big] + J n_\uparrow n_\downarrow + 2J \sum_\beta n_{\beta\uparrow} n_{\beta\downarrow} \Big\} \\
= \sum_{\vec{k}\alpha\sigma} \Big\{ & \Big(\epsilon^X_{k_y\alpha} - \tilde{B}\sigma - \tilde{\mu} - (U - J) n_{X\sigma} + 2J n_{X\bar{\sigma}} \Big) X^\dagger_{\vec{k}\alpha\sigma} X_{\vec{k}\alpha\sigma} \\
& + \Big(\epsilon^X_{k_x\alpha} - \tilde{B}\sigma - \tilde{\mu} - (U - J) n_{X\sigma} + 2J n_{X\bar{\sigma}} \Big) Y^\dagger_{\vec{k}\alpha\sigma} Y_{\vec{k}\alpha\sigma} \\
& + \Big(\epsilon^Z_{\vec{k}} - \tilde{B}\sigma - \tilde{\mu} - (U - J) n_{Z\sigma} + 2J n_{Z\bar{\sigma}} \Big) Z^\dagger_{\vec{k}\alpha\sigma} Z_{\vec{k}\alpha\sigma} \Big\} \\
& - \mathcal{N} \Big\{ \frac{1}{2}(U - J) \Big[n^2 - \Big(\sum_{\beta\sigma} n_{\beta\sigma} \Big)^2 \Big] + J n_\uparrow n_\downarrow + 2J \sum_\beta n_{\beta\uparrow} n_{\beta\downarrow} \Big\}. \qquad (4.119)
\end{aligned}
$$

where as in section 4.2 we have introduced an *internal chemical potential*,

$$
\tilde{\mu} = \mu - \left(U - \frac{J}{2} \right) n, \qquad (4.120)
$$

and in addition we have have introduced the parameter,

$$
\tilde{B} = B + \frac{J}{2} M, \qquad (4.121)
$$

which we call the *internal magnetic field*. It is quite useful to work with these two parameters because for given values of $\tilde{\mu}$ and $\tilde{B}$ the occupancy of each of the orbital species can be determined independently of each other as the solutions of pairs of coupled equations, the internal equations, which we describe explicitly in appendix C. The value of $\tilde{\mu}$ is set by the constraint that the number holes per site be fixed, and the value of $\tilde{B}$ is set for a given value of the real magnetic field B by the equation 4.121.

In calculating the magnetisation of the system as a function of B, the methodology is therefore to

find the correct values $\tilde{\mu}$ and $\tilde{B}$ for each value of B, that is to solve,

$$n = 2, \tag{4.122}$$

$$B = \tilde{B} - \frac{J}{2}M, \tag{4.123}$$

which we refer to as external equations. We find the values of $\tilde{\mu}$ and $\tilde{B}$ which satisfy the external equations using a Newton-Raphson procedure which is described in appendix C; each iteration of this procedure requires the evaluation of the total number of holes n and the magnetisation M which requires calculating the band occupation numbers by solving the internal equations.

Our computational procedures to solve the external equations and the internal equations converge to provide a highly accurate solution to the mean field theory provided that these procedures are seeded with initial estimates that are sufficiently close to the solution. The exception to this is in scenarios where there are multiple closely positioned solutions to the internal equations, for which the procedures for the internal equations can fail. If one is attempting to find the solution in close proximity to where the solution is already known, ie for a small change in the magnetic field, one can use the values of $\tilde{\mu}$, $\tilde{B}$ and the occupation numbers of that known solution as the inital values for the Newton-Raphson procedures. This methodology has been applied throughout the mean field calculations: we trace out the solutions by incrementally increasing the value of B.

In the situations involving multiple closely positioned roots in which the procedures to solve the internal equations fail, we consequently have not been able to calculate the mean field solutions. In the plots of the solutions as functions of B which we exhibit in the section 4.6, there are small gaps in some of the curves, which correspond to regions in which it is difficult or impossible for our numerical procedures to find the solution. In the majority of these cases, the continuity of the solutions strongly implies that solutions do indeed exist in these regions, and therefore the gaps in our curves are entirely a computational issue and have no physical significance. In section 4.6.3 we shall discuss cases in which our procedures fail to provide solutions where we cannot rule out that the solution does not exist.

4.6 Mean Field Theory Calculations

In this section we exhibit mean field solutions of the model with onsite interactions. The main physical phenomenon which is reproduced in the mean field theory is the metamagnetic jump seen in the magnetisation curve. We shall mostly examine the mean field solutions in the form of plots of their

corresponding magnetisation curves. We shall often obtain multiple mean field solutions at the same field; in most scenarios the system adopts whichever solution has the lowest energy, which is given by

$$E = \sum_{\sigma} \Big[-2(t-t_2)\frac{\sin(\pi n_{X,+,\sigma})}{\pi} - 2(t+t_2)\frac{\sin(\pi n_{X,-,\sigma})}{\pi} - t n_{X,+,\sigma} + t n_{X,-,\sigma} \\ - 4t\mathcal{Q}_1(\tilde{\mu} + \tilde{B}\sigma + (U-J)n_{Z\sigma} - 2Jn_{Z\bar{\sigma}}) + 4t_2\mathcal{Q}_2(\tilde{\mu} + \tilde{B}\sigma + (U-J)n_{Z\sigma} - 2Jn_{Z\bar{\sigma}}) \Big] \\ + \frac{1}{2}(U-J)\Big[n^2 - \sum_{\beta\sigma}(n_{\beta\sigma})^2\Big] + \frac{J}{4}(n^2 - M^2) + 2J\sum_{\beta} n_{\beta\uparrow}n_{\beta\downarrow} - BM. \quad (4.124)$$

An important exception occurs in the vicinity of the metamagnetism, where the lowest energy solution is a *mixed phase* which is a phase separated mixture of two different mean field solutions. The prediction of the existence of a phase separation in the vicinity of the metamagnetism is the primary physical prediction of this work, and we suggest that the phase separated state corresponds to the nematic phase in $Sr_3Ru_2O_7$.

Section 4.6.1 contains calculations which exhibit the effects of the two parameters of the onsite Coulomb interaction U and J. If the interactions are small, the magnetisation is qualitatively the same as for the pure tight binding model: at a certain field the system crosses over from the 6-band state to the 5-band state with a kink in the magnetisation. If large enough interactions are included, the kink is replaced with a steep rise in the magnetisation, which is precisely metamagnetism. Coincident with this steep rise in the magnetisation the groundstate is a phase separated mixture of 6- and 5-band solutions. Section 4.6.2 is devoted to a discussion of this mixed phase; we describe how the mixed solution is calculated, exhibit some calculations which evince the properties of the mixed phase, and give some discussion of the physical implications for the real material. In particular, the two subphases are not charge-neutral; the implication is that there must be domains of the two subphases on a microscopic or mesoscopic scale, and that the size of the domains is largely controlled by the long-range Coulomb interaction which is entirely absent from our modelling.

We then move on to a set of mean field calculations which make alterations to the model, with the aim of investigating the possible relevance of the Z-bands to the experimental metamagnetism. Each of these alterations is related to increasing the Z-band density of states at the Fermi level, and therefore promote Z-mediated Stoner ferromagnetism. In section 4.6.3 we investigate the effect of altering the second neighbour hopping energy. Changing the second neighbour hopping moves the van Hove singularity in the Z band structure. There is a range of second neighbour hopping energies for which an additional metamagnetic jump occurs, at a field which depends sensitively on the seond

neighbour hopping. The jump is between states which differ in the topology of one of the Z-band Fermi surfaces, and the metamagnetic region is associated with a phase separated mixture of the two phases that is completely analogous to the X/Y metamagnetism. Section 4.6.4 investigates the effect of reducing the Z-band hopping energies while keeping the X/Y hopping energies fixed, which has the effect of increasing the Z-band density of states. We find that this can promote a large-moment state in which the spin-$\downarrow$ Z fermi surface has vanished. The associated magnetic moment is significantly larger than what is observed in $Sr_3Ru_2O_7$. Then in section 4.6.5 we investigate the effects of a crystal field splitting of the t_{2g} shell, such that the energy of the Z bands is lowered relative to that of the X/Y bands by an amount Δ, which is another way of moving the van Hove singularity close to the Fermi surface at zero field. We find that in this scenario the Z-bands do not become relevant. We argue that all of these findings suggest that it is unlikely that the metamagnetism in $Sr_3Ru_2O_7$ is controlled by the Z bands: whether Z metamagnetism occurs at all, and whether its effect is too small or much too large, is dependent on careful tuning of these parameters. By contrast, the X/Y metamagnetism is comparatively robust: it is always seen provided the interactions are sufficiently large, and the size of the associated magnetisation jump can quite easily be made to match the experiments.

Finally in section 4.6.6 we exhibit mean field calculations for the system when it is subject to a small amount of doping. We find that doping alters the field at which the X/Y metamagnetism occurs, with hole doping pushing the field to higher values and electron doping pushing the field to smaller values. This is the opposite trend to what is suggested by the electron-doping experiments.

4.6.1 Effect of varying U and J

In this section we exhibit mean field calculations for the model with onsite interactions, and examine the effect of varying the parameters U and J. For sufficiently large interactions, the crossing over from the 6-band solution to the 5-band solution as a function of magnetic field occurs with a metamagnetic jump. There occurs a small range of values of the applied field in which the energetically preferred mean field solution is a phase separated mixture of 6- and 5-band solutions, which produces an associated steep increase in the magnetisation with field. Of the two interaction parameters U and J, a large U alone is sufficient to produce all of the key features of the solution, but to obtain a metamagnetic jump which is the same size as experiments J must be included.

We begin with calculations which set $J = 0$. Calculations of the magnetisation as a function of field are shown for $U = 1$, $U = 2$ and $U = 3$ respectively. The case $U = 1$ is qualitatively the same as

the pure tight binding model: the top-lying X/Y band is pushed past the chemical potential by the application of a sufficient magnetic field, and this occurs at the crossing of the 6- and 5-band solutions. Like the case of the pure tight binding model, this simply produces a kink in the magnetisation, not the jump in the magnetisation that constitutes metamagnetism.

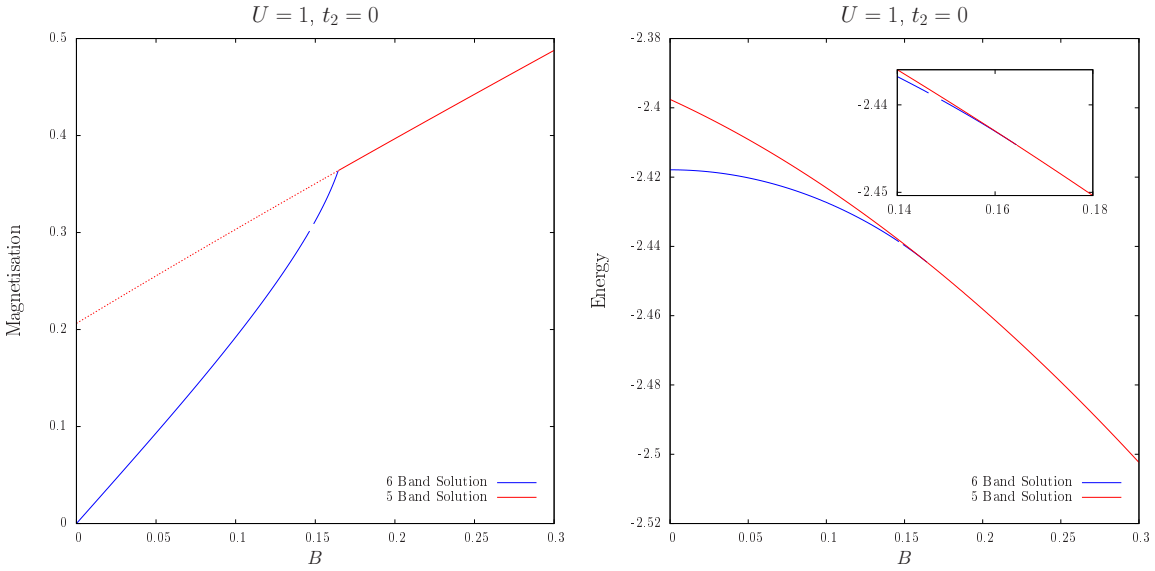

Figure 4.8: Mean field solutions, $U = t$, $t_2 = 0$

The mean field calculations exhibit metamagnetism if strong enough interactions are included. All of the important features to be discussed in this section are already exhibited in the calculation for $U = 2$ (figure 4.9), but they are more visible in the $U = 3$ calculation in figure 4.10. The magnetisation jump itself corresponds to a new type of solution which is shown as a green curve in these figures. This solution is a phase separated mixture of 6- and 5-band solutions. It is found that such a mixed phase has a lower energy than either a wholly 6- or 5-band solution in the field-region for which it is plotted. As a function of the increasing magnetic field, the fractional makeup of the mixed phase smoothly changes to connect up with the purely 6- and 5-band solutions. In the region of the mixed phase, the magnetisation shows a steep increase with field: this is precisely the behaviour associated with metamagnetism. Increasing the Coulomb interaction U increases the size of the magnetisation jump, and pushes the jump towards smaller values of the applied field.

Another feature to emerge with sufficient interactions is the appearance of a second 6-band solution. Comparing with the original 6-band solution, which occurs in the tight binding model and has zero magnetisation at zero field, the new solution is characterised by having a larger magnetisation at the

same field. The magnetisation of this solution is actually *decreasing* with increasing field to smoothly connect up with the other 6-band solution, at which point both solutions cease to exist. The new 6-band solution is always higher energy than the original 6-band solution, and has no relevance to the groundstate of the system.

Figures 4.10 and 4.11 show the calculations for $t_2 = 0$ and $t_2 = 0.4t$ respectively. Although the $t_2 = 0.4t$ calculation shows a larger magnetisation, the two pictures are qualitatively similar.

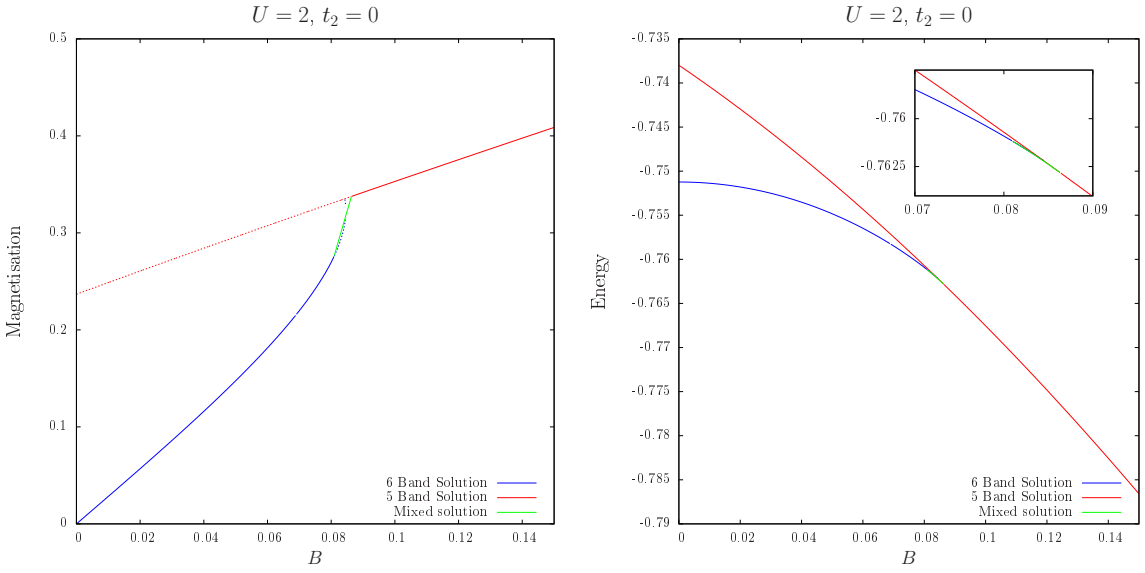

Figure 4.9: Mean field solutions, $u = 2t$, $t_2 = 0$

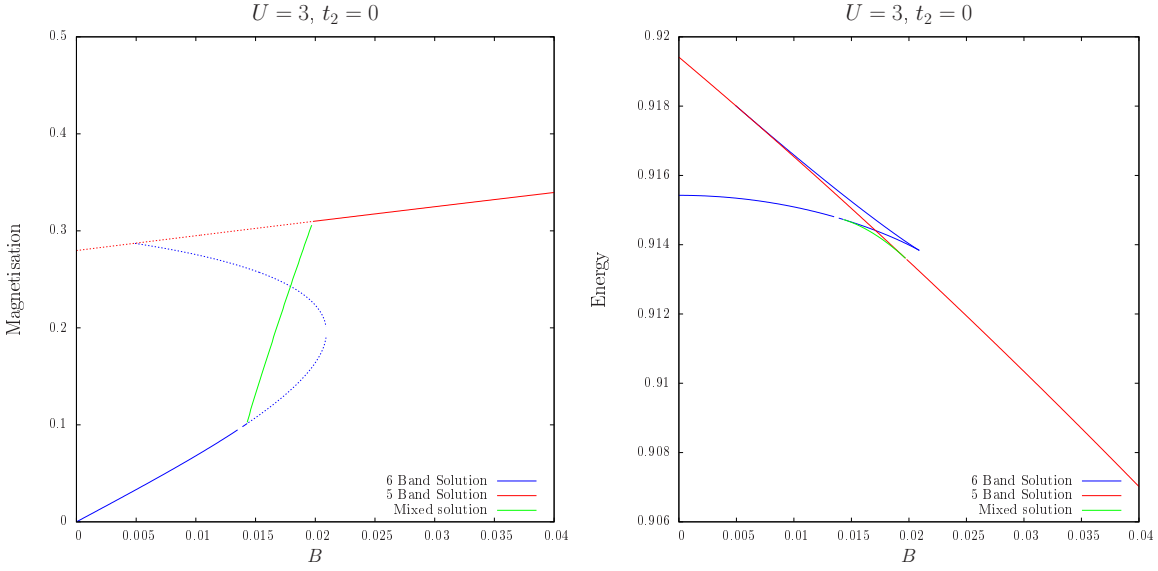

Figure 4.10: Mean field solutions, $U = 3t$, $t_2 = 0t$

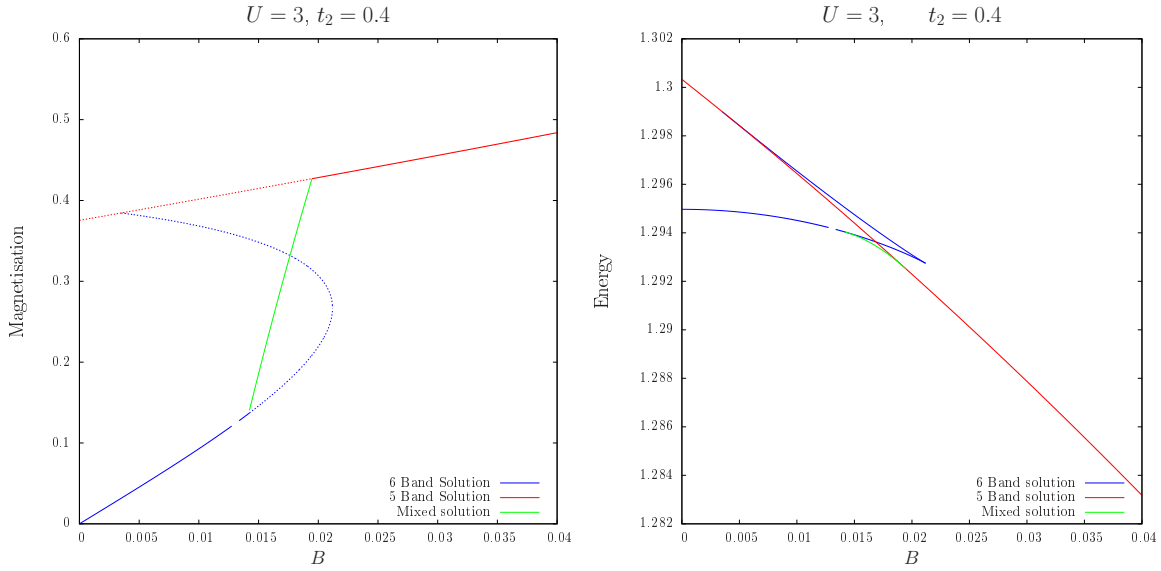

Figure 4.11: Mean field solutions, $U = 3t$, $t_2 = 0.4t$

Increasing U even further drives the system ferromagnetic at zero field. In terms of the plots of magnetisation versus field for the mean field solutions, increasing U pushes the termination point of the 6-band solution to smaller fields, until the solutions cease to exist entirely. This is illustrated in figures 4.12 and 4.13. Figure 4.12 has the metamagnetism pushed to smaller fields and and figure 4.13 is certainly ferromagnetic at zero field. In the latter instance we have not calculated a phase separated solution, but the 5-band solution being lower energy than the 6-band solution at zero-field indicates the zero-field solution must be either the 5-band solution or a mixture.

The driving of the system ferromagnetic with increasing U can also be viewed in terms of the magnetic susceptibility associated with the paramagnetic solution, which is exhibited as a function of U in figure 4.14. This quantity is calculated by calculating the magnetisation of the 6-band solution at a small field value $B = 0.0001$, and then obtaining the susceptibility as the magnetisation divided by the field M/B. The susceptibility appears to diverge at some value of U slightly greater than $U = 3$, corresponding to the ferromagnetic instability. The energies of the 6-band and 5-band solutions at zero field are plotted as a function of U in figure 4.15, showing the crossing of the two energies with increasing U. We expect that there is a range of values of U, for which the energies of the two solutions are especially close, for which the groundstate will be a phase separated mixture of the nonmagnetic 6-band solution and the ferromagnetic 5-band solution, and increasing U smoothly changes the fractional makeup between the purely 6-band and purely 5-band solutions in an analogous

fashion to mixed solutions in the magnetisation curves.

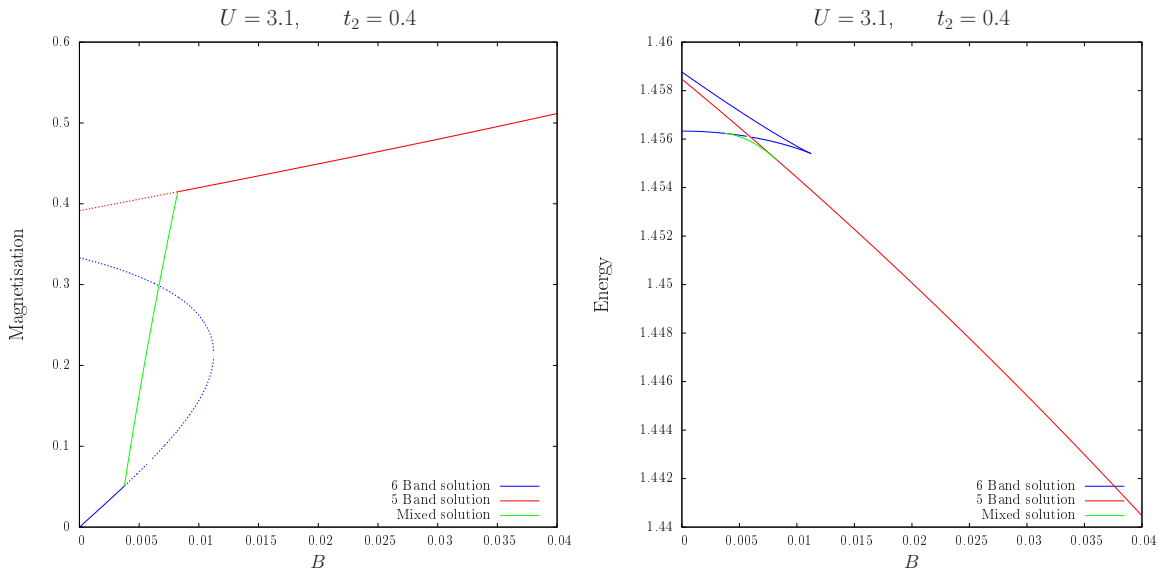

Figure 4.12: Mean field solutions, $U = 3.1t$, $t_2 = 0.4t$

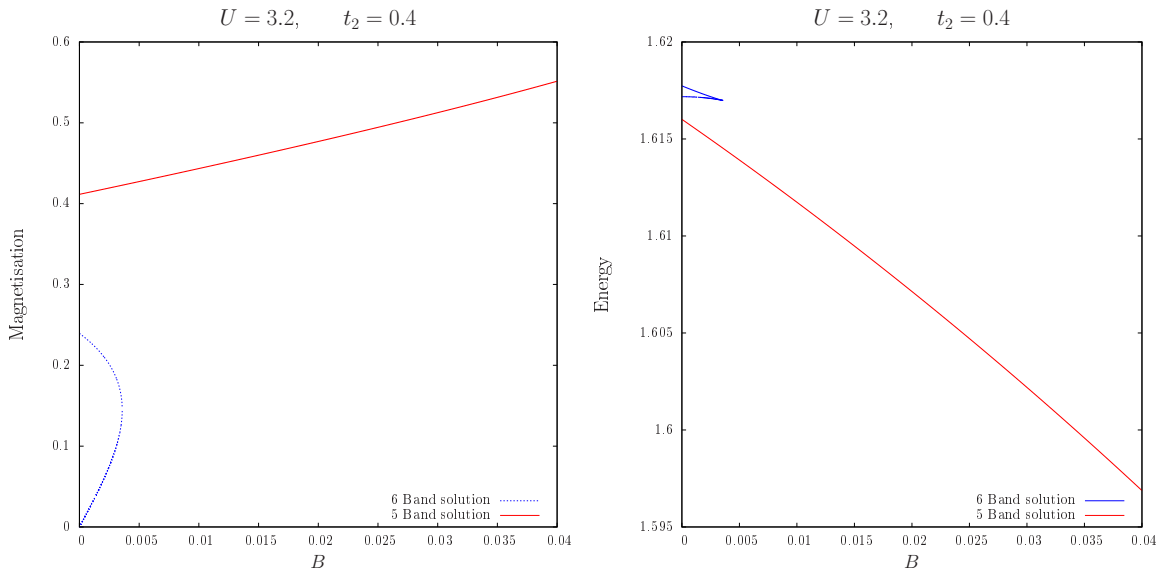

Figure 4.13: Mean field solutions, $U = 3.2t$, $t_2 = 0.4t$

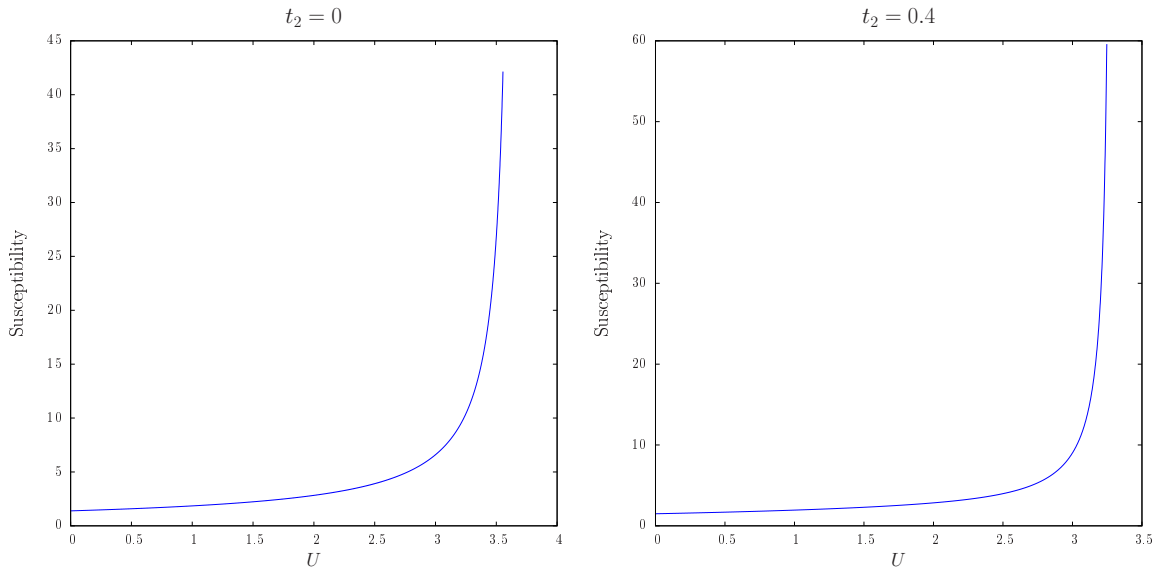

Figure 4.14: Magnetic susceptibility associated with the paramagnetic 6-band solution as a function of U.

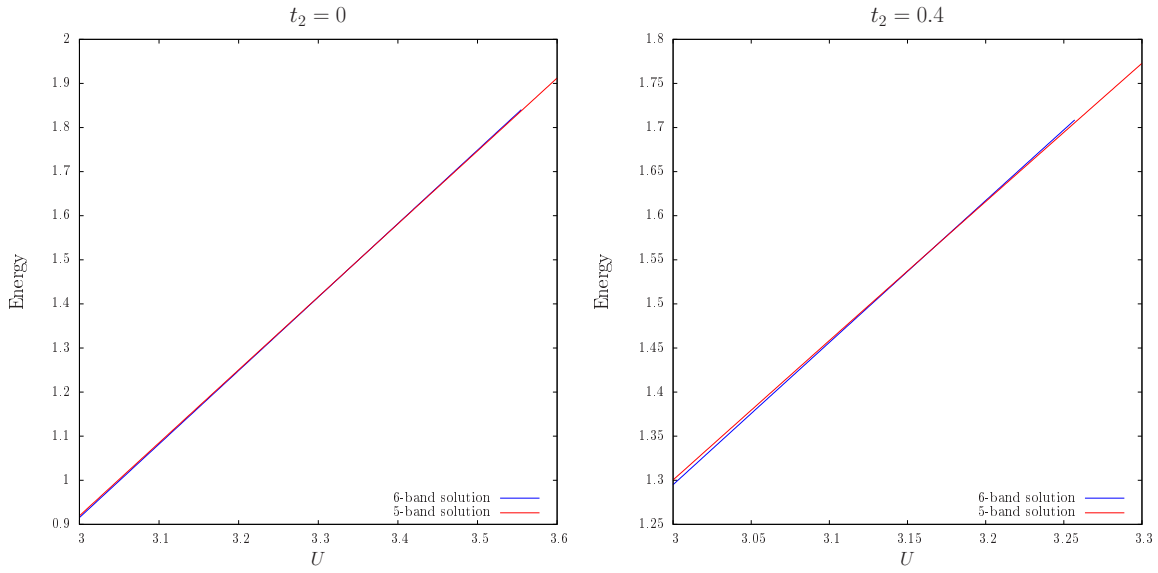

Figure 4.15: Energy of the 6-band and 5-band solutions at zero field as a function of U.

We now come to the effect of including the Hund coupling J. The effect of including a small value of J on the magnetisation curves is illustrated in figures 4.16 and 4.17, which provide the mean field solutions for $U = 3t$, $t_2 = 0.4t$ with J having the values $0.05t$ and $0.1t$ respectively. The effect of increasing J is similar to the effect of increasing U: the "loop" of 6-band solutions is pushed to smaller fields and the size of the metamagnetic jump is increased.

The magnetic susceptibility as a function of J is indicated in figure 4.18. The susceptibility is found to diverge, indicating that the Hund coupling is driving the system ferromagnetic at zero field. Note that only a moderate J is required to drive the system ferromagnetic. The energy of the 6-band and 5-band solutions at zero field is shown are shown as functions of J in figure 4.19, illustrating that the 5-band solution becomes becomes energetically preferred at modest values of J. Again, we expect there to be a range of values of J for which the groundstate is a phase-separated mixture of the 6-band solution and the 5-band solution, in which the fractional makeup of the mixture is smoothly changed from the purely 6-band state to the purely 5-band state by increasing J.

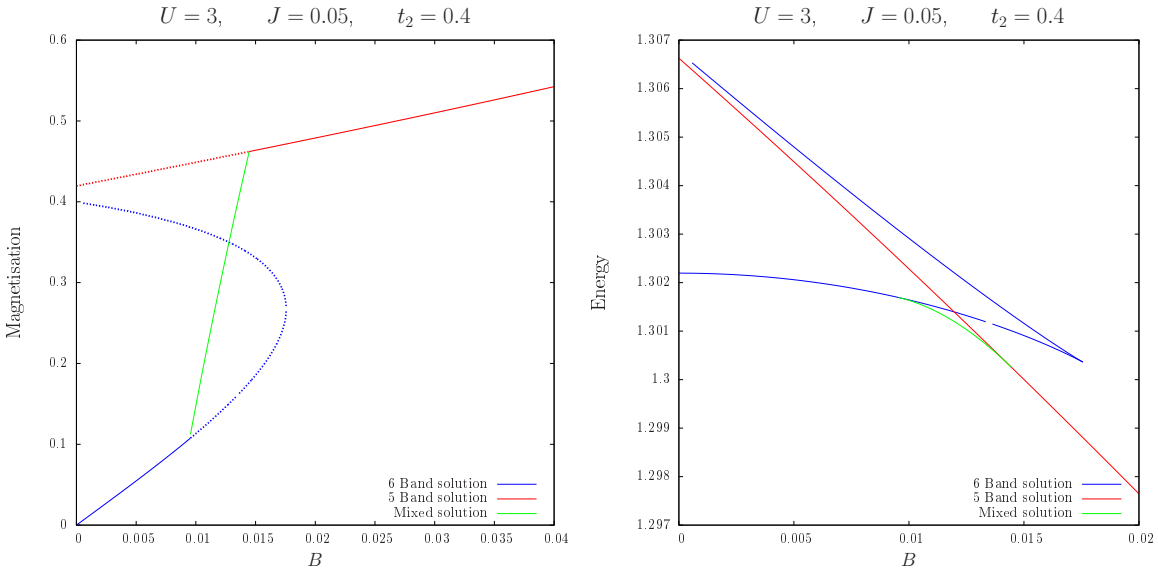

Figure 4.16: Mean field solutions, $U = 3t$, $J = 0.05t$, $t_2 = 0.4t$.

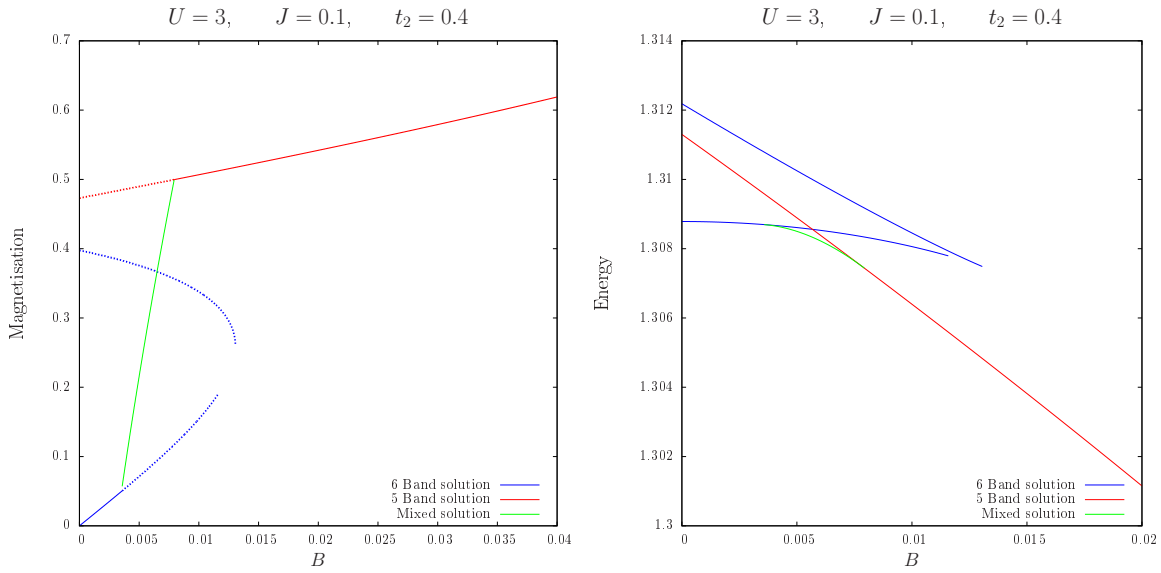

Figure 4.17: Mean field solutions, $U = 3t$, $J = 0.1t$, $t_2 = 0.4t$.

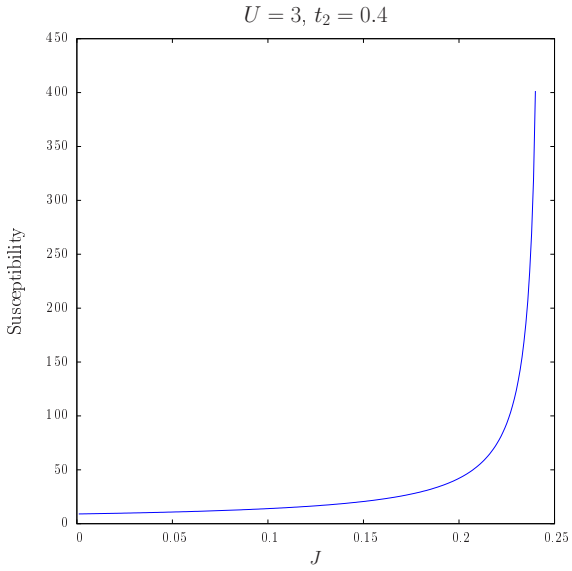

Figure 4.18: Magnetic susceptibility associated with the paramagnetic 6-band solution as a function of J.

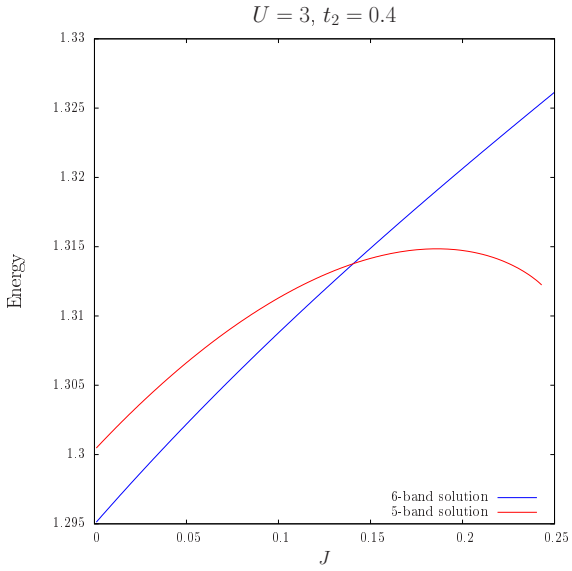

Figure 4.19: Energy of the 6-band and 5-band solutions at zero field as a function of J.

In attempting to tune the parameters to obtain a magnetisation curve that best matches that observed in $Sr_3Ru_2O_7$, we have obtained the values $U = 3t$, $J = 0.13t$ provided $t_2 = 0.4t$, which is implied by the experimental Fermi surface. The mean field magnetisation curve for these values of the parameters is shown in figure 4.20.

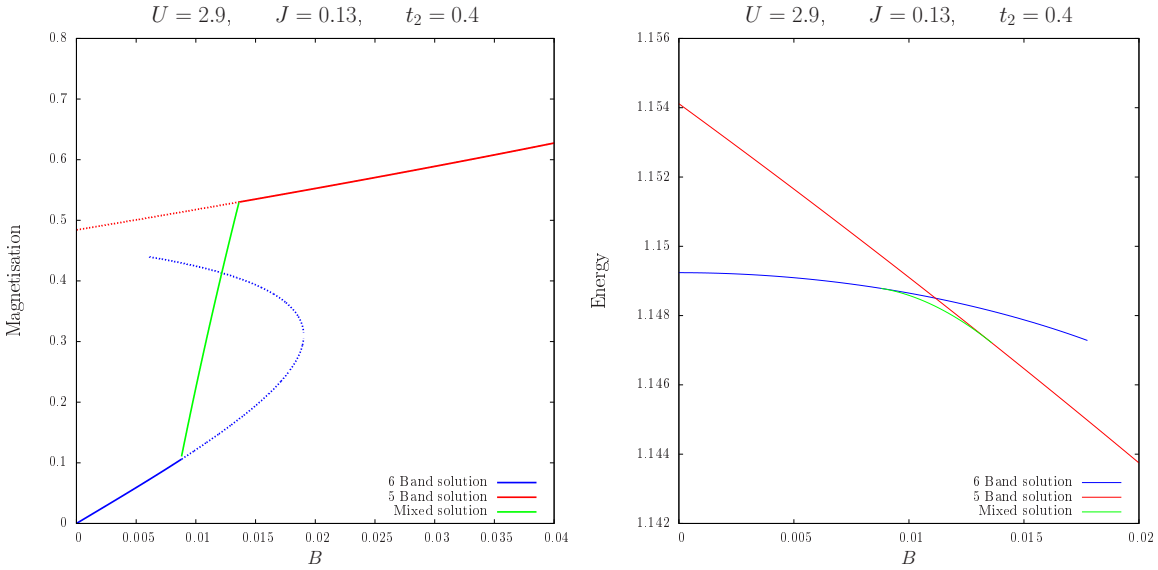

Figure 4.20: Mean field solutions, $U = 2.9t$, $J = 0.13t$, $t_2 = 0.4t$.

These calculations constitute the primary results of our work, and it is worth re-iterating them: for

sufficiently large interactions, the mean field calculations exhibit metamagnetism, and this is controlled by the X/Y bands, the low- and high-magnetisation states corresponding to the presence or absence of the $X_{-,\downarrow}$ Fermi surface; the metamagnetic region corresponds to a phase separated mixture of low- and high-magnetisation states.

By tuning the parameters of the Coulomb interaction the jump in the magnetisation can be made to match the value of $\approx 0.4\mu_B$/Ru observed in experiments. By contrast, the prediction for the metamagnetic field in this theory is wildly inaccurate. The metamagnetic field in figure 4.20 corresponds to an energy of $0.01t$, which is 0.004eV using the value $t = 0.35$eV implied by Density Functional Theory calculations(73), and this corresponds to a magnetic field of approximately 60 Tesla, which is almost ten times the experimental value. This is one of the inadequacies of mean field theory we have discussed in section 4.3.7.

There are substantial disagreements between our theory and experiments concerning the Z bands, and these are closely associated with each other and also with the choice of the second neighbour hopping. $Sr_3Ru_3O_7$ has the 2 holes per Ru site approximately equally distributed between the X, Y and Z orbital species at zero field, but our zero field calculation has a considerable excess of Z holes and detriment of X/Y holes:

$$n_{X\sigma} = 0.26, \qquad n_{Z\sigma} = 0.48.$$

The larger occupancy of the Z bands means that the van Hove singularity in the square lattice density of states is pushed far below the chemical potential, while experimentally the singularity is observed to be in close proximity to the chemical potential. The connection with the second neighbour hopping is that the experimental Fermi surface is holelike and therefore t_2 must be large enough to push the van Hove singularity past the chemical potential. Our value of $t_2 = 0.4t$ is strongly mandated by the experiments, because it is almost the minimum value required to have both a holelike Fermi surface and the experimental occupation numbers.

Because of the importance of the proximity of van Hove singularities to the chemical potential with regard to Stoner magnetism, these discrepancies relate closely to the question of whether the metamagnetism in $Sr_3Ru_2O_7$ is associated with the X/Y bands, as we propose, or the Z bands as has been suggested by some other authors(75). The calculations in sections 4.6.3, 4.6.4 and 4.6.5 seek to address this, by considering a number of modifications to the model aimed at promoting Z induced magnetism.

A further major discrepancy in our mean field solution arises when we calculate the density of

states at the Fermi level as a function of the applied field, which we exhibit in figure 4.21. This quantity should be proportional to the specific heat γ, which we exhibited in the previous chapter, in the right panel of figure 3.16 and panel B of figure 3.29. The experimental γ value has a strongly symmetric peak centred on the metamagnetic region. The mean field density of states by contrast is highly asymmetric. This is inevitable in the picture we are proposing of the vanishing of one of the one-dimensional Fermi surfaces. However, the experiments much more closely resemble the form that would be obtained from a metamagnetic jump associated with the Z bands, and this is a further reason for the further investigations in the following sections.

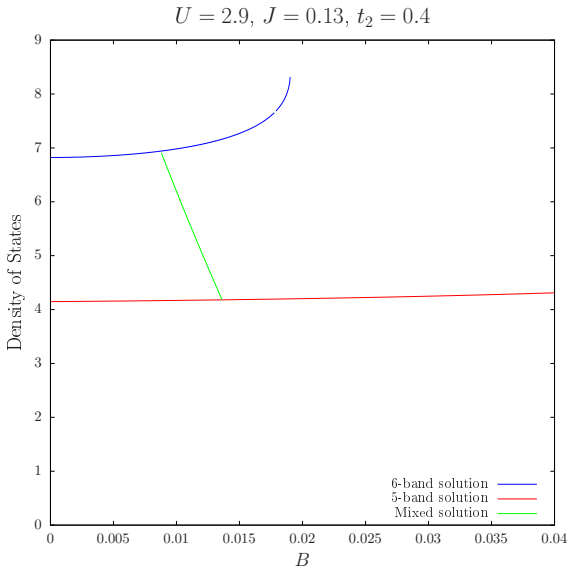

Figure 4.21: Density of states at the Fermi level for the mean field solutions of figure 4.20 as a function of the applied field.

4.6.2 The nature of the mixed phase

One of the main implications of our work is that the mixed phase which occurs with the metamagnetism in the mean field solution corresponds to the nematic phase in $Sr_3Ru_2O_7$. In this section we discuss the phase separated mixed phase in some detail. We begin by explaining how the mixed solutions plotted in the previous section have been calculated. We then give some discussion of the physical properties of the mixed phase, emphasising the implication that the system will exhibit microscopic or mesoscopic domains of the two subphases. The two subphases are both charged, so that the domain-sizes must be governed by long-range Coulomb forces which we have not included in our modelling. We have not undertaken any modelling of the experimental features which characterise the mixed phase, but we

give some discussion of how one might seek to explain some of these features within the picture of the nematic phase which we are suggesting.

The starting point for our calculation of the mixed phase is that the chemical potential μ should be constant throughout the system, and to seek a 6-band and a 5-band solution at the same given value of μ. The calculation of these two solutions is performed as laid out in appendix C, but where the internal parameters $\tilde{\mu}$ and $\tilde{B}$ must now be chosen to provide not the correct particle number, but instead the correct chemical potential μ. The external equations are therefore,

$$\tilde{\mu} + \left(U - \frac{J}{2}\right) n = \mu, \tag{4.125}$$

$$\tilde{B} - \frac{J}{2} M = B. \tag{4.126}$$

Let the total number of holes per Ru site in the 6- and 5-band solutions for chemical potential μ and magnetic field B be n_6 and n_5 respectively. If the fraction of the system in the 5-band phase is λ, then the total number of holes per site in the system is given by $(1-\lambda)n_6 + \lambda n_5$, and there is a unique mixing fraction which provides the correct occupancy of two holes per site. The energy of the mixed phase is given by

$$E_{\mathrm{mix}} = (1-\lambda)E_6 + \lambda E_5 \tag{4.127}$$

where E_6 and E_5 are the energy of the 6- and 5-band solutions respectively.

The mixing energy is plotted in figure 4.22 for parameters for which the groundstate is the mixed phase shown in figure 4.20. There is a clear chemical potential μ and corresponding mixing fraction λ for which the energy is minimum, and this minimum moves to larger values of μ and λ as the field is increased. To calculate the mixed solution, the chemical potential which minimises the energy must be found. In principle, this requires a further iterative procedure in addition to those for solving the internal and external equations described in appendix C, so that the full calculation would involve three nested iterative processes. In practice, we start with an approximation of where the minimum of $E_{\mathrm{mix}}(\mu)$ should lie, we calculate the energy for just three values of μ in the near-vicinity, $E_{\mathrm{mix}}(\mu)$, $E_{\mathrm{mix}}(\mu+\delta\mu)$ and $E_{\mathrm{mix}}(\mu+2\delta\mu)$, and we calculate the minimum of the parabola which passes through the three calculated points,

$$\mu_{\mathrm{min}} = \frac{1}{2}\frac{(2\mu+3\delta\mu)E_{\mathrm{mix}}(\mu) - (4\mu+4\delta\mu)E_{\mathrm{mix}}(\mu+\delta\mu) + (2\mu+\delta\mu)E_{\mathrm{mix}}(\mu+2\delta\mu)}{E_{\mathrm{mix}}(\mu) - 2E_{\mathrm{mix}}(\mu+\delta\mu) + E_{\mathrm{mix}}(\mu+2\delta\mu)}. \tag{4.128}$$

This provides a good approximation to the correct chemical potential provided that one starts in the near-vicinity of the correct value, but this can always be ensured by appealing to the continuity of the mean field solutions and performing the calculations where the parameters are only deviated a small amount from a previously known solution.

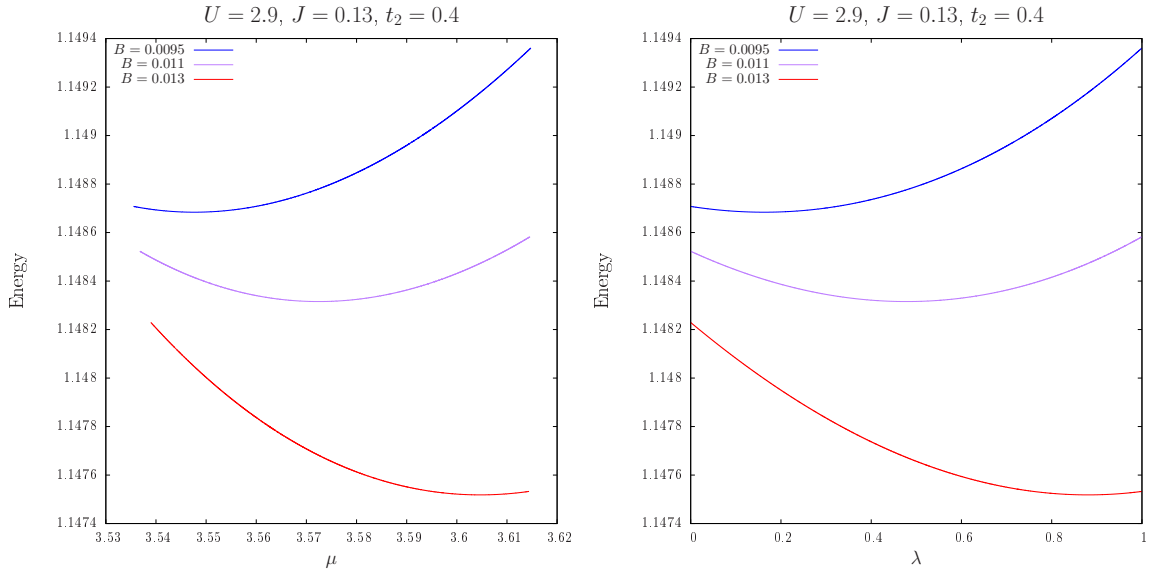

Figure 4.22: Energy of phase mixture as function of the chemical potential and mixing fraction.

Figures 4.23 and 4.24 provide some details of the mixed phase from figure 4.20 as functions of the field. Figure 4.24 makes very clear a very important point, which is that in the mixed phase the two subphases have unequal numbers of particles and are not charge-neutral: the 6-band phase has an excess of holes and is therefore positively charged, and the 5-band phase has a detriment of holes and is therefore negatively charged.

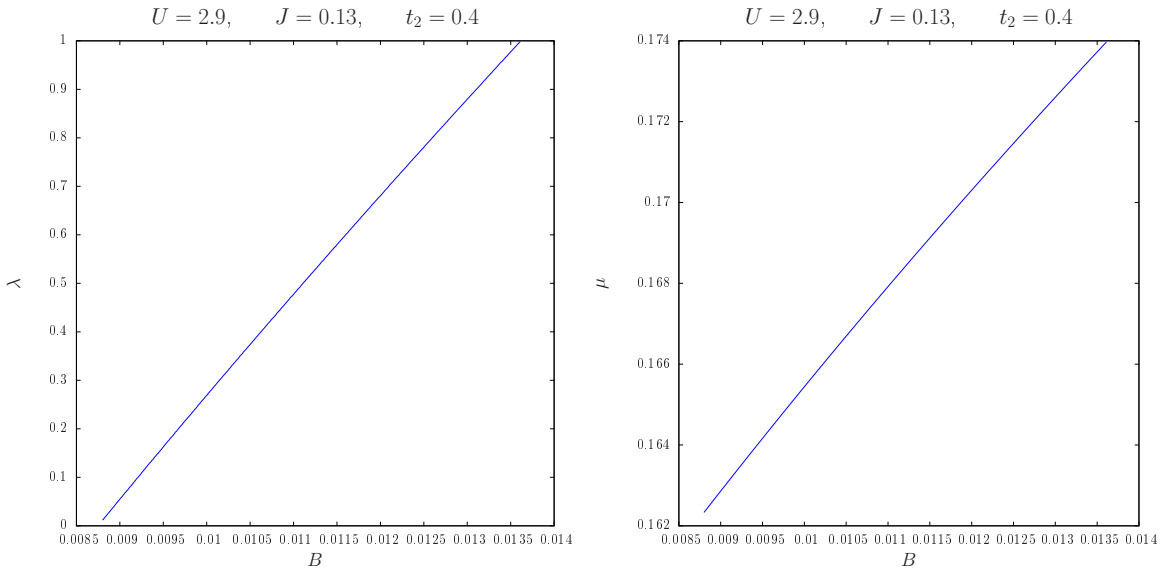

Figure 4.23: Mixing fraction (left) and chemical potential (right) of the groundstate mixed phase plotted in figure 4.20 as functions of field.

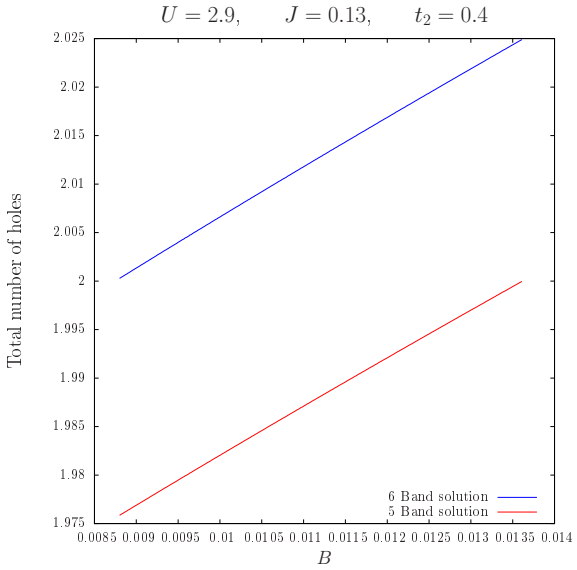

Figure 4.24: Number of holes per Ru site for the 6- and 5-band phases in the groundstate mixed phase plotted in figure 4.20 as functions of field.

The implication of the mixed solution is that some fraction of the material will be in the 6-band subphase and the remaining fraction in the 5-band subphase. Because the subphases are charged, the spatial arrangement of domains of the two subphases will be dominantly controlled in the real material by the long-range Coulomb interaction, which we have not included in our modelling. The Coulomb

interaction will enforce domains on a microscopic or mesoscopic scale.

We suggest that the mixed phase which occurs in our mean field solution corresponds to the nematic phase in $Sr_3Ru_2O_7$. However, we have not attempted any modelling at a sufficiently sophisticated level to reproduce any of the experimental features which are associated with the nematic phase, which we discussed in the previous chapter, section 3.4.

One definitive experimental feature is the step-like changes in the in-plane electrical resistivity close to the metamagnetism. It has been proposed that the increase in the resistivity is due to the scattering of conduction electrons off of domain walls in the system(75; 96). Therefore, in the picture of the nematic phase we are proposing, we tentatively suggest that this is the case, where the domains are associated with the two subphases in the mixed phase. This suggests that the step-like changes in the resistivity are associated with the appearance and disappearance of domain walls on entering and leaving the mixed phase.

As we mentioned in the previous chapter, section 3.4, the nematic phase in $Sr_3Ru_2O_7$ does not exhibit two features which would usually be indicative of the existence of domains: hysteresis and dependence on sample shape. We tentatively suggest that this discrepancy might be resolved if the length scale of the domains is extremely short. Given that in our mixed phase this length scale will be controlled by the long-range Coulomb interaction and that this is a large energy scale we indeed expect this length scale to be short. However, we have not made any attempts to quantify this.

A second major feature is the anisotropy that occurs when the magnetic field is tilted a small angle away from the c-axis, where the sharp plateau in the resistivity is absent in the resistivity perpendicular to the field. In our model, there is no dependence on the direction of the magnetic field. The lowest-level miscroscopic interaction that would give rise to a dependence on the field direction is the spin-orbit interaction, and we postulate that the spin-orbit interaction is the primary cause of the dependence seen in $Sr_3Ru_2O_7$. With regards to the actual features seen in the resistivity, if the resistivity plateau is to be attributed to the scattering of electrons off of domain walls, then the absence of this feature in the resistivity perpendicular to the in-plane field implies domain walls that are in the perpendicular direction. The domain pattern then would be stripes of the two subphases parallel to the perpendicular in-plane direction. When there is a nonzero in-plane field, one presumes that the spin-orbit interaction leads to a splitting of the degeneracy of the X and Y bands, but the connection between this and the orientation of domains of high- and low-magnetisation subphases is unclear.

These remarks constitute the starting-point for how one would attempt to seek an explanation for

the features in the in-plane resistivity seen in $Sr_3Ru_2O_7$ within the picture of the nematic phase which we are suggesting. We again stress that we have made no attempts to actually model these features.

There is another route by which an anisotropy between the two in-plane directions might be sought using the same level of modelling as we have undertaken. This is to seek a mean field solution of our model in which the occupancies of the X and Y bands differ. One can imagine a scenario in which the Fermi surface associated with one of the in-plane directions vanishes but the other remains: such a mean field solution would imply a differing electrical conductivity between the two in-plane directions directly without the need to invoke the role of domain walls, although it is not clear how the actual features in the resistivity might be reproduced. Regrettably, these styles of mean field solution have not been investigated in this thesis. Some early calculations by M. W. Long indicated that these anisotropic solutions were unlikely to ever have a lower energy than the solutions which preserve the symmetry of the in-plane directions. The solutions which preserve the symmetry have been prioritised, both for this reason and because they are easier calculations and therefore provide a more natural starting point for investigations. A thorough investigation of the anisotropic mean field solutions is an obvious extension to this work which time has not permitted.

Our modelling is entirely at zero-temperature, and so we are not able to model the thermodynamic properties relating to the appearance of the nematic phase in $Sr_3Ru_2O_7$ in any detail. We suggest that the transition of the system into and out of the mixed phase will show up at low-temperature as two first order transitions at the appearance and disappearance of the mixed phase, in accord with the two first order transitions seen in $Sr_3Ru_2O_7$. The mixed phase is found as the lowest energy mean field solution and is the true groundstate rather than a metastable state. This is consistent with the nematic phase in $Sr_3Ru_2O_7$ being an equilibrium phase.

4.6.3 Effect of varying t_2

In this section we show mean field calculations exhibiting the effect of varying the second neighbour hopping t_2. The most important effect of changing this parameter is that it moves the position of the van Hove singularity in the Z band structure. We have already argued that a sizeable t_2 must be included in order that the zero-field Fermi surface matches the experimental $Sr_3Ru_2O_7$ Fermi surface; changing from $t_2 = 0$ to $t_2 = 0.4t$ moves the singularity, in the hole picture, from well above the chemical potential to well below the chemical potential, and therefore alters the topology of the Z Fermi surface. In this section we show the effect of gradually tuning t_2 between these two values.

In particular, if the van Hove singularity is positioned in close proximity to the chemical potential, this can lead to more metamagnetic transitions, in addition to the transition associated with the X/Y bands. The field at which this second metamagnetic jump occurs has extremely sensitive dependence on t_2, and by varying t_2 jumps can be made to occur below, above or on top of the X/Y metamagnetism. Because t_2 must be finely tuned in order for the Z metamagnetism to be observed, we argue that this is unlikely to be the case in the real material, and that this is additional evidence that the metamagnetism in $Sr_3Ru_2O_7$ is the X/Y metamagnetism already described.

Figure 4.25 shows the susceptibility associated with the zero-field mean field theory as a function of t_2, calculated as M/B for the small field $B = 0.0001t$. The divergence around the value $t_2 = 0.225t$ corresponds to the system being driven ferromagnetic in this region by the Z band van Hove singularity being positioned extremely close to the chemical potential, so that the Stoner criterion is fulfilled. For values of t_2 below the peak, the zero field Fermi surface has the form of figure 4.5, and for values above the peak the zero field Fermi surface has the form of figure 4.6 which is the topology seen in the experimental $Sr_3Ru_2O_7$ Fermi surface.

Figure 4.26, which plots the energies of paramagnetic and ferromagnetic 6-band solutions at zero field as a function of t_2 in the vicinity of the FM instability, shows explicitly that ferromagnetism is energetically preferred at zero field close to where the susceptibility diverges. The paramagnetic solutions are the same as the ones calculated in figure 4.25 except the field is set to zero, so that they have both the Z Fermi surfaces the same topology, and the ferromagnetic solution has the $Z_\uparrow$ Fermi surface electronlike and the $Z_\downarrow$ Fermi surface holelike. Sufficiently close to the FM instability the ferromagnetic solution is energetically preferred, and on even closer approach to the instability the paramagnetic solutions apparently cease to exist. We expect the true groundstate to be a phase separated mixture of paramagnetic and feromagnetic solutions for some values of t_2 in this region.

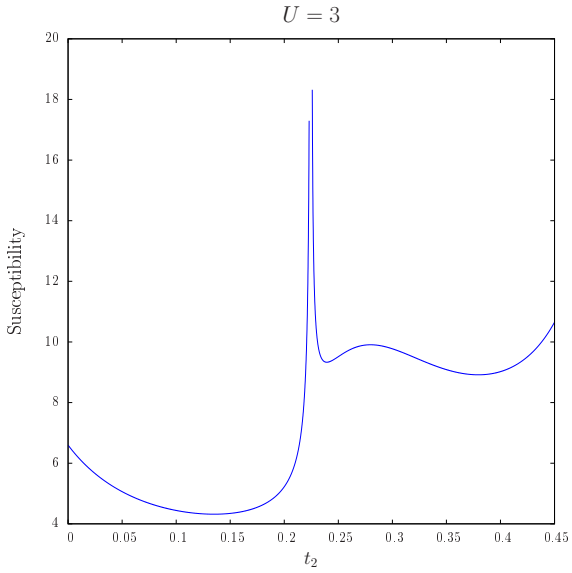

Figure 4.25: Magnetic susceptibility as a function of t_2.

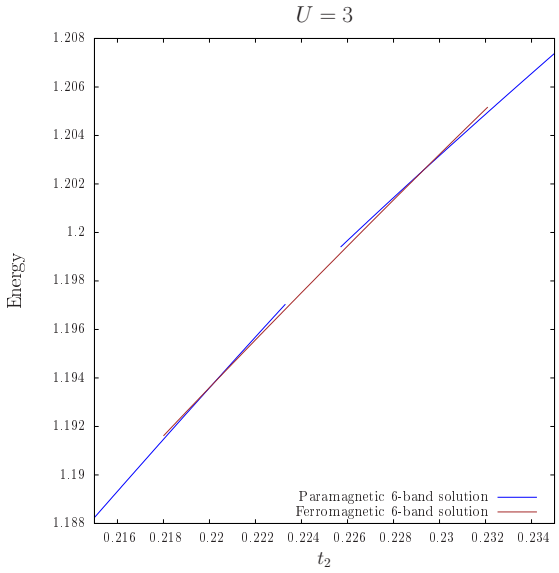

Figure 4.26: Energy of paramagnetic and ferromagnetic 6-band solutions at $B = 0$ as a function of t_2 in the vicinity of the FM instability.

The changes to the Fermi surface with the application of a magnetic field are indicated, for t_2 below the FM instability and t_2 above the FM instability, in figures 4.27 and 4.28 respectively. In both figures, the lefthand member shows the zero-field Fermi surface and the righthand member shows the high-field Fermi surface, where both the X/Y metamagnetic jump and the Z metamagnetic jump have already occurred. The change associated with the X/Y-metamagnetism is that the lines of

Fermi surface associated with the top-lying spin-$\downarrow$ X/Y bands have vanished, corresponding to the bands in question having been pushed past the chemical potential. The change associated with the Z metamagnetism is that one of the Z Fermi surfaces has changed from being holelike to electronlike or vice versa corresponding to the van Hove singularity in the corresponding band having been moved past the chemical potential.

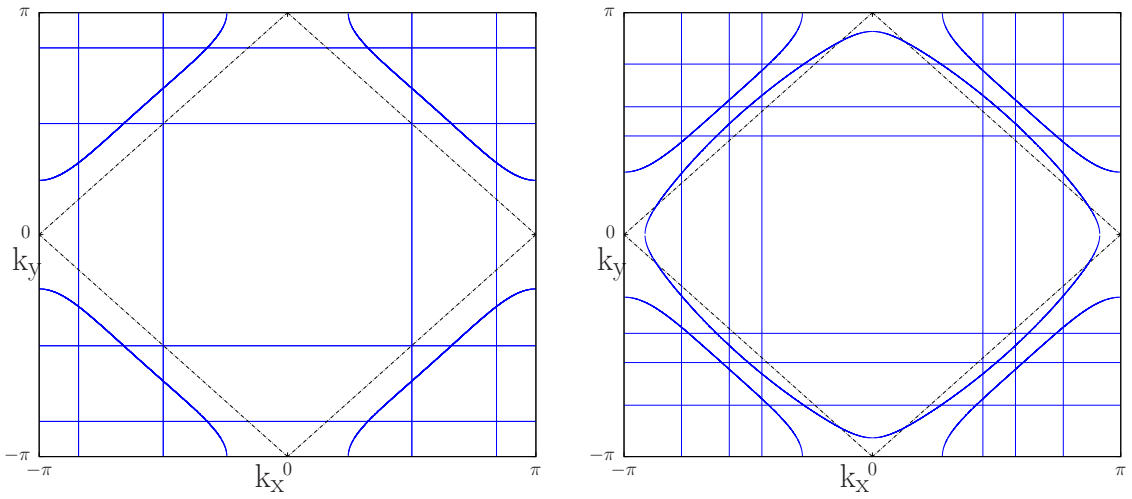

Figure 4.27: Fermi surfaces for $U = 3$, $t_2 = 0.14$. Left: $B = 0$; Right: $B = 0.08$

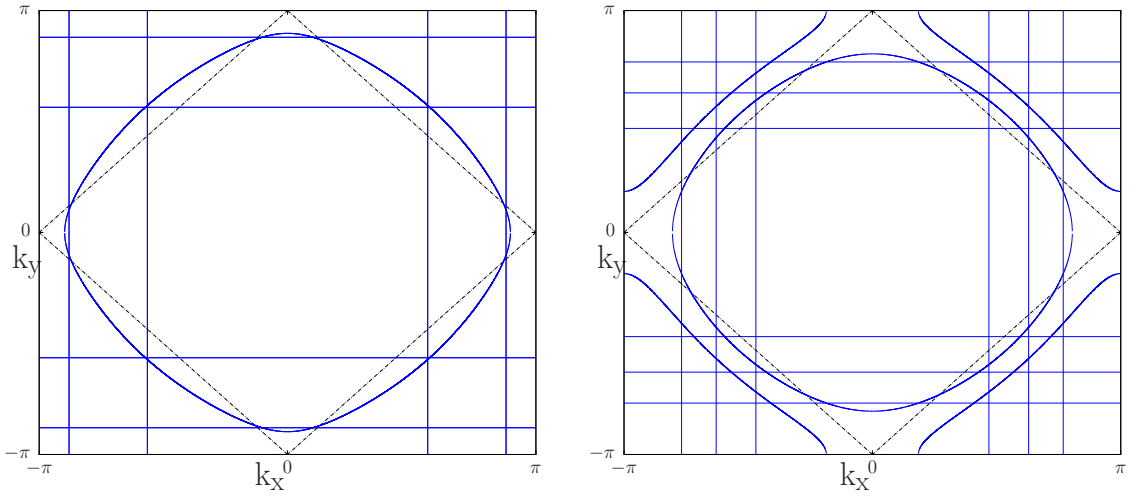

Figure 4.28: Fermi surfaces for $U = 3$, $t_2 = 0.24$. Left: $B = 0$; Right: $B = 0.08$

Figures 4.29 to 4.32 show the magnetisation curves for the mean field solutions for values of t_2 which move incrementally past the FM instability. The $t_2 = 0.14t$ and $t_2 = 0.21t$ cases, figures 4.29 and 4.30, have t_2 below the FM instability, and so involve the Fermi surface forms indicated in figure 4.27. $t_2 = 0.14t$ has the square lattice far enough below the chemical potential at zero field that the Z metamagnetism occurs at a substantially higher applied field than the X/Y metamagnetism. $t_2 = 0.21t$ has the van Hove singularity close to the chemical potential at zero field, such that the Z metamagnetism occurs at a substantialy smaller field than than the X/Y metamagnetism. The $t_2 = 0.232t$ and $t_2 = 0.24t$ cases, figures 4.31 and 4.32, have t_2 above the FM instability, and so the picture of both metamagnetic jumps in terms of the Fermi surface is that of figure 4.28. $t_2 = 0.232t$ has the square lattice van Hove singularity slightly above the chemical potential at zero field so that the Z metamagnetism occurs below the X/Y metamagnetism; $t_2 = 0.24t$ has the van Hove singularity far enough above the chemical potential at zero field that the Z metamagnetism occurs at substantially higher field than the X/Y metamagnetism.

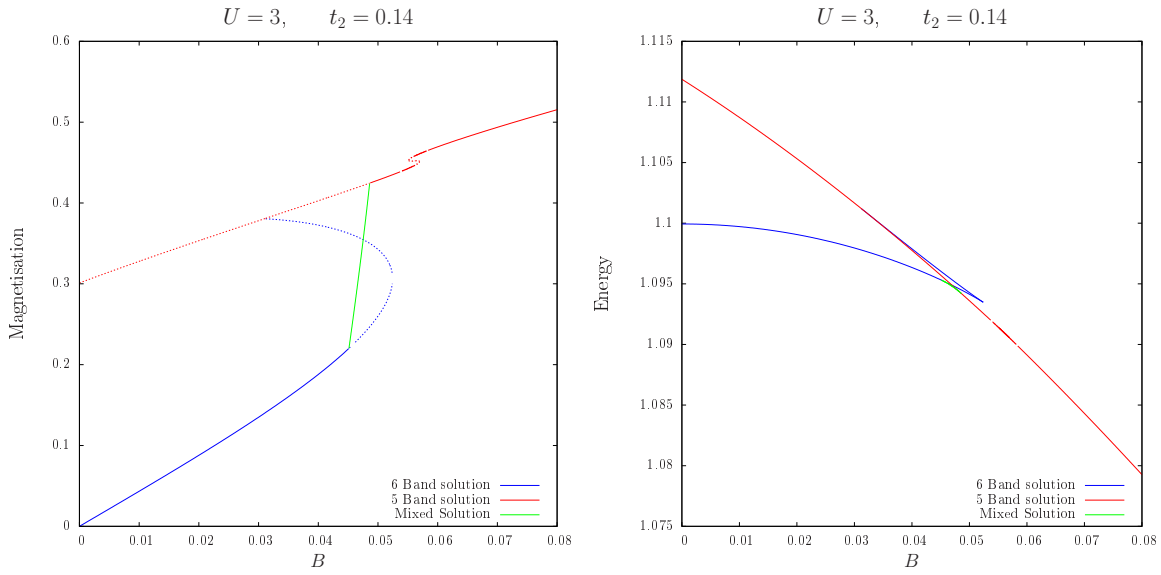

Figure 4.29: Mean field solutions for $U = 3t$, $t_2 = 0.14t$, $J = 0$.

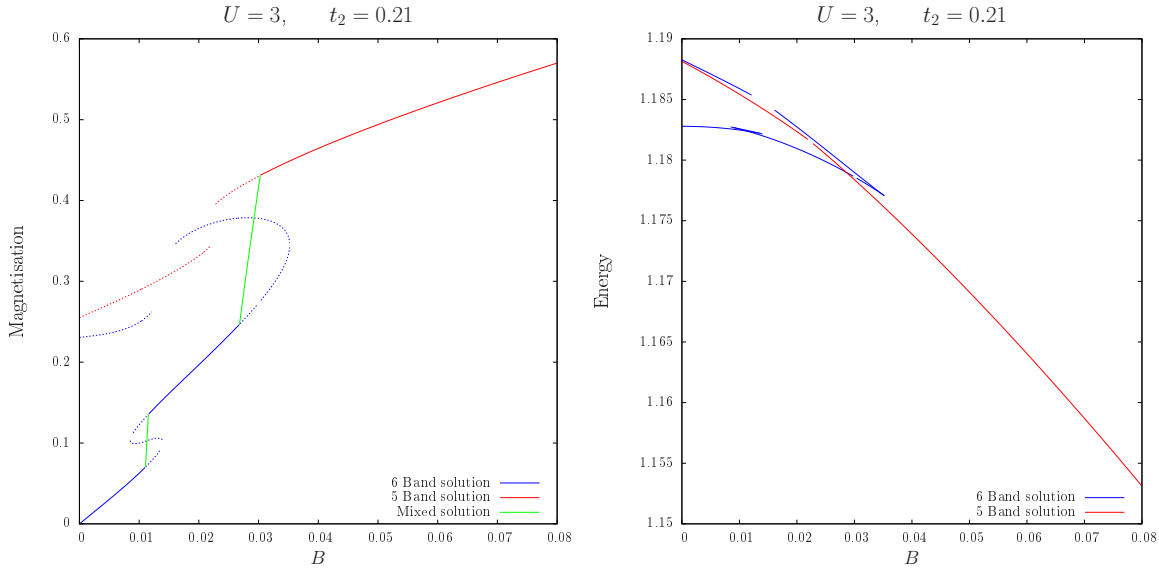

Figure 4.30: Mean field solutions for $U = 3t$, $t_2 = 0.21t$, $J = 0$.

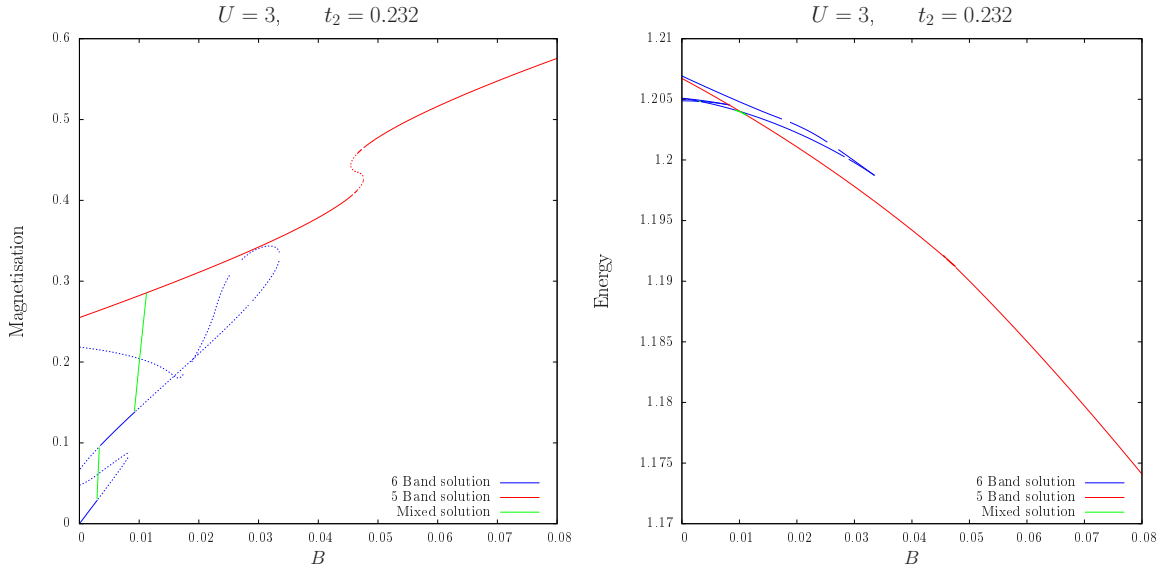

Figure 4.31: Mean field solutions for $U = 3t$, $t_2 = 0.232t$, $J = 0$.

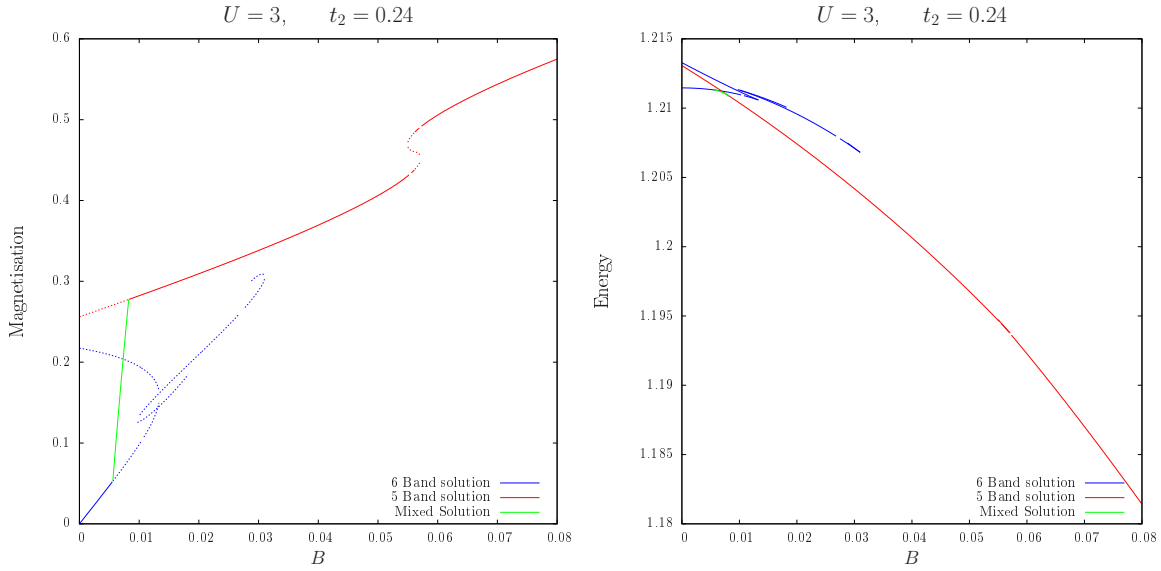

Figure 4.32: Mean field solutions for $U = 3t$, $t_2 = 0.24t$, $J = 0$.

Note that the magnetisation for the $t_2 = 0.232t$ case exhibits *three* metamagnetic jumps. Increasing the magnetic field from zero, there is first a Z band mediated jump in which the Fermi surface associated with the spin-$\downarrow$ Z holes becomes electronlike. At a higher field, the X/Y metamagnetism occurs, and the system transitions into a state where the top-lying spin-$\downarrow$ X/Y-Fermi surface vanishes, but where both Z Fermi surfaces are again holelike. Increasing the field still further, the Z metamagnetism occurs "again", with the third jump in the magnetisation.

In the vicinity of the Z transition, there occur three mean field solutions at the same field, in the form of an "S" shaped feature in the magnetisation curve (see figures 4.29 to 4.32); the same analytic structure was obtained in relation to the Z band metamagnetism in calculations by Binz *et al*(75). The lower and upper solutions have the Fermi surface form of the low- and high-field regions respectively. The middle solution moves smoothly between the two forms and joins up with the upper and lower solutions; this is a high energy metastable solution which we do not think is physically relevant to the groundstate of the system. This solution is analogous to the upper branch 6-band solution discussed in section 4.6.1.

For the cases $t_2 = 0.21t$ and $t_2 = 0.232t$, the low-field Z transition occurs with the adoption of a phase-separated mixture of the upper and lower solutions, in a similar manner to the phase separation associated with the X/Y metamagnetism. These mixed solutions are shown on figures 4.30 and 4.31. We have not been able to find such mixed solutions in proximity to the Z transitions that occur

at higher fields than the X/Y transition. The analytic structures of the mean field solutions in the vicinity of the Z transition whether this be below or above the X/Y transition are perfect analogues, which suggests that the high-field Z transition should be associated with a phase separation analogous to the low-field case. A mixed solution requires that there exist solutions of both types at the same chemical potential. We have attempted to find a range of chemical potentials for which both solutions exist by incrementally altering the chemical potentials of both solutions from the $n = 2$ solutions, but we do not find any chemical potential for which both solutions appear to exist. In the vicinity of where the solutions could co-exist at the same chemical potential, we find that the self-consistent equations for the Z band have two very closely positioned solutions. In this scenario our Newton-Raphson procedures can fail, as we have already discussed. We therefore believe that a mixed phase does exist in these regions, and that our computational procedures are not sophisticated enough to find the corresponding solutions to the self-consistent equations. However we cannot rule out that the possibility that the mixed solution does not exist, which would imply that these Z transitions occur with a discontinuous jump between the lower and upper solutions when their energies cross.

4.6.4 Effect of changing the Z band hopping energy

We now come to the effect of altering the Z band hopping energies. Changing the hopping energy by multiplying by the factor $r < 1$ increases the Z density of states by a factor $1/r$ and this acts as an aggressive promoter of Z-associated Stoner ferromagnetism. We have performed calculations where we reduce the Z hopping energies but keep the X/Y hopping energies fixed. We are motivated to investigate this effect in an effort to force the Z-mediated metamagnetism for the physical value of the second neighbour hopping, $t_2 = 0.4t$. In addition, it is an attempt to address the issue in our calculations in section 4.6.1 that there is an excess of Z holes, and a detriment of X/Y holes, in comparison with experiments.

The alteration we make to the model is to multiply the Z band hopping by a factor r which is less than one, while leaving the X/Y hopping energies unchanged, so that $t_Z/t_{X/Y} = r$. This is easily incorporated into the mean field calculations with the modification that the effective chemical potentials for the Z bands defined in equation C.20 are rescaled as $\mu^{\text{eff}}_{Z\sigma} \to \mu^{\text{eff}}_{Z\sigma}/r$, and that the Z band

energy and density of states are rescaled as,

$$E_Z(\mu^{\text{eff}}_{Z\sigma}) \to rE_Z(\mu^{\text{eff}}_{Z\sigma}/r) \tag{4.129}$$

$$\rho_Z(\mu^{\text{eff}}_{Z\sigma}) \to \frac{1}{r}\rho_Z(\mu^{\text{eff}}_{Z\sigma}/r). \tag{4.130}$$

We include a second neighbour hopping of the same *relative* size of 0.4 for both the Z and X/Y bands.

The energy of various mean field solutions at zero field is shown as a function of the reduction in the Z band hopping energies in figure 4.33. These include the two states which are relevant to the X/Y metamagnetism shown in section 4.6.1, the 6-band solution (which has no magnetic moment at zero field), and the 5-band solution in which the $X_{-,\downarrow}$ is absent. We also include a number of large-moment solutions which we have not hitherto considered, the solution which has the $Z_\downarrow$ band completely absent, the solution which has both the $X_{-,\downarrow}$ and the $Z_\downarrow$ bands absent, and the solution which has both the $X_{-,\downarrow}$ and the $X_{+,\downarrow}$ bands absent. In addition, there is a 6-band solution with Z-induced ferromagnetism; this state is analogous to the high magnetisation state in the Z metamagnetic transitions in section 4.6.3.

Figure 4.33 shows that reducing the Z band hopping energy drives the system into the highly magnetised state where the $Z_\downarrow$ Fermi surface has vanished. Note that the 6-band Z-mediated ferromagnetism never comes into play: the topology of the $Z_\downarrow$ Fermi surface does not change as the system is driven ferromagnetic, but vanishes. It is striking that the system is pushed into a state with such a large magnetic moment for a modest change in the hopping energies.

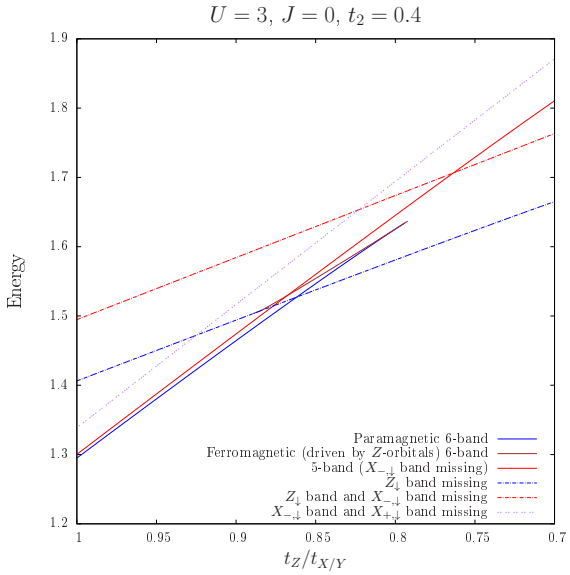

Figure 4.33: Mean field solutions at zero field as a function of changing the Z band hopping energy.

We have also calculated the high moment solutions as a function of field for $t_Z/t_{X/Y} = 1$ in one of the scenarios of X/Y metamagnetism we have already exhibited in section 4.6.1, in order to assess the energetics of these solutions and in particular any possibility of the high-moment Z-ferromagnetic state being relevant for the cases discussed in section 4.6.1. Magnetisation curves and energies of all of the high moment solutions are shown in figure 4.34, together with the same curves displayed in figure 4.11, section 4.6.1. The energetics show that the Z-driven highly magnetised state (where the $Z_\downarrow$ Fermi surface has disappeared) is completely irrelevant. If the field is pushed past the X/Y metamagnetic jump, the system chooses to evacuate the next X/Y band before the Z band.

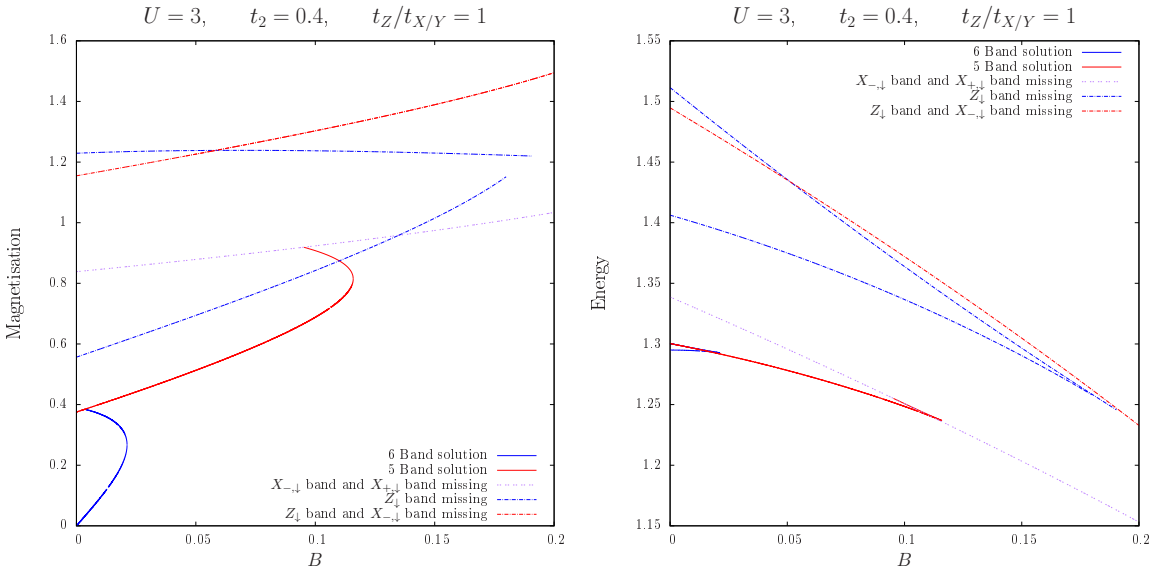

Figure 4.34: The mean field solutions shown in figure 4.11 (here labelled as 6-band solution and 5-band solution) together with the highly-magnetised states in which more components of the Fermi surface have vanished.

4.6.5 Effect of crystal field splitting of the t_{2g} shell

Here we exhibit calculations where we impose a crystal field splitting which lowers the energy of the Z bands relative to the X/Y bands by an amount Δ. This is another alteration to the model intended to promote Z-induced metamagnetism, and to bring the distribution of particles between the orbital species more in line with experiment. In shifting the Z bands down, their occupancy is expected to increase, and in addition, the Z band van Hove singularity is moved closer to the zero field chemical potential which we anticipate to promote Z band Stoner ferromagnetism.

The modification we make to the model is the addition of the term,

$$-\Delta \sum_{j\sigma} Z^\dagger_{j\sigma} Z_{j\sigma}, \tag{4.131}$$

and the change in the calculations to incorporate this is to shift the Z band effective chemical potentials defined in equation C.20, $\mu^{\text{eff}}_{Z\sigma} \to \mu^{\text{eff}}_{Z\sigma} - \Delta$, and to add onto the mean field energy the term $-\Delta(n_{Z\uparrow} + n_{Z\downarrow})$.

The energy of the various zero field mean field solutions are plotted versus Δ in figure 4.35; these include the large-moment solutions from section 4.6.4. The system is driven ferromagnetic by the band-shift, but it is the X/Y-mediated ferromagnetism. The system is first driven into the same

magnetic instability associated with the X/Y metamagnetism, and adopts the 5-band state where the $X_{-,\downarrow}$ Fermi surface is absent, and subsequently into a second X/Y associated magnetic instability where the $X_{+,\downarrow}$ Fermi surface vanishes. These are the same magnetic instabilities that occur with field in figure 4.34. The Z-mediated large moment ferromagnetic state where the $Z_{\downarrow}$ Fermi surface has vanished is not energetically relevant.

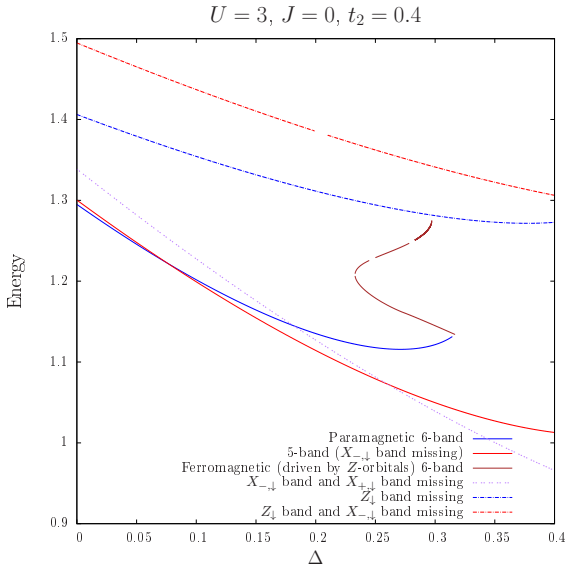

Figure 4.35: Mean field solutions at zero field as a function of crystal field splitting Δ.

Some insight is gained from plotting the effective chemical potential $\mu^{\text{eff}}_{Z\downarrow}$ and the occupation number for the $Z_{\downarrow}$ for these mean field solutions. See figure 4.36. Firstly, the system is pushed into the X/Y magnetic instability before the Z instability is reached; this is seen in the fact that at the value $\Delta \sim 0.075t$ of the first X/Y instability $\mu^{\text{eff}}_{Z\downarrow}$ is far removed from the position of the square lattice singularity $-4t_2$. One telltale sign of the square lattice singularity in the mean field calculations is in the appearance of the second 6-band solution with Z-induced ferromagnetism, where the $Z_{\downarrow}$ Fermi surface is holelike; this solution only appears at $\Delta \sim 0.25t$ which is considerably higher than the X/Y instability at $\Delta \sim 0.075t$. Secondly, in the X/Y mediated jumps which evacuate the $X_{-,\downarrow}$-band and then the $X_{+,\downarrow}$-band, the occupancy of the $Z_{\downarrow}$ band is increased and the singularity is shifted further from the chemical potential. This is another example of what is seen in the calculations which vary t_2 in section 4.6.3, that the Z bands effectively act as a reservoir of holes for the X/Y transitions, filling up as required when the X/Y bands are evacuated. The system pays energy in increasing the $Z_{\downarrow}$ occupancy because there is a considerably greater energy to be gained in the X/Y jumps.

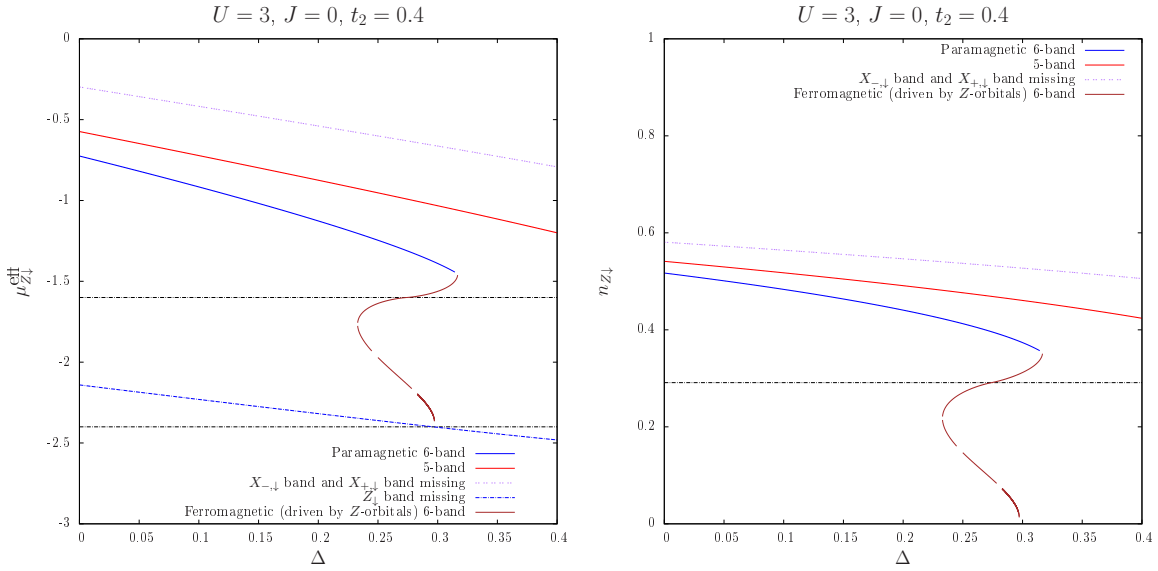

Figure 4.36: $Z_\downarrow$ effective chemical potential and occupancy as function of Δ.
Left: Effective chemical potential $\mu^{\rm eff}_{Z\downarrow}$. The two horizontal black dashed lines mark the position of the van Hove singularity $\mu = -4t_2$ and the bottom of the square lattice band $\mu = -4t + 4t_2$ for $t_2 = 0.4t$.
Right: The occupation number of the $Z_\downarrow$-band. The horizontal black dashed line marks the occupancy corresponding to the van Hove singularity.

4.6.6 Effect of electron doping

In this section we exhibit some calculations which model the experiment discussed in section 3.6 on the electron-doping of $Sr_3Ru_2O_7$. Those authors considered the compound $Sr_{3-y}La_yRu_2O_7$ for small values of y, one effect of which is to electron-dope $Sr_3Ru_2O_7$ in the amount of $y/2$ electrons per Ru site. It is extremely straightforward to incorporate doping into the mean field theory, as this simply changes the number of particles from the 2 holes per site of the reference compound,

$$2 \to 2 - \frac{y}{2}, \tag{4.132}$$

and so the only modification to the mean field theory is that the external equations become,

$$n = 2 - \frac{y}{2}, \tag{4.133}$$

$$B = \tilde{B} - \frac{J}{2}M. \tag{4.134}$$

Positive values of y correspond to electron doping, but we are equally able to explore the effect of hole doping by making y take negative values.

In figure 4.37 we exhibit the magnetic susceptibility as a function of y for both hole doping and electron doping. The susceptibility is made larger with electron doping, and diverges at a modest value of y, while it is descreased for hole doping. This is entirely what would be naively expected: adding electrons to the system decreases the number of holes, and therefore in the hole picture the chemical potential is lowered, towards the bottom of the top-lying X/Y-band. Electron doping therefore pushes the system towards the X/Y magnetic instability. This is seen in figure 4.38 which plots the energies of the zero-field 6-band and 5-band solutions as a function of y: for sufficent electron doping $y \approx +0.1$ the energies cross and the 5-band solution becomes the lowest energy, indicating that the system adopts the 5-band solution, or a mixed state of 6- and 5-band solutions, and is therefore ferromagnetic, at zero field.

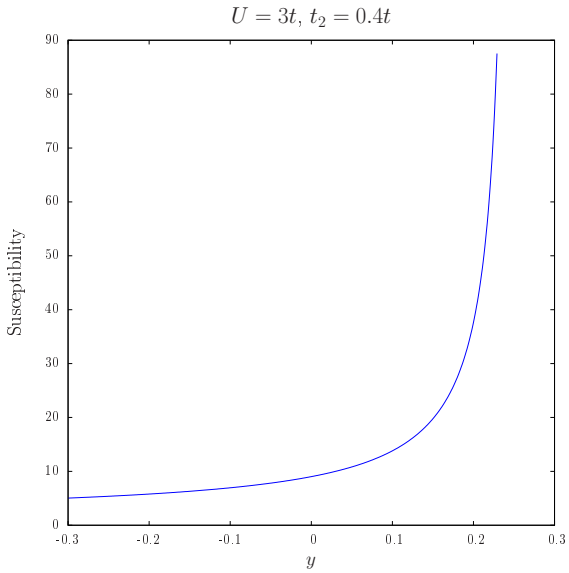

Figure 4.37: Magnetic susceptibility associated with the paramagnetic 6-band solution as a function of doping.

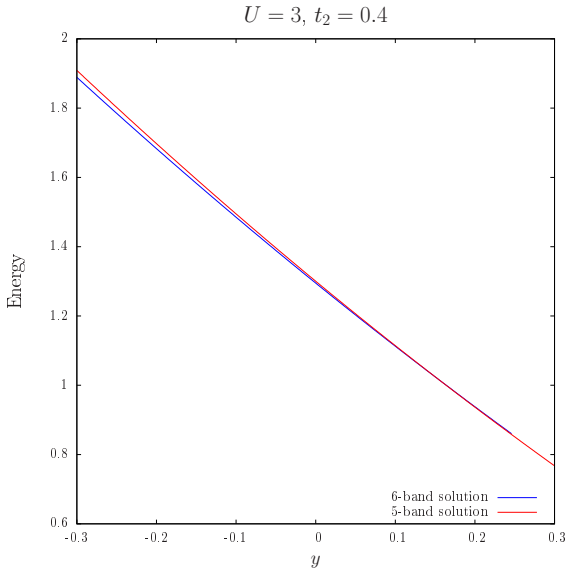

Figure 4.38: Energy 6- and 5-band solutions as a function of doping.

Figures 4.39 and 4.40 show examples of magnetisation curves for electron-doped and hole-doped cases respectively. These figures are for the same parameters $U = 2.9t$, $J = 0.13t$, $t_2 = 0.4t$ as in the calculations in figure 4.20, and should be compared with that figure. The electron-doped case, corresponding to the system being driven towards ferromagnetism, has the metamagnetic transition pushed to lower fields. Conversely, the hole-doped case has the metamagnetic transition pushed to larger fields.

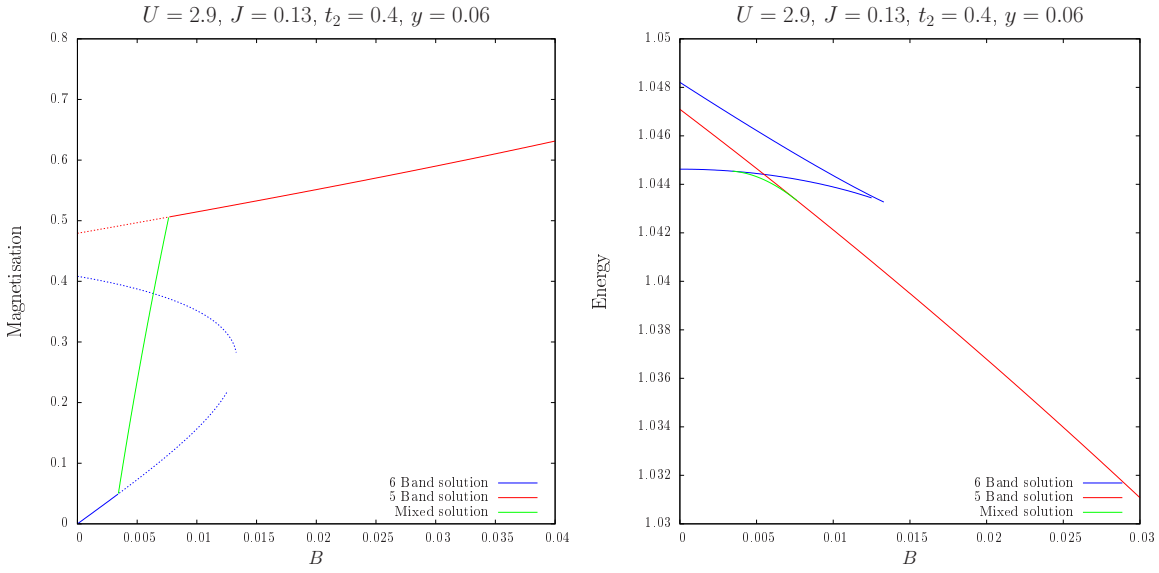

Figure 4.39: Mean field solutions for small electron doping, $y = 0.06$.

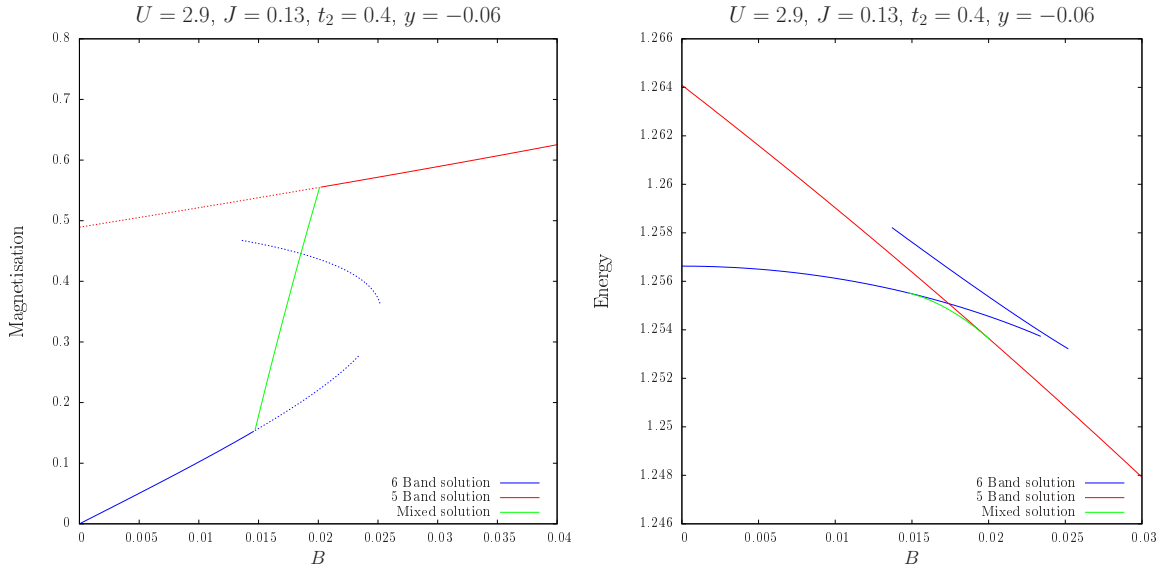

Figure 4.40: Mean field solutions for small hole doping, $y = -0.06$.

All of the mean field calculations are entirely consistent with one's expectations regarding the effects of doping. However, they are the complete converse of what is seen in the experiment on $Sr_{3-y}La_yRu_2O_7$(103). (see section 3.6) where electron-doping is found to push the system away from the magnetic instability.

Clearly the substitution of La for Sr has some other effect on the system that acts to make it less susceptible to ferromagnetism. One might argue that large effects are to be expected, as if one compares members of the strontium ruthenate series $Sr_{n+1}Ru_nO_{3n+1}$ with the corresponding members of the calcium ruthenate series $Ca_{n+1}Ru_nO_{3n+1}$, for which the valency of the Ru ion is the same, one sees quite different groundstates, that is a sensitive dependence of the physical properties on the differing sizes of the Sr and Ca ions(111). For example, in stark contrast to $Sr_3Ru_2O_7$, the groundstate of $Ca_3Ru_2O_7$ is insulating, and exhibits bilayer ferromagnetic order, with antiferromagnetic coupling between bilayers(112). The possible effects of substituting another atom for Sr in $Sr_3Ru_2O_7$, besides moving the chemical potential, are the altering of the crystal structure in the form of twisting and tilting of the RuO_6 octahedra, and the splitting of the t_{2g} orbitals related to a Jahn-Teller distortion of the RuO_6 octahedra(111). The twisting and tilting of the octahedra affects the hybridisation energies, and therefore the density of states, because it effects the overlap between wavefunctions on neighbouring Ru sites. Naively one would expect the hopping energy to be lowered and the density of states increased, and this clearly does not explain the experiments. Jahn-Teller distortion affects the occupancy of the

t_{2g} orbitals and in many oxide compounds is associated with transitions from metallic to insulating states(113); one might naively expect the change in the t_{2g} occupancies might result in the system being moved away from Stoner ferromagnetism. Although it must be noted that the experimenters suggest that La produces a milder lattice distortion than substituting Ca for Sr, we suggest that the effects we have desribed must be in some way responsible for the experimental findings.

4.7 Summary and Discussion

We have built a 3-band Hubbard-type model for the correlated paramagnetic metal $Sr_3Ru_2O_7$, and calculated Hartee-Fock mean field theory solutions. The mean field solution exhibits metamagnetism, an abrupt increase in the curve of magnetisation versus field, and the size of the magnetic jump can be made to match that seen in $Sr_3Ru_2O_7$. The metamagnetic jump is associated with a van Hove singularity in the X/Y bands which are one-dimensional at the level of our modelling; the high magnetisation state corresponds to one of the X/Y bands having been pushed past the chemical potential by the magnetic field, with the disappearance of the corresponding Fermi surface. In the region where the magnetisation rises steeply with field the mean field solution is a phase separated mixture of a state in which all of the X/Y Fermi surfaces are present and a state in which one of the X/Y Fermi surfaces has vanished. The implication of our calculations is that the metamagnetism in $Sr_3Ru_2O_7$ is associated with the X/Y bands and close to the metamagnetic transitions the material will undergo a phase separation in the manner of our mean field solution. We postulate that this phase separated solution is precisely the electronic nematic phase which occurs in $Sr_3Ru_2O_7$ close to the metamagnetism. This simple interpretation of the nematic phase is the main contribution of our work over previous works on X/Y mediated metamagnetism using more sophisticated models(101; 102).

We have not attempted modelling at an advanced enough level to reproduce any of the features which characterise the nematic phase in $Sr_3Ru_2O_7$. We postulate the dependence on the direction of the applied magnetic field to be in the main due to the spin-orbit interaction, which we have not included in our modelling. With regard to the anisotropy of the nematic phase, it should be stressed that throughout all of the calculations in this thesis the two principal in-plane directions have been kept completely equivalent. Therefore, any potential explanation of the anisotropy of the nematic phase within the picture we are proposing would have to be sought as being due to the orientation of the low- and high-magnetisation domains while the system is phase-separated. Any modelling of this would require the inclusion of the long-range Coulomb interaction, which has also been entirely

neglected in this work. Another route to anisotropy within the framework of our mean field approach is to seek a mean field solution with an anisotropy between the two in-plane directions in the form of imposing different occupancies of the X and Y bands. Although early calculations by M. W. Long indicated that such solutions were unlikely to be the groundstate, it is the author's view that this is deserving of a more thorough investigation and that this should be the immediate target for any continuation of this work.

The picture of the nematic phase as a phase-separated mixture of low- and high-magnetisation phases which we are offering in this thesis is to be contrasted with previous suggestions of essentially the same picture, but with a ferromagnetic instability which is associated with the two-dimensional features, rather than the one-dimensional features, of the electronic structure(75). At the level of our modelling, this would imply that the metamagnetism is associated with the van Hove singularity in the Z band being pushed past the chemical potential. This is an attractive picture because experiments show that in $Sr_3Ru_2O_7$ the relevant van Hove singularity is in the near-vicinity of the chemical potential at zero field(70; 65). We have investigated the possibility of a Z band instability by making a number of alterations to the model, and we have made two alterations which result in the mean field solution exhibiting Z-mediated metamagnetism. The first of these is to alter the size of the second neighbour hopping t_2. There is a range of values of t_2 for which Z associated magnetisation jumps occur, at fields which depend sensitively on t_2. In these solutions one sees precisely the styles of state that have been proposed to be relevant in $Sr_3Ru_2O_7$(75), with low- and high-magnetisation phases differing in the Z Fermi surface topology. However, these changes to the Z Fermi surface are undone by the X/Y metamagnetism, which also occurs in these solutions at a field which is comparatively robust as t_2 is varied. The Z bands act largely as a particle reservoir, whose occupancy is dictated by the X/Y magnetic instability which is the dominant effect in the mean field solution.

The second alteration to the model we have made which gives rise to Z-mediated metamagnetism is to reduce the Z band hopping energies while keeping the X/Y hopping energies fixed. This promotes the Z-associated magnetic instability so aggressively that a high-magnetisation state emerges in which the Z Fermi surface for one of the spin components has vanished. The corresponding magnetic jump is considerably larger than what is seen experimentally.

The position of the van Hove singularity in the Z density of states depends sensitively on the value that is chosen for t_2. The situation implied by quantum oscillations, photoemission and density functional theory calculations - that the holes are distributed approximately equally between the X,

Y and Z orbitals and that the Z Fermi surface is electronlike with the Z van Hove singularity situated within a few meV of the chemical potential - strongly implies the value $t_2 = 0.4t$. However, one finds that the mean field solution for $t_2 = 0.4t$ opts to have a larger occupancy of Z holes, with the Z van Hove singularity shifted to be far removed from the chemical potential. In an attempt to alleviate this large discrepancy between our mean field solution and the situation in $Sr_3Ru_2O_7$, we have investigated the effect of shifting the energy of the Z bands relative to the X/Y bands by an amount Δ. This is found to make the mean field solution more susceptible to the X/Y metamagnetism, and ferromagnetism occurs at zero-field before the experimental electronic structure is arrived at.

All of these issues relating to the Z bands are closely interrelated. We do not rule out that some combination of the parameters we have investigated will more closely match the experiments at zero-field, and will exhibit a Z-mediated metamagnetic jump that matches that seen in $Sr_3Ru_2O_7$. However, we hope to have convinced the reader that this would require the model to be quite finely tuned, and the Z magnetic instability can also not come into play at all, have an effect which is subservient to the X/Y metamagnetism or result in a state where one of the Z Fermi surfaces has vanished for which the magnetisation is much larger than what is seen in $Sr_3Ru_2O_7$. By contrast, magnetisation curves which match the experiments are much more easily obtained with X/Y metamagnetism.

The picture of metamagnetic transition we have given in this thesis, that of arising through a mean field description with the occurrence of a phase-separated mixture, is actually quite general, and could arise in mean field treatments on a great variety of Hubbard-type models. One requires large peaks or divergences in the density of states in proximity to the chemical potential. In the case of Z-mediated metamagnetism in our own mean field solution, this requires parameters in the model to be carefully tuned. In contrast, the van Hove singularity associated with one of the X/Y bands is naturally placed close to the chemical potential as a result of the bilayer splitting. This is why the X/Y metamagnetism is comparatively robust in the mean field solution.

Finally we have investigated the effect of doping the material. In the mean field solution the effect of removing holes is to push the system towards the X/Y magnetic instability and push the X/Y metamagnetism towards smaller fields, but the experiments on substituting Sr with La show the opposite trend(103). We have speculated that, in addition to moving the chemical potential, the atomic substitution could result in either the twisting and tilting of the RuO_6 octahedra, or a Jahn-Teller distortion, either of which could have a large affect on the electronic structure, and that this might provide an explanation for the experiments.

Appendix B

Tight binding calculations

We here provide in full detail the calculations relating to the bandstructure of the X/Y and Z orbitals. This is simply to solve a tight-binding model on a ladder geometry for the X/Y orbitals, and on a square lattice for the Z orbitals. We include a hybridisation between nearest neighbour lattice sites, with a matrix element $-t$, and a hybrisation between next nearest neighbour lattice sites, with a matrix element $+t_2$.

B.1 X/Y orbital band-structure

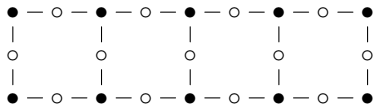

Figure B.1: Illustration of the ladder geometry for the X/Y holes. The filled circles correspond to Ru sites and the open circles to O sites.

Consider a ladder geometry as pictured in figure B.1. This geometry is effectively a linear chain with two atoms per unit cell, corresponding to the lower and upper rung of the ladder; let j label the sites on the linear chain, and let the total length of the chain be L_x. We assume periodic boundary conditions. Let $X^\dagger_{j,U,\sigma}$ and $X^\dagger_{j,L,\sigma}$ be creation operators for holes on the upper and lower rungs respectively at position j.

We immediately make the Bloch transform, In terms of the Bloch states,

$$X^\dagger_{k,U,\sigma} = \frac{1}{\sqrt{L_x}} \sum_j e^{ijk} X^\dagger_{j,U,\sigma} \text{ and } X^\dagger_{k,L,\sigma} = \frac{1}{\sqrt{L_x}} \sum_j e^{ijk} X^\dagger_{j,L,\sigma},$$

the tight-binding model with first and second-nearest neighbour hopping is

$$H_X = \sum_{k\sigma} \begin{pmatrix} X^\dagger_{k,U,\sigma} & X^\dagger_{k,L,\sigma} \end{pmatrix} \begin{pmatrix} -2t\cos k & -t + 2t_2\cos k \\ -t + 2t_2\cos k & -2t\cos k \end{pmatrix} \begin{pmatrix} X_{k,U,\sigma} \\ X_{k,L,\sigma} \end{pmatrix}. \tag{B.1}$$

This Hamiltonian is diagonalised by the states

$$X^\dagger_{j,\pm,\sigma} = \frac{1}{\sqrt{2}}(X^\dagger_{k,U,\sigma} \pm X^\dagger_{k,L,\sigma}). \tag{B.2}$$

We introduce the label $\alpha = \pm 1$ for the eigenstates, which we indicate by $X^\dagger_{j,\alpha,\sigma}$; the corresponding band-structure is given by,

$$\epsilon^X_{k\alpha} = -2(t - \alpha t_2)\cos k - \alpha t. \tag{B.3}$$

The band-structure is depicted in Figure B.2. There are two bands which have the cosine form expected of a linear chain, the low-lying symmetric band labelled by $\alpha = +1$, and the high-lying antisymmetric band labelled by $\alpha = -1$.

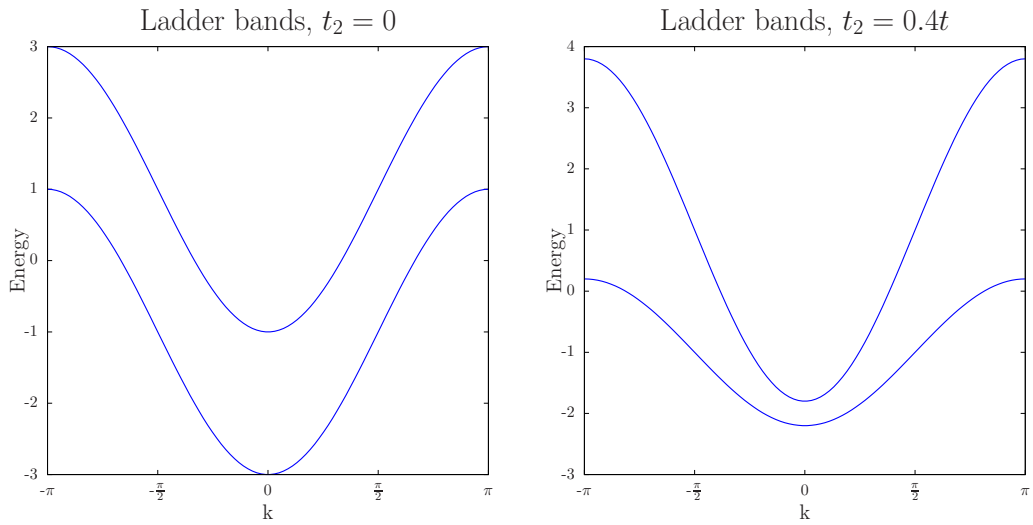

Figure B.2: Band structure of the t,t_2 model on the ladder.

The occupation of the bands as a function of the chemical potential and the energy are provided by the correlations $\langle X^\dagger_{j,\alpha,\sigma} X_{j',\alpha',\sigma}\rangle$. These are easily calculated by writing the in terms of the correlations

in the eigenstates which are diagonal

$$\langle X^{\dagger}_{j,\alpha,\sigma} X_{j',\alpha',\sigma} \rangle = \frac{1}{L_X} \sum_k e^{i(j-j')k} \delta_{\alpha,\alpha'} \langle X^{\dagger}_{k,\alpha,\sigma} X_{k,\alpha,\sigma} \rangle. \tag{B.4}$$

The occupancy of the eigenstates is given by the Fermi function and at zero temperature they are all fully occupied below the chemical potential and equal to zero above the chemical potential, providing the real space correlations as

$$\langle X^{\dagger}_{j,\alpha,\sigma} X_{j',\alpha',\sigma} \rangle = \delta_{\alpha,\alpha'} \int_{-K_{\alpha\sigma}}^{K_{\alpha\sigma}} \frac{dk}{2\pi} e^{imk} \tag{B.5}$$

where the wavenumber $K_{\alpha\sigma}$ provides the Fermi surface,

$$-2(t - \alpha t_2) \cos K_{\alpha\sigma} - \alpha t = \mu \tag{B.6}$$

This immediately provides the occupation number of the two bands as

$$n_{X\alpha\sigma} = \langle X^{\dagger}_{j,\alpha,\sigma} X_{j,\alpha,\sigma} \rangle = \frac{K_{\alpha\sigma}}{\pi} \tag{B.7}$$

and the off-site correlations as

$$\langle X^{\dagger}_{j,\alpha,\sigma} X_{j+m,\alpha,\sigma} \rangle = \frac{\sin(\pi n_{X\alpha\sigma} m)}{m\pi}. \tag{B.8}$$

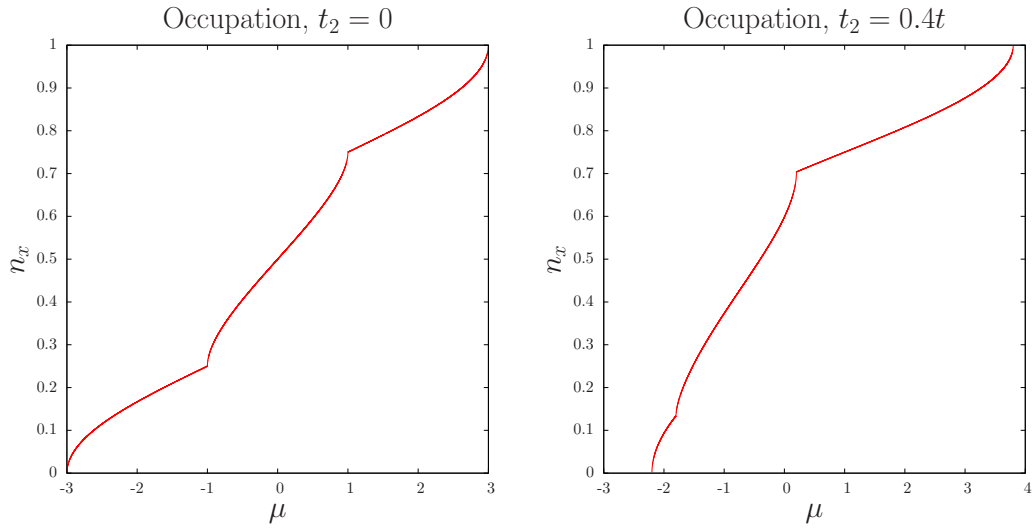

Figure B.3: The total number of holes per site of the band-structure indicated in figure B.2 as a function of the chemical potential.

The total spin-σ occupation per site $n_{X\sigma} = \frac{1}{2}(n_{X,+,\sigma} + n_{X,-,\sigma})$ as a function of the chemical potential is depicted in Figure B.3. There are three distinct regions. For $-3t+2t_2 \leq \mu < -t-2t_2$, the chemical potential is below the bottom of the antisymmetric band, so that only the symmetric band is active. The occupation numbers are then given by

$$\begin{aligned} 2(t-t_2)\cos(\pi n_{X,+,\sigma}) + t + \mu &= 0\,, \\ n_{X,-,\sigma} &= 0\,, \end{aligned} \tag{B.9}$$

and as a result

$$n_{X\sigma} = \frac{1}{2\pi}\arccos\left(\frac{-t-\mu}{2(t-t_2)}\right). \tag{B.10}$$

In the region $-t-2t_2 \leq \mu \leq t-2t_2$ both the symmetric and antisymmetric bands are active, and we have

$$\begin{aligned} 2(t-t_2)\cos(\pi n_{X,+,\sigma}) + t + \mu &= 0\,, \\ 2(t+t_2)\cos(\pi n_{X,-,\sigma}) - t + \mu &= 0\,, \end{aligned} \tag{B.11}$$

and the total number of holes is given by,

$$n_{X\sigma} = \frac{1}{2\pi}\arccos\left(\frac{-t-\mu}{2(t-t_2)}\right) + \frac{1}{2\pi}\arccos\left(\frac{t-\mu}{2(t+t_2)}\right). \tag{B.12}$$

Finally, in the region $t-2t_2 < \mu \leq 3t+2t_2$, the symmetric band is fully occupied, only the antisymmetric

band is active and we have

$$\begin{aligned} n_{X,+,\sigma} &= 1\,, \\ 2(t+t_2)\cos\left(\pi n_{X,-,\sigma}\right) - t + \mu &= 0\,. \end{aligned} \tag{B.13}$$

It follows that the occupation is given by

$$n_{X\sigma} = \frac{1}{2} + \frac{1}{2\pi}\arccos\left(\frac{t-\mu}{2(t+t_2)}\right). \tag{B.14}$$

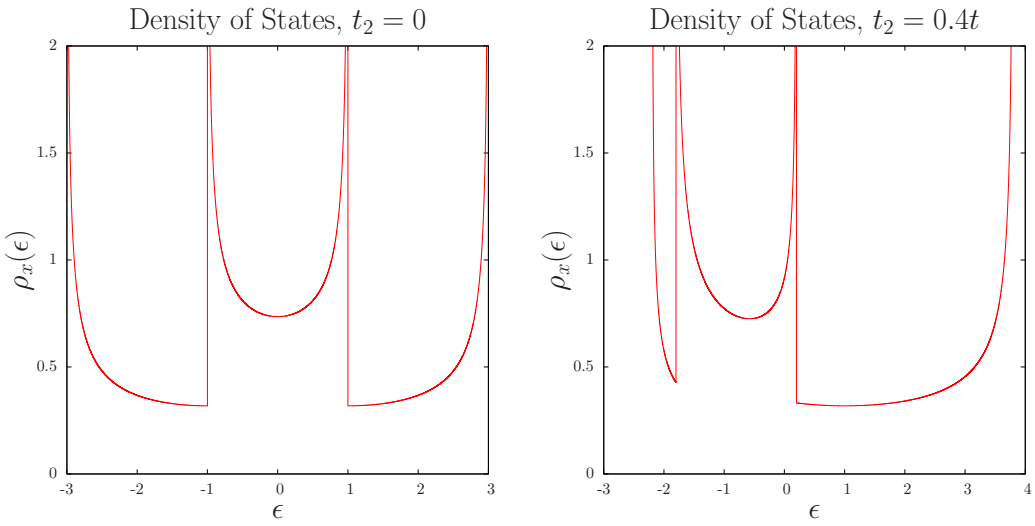

Figure B.4: X-band density of states $\rho_X(\epsilon)$.

The density of states is depicted in B.4. This is simply the sum of contributions from the symmetric and antisymmetric bands:

$$\begin{aligned} \rho_X(\epsilon) &= \frac{1}{2L_x}\sum_k \left[\delta(\epsilon + 2(t-t_2)\cos k + t) + \delta(\epsilon + 2(t+t_2)\cos k - t)\right] \\ &\to \frac{1}{2}\int_{-\pi}^{\pi}\frac{dk}{2\pi}\left[\delta(\epsilon + 2(t-t_2)\cos k + t) + \delta(\epsilon + 2(t+t_2)\cos k - t)\right] \\ &= \frac{(t-t_2)}{\pi}\int_{-2(t-t_2)}^{2(t-t_2)}\frac{dx}{\sqrt{(2(t-t_2))^2 - x^2}}\delta(\epsilon + x + t) \\ &\quad + \frac{(t+t_2)}{\pi}\int_{-2(t+t_2)}^{2(t+t_2)}\frac{dx}{\sqrt{(2(t-t_2))^2 - x^2}}\delta(\epsilon + x - t) \\ &= \frac{(t-t_2)}{\pi\sqrt{(2(t-t_2))^2 - (\epsilon+t)^2}}\Theta\left(-2(t-t_2) - t < \epsilon < 2(t-t_2) - t\right) \\ &\quad + \frac{(t+t_2)}{\pi\sqrt{(2(t+t_2))^2 - (\epsilon-t)^2}}\Theta\left(-2(t+t_2) + t < \epsilon < 2(t+t_2) + t\right)\,. \end{aligned} \tag{B.15}$$

And so, in the three distinct regions discussed in relation to the occupation, the density of states takes the form

$$\rho_X(\epsilon) = \begin{cases} \frac{(t-t_2)}{\pi\sqrt{(2(t-t_2))^2-(\epsilon+t)^2}}, & -3t+2t_2 \leq \mu < -t-2t_2 \\ \frac{(t-t_2)}{\pi\sqrt{(2(t-t_2))^2-(\epsilon+t)^2}} + \frac{(t+t_2)}{\pi\sqrt{(2(t+t_2))^2-(\epsilon-t)^2}}, & -t-2t_2 \leq \mu \leq t-2t_2 \\ \frac{(t+t_2)}{\pi\sqrt{((t+t_2))^2-(\epsilon-t)^2}}, & t-2t_2 < \mu \leq 3t+2t_2\,. \end{cases} \tag{B.16}$$

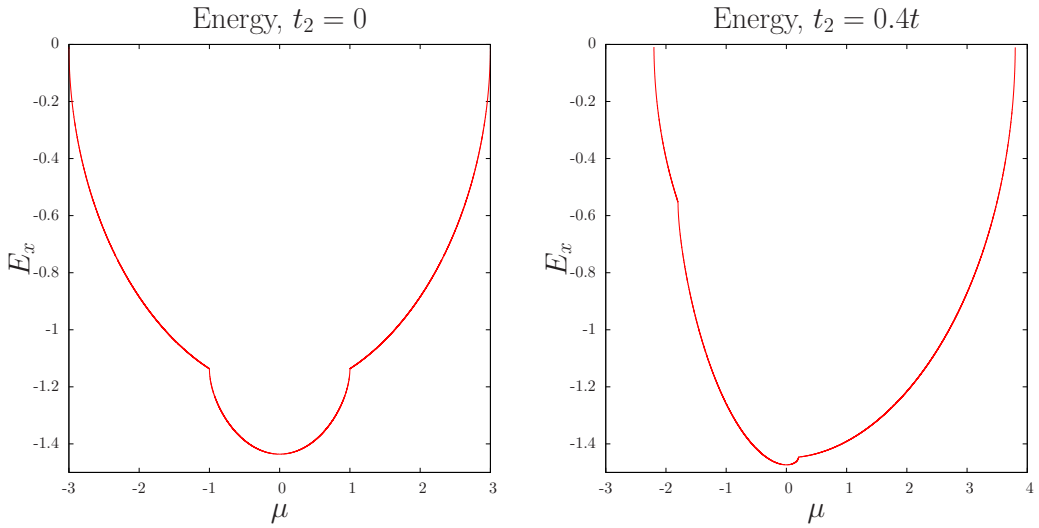

Figure B.5: X-band energy E_X as a function of chemical potential

Finally, we depict the energy of the tight-binding model in B.5. It is straightforward to represent the energy in terms of the occupancies as

$$\begin{aligned} E_X = \frac{\langle H_X\rangle}{2L_x} &= \frac{1}{2L_x}\sum_{j\alpha\sigma}\langle -(t-\alpha t_2)(X^\dagger_{j\alpha\sigma}X_{j+1\alpha\sigma} + X^\dagger_{j\alpha\sigma}X_{j-1\alpha\sigma}) - \alpha t X^\dagger_{j\alpha\sigma}X_{j\alpha\sigma}\rangle \\ &= \frac{1}{2}\sum_{\alpha\sigma}\left[-2(t-\alpha t_2)\frac{\sin(\pi n_{X\alpha\sigma})}{\pi} - \alpha t n_{X\alpha\sigma}\right] \end{aligned} \tag{B.17}$$

B.2 Z orbital band-structure

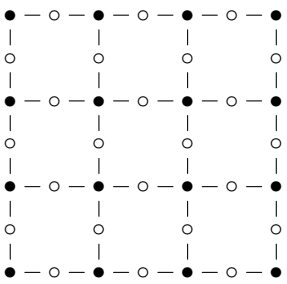

Figure B.6: Illustration of the square lattice geometry for the Z holes. The filled circles correspond to Ru sites and the open circles to O sites.

The tight-binding Hamiltonian on the square lattice is given by

$$H_Z = \sum_{\vec{k}\sigma} \left(-2t\cos k_x - 2t\cos k_y + 4t_2 \cos k_x \cos k_y\right) Z^\dagger_{\vec{k}\sigma} Z_{\vec{k}\sigma}, \tag{B.18}$$

where the operators $Z^\dagger_{\vec{k}\sigma}$ correspond to the usual Bloch states,

$$Z^\dagger_{\vec{k}\sigma} = \frac{1}{\sqrt{L_x L_y}} \sum_j e^{i\vec{k}\cdot\vec{R}_j} Z^\dagger_{j\sigma},$$

where the index j labels the sites on the square lattice, and L_x and L_y are the dimensions of the system. We have assumed periodic boundary conditions in both of the principal directions of the square lattice. The band-structure,

$$\epsilon^Z_{\vec{k}} = 2t\cos k_x - 2t\cos k_y + 4t_2 \cos k_x \cos k_y, \tag{B.19}$$

is depicted in figure B.7.

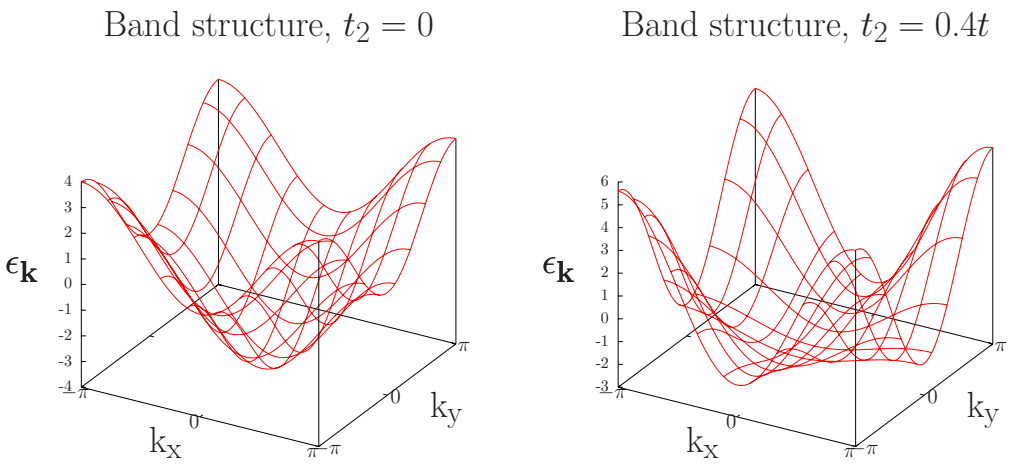

Figure B.7: Band structure of the t,t_2 model on the square lattice.

The density of states is given by

$$\rho_Z(\epsilon) = \sum_{\vec{k}} \delta(\epsilon - \epsilon^Z_{\vec{k}}) = \int_{-\pi}^{\pi} \frac{dk_x}{2\pi} \int_{-\pi}^{\pi} \frac{dk_y}{2\pi} \delta(\epsilon + 2t\cos k_x + 2t\cos k_y - 4t_2 \cos k_x \cos k_y)$$
$$= \frac{1}{\pi^2} \int_{-1}^{1} \frac{dx}{\sqrt{1-x^2}} \int_{-1}^{1} \frac{dy}{\sqrt{1-y^2}} \delta(\epsilon + 2tx + 2ty - 4t_2 xy), \tag{B.20}$$

and the single-particle correlations are given by

$$\langle Z^\dagger_{j\sigma} Z_{j+m_1\hat{x}+m_2\hat{y}\sigma} \rangle = \frac{1}{L_x L_y} \sum_{\mathbf{k}} e^{i(m_1 k_x + m_2 k_y)} \langle Z^\dagger_{\mathbf{k}\sigma} Z_{\mathbf{k}\sigma} \rangle$$
$$= \int_{-\pi}^{\pi} \frac{dk_x}{2\pi} \int_{-\pi}^{\pi} \frac{dk_y}{2\pi} e^{i(m_1 k_x + m_2 k_y)} \Theta(-2t\cos k_x - 2t\cos k_y + 4t_2 \cos k_x \cos k_y - \mu)$$
$$= \frac{1}{\pi^2} \int_{-1}^{1} \frac{dx}{\sqrt{1-x^2}} \int_{-1}^{1} \frac{dy}{\sqrt{1-y^2}} x^{m_1} y^{m_2} \Theta(-2t(x+y) + 4t_2 xy - \mu), \tag{B.21}$$

where the theta function ensures that the integration is only taken over the states below the chemical potential.

The single-particle correlations and the density of states can be represented in the form of elliptic integrals. Practically speaking, each of these quantities can be represented as a single definite integral which can easily be calculated using a computer. Such a representation is obtained by performing one of the two integrals in the expressions B.20 and B.21 analytically. In the following, we will derive representations for the particle number $n_{Z\sigma} = \langle Z^\dagger_{j\sigma} Z_{j\sigma} \rangle$, the density of states $\rho_Z(\epsilon)$ and the energy

E_Z, which is composed of nearest- and next-nearest-neighbour correlations. We discuss the occupation number in the most detail, and thereafter apply the same parameterisation to the other quantities.

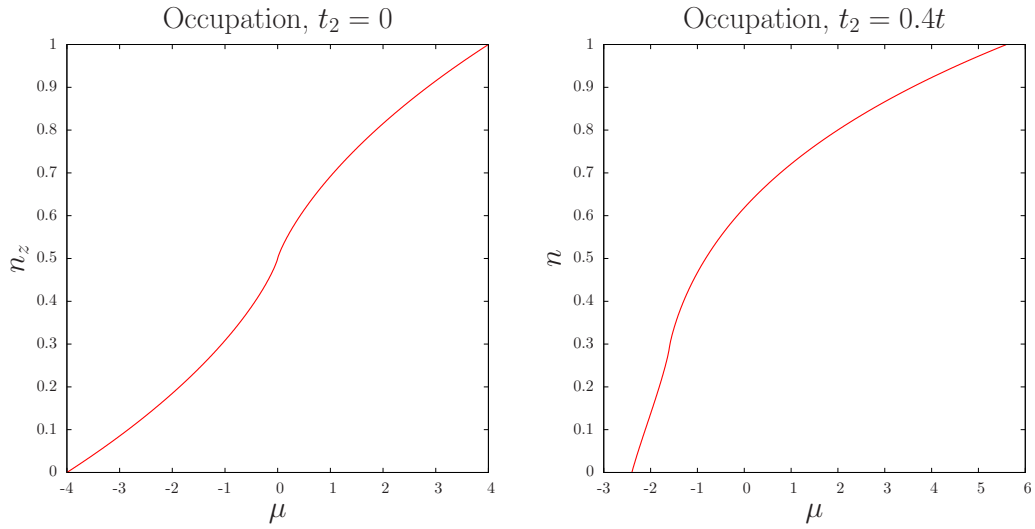

Figure B.8: Occupation of the t,t_2 model on the square lattice as a function of chemical potential.

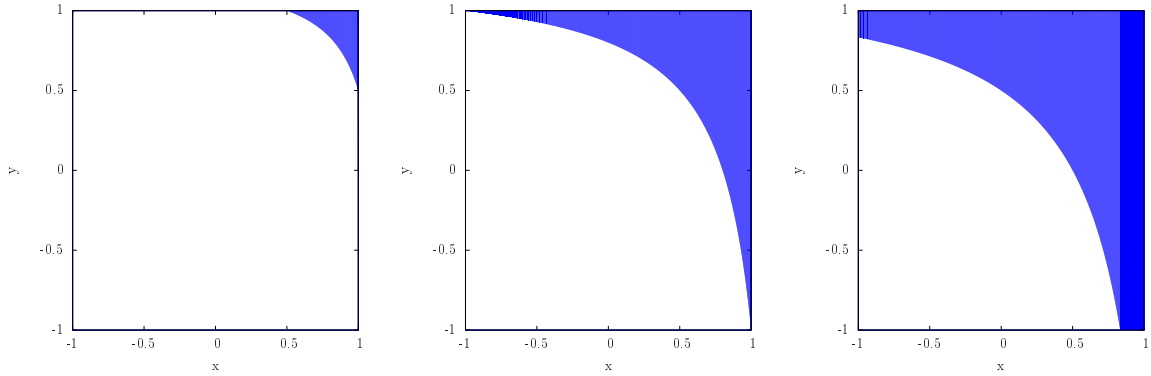

Figure B.9: Illustrative examples of the regions of integration $-2t(x+y)+4t_2xy-\mu>0$ (indicated by the shaded region) of the square lattice integrals, for the three cases $-4t+4t_2<\mu<-4t_2$ (left), $\mu=-4t_2$ (middle) and $-4t_2<\mu<4t+4t_2$ (right).

The occupation number $n_{Z\sigma}=\langle Z^\dagger_{j\sigma}Z_{j\sigma}\rangle$ is shown as a function of the chemical potential in B.8. If we examine the argument of the theta function in the expression for the correlation, we are required to integrate over the region where

$$y>\frac{-\mu-2tx}{2t-4t_2x}$$

The region of integration corresponding to the occupied states is pictured in B.9 for the three cases which must be distinguished, $-4t+4t_2\leq\mu<-4t_2$, $\mu=-4t_2$ and $-4t_2<\mu\leq 4t+4t_2$. For the case

$-4t + 4t_2 \leq \mu < -4t_2$ the integral is

$$n_{Z\sigma} = \frac{1}{\pi^2} \int_{\frac{-\mu-2t}{2t-4t_2}}^{1} \frac{dx}{\sqrt{1-x^2}} \int_{\frac{-\mu-2tx}{2t-4t_2x}}^{1} \frac{dy}{\sqrt{1-y^2}} \tag{B.22}$$

The integration over y can be performed exactly to give,

$$n_{Z\sigma} = \frac{1}{\pi^2} \int_{\frac{-\mu-2t}{2t-4t_2}}^{1} \frac{dx}{\sqrt{1-x^2}} \cos^{-1}\left(\frac{-\mu-2tx}{2t-4t_2x}\right). \tag{B.23}$$

The case $\mu > -4t_2$ is most conveniently represented in terms of the integral over the *unoccupied* states. The fully occupied band of course has $n_z = 1$ and so we may write,

$$n_{Z\sigma} = 1 - \frac{1}{\pi^2} \int_{-1}^{\frac{2t-\mu}{2t+4t_2}} \frac{dx}{\sqrt{1-x^2}} \int_{-1}^{\frac{-\mu-2tx}{2t-4t_2x}} \frac{dy}{\sqrt{1-y^2}} \tag{B.24}$$

The integral in this expression can be carefully rewritten to obtain a form very similar to that of the first case

$$\begin{aligned}
\frac{1}{\pi^2} \int_{-1}^{\frac{2t-\mu}{2t+4t_2}} \frac{dx}{\sqrt{1-x^2}} \int_{-1}^{\frac{-\mu-2tx}{2t-4t_2x}} \frac{dy}{\sqrt{1-y^2}} &= \frac{1}{\pi^2} \int_{-1}^{\frac{2t-\mu}{2t+4t_2}} \frac{dx}{\sqrt{1-x^2}} \int_{\frac{\mu+2tx}{2t-4t_2x}}^{1} \frac{dy}{\sqrt{1-y^2}} \\
&= \frac{1}{\pi^2} \int_{-1}^{\frac{2t-\mu}{2t+4t_2}} \frac{dx}{\sqrt{1-x^2}} \cos^{-1}\left(\frac{\mu+2tx}{2t-4t_2x}\right)
\end{aligned}$$

$$n_{Z\sigma} = 1 - \frac{1}{\pi^2} \int_{\frac{-2t+\mu}{2t+4t_2}}^{1} \frac{dx}{\sqrt{1-x^2}} \cos^{-1}\left(\frac{\mu-2tx}{2t+4t_2x}\right) \tag{B.25}$$

In both cases, we must calculate the integral

$$\mathcal{J}(\mu) = \frac{1}{\pi^2} \int_{\frac{-2t+\tau\mu}{2t+4\tau t_2}}^{1} \frac{dx}{\sqrt{1-x^2}} \cos^{-1}\left(\frac{-2tx+\tau\mu}{2t+4\tau t_2x}\right) \tag{B.26}$$

where we define

$$\tau(\mu) = \begin{cases} 1, & -4t_2 < \mu \leq 4t + 4t_2 \\ -1, & 4t + 4t_2 \leq \mu < -4t_2 \end{cases}. \tag{B.27}$$

The occupation number is

$$n_{Z\sigma} = \begin{cases} 1 - \mathcal{J}(\mu), & -4t_2 < \mu \leq 4t + 4t_2 \\ \mathcal{J}(\mu), & 4t + 4t_2 \leq \mu < -4t_2 \end{cases} \tag{B.28}$$

We obtain a cleaner representation for $\mathcal{J}(\mu)$ by making the change of variable $x = \cos\theta$:

$$\mathcal{J}(\mu) = \frac{1}{\pi^2}\int_0^q d\theta \cos^{-1}\left(\frac{2t + (2t + 4\tau t_2)\cos q - 2t\cos\theta}{2t + 4\tau t_2 \cos\theta}\right)$$

where,

$$\cos q = \frac{-2t + \tau\mu}{2t + 4\tau t_2}. \tag{B.29}$$

For performing the numerical calculations, it is not desirable for the limits of integration be dependant on the parameters μ and t_2. We choose to remove this dependence by making the recaling $\theta = q\phi$ which provides

$$\mathcal{J}(\mu) = \frac{q}{\pi^2}\int_0^1 d\phi \cos^{-1}\left(\frac{2t + (2t + 4\tau t_2)\cos q - 2t\cos q\phi}{2t + 4\tau t_2 \cos q\phi}\right)$$

Finally, it is found that the error in a finite element numerical integration is considerably reduced by making the change of variable $\phi = 1 - u^2$:

$$\mathcal{J}(\mu) = \frac{2q}{\pi^2}\int_0^1 u\cos^{-1}\left(\frac{1 + (1 + 2\tau\frac{t_2}{t})\cos q - \cos\left(q(1-u^2)\right)}{1 + 2\tau\frac{t_2}{t}\cos\left(q(1-u^2)\right)}\right)du \tag{B.30}$$

The occupation number $n_{Z\sigma}$ shows a kink at the special point $-4t_2$ which shows up as a divergence in the density of states, depicted in figure B.10. Such logarithmic divergences are a generic feature in two-dimensional band-structures.

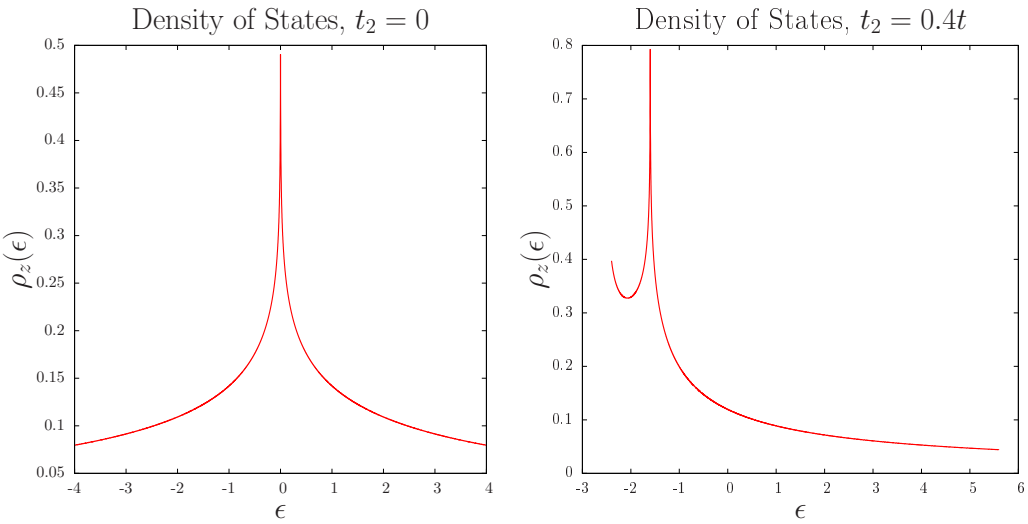

Figure B.10: Density of states $\rho_z(\epsilon)$ of the t,t_2 model on the square lattice.

The density of states is shown in Figure B.10. This is of course given by

$$\begin{aligned}\rho_Z(\epsilon) = \sum_{\vec{k}} \delta(\epsilon - \epsilon_{\vec{k}}) &= \int_{-\pi}^{\pi} \frac{dk_x}{2\pi} \int_{-\pi}^{\pi} \frac{dk_y}{2\pi} \delta(\epsilon + 2t\cos k_x + 2t\cos k_y - 4t_2 \cos k_x \cos k_y) \\ &= \frac{1}{\pi^2} \int_{-1}^{1} \frac{dx}{\sqrt{1-x^2}} \int_{-1}^{1} \frac{dy}{\sqrt{1-y^2}} \delta(\epsilon + 2tx + 2ty - 4t_2 xy) \\ &= \frac{1}{\pi^2} \int_{-1}^{1} \frac{dx}{\sqrt{1-x^2}} \frac{1}{(2t - 4t_2 x)} \int_{-1}^{1} \frac{dy}{\sqrt{1-y^2}} \delta\left(y + \frac{\epsilon + 2tx}{2t - 4t_2 x}\right) \\ &= \frac{1}{2\pi^2 t} \int_{-1}^{1} \frac{dx}{\sqrt{1-x^2}} \frac{1}{(1 - 2\frac{t_2}{t} x)} \frac{1}{\sqrt{1 - \left(\frac{-2tx-\epsilon}{2t-4t_2 x}\right)^2}} \Theta\left(-1 < \frac{-2tx-\epsilon}{2t-4t_2 x} < 1\right)\end{aligned} \tag{B.31}$$

$$\rho_Z(\epsilon) = \frac{1}{2\pi^2 t} \int_{\frac{-2t-\epsilon}{2t-4t_2}}^{1} \frac{dx}{\sqrt{1-x^2}} \frac{1}{(1 - 2\frac{t_2}{t} x)\sqrt{1 - \left(\frac{-2tx-\epsilon}{2t-4t_2 x}\right)^2}} \quad \text{for} -4t + 4t_2 \leq \epsilon < -4t_2$$

$$\rho_Z(\epsilon) = \frac{1}{2\pi^2 t} \int_{-1}^{\frac{2t-\epsilon}{2t+4t_2}} \frac{dx}{\sqrt{1-x^2}} \frac{1}{(1 - 2\frac{t_2}{t} x)\sqrt{1 - \left(\frac{-2tx-\epsilon}{2t-4t_2 x}\right)^2}} \quad \text{for} -4t_2 < \epsilon \leq 4t + 4t_2$$

Applying the same parameterisation as for the occupation number, we obtain

$$\begin{aligned}\rho_Z(\epsilon) &= \frac{1}{2\pi^2 t} \int_0^q \frac{d\theta}{\sqrt{\left(1 + 2\tau\frac{t_2}{t}\cos\theta\right)^2 - \left(1 + (1 + 2\tau\frac{t_2}{t})\cos q - \cos\theta\right)^2}} \\ &= \frac{q}{\pi^2 t} \int_0^1 \frac{udu}{\sqrt{\left(1 + 2\tau\frac{t_2}{t}\cos\left(q(1-u^2)\right)\right)^2 - \left(1 + (1 + 2\tau\frac{t_2}{t})\cos q - \cos\left(q(1-u^2)\right)\right)^2}}\end{aligned} \tag{B.32}$$

where the latter form is more computationally effective, and where

$$\cos q = \frac{-2t + \tau\epsilon}{2t + 4\tau t_2}, \qquad \tau = \begin{cases} 1, & -4t_2 < \epsilon \leq 4t + 4t_2 \\ -1, & 4t + 4t_2 \leq \epsilon < -4t_2. \end{cases} \tag{B.33}$$

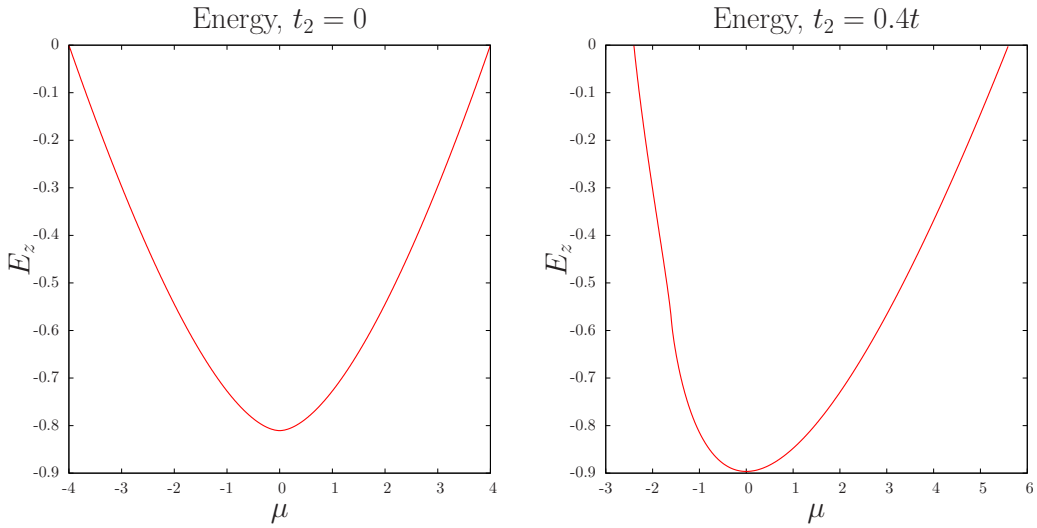

Figure B.11: Energy of the t,t_2 model on the square lattice as a function of chemical potential.

The energy is shown in Figure B.11. The energy is given in terms of single-particle correlations by

$$\begin{aligned} E_Z = \frac{\langle H_z \rangle}{L_x L_y} &= \frac{1}{L_x L_y} \langle -t \sum_{\langle jj' \rangle_1 \sigma} Z^\dagger_{j\sigma} Z_{j'\sigma} + t_2 \sum_{\langle jj' \rangle_2 \sigma} Z^\dagger_{j\sigma} Z_{j'\sigma} \rangle \\ &= -4t \left(\langle Z^\dagger_{j\uparrow} Z_{j+\hat{y}\uparrow} \rangle + \langle Z^\dagger_{j\downarrow} Z_{j+\hat{y}\downarrow} \rangle \right) + 4t_2 \left(\langle Z^\dagger_{j\uparrow} Z_{j+\hat{x}+\hat{y}\uparrow} \rangle + \langle Z^\dagger_{j\downarrow} Z_{j+\hat{x}+\hat{y}\downarrow} \rangle \right) \end{aligned} \tag{B.34}$$

The two correlations which we require, for the case $\mu < -4t_2$ can be written as

$$\begin{aligned} \langle Z^\dagger_{j\sigma} Z_{j+\hat{y}\sigma} \rangle &= \frac{1}{\pi^2} \int_{\frac{-2t-\mu}{2t-4t_2}}^{1} \frac{dx}{\sqrt{1-x^2}} \int_{\frac{-2tx-\mu}{2t-4t_2 x}}^{1} \frac{ydy}{\sqrt{1-y^2}} \\ &= \frac{1}{\pi^2} \int_{\frac{-2t-\mu}{2t-4t_2}}^{1} \frac{dx}{\sqrt{1-x^2}} \sqrt{1 - \left(\frac{-2tx-\mu}{2t-4t_2 x} \right)^2} \end{aligned} \tag{B.35}$$

$$\begin{aligned} \langle Z^\dagger_{j\sigma} Z_{j+\hat{x}+\hat{y}\sigma} \rangle &= \frac{1}{\pi^2} \int_{\frac{-2t-\mu}{2t-4t_2}}^{1} \frac{xdx}{\sqrt{1-x^2}} \int_{\frac{-2tx-\mu}{2t-4t_2 x}}^{1} \frac{ydy}{\sqrt{1-y^2}} \\ &= \frac{1}{\pi^2} \int_{\frac{-2t-\mu}{2t-4t_2}}^{1} \frac{xdx}{\sqrt{1-x^2}} \sqrt{1 - \left(\frac{-2tx-\mu}{2t-4t_2 x} \right)^2} \end{aligned} \tag{B.36}$$

For the case $\mu > -4t_2$ we again represent the integral over the occupied states as the fully occupied

band minus the unoccupied states:

$$\begin{aligned}
\langle Z^{\dagger}_{j\sigma} Z_{j+\hat{y}\sigma} \rangle &= 0 - \frac{1}{\pi^2} \int_{-1}^{\frac{2t-\mu}{2t+4t_2}} \frac{dx}{\sqrt{1-x^2}} \int_{-1}^{\frac{-2tx-\mu}{2t-4t_2x}} \frac{ydy}{\sqrt{1-y^2}} \\
&= \frac{1}{\pi^2} \int_{-1}^{\frac{2t-\mu}{2t+4t_2}} \frac{dx}{\sqrt{1-x^2}} \sqrt{1-\left(\frac{-2tx-\mu}{2t-4t_2x}\right)^2} \\
&= \frac{1}{\pi^2} \int_{\frac{-2t+\mu}{2t+4t_2}}^{1} \frac{dx}{\sqrt{1-x^2}} \sqrt{1-\left(\frac{2tx-\mu}{2t+4t_2x}\right)^2} \qquad \text{(B.37)} \\
\langle Z^{\dagger}_{j\sigma} Z_{j+\hat{x}+\hat{y}\sigma} \rangle &= 0 - \frac{1}{\pi^2} \int_{-1}^{\frac{2t-\mu}{2t+4t_2}} \frac{xdx}{\sqrt{1-x^2}} \int_{-1}^{\frac{-2tx-\mu}{2t-4t_2x}} \frac{ydy}{\sqrt{1-y^2}} \\
&= \frac{1}{\pi^2} \int_{-1}^{\frac{2t-\mu}{2t+4t_2}} \frac{xdx}{\sqrt{1-x^2}} \sqrt{1-\left(\frac{-2tx-\mu}{2t-4t_2x}\right)^2} \\
&= -\frac{1}{\pi^2} \int_{\frac{-2t+\mu}{2t+4t_2}}^{1} \frac{xdx}{\sqrt{1-x^2}} \sqrt{1-\left(\frac{2tx-\mu}{2t+4t_2x}\right)^2} \qquad \text{(B.38)}
\end{aligned}$$

We process these integrals in exactly the manner as in the calculation of $n_{Z\sigma}$, with the convention

$$\tau = \begin{cases} +1, & -4t_2 < \mu \leq 4t + 4t_2 \\ -1, & 4t + 4t_2 \leq \mu < -4t_2 \end{cases}, \qquad \text{(B.39)}$$

to obtain the representations

$$\langle Z^{\dagger}_{j\sigma} Z_{j+\hat{y}\sigma} \rangle = \mathcal{Q}_1(\mu), \qquad \langle Z^{\dagger}_{j\sigma} Z_{j+\hat{x}+\hat{y}\sigma} \rangle = \mathcal{Q}_2(\mu), \qquad \text{(B.40)}$$

where

$$\mathcal{Q}_1(\mu) = \frac{2q}{\pi^2} \int_0^1 u \sqrt{1-\left(\frac{1+(1+2\tau\frac{t_2}{t})\cos q - \cos\left(q(1-u^2)\right)}{1+2\tau\frac{t_2}{t}\cos\left(q(1-u^2)\right)}\right)^2} du, \qquad \text{(B.41)}$$

$$\mathcal{Q}_2(\mu) = -\tau\frac{2q}{\pi^2} \int_0^1 u\cos\left(q(1-u^2)\right) \sqrt{1-\left(\frac{1+(1+2\tau\frac{t_2}{t})\cos q - \cos\left(q(1-u^2)\right)}{1+2\tau\frac{t_2}{t}\cos\left(q(1-u^2)\right)}\right)^2} du. \qquad \text{(B.42)}$$

Appendix C

Procedures for the mean field theory calculations

In this appendix we describe the computational procedures which we use to calculate the mean field solutions. For given values of the internal parameters $\tilde{\mu}$ and $\tilde{B}$, the six band occupation numbers $n_{X\uparrow}$, $n_{X\downarrow}$, $n_{Z\uparrow}$ and $n_{Z\uparrow}$ are obtained as the solutions of a set of *internal equations*; these occupation numbers determine the total number of holes and the magnetisation as

$$n = n_{X\uparrow} + n_{X\downarrow} + n_{Z\uparrow} + n_{Z\downarrow}, \tag{C.1}$$

$$M = n_{X\uparrow} + n_{Z\uparrow} - n_{X\downarrow} - n_{Z\downarrow}. \tag{C.2}$$

The values of $\tilde{\mu}$ and $\tilde{B}$ must then be tuned to provide the correct number of holes and external magnetic field, that is to satisfy the *external equations*,

$$n = 2, \tag{C.3}$$

$$B = \tilde{B} - \frac{J}{2}M. \tag{C.4}$$

The solutions of both the internal equations and the external equations are solved using Newton-Raphson procedures. A full calculation therefore involves two nested Newton-Raphson procedures, with each iteration of the procedure for the external equations requiring the solving of the internal equations.

C.1 Internal equations

The use of the parameters $\tilde{B}$ and $\tilde{\mu}$ as independent variables allows the mean field theory to be parameterised in such a way that the self-consistent equations for the band occupation numbers contain no terms which couple the occupation numbers of distinct orbital species. One has to deal with pairs of coupled equations for the spin-$\uparrow$ and spin-$\downarrow$ holes of each orbital species. Because we treat the X and Y orbitals as equivalent, these are governed by the same set of occupation numbers; there are therefore just two pairs of coupled equations, one pair for the X/Y occupation numbers $n_{X\uparrow}$ and $n_{X\downarrow}$, and one pair for the Z occupation numbers $n_{Z\uparrow}$ and $n_{Z\downarrow}$.

C.1.1 X/Y occupation numbers

In the 6-band case, the four occupation numbers $n_{X\alpha\sigma}$ are deteremined by the four self-consistent equations,

$$2(t-\alpha t_2)\cos(\pi n_{X,+,\sigma}) + \alpha t + \tilde{\mu} + \tilde{B}\sigma + (U-J)n_{X\sigma} - 2Jn_{X\bar{\sigma}} = 0. \tag{C.5}$$

One can eliminate the occupancies of the individual bands to obtain an equation purely in $n_{X\uparrow}$ and $n_{X\downarrow}$. We first represent the equations in terms of $n_{X\sigma} = \frac{1}{2}(n_{X,+,\sigma} + n_{X,-,\sigma})$ and the difference in the individual band occupancies, $w_{X\sigma} = \frac{1}{2}(n_{X,+,\sigma} - n_{X,-,\sigma})$. Taking the sum of the two spin-σ cases of C.5 gives

$$2t\cos(\pi n_{X\sigma})\cos(\pi w_{X\sigma}) + 2t_2\sin(\pi n_{X\sigma})\sin(\pi w_{X\sigma}) + \tilde{\mu} + \tilde{B}\sigma + (U-J)n_{X\sigma} - 2Jn_{X\bar{\sigma}} = 0 \tag{C.6}$$

and taking the difference of these two equations gives,

$$-2t\sin(\pi n_{X\sigma})\sin(\pi w_{X\sigma}) - 2t_2\cos(\pi n_{X\sigma})\cos(\pi w_{X\sigma}) + t = 0. \tag{C.7}$$

Taking appropriate linear combinations of equations C.6 and C.7 to eliminate each of the quantities $\cos(\pi n_{X\sigma})\cos(\pi w_{X\sigma})$ and $\sin(\pi n_{X\sigma})\sin(\pi w_{X\sigma})$ we obtain,

$$2t\left(1-(\tfrac{t_2}{2})^2\right)\cos(\pi n_{X\sigma})\cos(\pi w_{X\sigma}) = -t_2 - \left(\tilde{\mu} + \tilde{B}\sigma + (U-J)n_{X\sigma} - 2Jn_{X\bar{\sigma}}\right), \tag{C.8}$$

$$-2t\left(1-(\tfrac{t_2}{2})^2\right)\sin(\pi n_{X\sigma})\sin(\pi w_{X\sigma}) = -t - \tfrac{t_2}{t}\left(\tilde{\mu} + \tilde{B}\sigma + (U-J)n_{X\sigma} - 2Jn_{X\bar{\sigma}}\right). \tag{C.9}$$

We now square both sides of each of these equations, and eliminate the variable $\sin^2(\pi w_{X\sigma}) = 1 - \cos^2(\pi w_{X\sigma})$ to finally obtain

$$\frac{\left(t_2 + \tilde{\mu} + \tilde{B} + (U-J)n_{X\sigma} - 2Jn_{X\bar{\sigma}}\right)^2}{t^2\cos^2(\pi n_{X\sigma})} + \frac{\left(t + \frac{t_2}{t}\left(\tilde{\mu} + \tilde{B} + (U-J)n_{X\sigma} - 2Jn_{X\bar{\sigma}}\right)\right)^2}{t^2\sin^2(\pi n_{X\sigma})} - 4\left(1 - (\tfrac{t_2}{t})^2\right)^2 = 0 \tag{C.10}$$

In the 6-band solution, $n_{X\uparrow}$ and $n_{X\downarrow}$ therefore satisfy the two coupled equations,

$$\frac{\left(t_2 + \tilde{\mu} + \tilde{B} + (U-J)n_{X\uparrow} - 2Jn_{X\downarrow}\right)^2}{t^2\cos^2(\pi n_{X\uparrow})} + \frac{\left(t + \frac{t_2}{t}\left(\tilde{\mu} + \tilde{B} + (U-J)n_{X\uparrow} - 2Jn_{X\downarrow}\right)\right)^2}{t^2\sin^2(\pi n_{X\uparrow})} - 4\left(1 - (\tfrac{t_2}{t})^2\right)^2 = 0 \tag{C.11}$$

$$\frac{\left(t_2 + \tilde{\mu} - \tilde{B} + (U-J)n_{X\downarrow} - 2Jn_{X\uparrow}\right)^2}{t^2\cos^2(\pi n_{X\downarrow})} + \frac{\left(t + \frac{t_2}{t}\left(\tilde{\mu} - \tilde{B} + (U-J)n_{X\downarrow} - 2Jn_{X\uparrow}\right)\right)^2}{t^2\sin^2(\pi n_{X\downarrow})} - 4\left(1 - (\tfrac{t_2}{t})^2\right)^2 = 0 \tag{C.12}$$

In the 5-band solution, we exclude the occupation number $n_{X,-,\downarrow}$ from consideration. The total number of spin-$\downarrow$ holes per site is then $n_{X\downarrow} = \frac{n_{X,-,\downarrow}}{2}$. The equation C.11 still holds and the second equation is provided by C.5:

$$\frac{\left(t_2 + \tilde{\mu} + \tilde{B} + (U-J)n_{X\uparrow} - 2Jn_{X\downarrow}\right)^2}{t^2\cos^2(\pi n_{X\uparrow})} + \frac{\left(t + \frac{t_2}{t}\left(\tilde{\mu} + \tilde{B} + (U-J)n_{X\uparrow} - 2Jn_{X\downarrow}\right)\right)^2}{t^2\sin^2(\pi n_{X\uparrow})} - 4\left(1 - (\tfrac{t_2}{t})^2\right)^2 = 0 \tag{C.13}$$

$$2(t - t_2)\cos(2\pi n_{X\downarrow}) + t + \tilde{\mu} - \tilde{B} + (U-J)n_{X\downarrow} - 2Jn_{X\uparrow} = 0 \tag{C.14}$$

We solve the two coupled equations using a Newton-Raphson procedure. Let

$$f_{X\uparrow}(n_{X\uparrow}, n_{X\downarrow}) = \frac{\left(t_2 + \tilde{\mu} + \tilde{B} + (U-J)n_{X\uparrow} - 2Jn_{X\downarrow}\right)^2}{t^2\cos^2(\pi n_{X\uparrow})} + \frac{\left(t + \frac{t_2}{t}\left(\tilde{\mu} + \tilde{B} + (U-J)n_{X\uparrow} - 2Jn_{X\downarrow}\right)\right)^2}{t^2\sin^2(\pi n_{X\uparrow})} - 4\left(1 - (\tfrac{t_2}{t})^2\right)^2 \tag{C.15}$$

and let

$$f_{X\downarrow}(n_{X\uparrow}, n_{X\downarrow}) = \frac{\left(t_2 + \tilde{\mu} - \tilde{B} + (U-J)n_{X\downarrow} - 2Jn_{X\uparrow}\right)^2}{t^2\cos^2(\pi n_{X\downarrow})} + \frac{\left(t + \frac{t_2}{t}\left(\tilde{\mu} - \tilde{B} + (U-J)n_{X\downarrow} - 2Jn_{X\uparrow}\right)\right)^2}{t^2\sin^2(\pi n_{X\downarrow})} - 4\left(1 - (\tfrac{t_2}{t})^2\right)^2 \tag{C.16}$$

in the 6-band case and

$$f_{X\downarrow}(n_{X\uparrow}, n_{X\downarrow}) = 2(t - t_2)\cos(2\pi n_{X\downarrow}) + t + \tilde{\mu} - \tilde{B} + (U-J)n_{X\downarrow} - 2Jn_{X\uparrow} \tag{C.17}$$

in the 5-band case. We can converge to the solution $f_{X\uparrow} = 0 = f_{X\downarrow}$ by repeated application of the mapping,

$$n_{X\uparrow} \to n_{X\uparrow} - \frac{f_{X\uparrow}\frac{\partial f_{X\downarrow}}{\partial n_{X\downarrow}} - \frac{\partial f_{X\uparrow}}{\partial n_{X\downarrow}} f_{X\downarrow}}{\frac{\partial f_{X\uparrow}}{\partial n_{X\uparrow}}\frac{\partial f_{X\downarrow}}{\partial n_{X\downarrow}} - \frac{\partial f_{X\uparrow}}{\partial n_{X\downarrow}}\frac{\partial f_{X\downarrow}}{\partial n_{X\uparrow}}}, \tag{C.18}$$

$$n_{X\downarrow} \to n_{X\downarrow} - \frac{\frac{\partial f_{X\uparrow}}{\partial n_{X\uparrow}} f_{X\downarrow} - f_{X\uparrow}\frac{\partial f_{X\downarrow}}{\partial n_{X\uparrow}}}{\frac{\partial f_{X\uparrow}}{\partial n_{X\uparrow}}\frac{\partial f_{X\downarrow}}{\partial n_{X\downarrow}} - \frac{\partial f_{X\uparrow}}{\partial n_{X\downarrow}}\frac{\partial f_{X\downarrow}}{\partial n_{X\uparrow}}}. \tag{C.19}$$

C.1.2 Z occupation numbers

To obtain the self-consistent equations for the occupation numbers $n_{Z\sigma}$ we apply the formula B.28 substituting the two effective chemical potentials,

$$\begin{aligned} \mu^{\text{eff}}_{Z\uparrow} &= \tilde{\mu} + \tilde{B} + (U-J)n_{Z\uparrow} - 2Jn_{Z\downarrow}, \\ \mu^{\text{eff}}_{Z\downarrow} &= \tilde{\mu} - \tilde{B} + (U-J)n_{Z\downarrow} - 2Jn_{Z\uparrow}, \end{aligned} \tag{C.20}$$

so that the two self-consistent equations are,

$$n_{Z\uparrow} = \begin{cases} 1 - \mathcal{J}(\mu^{\text{eff}}_{Z\uparrow}), & -4t_2 < \mu^{\text{eff}}_{Z\uparrow} \le 4t + 4t_2 \\ \mathcal{J}(\mu^{\text{eff}}_{Z\uparrow}), & 4t + 4t_2 \le \mu^{\text{eff}}_{Z\uparrow} < -4t_2 \end{cases} \tag{C.21}$$

$$n_{Z\downarrow} = \begin{cases} 1 - \mathcal{J}(\mu^{\text{eff}}_{Z\downarrow}), & -4t_2 < \mu^{\text{eff}}_{Z\downarrow} \le 4t + 4t_2 \\ \mathcal{J}(\mu^{\text{eff}}_{Z\downarrow}), & 4t + 4t_2 \le \mu^{\text{eff}}_{Z\downarrow} < -4t_2 \end{cases} \tag{C.22}$$

where

$$\mathcal{J}(\mu_{Z\sigma}^{\rm eff}) = \frac{2q}{\pi^2}\int_0^1 u\cos^{-1}\left(\frac{1+(1+2\tau\frac{t_2}{t})\cos q - \cos\left(q(1-u^2)\right)}{1+2\tau\frac{t_2}{t}\cos\left(q(1-u^2)\right)}\right)du, \tag{C.23}$$

$$\cos\left(q(\mu_{Z\sigma}^{\rm eff})\right) = \frac{-2t+\tau\mu_{Z\sigma}^{\rm eff}}{2t+4\tau t_2}, \tag{C.24}$$

$$\tau(\mu_{Z\sigma}^{\rm eff}) = \begin{cases} 1, & -4t_2 < \mu_{Z\sigma}^{\rm eff} \leq 4t+4t_2 \\ -1, & 4t+4t_2 \leq \mu_{Z\sigma}^{\rm eff} < -4t_2 \end{cases}. \tag{C.25}$$

These equations are solved using the same Newton-Raphson procedure as for the X/Y occupation numbers. We define

$$f_{Z\sigma}(n_{Z\uparrow}, n_{Z\downarrow}) = \begin{cases} 1-\mathcal{J}(\mu_{Z\sigma}^{\rm eff}) - n_{Z\sigma}, & -4t_2 < \mu_{Z\sigma}^{\rm eff} \leq 4t+4t_2 \\ \mathcal{J}(\mu_{Z\sigma}^{\rm eff}) - n_{Z\sigma}, & 4t+4t_2 \leq \mu_{Z\sigma}^{\rm eff} < -4t_2 \end{cases} \tag{C.26}$$

and we repeately apply the mapping,

$$n_{Z\uparrow} \to n_{Z\uparrow} - \frac{f_{Z\uparrow}\frac{\partial f_{Z\downarrow}}{\partial n_{Z\downarrow}} - \frac{\partial f_{Z\uparrow}}{\partial n_{Z\downarrow}}f_{Z\downarrow}}{\frac{\partial f_{Z\uparrow}}{\partial n_{Z\uparrow}}\frac{\partial f_{Z\downarrow}}{\partial n_{Z\downarrow}} - \frac{\partial f_{Z\uparrow}}{\partial n_{Z\downarrow}}\frac{\partial f_{Z\downarrow}}{\partial n_{Z\uparrow}}}, \tag{C.27}$$

$$n_{Z\downarrow} \to n_{Z\downarrow} - \frac{\frac{\partial f_{Z\uparrow}}{\partial n_{Z\uparrow}}f_{Z\downarrow} - f_{Z\uparrow}\frac{\partial f_{Z\downarrow}}{\partial n_{Z\uparrow}}}{\frac{\partial f_{Z\uparrow}}{\partial n_{Z\uparrow}}\frac{\partial f_{Z\downarrow}}{\partial n_{Z\downarrow}} - \frac{\partial f_{Z\uparrow}}{\partial n_{Z\downarrow}}\frac{\partial f_{Z\downarrow}}{\partial n_{Z\uparrow}}}. \tag{C.28}$$

The derivatives are simply represented in terms of the square lattice density of states:

$$\frac{\partial f_{Z\sigma}}{\partial n_{Z\sigma}} = (U-J)\rho_Z(\mu_{Z\sigma}^{\rm eff}) - 1, \qquad \frac{\partial f_{Z\sigma}}{\partial n_{Z\bar{\sigma}}} = -2J\rho_Z(\mu_{Z\sigma}^{\rm eff}). \tag{C.29}$$

Both the functions $f_{Z\sigma}$ and their derivatives are calculated to a high accuracy by evaluating the appropriate integral numerically using finite element methods.

C.2 External equations

Let $F(\tilde{\mu},\tilde{B}) = n(\tilde{\mu},\tilde{B}) - 2$ and $G(\tilde{\mu},\tilde{B}) = B - \tilde{B} + \frac{J}{2}M(\tilde{\mu},\tilde{B})$, so that the external equations are $F=0$ and $G=0$. If $\tilde{\mu}^*$ and $\tilde{B}^*$ are the values which satisfy these equations, then for values $\tilde{\mu}$ and $\tilde{B}$ close

to these values we can write

$$F(\tilde{\mu},\tilde{B}) \approx (\tilde{\mu}-\tilde{\mu}^*)\frac{\partial F}{\partial \tilde{\mu}} + (\tilde{B}-\tilde{B}^*)\frac{\partial F}{\partial \tilde{B}} \tag{C.30}$$

$$G(\tilde{\mu},\tilde{B}) \approx (\tilde{\mu}-\tilde{\mu}^*)\frac{\partial G}{\partial \tilde{\mu}} + (\tilde{B}-\tilde{B}^*)\frac{\partial G}{\partial \tilde{B}} \tag{C.31}$$

and these equations can be inverted to provide,

$$\tilde{\mu}^* \approx \tilde{\mu} - \frac{F\frac{\partial G}{\partial \tilde{B}} - \frac{\partial F}{\partial \tilde{B}}G}{\frac{\partial F}{\partial \tilde{\mu}}\frac{\partial G}{\partial \tilde{B}} - \frac{\partial F}{\partial \tilde{B}}\frac{\partial G}{\partial \tilde{\mu}}} \tag{C.32}$$

$$\tilde{B}^* \approx \tilde{B} - \frac{\frac{\partial F}{\partial \tilde{\mu}}G - F\frac{\partial G}{\partial \tilde{\mu}}}{\frac{\partial F}{\partial \tilde{\mu}}\frac{\partial G}{\partial \tilde{B}} - \frac{\partial F}{\partial \tilde{B}}\frac{\partial G}{\partial \tilde{\mu}}}. \tag{C.33}$$

We therefore can obtain successively better approximations to $\tilde{\mu}^*$ and $\tilde{B}^*$ by the repeated application of the mapping,

$$\tilde{\mu} \to \tilde{\mu} - \frac{F\frac{\partial G}{\partial \tilde{B}} - \frac{\partial F}{\partial \tilde{B}}G}{\frac{\partial F}{\partial \tilde{\mu}}\frac{\partial G}{\partial \tilde{B}} - \frac{\partial F}{\partial \tilde{B}}\frac{\partial G}{\partial \tilde{\mu}}} \tag{C.34}$$

$$\tilde{B} \to \tilde{B} - \frac{\frac{\partial F}{\partial \tilde{\mu}}G - F\frac{\partial G}{\partial \tilde{\mu}}}{\frac{\partial F}{\partial \tilde{\mu}}\frac{\partial G}{\partial \tilde{B}} - \frac{\partial F}{\partial \tilde{B}}\frac{\partial G}{\partial \tilde{\mu}}}. \tag{C.35}$$

At each iteration the left hand sides are calculated by solving the internal equations. The derivatives are approximated by first calculating F and G for the three sets of parameters, $(\tilde{\mu},\tilde{B})$, $(\tilde{\mu}+\delta\tilde{\mu},\tilde{B})$ and $(\tilde{\mu},\tilde{B}+\delta\tilde{B})$ for fixed values of $\delta\tilde{\mu}$ and $\delta\tilde{B}$ which can be regarded as tunable parameters of the *algorithm*, and then computing

$$\frac{\partial F}{\partial \tilde{\mu}} \approx \frac{F(\tilde{\mu}+\delta\tilde{\mu},\tilde{B}) - F(\tilde{\mu},\tilde{B})}{\delta\tilde{\mu}} \tag{C.36}$$

and the analogous expressions.

References for Part 2

[50] Y. Maeno *et al.*, Superconductivity in a layered perovskite without copper, Nature **372**, 532 (1994).

[51] A. P. Mackenzie *et al.*, Extremely strong dependence of superconductivity on disorder in Sr_2RuO_4, Phys. Rev. Lett. **80**, 161 (1998).

[52] G. Cao, S. K. McCall, J. E. Crow, and R. P. Guertin, Ferromagnetism in $Sr_4Ru_3O_{10}$: Relationship to other layered metallic oxides, Phys. Rev. B **56**, R5740 (1997).

[53] M. K. Crawford *et al.*, Structure and magnetism of single crystal $Sr_4Ru_3O_{10}$: A ferromagnetic triple-layer ruthenate, Phys. Rev. B **65**, 214412 (2002).

[54] A. Callaghan, C. Moeller, and R. Ward, Magnetic interactions in ternary ruthenium oxides, Inorganic Chemistry **5**, 1572 (1966).

[55] J. Longo, P. Raccah, and J. Goodenough, Magnetic properties of $SrRuO_3$ and $CaRuO_3$, Journal of Applied Physics **39**, 1327 (1968).

[56] R. S. Perry *et al.*, Metamagnetism and critical fluctuations in high quality single crystals of the bilayer ruthenate $Sr_3Ru_2O_7$, Phys. Rev. Lett. **86**, 2661 (2001).

[57] E. Ohmichi *et al.*, Double metamagnetic transition in the bilayer ruthenate $Sr_3Ru_2O_7$, Phys. Rev. B **67**, 024432 (2003).

[58] S. A. Grigera *et al.*, Magnetic field-tuned quantum criticality in the metallic ruthenate $Sr_3Ru_2O_7$, Science **294**, 329 (2001).

[59] M. Chiao *et al.*, Effect of pressure on metamagnetic $Sr_3Ru_2O_7$, Physica B: Condensed Matter **312–313**, 698 (2002), The International Conference on Strongly Correlated Electron Systems.

[60] R. S. Perry *et al.*, Multiple first-order metamagnetic transitions and quantum oscillations in ultrapure $Sr_3Ru_2O_7$, Phys. Rev. Lett. **92**, 166602 (2004).

[61] Y. Tokiwa, M. Mchalwat, R. S. Perry, and P. Gegenwart, Multiple metamagnetic quantum criticality in $Sr_3Ru_2O_7$, Phys. Rev. Lett. **116**, 226402 (2016).

[62] L. Capogna *et al.*, Observation of two-dimensional spin fluctuations in the bilayer ruthenate $Sr_3Ru_2O_7$ by inelastic neutron scattering, Phys. Rev. B **67**, 012504 (2003).

[63] C. Lester *et al.*, Field-tunable spin-density-wave phases in $Sr_3Ru_2O_7$, Nature Materials **14**, 373 (2015).

[64] H. Shaked, J. D. Jorgensen, O. Chmaissem, S. Ikeda, and Y. Maeno, Neutron diffraction study of the structural distortions in $Sr_3Ru_2O_7$, J. Solid State Chem **154**, 361 (2000).

[65] A. Tamai *et al.*, Fermi surface and van hove singularities in the itinerant metamagnet $Sr_3Ru_2O_7$, Phys. Rev. Lett. **101**, 026407 (2008).

[66] J.-F. Mercure *et al.*, Quantum oscillations near the metamagnetic transition in $Sr_3Ru_2O_7$, Phys. Rev. B **81**, 235103 (2010).

[67] A. Damascelli *et al.*, Fermi surface of Sr_2RuO_4 from angle resolved photoemission, Journal of Electron Spectroscopy and Related Phenomena **114**, 641 (2001), Proceeding of the Eight International Conference on Electronic Spectroscopy and Structure.

[68] J.-F. Mercure *et al.*, Quantum oscillations in the anomalous phase in $Sr_3Ru_2O_7$, Phys. Rev. Lett. **103**, 176401 (2009).

[69] C. Bergemann, A. P. Mackenzie, S. R. Julian, D. Forsythe, and E. Ohmichi, Quasi-two-dimensional fermi liquid properties of the unconventional superconductor Sr_2RuO_4, Advances in Physics **52**, 639 (2003).

[70] K. Iwaya *et al.*, Local tunneling spectroscopy across a metamagnetic critical point in the bilayer ruthenate $Sr_3Ru_2O_7$, Phys. Rev. Lett. **99**, 057208 (2007).

[71] Z. V. Pchelkina *et al.*, Evidence for strong electronic correlations in the spectra of Sr_2RuO_4, Phys. Rev. B **75**, 035122 (2007).

[72] D. J. Singh and I. I. Mazin, Electronic structure and magnetism of $Sr_3Ru_2O_7$, Phys. Rev. B **63**, 165101 (2001).

[73] C. Piefke and F. Lechermann, LDA plus slave-boson approach to the correlated electronic structure of the metamagnetic bilayer ruthenate $Sr_3Ru_2O_7$, physica status solidi (b) **248**, 2269 (2011).

[74] B. Binz and M. Sigrist, Metamagnetism of itinerant electrons in multi-layer ruthenates, EPL (Europhysics Letters) **65**, 816 (2004).

[75] B. Binz, H. B. Braun, T. M. Rice, and M. Sigrist, Magnetic domain formation in itinerant metamagnets, Phys. Rev. Lett. **96**, 196406 (2006).

[76] D. Fobes *et al.*, Anisotropy of magnetoresistivities in $Sr_4Ru_3O_{10}$: Evidence for an orbital-selective metamagnetic transition, Phys. Rev. B **81**, 172402 (2010).

[77] D. Belitz, T. R. Kirkpatrick, and J. Rollbühler, Tricritical behavior in itinerant quantum ferromagnets, Phys. Rev. Lett. **94**, 247205 (2005).

[78] M. Uhlarz, C. Pfleiderer, H. von Löhneysen, S. Hayden, and G. Lonzarich, Pressure dependence of the ferromagnetic ordering temperature in single-crystal $ZrZn_2$, Physica B: Condensed Matter **312**, 487 (2002), The International Conference on Strongly Correlated Electron Systems.

[79] M. Uhlarz, C. Pfleiderer, and S. M. Hayden, Quantum phase transitions in the itinerant ferromagnet $ZrZn_2$, Phys. Rev. Lett. **93**, 256404 (2004).

[80] W. Wu *et al.*, Quantum critical metamagnetism of $Sr_3Ru_2O_7$ under hydrostatic pressure, Phys. Rev. B **83**, 045106 (2011).

[81] S. A. Grigera *et al.*, Angular dependence of the magnetic susceptibility in the itinerant metamagnet $Sr_3Ru_2O_7$, Phys. Rev. B **67**, 214427 (2003).

[82] Y. V. Sushko *et al.*, Hydrostatic pressure effects on the magnetic susceptibility of ruthenium oxide $Sr_3Ru_2O_7$: evidence for pressure-enhanced antiferromagnetic instability, Solid State Communications **130**, 341 (2004).

[83] S.-I. Ikeda *et al.*, The pressure dependence of magnetization of layered perovskite oxides with $4d$-electron metal, Physica C: Superconductivity and its Applications **364–365**, 376 (2001).

[84] J. A. Hertz, Quantum critical phenomena, Phys. Rev. B **14**, 1165 (1976).

[85] A. J. Millis, Effect of a nonzero temperature on quantum critical points in itinerant fermion systems, Phys. Rev. B **48**, 7183 (1993).

[86] A. J. Schofield, Quantum criticality and novel phases: Summary and outlook, physica status solidi (b) **247**, 563 (2010).

[87] K. Kitagawa *et al.*, Metamagnetic quantum criticality revealed by $^{17}O-$NMR in the itinerant metamagnet $Sr_3Ru_2O_7$, Phys. Rev. Lett. **95**, 127001 (2005).

[88] P. Gegenwart, F. Weickert, M. Garst, R. S. Perry, and Y. Maeno, Metamagnetic quantum criticality in $Sr_3Ru_2O_7$ studied by thermal expansion, Phys. Rev. Lett. **96**, 136402 (2006).

[89] J. Okamoto *et al.*, Correlation effects in the electronic structure of $SrRuO_3$, Phys. Rev. B **60**, 2281 (1999).

[90] G. R. Stewart, Heavy-fermion systems, Rev. Mod. Phys. **56**, 755 (1984).

[91] R. A. Borzi *et al.*, de haas˘van alphen effect across the metamagnetic transition in $Sr_3Ru_2O_7$, Phys. Rev. Lett. **92**, 216403 (2004).

[92] Y. Tokiwa, T. Radu, C. Geibel, F. Steglich, and P. Gegenwart, Divergence of the magnetic grüneisen ratio at the field-induced quantum critical point in $YbRh_2Si_2$, Phys. Rev. Lett. **102**, 066401 (2009).

[93] A. Mackenzie, J. Bruin, R. Borzi, A. Rost, and S. Grigera, Quantum criticality and the formation of a putative electronic liquid crystal in $Sr_3Ru_2O_7$, Physica C: Superconductivity **481**, 207 (2012).

[94] A. G. Green *et al.*, Phase bifurcation and quantum fluctuations in $Sr_3Ru_2O_7$, Phys. Rev. Lett. **95**, 086402 (2005).

[95] S. A. Grigera *et al.*, Disorder-sensitive phase formation linked to metamagnetic quantum criticality, Science **306**, 1154 (2004).

[96] C. Stingl, R. S. Perry, Y. Maeno, and P. Gegenwart, Symmetry-breaking lattice distortion in $Sr_3Ru_2O_7$, Phys. Rev. Lett. **107**, 026404 (2011).

[97] A. W. Rost, R. S. Perry, J.-F. Mercure, A. P. Mackenzie, and S. A. Grigera, Entropy landscape of phase formation associated with quantum criticality in $Sr_3Ru_2O_7$, Science **325**, 1360 (2009).

[98] F. Weickert, P. Gegenwart, R. Perry, and Y. Maeno, Alternating-field magnetoresistance measurements on $Sr_3Ru_2O_7$, Physica C: Superconductivity and its Applications **460-462**, 520 (2007), Proceedings of the 8th International Conference on Materials and Mechanisms of Superconductivity and High Temperature Superconductors.

[99] R. A. Borzi *et al.*, Formation of a nematic fluid at high fields in sr3ru2o7, Science **315**, 214 (2007), http://science.sciencemag.org/content/315/5809/214.full.pdf.

[100] H.-Y. Kee and Y. B. Kim, Itinerant metamagnetism induced by electronic nematic order, Phys. Rev. B **71**, 184402 (2005).

[101] W.-C. Lee and C. Wu, Theory of unconventional metamagnetic electron states in orbital band systems, Phys. Rev. B **80**, 104438 (2009).

[102] S. Raghu *et al.*, Microscopic theory of the nematic phase in $Sr_3Ru_2O_7$, Phys. Rev. B **79**, 214402 (2009).

[103] J. Farrell *et al.*, Effect of electron doping the metamagnet $Sr_{3-y}La_yRu_2O_7$, Phys. Rev. B **78**, 180409 (2008).

[104] E. P. Wohlfarth and P. Rhodes, Collective electron metamagnetism, Philosophical Magazine **7**, 1817 (1962).

[105] A. A. Abrikosov, L. P. Gorkov, and I. E. Dzyaloshinski, *Methods of Quantum Field Theory in Statistical Physics* (Dover, New York, 1963).

[106] P. W. Anderson, *Concepts in Solids* (Addison-Wesley, Redwood City, California, 1963).

[107] J. Hubbard, Electron correlations in narrow energy bands, Proc. R. Soc. London A **276**, 238 (1963).

[108] C. Martins, M. Aichhorn, and S. Biermann, Coulomb correlations in 4*d* and 5*d* oxides from first principles - or how spin–orbit materials choose their effective orbital degeneracies, Journal of Physics: Condensed Matter **29**, 263001 (2017).

[109] S. J. Moon and T. W. Noh, Spectroscopic studies of strong spin-orbit coupling in 4*d*- and 5*d*-transition metal oxides, in *Frontiers of* 4*d*- *and* 5*d*- *Transition Metal Oxides*, edited by G. Cao and D. L., chap. 2, pp. 7–42, World Scientific, Singapore, 2013.

[110] W. von der Linden and D. M. Edwards, Ferromagnetism in the hubbard model, Journal of Physics: Condensed Matter **3**, 4917 (1991).

[111] G. Cao, L. E. DeLong, and P. Schlottmann, The contradictory physical properties and extreme anisotropy of $Ca_3Ru_2O_7$, in *Frontiers of* 4*d*- *and* 5*d*- *Transition Metal Oxides*, edited by G. Cao and D. L., chap. 2, pp. 179–214, World Scientific, Singapore, 2013.

[112] G.-Q. Liu, Mott transition and magnetic anisotropy in $Ca_3Ru_2O_7$, Phys. Rev. B **84**, 235137 (2011).

[113] J. B. Goodenough, Jahn - Teller phenomena in solids, Annual Review of Materials Science **28**, 1 (1998).